

# **Synthesis and characterization of new adsorbents for CO<sub>2</sub> capturing**

by  
Marvin Piet

A thesis submitted in partial fulfillment of the requirements for the  
degree of Doctor Scientiae, in the Department of Chemistry,  
University of the Western Cape.



**Supervisor:** Dr Salam Titinchi  
**Co-supervisor:** Dr Hanna Abbo

## Abstract

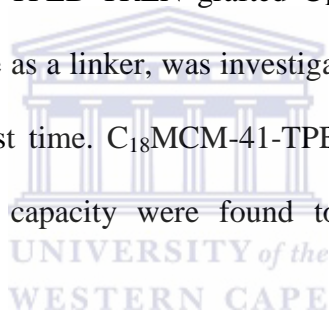
Carbon dioxide emissions have become a major concern as they are one of the contributing factors to the “green-house” effect. Recently, much effort has been put into separating carbon dioxide (CO<sub>2</sub>) from flue gases linked to the combustion processes at fixed point sources. The development of solid sorbents for adsorption based on CO<sub>2</sub> capture has attracted much attention. Ordered Mesoporous Silica (OMS) materials have recently attracted much attention as solid adsorbents for capturing CO<sub>2</sub>. OMS have been investigated for this purpose owing to their high pore volume, large surface area and ease of functionalization

In this work we report on the synthesis of OMS *viz.* MCM-41 and SBA-15 along with amorphous silica as adsorbents for CO<sub>2</sub> capture. MCM-41 was prepared with surfactants having different alkyl chain lengths (C<sub>14</sub>TABr, C<sub>16</sub>TABr and C<sub>18</sub>TABr) where TABr is trimethylammonium bromide. SBA-15 was prepared using a Triblock copolymer as a structure directing agent for the organization of polymerizing silica species. Commercial amorphous silica gel was used for comparative purposes. Initial characterization OMS with powder X-Ray diffraction (XRD) and small angle diffraction (SAXS) yielded diffraction patterns which may be associated with well-ordered structures of hexagonal mesoporous material. Ease of preparation for MCM-41 materials allowed for convenient scale-up, obtaining highly ordered mesoporous silica MCM-41 at room temperature. SBA-15 was also found to be scaled up with considerable ease through increasing the volume of the autoclave during hydrothermal treatment. Structural, morphological and textural properties of the adsorbents were characterized by N<sub>2</sub> physisorption measurements, Transmission Electron Microscopy (TEM),

Scanning Electron Microscopy (SEM) and Thermogravimetric Analysis (TGA). TEM confirmed the hexagonal structure; SEM showed that C<sub>14</sub>MCM-41 had spheroidal particle morphology whereas SBA-15 displayed rod-like structures. High surface areas of up to 1302, 1186, 1211 and 1024 m<sup>2</sup>/g for C<sub>14</sub>MCM-41, C<sub>16</sub>MCM-41, C<sub>18</sub>MCM-41 and SBA-15, respectively were obtained. The pore size of MCM-41 materials was increased from 2.6 nm for C<sub>14</sub>MCM-41 to 4.4 nm in diameter for C<sub>18</sub>MCM-41 using surfactants with different alkyl chain lengths. CO<sub>2</sub> adsorption characteristics of OMS were studied using CO<sub>2</sub>-temperature programmed desorption (TPD). The results showed that C<sub>14</sub>MCM-41, C<sub>16</sub>MCM-41, C<sub>18</sub>MCM-41 and SBA-15 desorbed 0.19, 0.16, 0.11 and 0.26 mmol/g respectively.

The synthesized OMS were then further modified by grafting various amine moieties on their surfaces in order to increase their CO<sub>2</sub> adsorptive capabilities. 3-(Aminopropyl)triethoxysilane (APS), N-[3-(trimethoxysilyl)propyl]ethylenediamine (TPED), 3-chloropropyl-trimethoxysilane (CPS), ethyl 2-bromopropanoate, tris(2-aminoethyl)amine (TREN) and guanidine. Several characterization techniques such as XRD, SAXS, HRTEM, HRSEM, TGA, Fourier Transform Infra-Red (FT-IR) spectroscopy, CO<sub>2</sub> isotherms and CO<sub>2</sub>-TPD were used to analyze amine grafted solid sorbents for CO<sub>2</sub> capture. The results revealed that the structural integrity of the amine modified sorbents was not compromised during the grafting process. The structural properties of the supports, such as surface area and pore size, nature of amine and the number of amine groups, affected the loading and CO<sub>2</sub> adsorption capacity of chemically grafted sorbents. APS grafted amorphous silica gel adsorbed 0.67 mmol/g CO<sub>2</sub>,

which proved to be the highest compared to C<sub>18</sub>MCM-41 and SBA-15 grafted with APS and TPED. C<sub>18</sub>MCM-41, SBA-15 and amorphous silica gel were also grafted with TREN and adsorbed 0.42, 0.51 and 0.27 mmol/g of CO<sub>2</sub>, respectively. A systematic study of guanidine grafted on C<sub>14</sub>MCM-41, C<sub>16</sub>MCM-41 and C<sub>18</sub>MCM-41 was investigated, for the first time, to the best of our knowledge. Structural properties like variation in pore size, proved to enhance the adsorption capacity of the adsorbent, coupled with the guanidine molecules grafted on MCM-41 materials. C<sub>18</sub>MCM-41-guanidine showed the highest CO<sub>2</sub> uptake of the guanidine grafted MCM-41 materials, adsorbing 0.30 mmol/g. A novel synthetic route to TPED-TREN grafted C<sub>18</sub>MCM-41 and SBA-15, using ethyl 2-bromopropanoate as a linker, was investigated as a potential adsorbent for CO<sub>2</sub> capture, for the first time. C<sub>18</sub>MCM-41-TPED-TREN and SBA-15-TPED-TREN CO<sub>2</sub> adsorption capacity were found to be 0.14 and 0.14 mmol/g, respectively.



## **Keywords**

Mesoporous silica, Surfactants, Amine groups, CO<sub>2</sub> adsorption, Temperature  
Programmed Desorption.



## Declaration

I declare that "**Synthesis and characterization of new adsorbents for CO<sub>2</sub> capturing**" is my own work, that it has not been submitted for any degree or examination in any other university, and that all the sources I have used or quoted have been indicated and acknowledged by complete references.

Full name:.....

Date:.....

Signed:.....



## **Acknowledgements**

I would first and foremost like to thank GOD ALMIGHTY for his guidance and grace in my life, for without him nothing would be possible. His mercies have granted me the strength and endurance to pursue my goals and ambitions on a daily basis.

I would like to take this opportunity to show my deepest gratitude to Dr. S.J.J Titinchi for allowing me to conduct my PhD studies under his prestigious supervision. His constant interest in his profession and his unwavering work ethic have added a new dimension to my once nonchalant approach to research problems, and have revived my sense of curiosity which guided me to the field where I currently find myself. His guidance, not only in a supervisory capacity, but also as a “father figure”, together with our daily talks (project and social orientated) in the morning and evening, made it a pleasure to conduct research under his supervision. For this I will be forever grateful. I would also like to thank my co-supervisor Dr H. Abbo for believing in my ability and offering to share some of her vast knowledge, experience and expertise from the time of my MSc studies up until the completion of my PhD. Her no nonsense approach to research has taught me valuable lessons, and has given me the ability to confidently handle myself in the research arena. Her insight and intellect as well as practical experience have added value to my set skills. These are valuable attributes a researcher requires, and I am grateful that I had the opportunity to observe and absorb some of these traits, which I will be carrying with me throughout my professional career.

I would also like to thank Prof. Dr. W. Schwieger for allowing me to conduct research under his supervision at the Friedrich Alexandra University, Erlangen, Germany. His guidance and vast experience taught me new approaches to tackling research problems. I would also like to thank Dr. Alexandra Inayat, Albert Machoke, Hendryk Partsch, Dennis Kreienbrink, Marion Bartsch and Stephanie Reuß for their academic and social support during my stay in Erlangen. Friendships that were forged during my stay in Erlangen will forever be close to my heart. I would like to show my appreciation to Dr. Alexandra Inayat for sharing her tremendous intellect and for the countless discussions regarding my work, and for opening the doors to her home and family.

I would also like to thank my lab colleagues in the catalysis laboratory, Gavin von Willing, Veruscha Paulsen, Joy-lynn Cook and Sylvia Pieters for their support during my studies in the lab. I would also like to thank the academic staff in the Chemistry department for their support during my PhD studies at the University of the Western Cape. I would like to thank Dr. F Cummings from the electron microscope unit (EMU) for all his expertise.

I would like to show my appreciation to my grandmother (Elizabeth Lilly Piet), mother (Bonniegirl Mercia Piet) and sister (Nerina Piet) for their resolute encouragement and support throughout my academic career. I take this opportunity to express my deepest gratitude for their die hard support and allowing me to pursue my life goals. I would also like to thank friends and family who have motivated me throughout my academic career.



I would like to thank the love of my life, Sylvia Pieters, for all her words of encouragement and relentless support, and for also setting me on the path of post graduate studies. For this I am eternally grateful.

Last but not least. I would like to thank the National Research Foundation (NRF) and German Academic Exchange Service (DAAD) funding bodies for providing the financial support that enabled me to pursue my post graduate studies.



## **Dedication**

I dedicate this work to my mother, Ms Bonniegirl Piet, my late father Nelson Masoka, grandmother Mrs Elizabeth Piet, and my sister, Mrs Nerina Peterson.



### **Oral presentations**

1. Marvin Piet. Research stay in Germany. 3rd DAAD-NRF In-Country Scholarship Holders Meeting. Protea Hotel, Stellenbosch, November 8-10, 2013.
2. Marvin Piet, Salam Titinchi, Hanna Abbo. Chemically modified solid sorbents for capturing CO<sub>2</sub>. Carbon Capture Workshop, New Life Science building, UWC, March 24-26, 2014.



## Table of contents

Abstract .....	ii
Keywords .....	v
Declaration .....	vi
Acknowledgements .....	vii
Dedication .....	x
Table of contents .....	xii
List of Figures .....	xviii
List of tables .....	xxiii
List of schemes .....	xxv
CHAPTER 1 .....	1
1.1 Introduction .....	1
1.1.1 Pre combustion capture .....	7
1.1.2 Post combustion capture .....	7
1.1.3 Oxy-combustion capture .....	8
1.2 Research scope .....	12
1.3 Structure of thesis .....	12
CHAPTER 2 : Literature review .....	17
2.1 Methods used to capture CO <sub>2</sub> .....	17
2.1.1 Absorption .....	17
2.1.2 Absorption methods .....	17

2.1.2.1 Physical absorption.....	17
2.1.2.2 Chemical absorption.....	18
2.1.3 Adsorbent.....	20
2.2 Solid adsorbents.....	22
2.2.1 Carbonaceous materials.....	22
2.2.2 Metal oxides.....	25
2.2.3 Hydrotalcites.....	26
2.2.4 Zeolites.....	28
2.2.5 MOFs.....	33
2.2.6 Zeolitic Imidazolate frameworks (ZIFs).....	37
2.2.7 Mesoporous materials.....	38
2.2.7.1 Ordered mesoporous silica (OMS).....	39
2.3 OMS (MCM-41 and SBA-15) CO <sub>2</sub> adsorbents.....	45
2.4 Functionalization of OMS.....	46
2.5 Methods used to functionalize OMS.....	47
2.5.1 Physical impregnation.....	47
2.5.2 Co-condensation.....	51
2.5.3 Anionic surfactant template method.....	52
2.5.4 Post synthesis chemical grafting.....	53
2.6 Factors influencing CO <sub>2</sub> adsorption capacity of amine modified mesoporous silica.....	55

2.7 Amine grafted mesoporous silica for CO <sub>2</sub> capture.....	55
CHAPTER 3 .....	82
3.1 Materials and methods .....	82
3.2 Methodology .....	83
3.2.1 MCM-41 synthesis (C <sub>14</sub> TABr, C <sub>16</sub> TABr and C <sub>18</sub> TABr).....	83
3.2.2 C <sub>18</sub> MCM-41 upscale synthesis .....	83
3.2.3 SBA-15 synthesis .....	84
3.2.4 Modified mesoporous silica with APS (1 <sup>st</sup> generation G1 adsorbents).....	84
3.2.5 TPED modified mesoporous silica's (G1).....	85
3.2.6 TREN modified mesoporous silica's (2 <sup>nd</sup> generation G2 adsorbents).....	86
3.2.7 Guanidine grafted mesoporous silica's (G2).....	86
3.2.8 Expansion of 1 <sup>st</sup> generation adsorbents (G3).....	87
3.3 Characterization .....	88
3.3.1 XRD.....	88
3.3.2 SAXS.....	90
3.3.3 Transmission Electron Microscopy (TEM) .....	91
3.3.4 Scanning Electron Microscopy (SEM) .....	92
3.3.5 Nitrogen (N <sub>2</sub> ) physisorption measurements .....	92
3.3.6 Thermogravimetric analysis (TGA).....	96
3.3.7 Fourier transform infrared (FTIR) .....	97

3.3.8 Elemental analysis.....	97
3.3.9 Nuclear magnetic resonance (NMR).....	98
3.3.10 Temperature Programmed Desorption (TPD).....	100
CHAPTER 4: Characterization of support materials.....	106
4.1 Systematic study of MCM-41 .....	106
4.2 SBA-15.....	110
4.3 FT-IR analysis.....	120
4.4 CO <sub>2</sub> -TPD analysis .....	122
CHAPTER 5: Functionalization of supports.....	127
5.1 Systematic loading of amine linker onto support.....	127
5.2 Functionalization with APS and TPED (G1) .....	133
5.3 XRD.....	134
5.4 SAXS.....	136
5.5 HRSEM.....	138
5.6 Textural properties.....	139
5.7 TG evaluation.....	146
5.8 FT-IR analysis.....	150
5.9 CO <sub>2</sub> isotherm studies.....	153
5.8 CO <sub>2</sub> -TPD measurements.....	158
CHAPTER 6: Supports functionalized with TREN.....	166
6.1 TREN grafted mesoporous silica .....	166

6.2 Structural properties of TREN grafted mesoporous silica .....	167
6.3 HRSEM images of TREN grafted mesoporous silica.....	169
6.4 Textural properties of TREN grafted mesoporous silica .....	171
6.6. TG analysis .....	175
6.7 FT-IR.....	180
6.8 CO <sub>2</sub> isotherm studies.....	183
6.9 CO <sub>2</sub> TPD.....	185
CHAPTER 7: Systematic study of guanidine grafted MCM-41 .....	190
7.1 Systematic study of guanidine grafted MCM-41 with different pore sizes ...	190
7.2 Systematic XRD study .....	191
7.5 TG studies of guanidine grafted MCM-41 supports .....	200
7.6 FT-IR.....	204
7.7 <sup>13</sup> C CPMAS NMR.....	207
7.8 CO <sub>2</sub> isotherms .....	210
7.9 CO <sub>2</sub> TPD.. .....	212
CHAPTER 8: Expansion of amine groups .....	219
8.1 XRD and SAXS of TPED-TREN grafted C <sub>18</sub> MCM-41 and SBA-15 .....	220
8.2 Textural properties of TPED-TREN grafted C <sub>18</sub> MCM-41 and SBA-15 .....	222
8.3 TG analysis .....	226
8.4 FT-IR analysis.....	229
8.5 CO <sub>2</sub> isotherms .....	232



8.6 CO <sub>2</sub> TPD studies .....	234
Conclusion .....	238
9.2 Future work .....	243



## List of Figures

Figure 1: The world CO <sub>2</sub> emissions between 1990 and 2020 [1].	1
Figure 2: Diagram of electricity generation from coal [7].	4
Figure 3: Tetrahedral arrangement of AlO <sub>4</sub> found in zeolite structures [39].	29
Figure 4: Structure of OMS	41
Figure 5: Different types of hysteresis loops according to the IUPAC classification [14].	93
Figure 6: Powder XRD patterns of calcined MCM-41 synthesized with different alkyl chain lengths.	106
Figure 7: Effect of surfactant chain length on pore size.	108
Figure 8: TEM images of synthesized C <sub>18</sub> MCM-41.	109
Figure 9: SEM images of C <sub>18</sub> MCM-41.	109
Figure 10: SAXS of calcined SBA-15.	110
Figure 11: TEM images of SBA-15.	111
Figure 12: SEM images of calcined SBA-15	111
Figure 13: N <sub>2</sub> isotherms plots and pore size distributions calculated by DFT of (a) MCM 41 materials synthesized using C <sub>14</sub> TABr, C <sub>16</sub> TABr and C <sub>18</sub> TABr surfactants, (b) SBA-15 and (c) silica gel.	114
Figure 14: Thermogravimetric (TG) profiles of (a) MCM 41 silica synthesized using C <sub>14</sub> TABr, C <sub>16</sub> TABr and C <sub>18</sub> TABr surfactants, (b) SBA-15 and (c) silica gel.	118
Figure 15: FT-IR spectra of mesoporous silica	120
Figure 16: CO <sub>2</sub> isotherms of mesoporous silica performed at 0 °C.	121

Figure 17: CO <sub>2</sub> TPD profiles of mesoporous silica at a rate of 3 °C min <sup>-1</sup> (flow rate = 30 ml/min).....	122
Figure 18: TGA profile of mesoporous silica grafted with different molar ratios of CPS. ....	129
Figure 19: TGA profile of mesoporous silica grafted with different molar ratios of APS. ....	130
Figure 20: Powder XRD patterns of (a) APS and (b) TPED grafted C <sub>18</sub> MCM-41. ....	134
Figure 21: SAXS of (a) APS and (b) TPED grafted SBA-15.....	136
Figure 22: HRSEM images of APS grafted C <sub>18</sub> MCM-41, SBA-15 and amorphous SG. ....	138
Figure 23: N <sub>2</sub> isotherms of APS and TPED grafted sorbents. ....	140
Figure 24: TG/DTA profiles of APS and TPED grafted sorbents .....	148
Figure 25: FT-IR spectra of APS and TPED grafted mesoporous silica .....	151
Figure 26: CO <sub>2</sub> isotherms of APS and TPED grafted mesoporous silica at °C (99.9 % CO <sub>2</sub> ).....	155
Figure 27: CO <sub>2</sub> isotherms of mesoporous silica grafted with APS and TPED at 0 °C. ....	157
Figure 28: CO <sub>2</sub> TPD profiles of APS and TPED grafted sorbents. ....	159
Figure 29: Powder X-ray diffraction patterns of TREN grafted (a) C <sub>18</sub> MCM-41 and (b) SAXS of TREN grafted SBA-15.....	167
Figure 30: HRSEM of (a) C <sub>18</sub> MCM-TREN, (b) SBA-15-TREN and (c) amorphous SG-TREN.....	169
Figure 31: N <sub>2</sub> physisorption isotherms of TREN grafted mesoporous silica.....	172

Figure 32: TGA/DTA profiles of TREN grafted mesoporous silica.....	177
Figure 33: FT-IR spectra of TREN grafted mesoporous silica.....	181
Figure 34: CO <sub>2</sub> isotherms of TREN and guanidine grafted mesoporous silica. .	184
Figure 35: CO <sub>2</sub> TPD profiles of (a) C <sub>18</sub> MCM-41 TREN, (b) SBA-15-TREN and (c) AM SG-TREN. ....	186
Figure 36: Powder X-ray diffractions guanidine grafted MCM-41.....	192
Figure 37: TEM images of (a) C <sub>18</sub> MCM-41, (b) C <sub>18</sub> MCM-41-CPS and (c) C <sub>18</sub> MCM-41-guanidine. ....	194
Figure 38: HRSEM images of (a) C <sub>18</sub> MCM-41, (b) C <sub>18</sub> MCM-41-CPS and (c) C <sub>18</sub> MCM-41-guanidine. ....	195
Figure 39: N <sub>2</sub> isotherms of CPS and guanidine grafted MCM-41(C <sub>14</sub> TABr, C <sub>16</sub> TABr and C <sub>18</sub> TABr). ....	198
Figure 40: TG profiles of guanidine grafted MCM-41(C <sub>14</sub> TABr, C <sub>16</sub> TABr and C <sub>18</sub> TABr).....	202
Figure 41: FT-IR of guanidine grafted MCM-41(C <sub>14</sub> TABr, C <sub>16</sub> TABr and C <sub>18</sub> TABr).....	205
Figure 42: <sup>13</sup> C CPMAS NMR spectrum of (a) C <sub>14</sub> MCM-41-guanidine, (b) C <sub>16</sub> MCM-41-guanidine and (c) C <sub>18</sub> MCM-41-guanidine. ....	208
Figure 43: CO <sub>2</sub> isotherms of guanidine grafted MCM-41(C <sub>14</sub> TABr, C <sub>16</sub> TABr and C <sub>18</sub> TABr).....	211
Figure 44: CO <sub>2</sub> -TPD profiles of C <sub>14</sub> MCM-41, C <sub>16</sub> MCM-41 and C <sub>18</sub> MCM-41 grafted with guanidine.....	212
Figure 45: Powder XRD and SAXS patterns of TPED-TREN grafted C <sub>18</sub> MCM-41 and SBA-15. ....	220

Figure 46: N <sub>2</sub> Physisorption isotherms of TPED-TREN grafted C <sub>18</sub> MCM-41 and SBA-15.....	223
Figure 47: TGA/DTA profiles of TPED-TREN grafted C <sub>18</sub> MCM-41 and SBA-15.....	227
Figure 48: FT-IR spectra of C <sub>18</sub> MCM-41, SBA-15, C <sub>18</sub> MCM-41-TPED-TREN and SBA-15-TPED-TREN.....	230
Figure 49: CO <sub>2</sub> isotherms of C <sub>18</sub> MCM-41- TPED-TREN and SBA-15- TPED-TREN performed at 0 °C.....	232
Figure 50: CO <sub>2</sub> TPD profiles of TPED-TREN modified C <sub>18</sub> MCM-41 and SBA-15.....	234





UNIVERSITY *of the*  
WESTERN CAPE

## List of tables

Table 1: CO <sub>2</sub> Emissions from various power generation technologies.....	3
Table 2: Summary of CO <sub>2</sub> capturing technologies, advantages and disadvantages	6
Table 3: CO <sub>2</sub> capturing methodologies for combustion processes .....	9
Table 4: Physical and chemical properties of commonly used absorbents.....	19
Table 5: Miller indices hkl, $2\theta_{hkl}$ , dhkl values and calculated unit cell parameters ( $a^0$ ) of the first peak in the diffraction patterns of the calcined MCM-41 phases.....	106
Table 6: Textural properties of MCM-41 materials synthesized using different alkyl chain lengths surfactants, SBA-15 and amorphous silica gel. ....	114
Table 7: TGA analysis results.....	117
Table 8: CO <sub>2</sub> uptake obtained from CO <sub>2</sub> -TPD.....	122
Table 9: Systematic study of CPD and APS loading using TGA. ....	130
Table 10: Textural properties of silica gel, MCM-41 and SBA-15 as well as APS and TPED modified mesoporous silica.....	140
Table 11: Summary of TG profiles of APS and TPED modified mesoporous silicas MS.....	149
Table 12: CO <sub>2</sub> adsorption capacities of APS and TPED modified MS. ....	159
Table 13: Textural properties of mesoporous silica grafted with TREN.....	171
Table 14: Summary of TG profiles of TREN grafted modified mesoporous silica. ....	177
Table 15: CO <sub>2</sub> adsorption capacities of TREN grafted mesoporous silica .....	187
Table 16: Textural properties of guanidine modified MCM-41 .....	197

Table 17: $^{13}\text{C}$ CPMAS NMR shifts of C14-MCM-41-guanidine shown as representative .....	209
Table 18: $\text{CO}_2$ adsorption capacities of guanidine grafted MCM-14 ( $\text{C}_{14}\text{TABr}$ , $\text{C}_{16}\text{TABr}$ and $\text{C}_{18}\text{TABr}$ ) .....	213
Table 19: Textural properties of TPED-TREN grafted $\text{C}_{18}\text{MCM-41}$ and SBA-15.....	223
Table 20: $\text{CO}_2$ adsorption capacities of TPED-TREN modified $\text{C}_{18}\text{MCM-41}$ and SBA-15.....	235





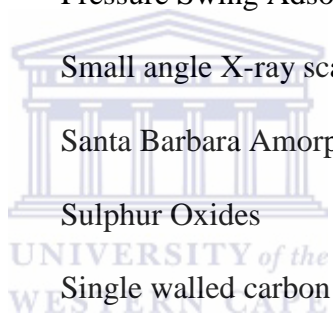
## List of schemes

Scheme 1: Reaction pathway for the synthesis of OMS.....	43
Scheme 2: The reaction pathway between CO <sub>2</sub> and amine groups under dry and humid conditions.....	48
Scheme 3: Reaction between surface silanol groups of silica support with the alkoxy part of the silane .....	54
Scheme 4: The different tethering linkages obtained through post grafting of aminosilanes on mesoporous supports .....	55
Scheme 5: Modes of bonding of silanes on mesoporous supports .....	122
Scheme 6: Synthetic route of CPS and APS grafted supports .....	122
Scheme 7: Synthetic route to TREN grafted mesoporous supports (G2) .....	150
Scheme 8: Synthetic route to guanidine grafted MCM-41 supports.....	190
Scheme 9: Synthetic route to TPED-TREN grafted supports.....	219

## List of Acronyms

ACs	Activated carbons
AMP	2-amino-2-methyl-1-propanol
APS	3-Aminopropyltrimethoxysilane
ASU	Air Separation Unit
BET	Brunauer-Emmet-Teller
BJH	Bopp-Jancso-Heinzinger
CP MAS	Cross Polarization Magic Angle Spinning
CPS	(3-Chloropropyl)triethoxysilane
CTABr	Cetyl trimethylammonium bromide
DEA	Diethanolamine
DFT	Density functional theory
FT-IR	Fourier transform-Infrared Spectroscopy
HAS	Hyperbranched Aminosilica
HMS	Hexagonal Mesoporous Silica
HRSEM	High Resolution Scanning Electron Microscopy
HRTEM	High Resolution Transmission Electron Microscopy
IEAGHG	International Energy Agency Greenhouse Gas
IGCC	Integrated Gasification Combined Cycle
LCT	Liquid crystal templating
LDH	Layered double hydroxides
MCM-41	Mobil Composition of Matter No. 41
MDEA	N-methyldiethanolamine
MEA	Monoethanolamine

MOFs	Metal Organic Frameworks
MWCNTs	Multiwalled carbon nanotubes
NGCC	Natural Gas Combined-Cycle
NMR	Nuclear Magnetic Resonance
NO <sub>x</sub>	Nitrogen oxides
OMS	Ordered Mesoporous Silica
PEI	Polyethyleneimine
Ppm	Parts per million
PSD	Pore size distribution
PSA	Pressure Swing Adsorption
SAXS	Small angle X-ray scattering
SBA-15	Santa Barbara Amorphous 15
SO <sub>x</sub>	Sulphur Oxides
SWCNTs	Single walled carbon nanotubes
TEOS	Tetraethyl orthosilicate
TGA	Thermogravimetric analysis
TMO	Tetramethyl orthosilicate
TPED	N-[3-(Trimethoxysilyl)propyl]ethylenediamine
TREN	Tris(2-aminoethyl)amine
XRD	Powder X-ray diffraction
ZIFs	Zeolitic Imidazolate Frameworks



## CHAPTER 1

### 1.1 Introduction

Carbon dioxide (CO<sub>2</sub>) emissions have become one of the major contributing factors influencing the climate changes which civilizations are experiencing today. CO<sub>2</sub> emissions have risen dramatically since the industrial revolution which started around 1750 to 1850, changing the socio-economic backdrop of many countries.

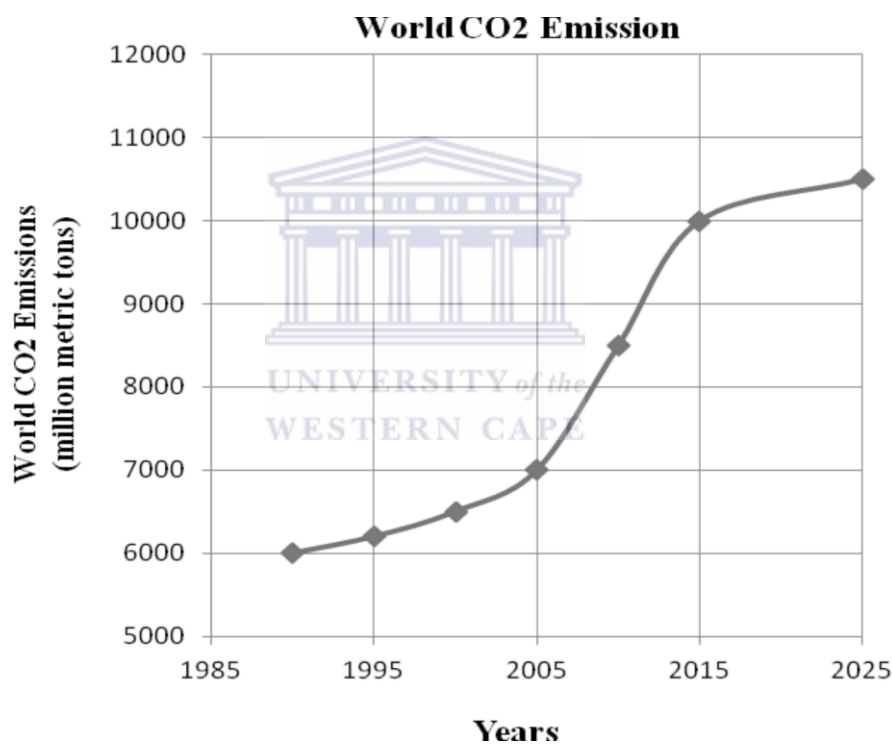


**Figure 1:** The world CO<sub>2</sub> emissions between 1990 and 2020 [1].

Figure 1 shows the CO<sub>2</sub> emissions from human activities from 1990 predicted up to 2020. The graph depicts the various sources of CO<sub>2</sub> emissions and how the volumes of CO<sub>2</sub> emitted have increased since the 1980's. The levels of CO<sub>2</sub> gradually rose from the 1980's but the levels emitted were not that high seeing as this was the time that various innovative processes took place. A steep increase in the CO<sub>2</sub> emission

came about from the early 2000's and the levels have continued to increase to supply the energy demands which civilizations require today. Since then, the excessive release of CO<sub>2</sub> has brought about an imbalance of the earth's "scale". CO<sub>2</sub> has been coined as one of the major factors giving rise to the "Greenhouse Effect".

The earth's "greenhouse effect" is what makes this planet suitable for life as we know it. The earth's atmosphere contains trace gases, some of which absorb heat. These gases (water vapor, carbon dioxide, methane, ozone, and nitrous oxide), are referred to as "greenhouse gases". The retention of part of the sun's energy in the earth's atmosphere in the form of heat is a direct result of the presence of greenhouse gases. Solar energy, mostly in the form of short-wavelength visible radiation, penetrates the atmosphere and is absorbed by the earth's surface. The heated surface then radiates some of that energy into the atmosphere in the form of longer-wavelength infrared radiation. Although some of this radiation escapes into space, much of it is absorbed by greenhouse gases in the lower atmosphere, which in turn re-radiate a portion back to the earth's surface. The atmosphere thus acts in a manner roughly analogous to the glass in a greenhouse, which allows sunlight to penetrate and warm the plants and soil but which traps most of the resulting heat energy inside. The greenhouse effect is essential to life on earth. Carbon dioxide is a major contributor to the "Greenhouse Effect", because it is a greenhouse gas, and elevated CO<sub>2</sub> levels contribute to additional absorption and emission of thermal infrared radiation in the earth's atmosphere, which produce net warming, and an overall increase in surface temperature. CO<sub>2</sub> concentrations of 7 giga tons per year need to be reduced by a factor of two thirds by the end of the century in order to mitigate the effect CO<sub>2</sub> would have on the environment [2-3].

The separation of CO<sub>2</sub> from light gases have been embarked on and practiced for decades. The majority of the work based on the separation of CO<sub>2</sub> concerned the separation of CO<sub>2</sub> from methane for the purification of natural gas, due to the fact that many of the natural gas reservoirs contain a considerable amount of CO<sub>2</sub>. Recently more effort has been put into separating CO<sub>2</sub> from flue gases linked to the combustion processes for e.g. exhaust gases of a typical coal-fired thermal power station, and this is due to the fact that CO<sub>2</sub> is thought to be one of the key anthropogenic greenhouse gases [4]. The harmful gases emitted from industrial processes compound the problem of Greenhouse gases, resulting in erratic weather patterns.

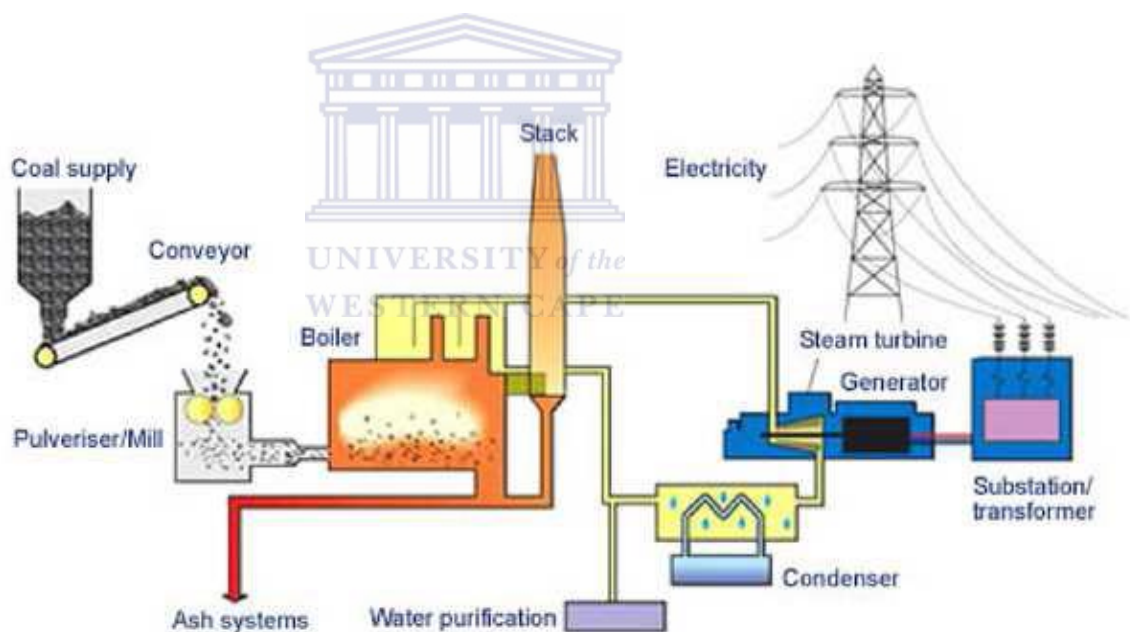
In light of this, new technologies have been developed in order to reduce the emissions of large scale industrial processes. IEAGHG has compiled a database of the major anthropogenic stationary sources of CO<sub>2</sub>, and stationary emission sources are considered to be power plants and large industrial manufacturing plants.

The main sources of CO<sub>2</sub> emissions are power plants. The rise in CO<sub>2</sub> concentrations has led researchers to develop mechanisms that would reduce CO<sub>2</sub> concentrations that are being emitted from these point sources.

**Table 1:** CO<sub>2</sub> Emissions from Various Power Generation Technologies [5].

<b>Technology</b>	<b>CO<sub>2</sub> Emissions (Kg/MWh)</b>
Pulverized Coal-fired subcritical	850
PC-fired supercritical	800
IGCC	670
NGCC	370
Nuclear	0

It is clear from Table 1 that pulverized coal fired plants emit the most CO<sub>2</sub> in comparison to the other technologies which are being used for power generations. Pulverized coal fired plants burn coal to generate electricity. The continuous use of coal to produce electricity makes it vitally important to study various factors that would make the whole process as environmentally friendly as possible. In doing so the amount of hazardous emissions will be reduced such as SO<sub>x</sub>, NO<sub>x</sub> and most importantly CO<sub>2</sub>. Current technologies are being implemented for the control of NO<sub>x</sub> and SO<sub>x</sub> which are widely used in industry, but not a lot of effort has been focus towards the mitigation of emitting CO<sub>2</sub>, according to the Coal Advisory Board [6].

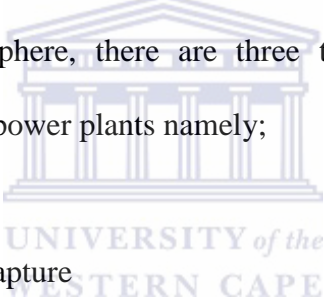


**Figure 2:** Diagram of electricity generation from coal [7].

According to Figure 2 the coal is pulverized before being fed into a boiler. The boiler is a high temperature unit where the pulverized coal is burned in air, which generates high pressure steam. The high pressure steam is then routed to a steam turbine. At this stage the high pressure steam drives the turbine which in turn generates

electricity. At the second stage of the plant a condenser and cooling water is also incorporated into the process to make the process more efficient. The third stage of a typical coal fired power plant would be the removal of particulate matter and various other pollutants from the effluent gas. During this stage, processes like the catalytic reduction of NO<sub>x</sub> and electrostatic precipitation of particulate matter as well as flue gas desulphurisation for the removal of SO<sub>x</sub> and mercury, are done. Therefore it is clear that an attempt to mitigate emissions released into the atmosphere is crucial to the process [8].

In combating the problem associated with reducing the amount of CO<sub>2</sub> being released into the atmosphere, there are three technological routes that can be explored from coal fired power plants namely;

- 
- Pre-combustion capture
  - Post-combustion capture
  - Oxy-combustion



**Table 2:** Summary of CO<sub>2</sub> capturing technologies.

<b>Type of combustion</b>	<b>Advantages</b>	<b>Disadvantages</b>
Pre-combustion	Synthesis gas is concentrated	Applicable mainly to new plants, as few gasification plants are currently in operation Availability, Cost of equipment, Extensive supporting systems requirements
Post-combustion	It may be used by existing coal fired plants	Dilute in CO <sub>2</sub> At ambient pressure Low CO <sub>2</sub> partial pressure Significantly higher performance or circulation volume required for high capture levels CO <sub>2</sub> produced at low pressure compared to sequestration requirements
Oxy-combustion	Very high CO <sub>2</sub> concentration in flue Retrofit and repowering technology option	Large cryogenic O <sub>2</sub> production requirement may be cost prohibitive Cooled CO <sub>2</sub> recycle required to maintain temperatures within limits of combustor materials Decreased process efficiency Added auxiliary load

### 1.1.1 Pre combustion capture

Primarily pre-combustion plants apply to gasification plants. Ideally CO<sub>2</sub> would be captured from a process stream before the stream is combusted. IGCC is a very good approach to capturing CO<sub>2</sub> from a process stream prior to combustion. The IGCC process makes use of coal that is first gasified with oxygen to produce synthesis gas (syngas), a mixture of mainly CO and H<sub>2</sub>. The steam is fed into a water gas shift reactor where CO is converted to CO<sub>2</sub> and more H<sub>2</sub>, and the CO<sub>2</sub> is eventually separated from H<sub>2</sub>. The separated H<sub>2</sub> is mixed with N<sub>2</sub> and gets fed into a combustion turbine. Membranes are also good candidates for pre combustion CO<sub>2</sub> capturing. Polymer based membranes like polybenzimidazole (PBI) membrane which are in the developmental stage at the DOE's Los Alamos National Laboratory (LANL), displayed extended periods of hydrothermal stability with temperatures as high as 400 °C, as well as displaying tolerance to sulphur while operating in a simulated industrial effluent from a coal fired plant.

Physical adsorbents have also proved to be very effective pre combustion capturing technology. This is normally accomplished through a solvent absorbing CO<sub>2</sub>. The process is primarily dependant on the pressure and temperature of the CO<sub>2</sub>. The most favourable conditions for physical absorption are higher partial pressures and low to moderate temperatures [9].

### 1.1.2 Post combustion capture

Post combustion capture involves the capture of CO<sub>2</sub> from the flue gas after combustion. Power plants combust coal in air that roughly consists of four fifths N<sub>2</sub>, and this combustion process generates a flue gas at atmospheric pressure and

generally has a CO<sub>2</sub> concentration of approximately 15%. The low concentrations of CO<sub>2</sub> under ambient conditions from post combustion processes make the process of capturing CO<sub>2</sub> from post combustions effluent sources thermodynamically unfavourable. Despite the challenges of the aforementioned facts of CO<sub>2</sub> capture from the post combustion process, it seems to be the most likely route in the foreseeable future in mitigating the amount of CO<sub>2</sub> being released into the atmosphere. The reason being that post combustion capture methods may be fitted to existing infrastructures which makes it ideal from an economical point of view.

### **1.1.3 Oxy-combustion capture**

Oxy-combustion capture is a process whereby, as the name states, the fuel is burnt with pure O<sub>2</sub> that is mixed with recycled flue gas. The reason why pure O<sub>2</sub> is mixed with recycled flue gas is that when coal is combusted with pure O<sub>2</sub>, it generates extremely high temperatures, and the current equipment that is used by these coal fired plants cannot withstand these high temperatures. A separation unit known as a cryogenic ASU feeds the high purity O<sub>2</sub> to the PC boiler where the combustion of the fuel takes place. The reason why oxy-combustion has been envisaged as one of the promising techniques for capturing CO<sub>2</sub> is due to the fact that the process produces a flue gas which mainly consists of CO<sub>2</sub> and water. Both these products may be removed by various techniques which are not that expensive [4].

**Table 3:** CO<sub>2</sub> capturing methodologies.

<b>CO<sub>2</sub> capture technology</b>	<b>Advantages</b>	<b>Challenges</b>
Cryogenic distillation	<ul style="list-style-type: none"> <li>• Minimal invasive bolt-on technology and provides highly efficient removal of most pollutants (Hg, SO<sub>x</sub>, NO<sub>2</sub>, HCl, etc.).</li> <li>• Possible energy storage capacity.</li> <li>• Potential water savings.</li> </ul>	<ul style="list-style-type: none"> <li>• High energy costs</li> </ul>
Chemical solvents	<ul style="list-style-type: none"> <li>• Provides high chemical potential for selective capture of CO<sub>2</sub> from streams with low partial pressures.</li> </ul>	<ul style="list-style-type: none"> <li>• Requires considerable amount of energy to heat, cool and pump non-reactive liquid</li> <li>• Energy intensive process to reverse chemical reaction and recover solvent.</li> </ul>
Membranes	<ul style="list-style-type: none"> <li>• No steam load</li> <li>• No chemicals</li> <li>• Simple and modular design.</li> <li>• Unit operation vs complex process</li> </ul>	<ul style="list-style-type: none"> <li>• Tend to be suited for high pressure processes like ICCG</li> <li>• A poor economy of scale</li> <li>• Requires multiple stages and recycle streams may be used.</li> </ul>
Solid sorbents	<ul style="list-style-type: none"> <li>• Chemical sites provide large capacities and fast kinetics which allow sorbents to capture CO<sub>2</sub> from effluent streams with a low partial pressure.</li> </ul>	<ul style="list-style-type: none"> <li>• Sorbent degradation.</li> <li>• Heat management in solid systems is difficult, in that it limits CO<sub>2</sub> adsorption capacity or creates additional problems when the reaction is exothermic.</li> </ul>

Cryogenic distillation is a process whereby the flue gas from a combustion process is cooled, and slightly compresses the flue gas so that it is just within the point where the CO<sub>2</sub> gas forms a solid. The gas is then expanded so that it cools down, precipitating some CO<sub>2</sub>, all of which is affected by the final temperature and pressure of the gas. The end result is CO<sub>2</sub> in a liquid phase and a nitrogen rich stream. The CO<sub>2</sub> absorption capacity depends on the temperature at the end of the expansion process. At atmospheric pressure, up to 99% of the CO<sub>2</sub> can be captured at -135 °C and 90% at 120 °C [10].

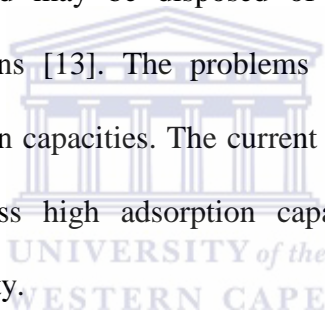
Membranes have also been considered a method for capturing CO<sub>2</sub> from combustion processes, in fact membranes have been widely used in a number of industrial separations processes for the last two decades. Membranes used in separation processes may be divided into two classes namely; polymeric and inorganic membranes. In industry, polymeric membranes are mostly used. Inorganic or polymeric membrane separation processes are expected to be more efficient than conventional CO<sub>2</sub> separation processes [11].

The absorption of CO<sub>2</sub> by liquid is widely established and is the current benchmark in terms of CO<sub>2</sub> capture and is practised commercially. The technique is based on the fact that the solvent generally contains alkanoamines acting as an absorbent and reacts with slightly acidic CO<sub>2</sub> to form dissolved carbamates and bicarbamates. The problem associated with this technique is that one requires a considerable amount of energy to regenerate the solvent [9].

The adsorption of CO<sub>2</sub> using solids with an affinity to CO<sub>2</sub> has recently attracted much attention. The affinity arises due to the fact that the surfaces of the adsorbents may be modified with amino groups that react with CO<sub>2</sub>. The advantage of the solid

adsorbents with respect to the liquid adsorbent lies in the fact that the adsorbent may be regenerated with an increase in pressure or by manipulating the adsorbent materials structural properties so that it may require much less energy (e.g. temperature) to regenerate the adsorbent material [12].

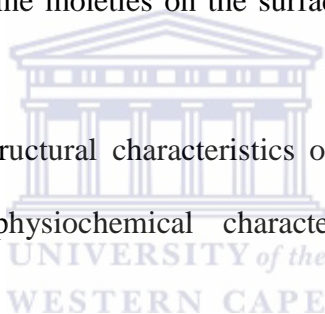
Solid adsorbents seem to be the most probable route to take in combating the problem associated the CO<sub>2</sub> capture from post combustion processes. Solid adsorbents, unlike liquids, can be used over a wide temperature range, i.e. from room temperature up to 700 °C. Using solid adsorbents also generates less waste compared to liquid absorption and may be disposed of without having to worry about environmental precautions [13]. The problems facing solid adsorbents for CO<sub>2</sub> capture are the adsorption capacities. The current requirement of solid adsorbents is that they should possess high adsorption capacities, fast kinetics as well as regenerability and stability.



## 1.2 Research scope

The aim of this project mainly focuses on constructing new mesoporous silica based materials that can be employed in capturing CO<sub>2</sub>. These synthesized materials have been optimized for CO<sub>2</sub> capture. The following points describe the specific aims of the proposed research:

- The first phase was to synthesize ordered mesoporous silica namely; SBA-15 and MCM-41 termed generation 0 (G0).
- Chemical modification of these mesoporous silica with amine moieties (G1).
- Expansion of amine moieties on the surfaces of the proposed sorbents (G2-G3).
- Evaluating the structural characteristics of the chemical modified sorbents using various physiochemical characterizations to confirm chemical modification.
- Studying the CO<sub>2</sub> adsorption capacity of the chemically modified sorbents.



## 1.3 Structure of thesis

The first chapter gives a brief but informative description of CO<sub>2</sub> emissions as well as some of the point sources. The chapter explains the different types of combustion processes that power plants use that generate Greenhouse gases and the technologies used by these combustion plants to mitigate CO<sub>2</sub> emissions. A detailed description of these technological approaches as well as the pros and cons of each of these processes are summarized. The scope of the proposed research is put forward as well as the objectives related to the proposed work.

Chapter 2 includes all the literature consulted in attempting to gain a deeper understanding of the topic concerning the proposed work. The literature review gives an overall scope of the various CO<sub>2</sub> capturing technologies used to capture CO<sub>2</sub> from fixed point sources, whether it is under high pressure, low pressure, gas mixtures or humid effluent streams with various CO<sub>2</sub> concentrations. Liquid and solid absorbents are discussed in detail as well as the main focus being put on solid adsorbents used to capture CO<sub>2</sub>.

Chapter 3 describes the synthetic protocols for synthesizing the ordered mesoporous silica as well as the chemically modified mesoporous silica. The characterization techniques used to evaluate the proposed materials is also discussed in this chapter.

Chapter 4 discusses the characterization of ordered mesoporous silica. A detailed description of the adsorbents is discussed in this chapter. Synthesis includes preparing ordered mesoporous silica with different pore sizes and ordered mesoporous silica with different morphology. A full account of structural characteristics is provided, which provides information for further modification in order to increase the sorbent's CO<sub>2</sub> adsorption capacity.

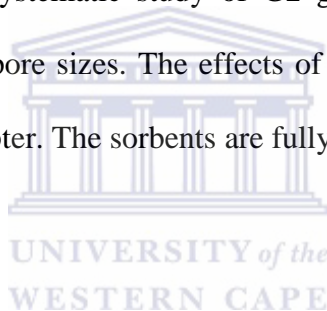
Chapter 5 discusses the synthesis and characterization of amine grafted ordered mesoporous silica. In this chapter the effect of the number of amines as well as the structural properties which the supports material has on the adsorption capacity, is discussed. The amine grafted sorbents, denoted as generation zero (G0), are fully



characterized and the adsorption capacity determined, using CO<sub>2</sub> temperature programmed desorption (TPD) studies.

Chapter 6 focuses on further chemically modifying the ordered mesoporous silica with amine groups as well as using novel amine functionality for the first time, to the best of our knowledge. The novel amine moiety is then grafted onto the mesoporous silica used in this study. The amine grafted sorbents (G2) are then fully characterized and the adsorption capacities determined with CO<sub>2</sub> TPD.

Chapter 7 discusses a systematic study of G2 grafted ordered mesoporous silica prepared with different pore sizes. The effects of amine functionality and pore size are discussed in this chapter. The sorbents are fully characterized and the findings are discussed.



Chapter 8 describes the functionalization of ordered mesoporous (G3) silica, where the number of amine groups on the surface of the supports were expanded using linkers. The increase in amine groups was executed in order to increase the adsorption capacity, as it has been well reported that the number of amine groups is directly proportional to the CO<sub>2</sub> uptake up until a certain point where the amine groups act as bulk material and gas diffusion is prohibited. The structural and chemical properties of the G2 sorbents are discussed in this chapter. The adsorption capacity of G3 sorbents were evaluated using CO<sub>2</sub> TPD.

Chapter 9 concludes with the findings of the study.

**References**

1. Demirbas, A. 2008, "Carbon dioxide emissions and carbonation sensors", Energy Sources, Part A: Recovery, Utilization and Environmental Effects, vol. 30, no. 1, pp. 70-78.
2. Stephens, J.C. van der Zwaan B. 2005. CO<sub>2</sub> Capture and Storage (CCS): Exploring the Research, Development, Demonstration and Deployment Continuum "BCSIA Discussion Paper 2005-08, Energy Technology Innovation Project, Kennedy School of Government, Harvard University, [Online]. Available: <http://belfercenter.hks.harvard.edu/files/stephensandvanderzwaan200508.pdf>.
3. Hirotaka Fujita, Takao Fujii, and Akiyoshi Sakoda, Institute of industrial science, University Tokyo, Japan, Adsorption of Carbon Dioxide on Phase Change Material/Amino-functionalized Mesoporous Silica Composite Adsorbent, [Online]. Available: [http://www3.ntu.edu.sg/pbast/\\_abstract/66.Fujita.pdf](http://www3.ntu.edu.sg/pbast/_abstract/66.Fujita.pdf).
4. Jose´ D. Figueroa, Timothy Fout, Sean Plasynski, Howard McIlvried, Rameshwar D. Srivastava, 2008. Advances in CO<sub>2</sub> Capture Technology-The U.S. Department of Energy's Carbon Sequestration Program international journal of greenhouse gas control 2, 9-20.
5. Narula, R.G., Wen, H. and Himes, K., 2002. Incremental cost of CO<sub>2</sub> reduction in power plants, Proceedings of IGTI ASME TURBO EXPO 2002, June 3-6, Amsterdam, The Netherlands.
6. Coal Industry Advisory Board, 1994. Industry Attitudes to Combined Cycle Clean Coal Technologies Survey of Current Status, Organization for Economic Co-operation and Development / International Energy Agency, France.
7. World coal institute, [Online]. Available: <http://www.worldcoal.org/coal/uses-of-coal/coal-electricity>.
8. S. Moazzem, M.G. Rasul and M.M.K. Khan (2012). A Review on Technologies for Reducing CO<sub>2</sub> Emission from Coal Fired Power Plants, Thermal Power Plants, Dr. Mohammad Rasul (Ed.). [Online]. Available:

<http://www.intechopen.com/books/thermal-power-plants/a-review-on-technologies-for-reducing-co2-emission-from-coal-fired-power-plants>

9. Chaffee, A.L., Knowles, G.P., Liang, Z., Zhang, J., Xiao, P. & Webley, P.A. 2007, "CO<sub>2</sub> capture by adsorption: Materials and process development", *International Journal of Greenhouse Gas Control*, vol. 1, no. 1, pp. 11-18.
10. Cryogenic CO<sub>2</sub> Capture to Control Climate Change Emissions, S. Burt, A. Baxter, L. Baxter, [Online]. Available: [sustainablees.com/documents/Clearwater.pdf](http://sustainablees.com/documents/Clearwater.pdf).
11. Yang, H., Xu, Z., Fan, M., Gupta, R., Slimane, R.B., Bland, A.E. & Wright, I. 2008, "Progress in Carbon Dioxide Separation and Capture: A review", *Journal of Environmental Sciences*, vol. 20, no. 1, pp. 14-27.
12. Zelenak, V., Halamova, D., Gaberova, L., Bloch, E. & Llewellyn, P. 2008, "Amine-modified SBA-12 Mesoporous Silica for Carbon Dioxide Capture: Effect of Amine Basicity on Sorption Properties", *Microporous and Mesoporous Materials*, vol. 116, no. 1-3, pp. 358-364.
13. D.P. Harrison. 2004, "The role of solids in CO<sub>2</sub> capture: A mini review", in: *Proceedings of the 7th International Conference on Greenhouse Gas Control Technologies Vancouver, Canada*, pp. 1101-1106.

## CHAPTER 2

Chapter 2 gives an overview of the literature covering the entire spectrum of solid adsorbents used for capturing CO<sub>2</sub>. This chapter briefly introduces the concepts of absorbents and adsorbents used for CO<sub>2</sub> capture. The emphasis is then placed on solid adsorbents and the various solid sorbents used for capturing CO<sub>2</sub>. The adsorption capacity of solid adsorbents is reported, as well as the factors influencing the adsorption capacity of the solid adsorbents such as temperature and pressure. An accurate account of recent literature related to the proposed work is summarized in this review.

### 2.1 Methods used to capture CO<sub>2</sub>.

#### 2.1.1 Absorption.

In general absorption processes use solvent based systems for CO<sub>2</sub> capturing from post combustion effluent streams. Absorption processes may be divided into two, i.e. physical and chemical absorption.

#### 2.1.2 Absorption methods.

##### 2.1.2.1 Physical absorption.

Physical absorption processes makes use of Henry's Law, i.e. the absorbent captures CO<sub>2</sub> through absorption by either applying pressure to the absorbent system at low temperatures or vice versa. Physical absorption processes are widely used in industry. The Selexeol process makes use of dimethylether or propylene glycol as absorbents while the Rectisol process makes use of methanol as an absorber [1].

These are not the only processes that are currently being used; processes such as the Morphysorb and Fluor processes are also being used in practice for the removal of CO<sub>2</sub> from post combustion effluent streams [2]. Physical absorbents are advantageous in the sense that they absorb CO<sub>2</sub> effectively under low temperatures and can be regenerated with a simple pressure drop.

### **2.1.2.2 Chemical absorption**

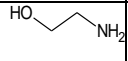
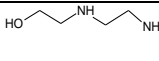
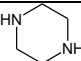
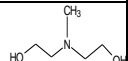
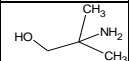
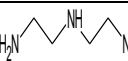
Chemical absorption process usually consists of an absorber and stripper, through which the absorbent may be regenerated. The post combustion flue gas passes through a packed bed absorber where it comes into contact with the absorbent. The absorbents used in these packed bed systems are solvents generally containing alkanolamines. The common structures of the alkanolamines used for chemical absorption processes are monoethanolamine (MEA), diethanolamine (DEA) and methyl diethanolamine (MDEA), all of which have at least one hydroxyl and amine group. The saturated absorbent solution is then passed through to a stripper, whereby the absorbent solution is regenerated through heat treatment. The released CO<sub>2</sub> is then handled appropriately, in its place of storage. The regenerated solvent is then reused. The process is therefore cyclic. The advantage of chemical absorption processes is that it can be fitted to existing infrastructures at combustion plants. The disadvantages though are that large equipment is required, the solvents give rise to corrosive problems and the energy requirement for these processes is not that beneficial - in spite of this, these processes are the benchmark in terms of CO<sub>2</sub> capturing from post combustion effluent streams [3].

Amine degradation is also a major contributing factor to the overall loss in efficiency of the chemical absorption process. In an attempt to combat these drawbacks of

chemical absorption process, mixing of amines has been explored as an alternative to increase the solvents absorption capacity.

lol

**Table 4:** Physical and chemical properties of commonly used liquid absorbents [4].

Property	MEA	AEEA	PZ	MDEA	NaOH	AMP	DETA
Molecular Structure					$\text{Na}^+$ $\text{OH}^-$		
Molecular Weight(g/mol)	61.08	104.15	86.1	119.16	40	89.14	103.17
Density (293)(g/cm <sup>3</sup> )	1.012	1.029	1.1	1.038	1.515	0.934	0.955
Boiling point (K)	443	513	420	243	1390	438	207
Vapour Pressure (293K)(kPa)	0.0085	0.00015	0.1066	0.0013	0.4	0.1347	0.02
Vapour Pressure (393K)(kPa)	15.9	0.969	41.66	-	-	-	-
Solubility (293K)	Freely soluble	Freely soluble	14 wt%	Freely soluble	Freely soluble	Freely soluble	Freely soluble
psuedo 1 <sup>st</sup> order rate constant 298 K (m <sup>3</sup> /kmol/s)	7000 [5].	12100 [6].	53700 [7].	3.5 [8].		681 [9].	49740 [10].
Activation energy (kJ/mol)	[11].	N/A	[12].	[13].		[14].	
CO <sub>2</sub> adsorption capacity(mol of CO <sub>2</sub> /mol of absorbent)	0.5	1.0	1.0	1.0	0.5	1.0	1.0

### 2.1.3 Adsorbent

An adsorbent or adsorbent material may be defined as a material that sorbs another substance; i.e. that has the capacity or tendency to take it up by either absorption or adsorption. Adsorption is a physical process that involves the attachment of a liquid or gas to a solid surface [15]. In terms of adsorption for CO<sub>2</sub> capturing, an adsorbent is a porous organic/inorganic material that has unique structural properties which makes it ideal for the specific application. An ideal adsorbent for capturing CO<sub>2</sub> from fixed point sources would have to have the following characteristics:

- Fast adsorption/desorption kinetics
- Stable under the operating conditions
- Tolerance of adsorbents to contaminants in the flue gas streams.
- Regenerable
- Low cost



It is of utmost importance that the adsorbent material must have fast adsorption/desorption kinetics. The kinetics would control the cycle time of a fixed bed system. In the case where the kinetics are fast, a sharp CO<sub>2</sub> breakthrough capacity would arise, coming from the effluent change with respect to time. In the case of slow adsorption kinetics, a gradual slope of the breakthrough capacity is obtained. In both cases it would determine how much of the adsorbent would need to be used by that particular process. The adsorbent therefore has to be tailored in a specific manner to increase the adsorption/desorption kinetics and improve the overall efficiency of the adsorbent.

The adsorbent should be stable under operating conditions such as high flow rates, humidity, vibration as well as temperature changes. The structural integrity of the adsorbent should not be compromised under operating conditions; therefore it is essential that the proposed adsorbent should display mechanical strength to be cost effective.

During operation the adsorbent material may be exposed to a number of components that might lower its overall adsorption capacity. In the flue gas contaminants such as heavy metals, SO<sub>x</sub> and NO<sub>x</sub> will be present which affects the adsorption capacity of the adsorbent material. The contaminants adsorb onto the material lowering the adsorption capacity of the adsorbent due to the block of adsorption sites for CO<sub>2</sub>.

The adsorbent material should be completely regenerable and should be thermodynamically favourable. The amount of energy used to regenerate the material should not be too high. In general the heat of adsorption for chemisorption and physisorption should be in the range of 60-90 mol<sup>-1</sup> kJ and 25-50 mol<sup>-1</sup> kJ respectively. During regeneration the adsorbent should be stable through several cycles of flue gas exposure and still maintain its CO<sub>2</sub> adsorption capacity.

The adsorbent should be economically viable in terms of power plants' overall running costs. For example, Tarka *et al.* approximated the cost of sorbents to be economically viable at \$5 per kg of adsorbent, to be good [16-17]. As soon as the cost rises above that value, e.g. \$15 per kg of sorbent, it becomes a costly and unfavourable exercise in terms of power plant operational costs.



## 2.2 Solid adsorbents

There are different types of solid supports that may be used for the capturing of CO<sub>2</sub> depending on the application and the chosen depends on the basis of the conditions the adsorbent would be exposed to. Whether it is high temperatures or pressures or under mild conditions and ambient pressure, it can therefore be envisaged that there is not one support that would be suitable for all post combustion capture processes.

Solids adsorbents that have been used to capture CO<sub>2</sub>:

- Carbonaceous materials
- Metal Oxides
- Hydrotalcites
- Zeolites
- MOFs
- ZIFs
- Mesoporous Silica Materials [18]



### 2.2.1 Carbonaceous materials

Activated carbons (ACs) have been used as solid adsorbents for capturing CO<sub>2</sub>. This was due to the structural properties displayed by the carbon based material. This is due to the fact that they do not cost that much, the various carbonaceous materials have high surface areas and the surfaces may be modified as well. ACs have been used in a number of industrial processes depending on the application, e.g. water treatment and gas purification due to the low cost of their raw materials and the

availability [19]. Activated carbons are prepared from raw carbonaceous materials. The first step involves carbonization of precursors in a heating and pyrolysis process which is done under inert conditions and during this step the char is formed. During the second stage elements such as hydrogen, nitrogen, oxygen etc. are released which leaves behind a skeletal carbon structure that has poor structural characteristics [20]. Thereafter the skeletal carbon material undergoes physical or chemical treatment that enhances the structural properties such as porosity, active site and the surface area. Carbonaceous material adsorbed CO<sub>2</sub> is through physical adsorption. The weak physical interaction results in carbonaceous materials having several drawbacks when it comes to CO<sub>2</sub> adsorption capacities. The CO<sub>2</sub> adsorption capacity of carbonaceous materials is very much dependent on changes in temperature and pressure.

At low CO<sub>2</sub> partial pressures ACs display less selectivity and adsorption capacities - this is mainly due to their less favorable adsorption isotherms. In spite of carbon based adsorbents' hydrophobic character, it still does not improve its CO<sub>2</sub> adsorption capacity due to the fact that the absorptivity is reduced when water vapour is present [21]. The typical CO<sub>2</sub> equilibrium adsorption capacities of activated carbons at 0.1 bar is 1.1 mmol/g at ambient temperature. This value however decreases to 0.25 mmol/g at elevated temperatures. Therefore activated carbons would be ideal solid adsorbents for the removal of CO<sub>2</sub>, but only at high pressure. The statement was justified by Himeno and co-workers who proved that Maxsorb AC had an adsorption capacity of 25.7 mmol/g at room temperature and pressure of 30 bar [22].

In light of the low CO<sub>2</sub> adsorption capacity under flue gas conditions, researchers have worked towards improving the adsorption capacity.

Studies have revealed that the CO<sub>2</sub> adsorption capacity reduces considerably when exposed to flue gas conditions, i. e. at a temperature of between 50-120 °C [23]. Na and co-workers also reported that AC could be used in a Pressure Swing Adsorption (PSA) to capture CO<sub>2</sub> from flue gas coming from a power plant. The adsorption capacity decreased from 3.2 mmol/g of adsorbent to 1.6 mmol/g when the temperature was raised from 288 to 388 K at atmospheric pressure [24]. The focus of researchers then shifted towards optimizing the adsorbent material in order to combat that problem. The main focus areas included increasing the surface areas, tuning of pores and using different precursors [25], or forming different structures such as single walled carbon nanotubes (SWCNTs) [26], multi walled carbon nanotubes (MWCNTs) [23], ordered mesoporous carbons (OMC) and microporous carbons.

Other approaches included modification of the surface, i.e. increasing the alkalinity of the surface. Alkalinity on the surface is achieved through introducing basic sites like nitrogen sites onto the surface, impregnation with compounds such as chloropropyl amine hydrochloride and polyethylene glycol or by the incorporation of nitrogen species into the carbonaceous framework [26]. The chemical modification of carbonaceous materials had led to a number of researchers trying to exploit the improved CO<sub>2</sub> adsorptivity which the solid adsorbents may or may not have.

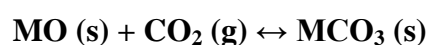
Arenillas *et al.* set out to prepare several impregnated organic based carbon materials, which have been synthesized from fly ash. The adsorbents yielded a CO<sub>2</sub> adsorption capacity of 1.13 mmol/g at 75 °C [23]. Cinke *et al.* evaluated the CO<sub>2</sub> adsorption capacity of purified single walled carbon nanotubes in the range of 0 to 200 °C. The CO<sub>2</sub> adsorptivity was found to be twice that of AC. At the same time Lu and his co-workers found that untreated CNT CO<sub>2</sub> adsorption capacity was relatively lower than that of granular AC at standard temperature [26].

In conclusion, carbonaceous materials are good candidates for the removal of CO<sub>2</sub> from effluent streams. The drawback of using carbonaceous materials is that they perform optimally when exposed to high pressures and ambient temperature.

### 2.2.2 Metal oxides

Metal oxides have been used to capture CO<sub>2</sub> mainly due to the fact that metal oxides provided basic sites for the slightly acidic nature of CO<sub>2</sub> [27]. A variety of metal oxides possessing the ability to provide these basic sites necessary for CO<sub>2</sub> chemisorption include alkaline earth metals such as calcium oxide (CaO), iron oxides (FeO), tantalum oxides (Ta<sub>2</sub>O), copper oxides (CuO), chromium oxides (CrO), aluminum oxides (Al<sub>2</sub>O<sub>3</sub>) and magnesium oxide (MgO) [28-30]. Alkaline metal oxides are also included in this group, metal oxides such as sodium oxide (Na<sub>2</sub>O), rubidium oxides (Rb<sub>2</sub>O), cesium oxides (Cs<sub>2</sub>O) as well as potassium oxide (K<sub>2</sub>O) [31-32]. The strong affinity of CO<sub>2</sub> to these types of metal oxides results in the formation of mono or multidendate species.

Metal oxides react with CO<sub>2</sub> in the following manner:



M: metal, eg. Ca, Mg, Fe, etc

Among the aforementioned groups Li<sub>2</sub>O were considered as the most effective when it came to CO<sub>2</sub> adsorption because of the high adsorption capacity they possessed. The industrial application of these materials were however hampered as a result of the diffusion resistance of these materials [33]. CaO was also seen as a good adsorbent for CO<sub>2</sub> adsorption and this was due to its high adsorption capacity, good

kinetics as well as durability and wide availability. The major problem attributed to CaO though is the relatively quick decline of its regenerability and also the surface availability of active sites decreased as a result of the formation of a CaCO<sub>3</sub> layer on CaO. As a result researchers have searched for alternative strategies to combat this problem, such as reactivation by steam hydration, modification of pore structure and incorporating inert materials. Manovic and Anthony showed that by reactivating CaCO<sub>3</sub> through a steam hydration process, an improvement in cyclic performance was obtained, and not only that, the pore volumes also increased [34].

### 2.2.3 Hydrotalcites

Hydrotalcite belongs to a group of anionic and basic clays that are also known as layered double hydroxides (LDH). Hydrotalcite-like compounds may be presented by the following formula:  $[\text{Mg}_{1-x}\text{Al}_x(\text{OH}_2)]^{x+} + [\text{A}_{x/n}{}^{n-}\text{mH}_2\text{O}]^{x-}$ , wherein  $0 < x < 0.33$  [35]. Where A represents an exchangeable anion having a valence of n. In recent years hydrotalcite materials have attracted much attention due to their wide range of applications such as being used as catalysts, decolorizing agents, ion exchangers, industrial adsorbents as well as adsorbents for capturing CO<sub>2</sub> [36].

The CO<sub>2</sub> adsorption capacities of hydrotalcites have been found to be lower in comparison to other chemisorbents. The CO<sub>2</sub> adsorption capacities of hydrotalcites are normally less than 1.0 mmol g<sup>-1</sup>. Nevertheless in spite of this fact, changes in the adsorption capacity have been documented, which was due to changing constituents of the hydrotalcites frameworks [18, 37]. Yong *et al.* and Sicar *et al.* investigated several factors that influenced the adsorption of CO<sub>2</sub> on hydrotalcite like compounds at elevated temperatures [38]. The study included investigating factors such as effect of water, the effect of aluminium content, type of anion used, temperature and the

effect it had during the adsorption of CO<sub>2</sub>, the number of cycles looking at the stability and last but not least, the effect of chemically modifying the HTlcs. The Sicar study revealed that a 0.52 mmol/g adsorption capacity was obtained when potassium carbonate promoted hydrotalcite was subjected to a dry gas mixture containing 70% CO<sub>2</sub> and 30% N<sub>2</sub> at a pressure of 1 bar, consequently when the same adsorbent was exposed to a wet stream, where the pressure was varied between 0.3 and 10 bar, the CO<sub>2</sub> adsorption capacity increased to 0.76 mmol/g when subjected to the same temperature [39]. Sicar also studied the stability and change in adsorption capacity of potassium-promoted hydrotalcite over multiple desorption/adsorption cycles [40]. The adsorption experiments were conducted over 1 hour periods. CO<sub>2</sub> adsorption was carried out at 673 K and desorption of CO<sub>2</sub> was achieved through purging with a N<sub>2</sub> stream at atmospheric pressure. The adsorption experiments revealed that after their first 10 cycles the CO<sub>2</sub> adsorption was found to decrease from 0.52 to 0.45 mmol/g, remaining constant after the initial 10 cycles. The phenomenon was explained through irreversible chemisorption that took place on the surface of the adsorbents, resulting in a lower capacity under cyclic conditions.

Rodrigues *et al.* [37] studied the effect of temperature on the CO<sub>2</sub> adsorption of a commercial hydrotalcite at three temperatures namely; 293, 473 and 573 K. The findings revealed that the highest CO<sub>2</sub> adsorption was achieved at 573 K. The observations were explained through a decrease in the interlayer spacing of the hydrotalcite at 473 K, and a void space that is formed during the removal of H<sub>2</sub>O molecules that generate hydroxyl groups that may occur at temperatures of 573 K, hence the increase in CO<sub>2</sub> adsorption.

The advances in characterization techniques have made it possible to study the effect which temperature has on the adsorption capacity of hydrotalcites. Hufton used

techniques such as high temperature X-ray diffraction, thermogravimetric analysis (TGA) and mass spectroscopy when heated in a vacuum to study the structural behaviour of the hydrotalcites during heating [40]. It was concluded that upon heating, the hydrotalcite underwent four stages of structural evolution, namely; dehydration, decarbonation, dehydroxylation, and decarbonation.

Costa studied the thermal decomposition and amorphization of hydrotalcites in further detail. The findings revealed that the framework of the hydrotalcites transformed into a three dimensional network, which mainly consisted of amorphous oxides. The removal of water and charge compensating anion  $\text{CO}_3^{2-}$  present in the interlayer space of the hydrotalcite framework, gave rise to a derivative known as a layered double oxide. Nevertheless LDO with its disordered framework still possessed enough basic character to adsorb  $\text{CO}_2$  [41].

The studies concluded that aluminium content and adsorption temperature strongly affected the  $\text{CO}_2$  adsorption capacity, the presence of moisture and steam favoured the adsorption of  $\text{CO}_2$  onto HTlcs and that chemical modification with e.g.  $\text{K}_2\text{CO}_3$  proved to increase the adsorption capacity of  $\text{CO}_2$  onto HTlcs [18].

#### 2.2.4 Zeolites

Zeolites are aluminosilicate minerals containing pores and cavities of molecular dimensions, i.e. micro porous silica with water. They are constructed of an infinite extending three-dimensional network of  $[\text{SiO}_4]^{4-}$  and  $[\text{AlO}_4]^{5-}$  ions that are tetrahedrons linked to one another through the sharing of oxygen atoms [42].

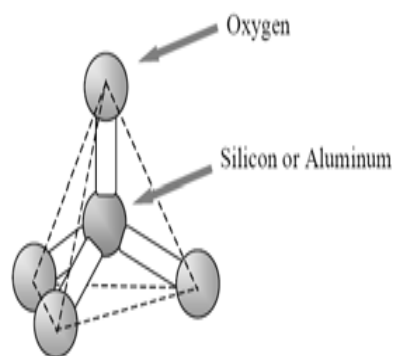


**Figure 3:** Tetrahedral arrangement of  $\text{AlO}_4$  found in zeolite structures [43].

The first naturally occurring zeolite mineral stilbite, was discovered by a Swedish mineralogist, Axel Fredrik Cronstedt, in 1756. Since the discovery was made by him, zeolites have been found in lakes, marine deposits, on land etc. [43-44].

In the past 200 years, 40 naturally occurring zeolites have been identified and more than 150 have been synthetically made. Naturally occurring zeolites include analcime, clinoptilolite, phillipsite, mordenite and chabazite. The more commonly known synthesized zeolites found today are zeolite A, zeolite X, zeolite Y as well as ZSM-5. In light of their physical properties, both synthetic and naturally occurring zeolites are used commercially. The ability of zeolites to act as adsorbents, undergo ion exchange and being able to act as a molecular sieve, makes them ideal for commercial use.

Zeolites have the ability to adsorb molecules according to their size and polarity, which makes them ideal for gas separation [45]. The cations found in zeolites create an electric field, which makes it ideal for  $\text{CO}_2$  that has a high quadrupole moment ( $-14.29 \times 10^{-40} \text{ Cm}^2$ ), resulting in a strong affinity of  $\text{CO}_2$  to zeolites [46, 13]. The resulting interaction gives rise to high adsorption of monolayer coverage [47]. Walton *et al.* [48-49] exchanged the zeolites X and Y with Li, K, Na, Rb, and Cs,



and investigated the effect that the exchange of ions would have on the zeolites' CO<sub>2</sub> adsorption capacity. The zeolite that was exchanged with Li ions proved to have the largest CO<sub>2</sub> adsorption capacity in comparison with the other zeolites that were exchanged with K, Na, Rb, and Cs. Zhang and co-workers prepared Chabazite (CHA) zeolites and exchanged them with alkali cations, namely; Li, Na, K and alkaline-earth cations such as Mg, Ca and Ba. NaX displayed the highest adsorption capacity of CO<sub>2</sub> at mild temperatures, whereas NaCHA and CaCHA showed similar CO<sub>2</sub> separation at high temperatures using vacuum swing adsorption [50, 15]. Early studies showed that the CO<sub>2</sub> adsorption capacity of zeolites was affected by the aluminium content that in effect determines the number of charge balancing cations. Barthomeuf studied the basic site strengths of zeolites such as X, Y, L, mordenite and ZSM-5. The studies showed that the number of basic site strength increased with an increase of aluminium content. The increase in basic site strength arose from the difference in electronegativity between that of aluminium in comparison to silicon [51]. CO<sub>2</sub> adsorptions were also carried out on a variety of natural occurring zeolites namely; mordenite, ferrierite, clinoptilolite, and chabazite as well as synthesized zeolites namely; 4A, 5A and 13X. Of the naturally occurring and synthesized zeolites, charbazaite and zeolite 13X respectively, proved to have superior CO<sub>2</sub> separation from N<sub>2</sub> in comparison to their counterparts.

Another study by Siriwardane and co-workers found that natural zeolites with high sodium content and the greatest surface area had the highest adsorption capacity, displaying high rates of CO<sub>2</sub> adsorption [52]. Siriwardane *et al.* performed another study whereby zeolites 13X and 4A were investigated for their CO<sub>2</sub> adsorption capacity capabilities [53]. It was found that at 25 °C and 1 atm of CO<sub>2</sub> partial

pressure, zeolites 13X and 4A exhibited adsorption capacities of  $3.64 \text{ mmol/g}^{-1}$  and  $3.07 \text{ mmol/g}^{-1}$  respectively.

The adsorption and selectivity of Mordendite (MOR) for  $\text{CO}_2$  was investigated at high pressures. The study concluded that the  $\text{CO}_2/\text{N}_2$  was higher in the protonated form due to the affinity of  $\text{N}_2$  in the protonated form, more so than the sodium form [54].

Zeolite NaY was investigated over a broad range of temperatures and at a pressure of 100 kPa for the adsorption of  $\text{CO}_2$  and  $\text{N}_2$  by Shoa *et al.* They found that NaY was an excellent adsorbent of  $\text{CO}_2$  for high temperature application, and to be the highest than any other porous material reported at the time [55]. Inui investigated CHA and zeolite 13X when subjected to pressure swing adsorption (PSA) conditions. The study showed that CHA and zeolite 13X were ideal adsorption for  $\text{CO}_2$  adsorption using pressure swing adsorption [56]. Merel showed that when zeolite 5A and zeolite 13X were subjected to indirect thermal swing adsorption conditions, zeolite 5A outperformed zeolite 13X [57].

Zeolites have also been used in membrane preparation for the separation of  $\text{CO}_2$  from a mixture of gas streams. Since zeolite membranes were first prepared in 1987 by Suzuki [58], much attention has been focused on zeolite membranes for gas separation.

$\text{CO}_2$  molecule has a kinetic diameter of 0.33 nm that makes zeolites ideal in membrane application for gas separation, as  $\text{CO}_2$  molecules are much smaller than the large and medium pores found in different types of zeolites. The separation of  $\text{CO}_2$  molecules and other gaseous molecules would occur through two competitive adsorption processes [59-61].

Zeolite membranes fall into the class of asymmetric membranes where a thin porous polymeric material is supported on zeolites. The thin films may be synthesized either using momentary supports, i.e. the support is removed after the preparation or permanent support. Examples of momentary supports are the stainless steel plate poly(tetrafluoroethylene) slab, Teflon sleeve, Vycor frit, silver and nickel [62]. In other examples of a thin layer supported zeolite membrane carbon, titania, alumina, and silicon carbide can be supported on a variety of substrates e.g. porous stainless steel,  $\gamma$ -alumina, zirconia, zeolite and  $\alpha$ -alumina [15, 45, 63-65].

The separation of gases through membranes is built on the kinetic size discriminations of the molecules inside the channels of the porous shapes. The separation of CO<sub>2</sub> occurs through molecular sieving as well as a diffusion mechanism in zeolite membranes [45]. Zeolitic membranes such as ZSM-5 have been shown to have a CO<sub>2</sub>/CH<sub>4</sub> selectivity of 2.4-5.5 at room temperature [66]. Zeolite Y membranes were found to have a CO<sub>2</sub>/CH<sub>4</sub> selectivities of roughly 10 [67], and CO<sub>2</sub>/CH<sub>4</sub> selectivities as high as 28 was obtained for zeolite type Y membranes [68]. Carreon and co-workers prepared inorganic membranes such as SAPO-34, silicate-1, zeolite T and zeolite DDR and studied their selectivities to CO<sub>2</sub>/CH<sub>4</sub>. The selectivity of these membranes was high due to the combination of adsorption and diffusion processes [69]. SAPO-34 selectivity was dramatically improved when synthesized on porous stainless steel tubes as well as Al<sub>2</sub>O<sub>3</sub> permeable supports. SAPO-34 on Al<sub>2</sub>O<sub>3</sub> porous support displayed separation selectivity for CO<sub>2</sub>/CH<sub>4</sub> which was higher than 170 at 295 K and gave a feed pressure of 2.2 atm. MFI-type membranes were synthesized on gamma alumina and stainless steel tubular supports by Sebastian *et al.*[70]. The MFI type zeolite membranes were evaluated for CO<sub>2</sub>/N<sub>2</sub> gas separation.

Recently an extremely good membrane was synthesized through in situ crystallization on a stainless steel porous tubular support. Noble and Falconer showed that the synthesized SAPO-34 membrane that had a Si/Al ratio of 0.1 achieved selectivity of  $\alpha = 170$  when exposed to a gas mixture of CO<sub>2</sub>/CH<sub>4</sub>, and a permeativity of  $P = 1.2 \times 10^{-7} \text{ mol m}^{-2}\text{s}^{-1}\text{Pa}^{-1}$  at 22 °C [71-72]. If the temperature was decreased the selectivity increased to  $\alpha = 560$ , but when the Si/Al ratio was increased to 0.15 the selectivity dropped to  $\alpha = 115$  at 35 °C. SAPO-34 membranes may be regarded as the ideal membrane for the separation of CO<sub>2</sub> from CH<sub>4</sub> for industrial application, but the presence of water would hamper the selectivity as water has a strong attraction towards the hydrophilic SAPO-34 membrane.

In conclusion, zeolites have been investigated thoroughly to determine what effects the types of ions substituted into the structure, temperature, kinetics and the presence of water vapor would have on the adsorption capacity towards CO<sub>2</sub>. Zeolitic membranes have also been viewed as a promising alternative for the separation of CO<sub>2</sub> from gas mixtures. It therefore becomes apparent that by tailoring factors such as the pore size of zeolites structures, the electric field strength caused by the presence of exchangeable cations, and the basicity, one can effectively control the adsorption capacity towards CO<sub>2</sub> for zeolites.

### 2.2.5 MOFs

MOFs are defined as a new class of hybrid material comprising metal ions that are co-ordinated with organic bridging molecules with a well-defined geometry and are viewed as the new interface between material sciences and molecular coordination chemistry [73-74].

In general bivalent or trivalent aromatic carboxylic acids or nitrogen containing aromatic compounds are commonly used in the synthesis of MOFs employing metals such as copper, aluminum, zinc and various other metals and incorporating these metals to form the frameworks [75-80].

The synthetic protocols have varied in terms of temperature, reactant ratios, reactant concentrations, solvent compositions as well as reaction times as all of these factors optimize the synthetic protocol employed to optimize the MOFs. Recently many techniques have been employed during the synthesis of MOFs such as microwave heating, and sonication techniques [81-83]. MOFs have unique structural properties such as high surface area, uniform pores, high pore volumes coupled with high metal content. All of the aforementioned characteristics make MOFs ideal materials for a number of applications such as, hydrocarbon adsorption/separation, energy storage and CO<sub>2</sub> adsorption just to mention a few [83-86].

MOFs may be categorized into four sub groups namely; flexible/dynamic, rigid, surface functionalized as well as open metal site frameworks. Flexible MOFs display changes in shape when molecules penetrate or leave its framework and respond to external stresses that may be applied such as temperature and pressure, whereas rigid MOFs tend to be stable and retain their permanent porosity. Upon adsorption of CO<sub>2</sub> by flexible MOFs, a phenomenon termed as a “breathing” mechanism occurs, changing the structural framework of the MOF, e.g. a change in pore width [87]. MOFs have exposed metal sites that provide mechanisms so that polar or non-polar gas pairs such as CO<sub>2</sub>/CH<sub>4</sub> may selectively adsorb onto them. CO<sub>2</sub> coordinates to the metal centres in an end-on-end fashion e.g. O=C=O...Cu<sup>2+</sup> [88]. The presence of water found in MOF frameworks hold marvellous improvements for their CO<sub>2</sub> adsorption capabilities.

MOFs were first investigated for their application as solid adsorbents for CO<sub>2</sub> capture at room temperature by Yaghi's group in 2005. Yaghi undertook the first systematic study to investigate the correlation between the surface area and the CO<sub>2</sub> adsorption capacity of MOF's. Yaghi investigated MOFs with structural properties such as pores with exposed metal sites like MOF-505 and Cu<sub>3</sub>(BTC)<sub>2</sub> square channels like MOF-2, amine and alkyl functionalized pores such as IRMOFs-3 and IRMOFs-6, exceptionally high porous IRMOF-1 and MOF-177 as well as hexagonally packed cylindrical channels of MOF-74. The study revealed that MOF-177, which consists of Zn and a large linker 4,4',4''-benzene-1,3,5- triyl-tribenzoic acid (H<sub>3</sub>BTB), showed the highest CO<sub>2</sub> adsorption at high pressure, reported at 60 wt % when subjected to a pressure of 35 bar [89]. The increased CO<sub>2</sub> adsorption was attributed to large pore space confined in MOF-177. The findings showed that the adsorption capacity of MOFs was directly correlated to their specific surface areas. The findings sparked interest in the development of new types of MOFs for capturing CO<sub>2</sub> [90-93]. MIL-53 (Al) and MIL-53 (Cr) have been investigated as potential solid adsorbents for CO<sub>2</sub>-capture by Bourrelly *et al.* who found that initially CO<sub>2</sub> would adsorb to the hydroxyl groups found in the framework of MIL-53 (Al), and evidently cause shrinkage to the structure. Further exposure to CO<sub>2</sub> under pressurized conditions resulted in the re-opening of pores and could therefore accommodate more CO<sub>2</sub>. MIL-53 (Al) adsorption capacity was reported to be 10.4 mol kg<sup>-1</sup> at 30 bar and 304 K, which at the time was higher than the standard zeolites used and comparable to microporous carbons [94]. In another study Yazaydin *et al.* established that when water molecules are coordinated to open metal areas of Cu-BTC (HKUST-1) this notably increased the adsorption of CO<sub>2</sub> of Cu-BTC [95]. Conversely water molecules coordinated in the MOF frameworks have been shown

to have detrimental effects on the MOFs CO<sub>2</sub> adsorption capacity. The effect of humidity on M/DOBDC series of MOFs (where M = Zn, Ni, Co and Mg; DOBDC = 2,5-dioxidobenzene-1, 4-dicarboxylate) was investigated by Kizzie *et al* [96]. The findings showed that when the series of MOFs (Mg/DOBDC and Zn/ DOBDC) were exposed to 70% relative humidity, only 16 % for Mg/DOBDC and 22% of Zn/DOBDC from the initial CO<sub>2</sub> adsorption could be recovered. Ni/DOBDC and Co/DOBDC showed that they could recover 61% and 85% of its initial capacity. The differences in initial recovery of CO<sub>2</sub> adsorption for the series of MOFs was attributed to the stability of MOFs towards hydrolysis.

In another study adenine containing MOF, bio-MOF-11 synthesized by An *et al.* have reported to show excellent selectivity and exceptional CO<sub>2</sub> adsorption [97].

Metal ions such as lithium cations have been proven to enhance CO<sub>2</sub>/CH<sub>4</sub> selectivity in MOFs. Bae *et al.* were the first to confirm experimentally when Li<sup>+</sup> was introduced into the MOF framework through both reduction and cation exchange, that it improved the selectivity [98]. The increased selectivity was as a result of displacement of the catenated framework and pore-volume diminution, whereas the improved selectivity in the Li<sup>+</sup> exchanged framework was due to the MOF-gaseous interaction between the quadrupole CO<sub>2</sub> and Li<sup>+</sup> charge from which the solvent has been removed. MOFs have been synthesized with iron incorporated into the framework. MOF Fe-BTT was synthesized by Sumida *et al.*, and it was pointed out that strong binding was found close to the Fe<sup>2+</sup> cation. As a result, preferential adsorption of CO<sub>2</sub> occurred inside Fe-BTT due to the affinity of CO<sub>2</sub> over N<sub>2</sub> [99].

In conclusion MOFs are ideal adsorbents for high CO<sub>2</sub> storage with pure CO<sub>2</sub> under high pressure. However MOFs show small increments of CO<sub>2</sub> uptake when exposed

to flue gas stream models, i.e. low pressure (0.1–0.2 bar). To compound the problem their adsorption capacity decreases if subjected to gas mixtures.

### 2.2.6 Zeolitic Imidazolate frameworks (ZIFs)

Zeolitic Imidazolate frameworks, more commonly abbreviated as ZIFs, are a new class of porous crystalline coordination polymers, with extended three dimensional structures made from tetrahedral metal ions that are bridged by imidazolate [100–101].

ZIFs are composed of transition metal ions such as  $\text{Zn}^{2+}$ ,  $\text{Co}^{2+}$ ,  $\text{Cu}^{2+}$  just to mention a few, which are connected by imidazolate like structures, and interestingly ZIFs have similar topologies to that of zeolites. The structural properties of ZIFs such as pore size and chemical functionality can be changed through just tuning the nature of the organic linkers, which would give rise to a variety of structures [102].

A number of ZIFs have been prepared to date that hold zeolite topologies, for example ANA, BCT, DFT, GIS, GME, LTA, MER, RHO and SOD and among them ZIF–60, ZIF–62, ZIF–68, ZIF–70, ZIF–73, ZIF–60 etc, have been synthesized from mixed linkers derived from single phase materials [103, 92]. ZIFs have been known to display exceptional chemical and thermal stability, high microporosity, high surface area and hold great promise for numerous applications [104]. The unique properties of ZIFs make them ideal for gas separation and storage. ZIF's–68, –69, –70, –78, –79, –81, –82, –95, and –100 have already been investigated as potential adsorbents for  $\text{CO}_2$  capture. These ZIFs have shown exceptional  $\text{CO}_2$  uptake and selectivity, when modelled with industrial gas effluent mixtures. ZIF–8 and ZIF–69 were investigated for their  $\text{CO}_2$  uptake capacity when exposed to industrial flue gas conditions. The results showed that even when these ZIFs were exposed to boiling



water, boiling benzene, and supercritical, their crystal structure's integrity remained unperturbed.

Yaghi and co-workers prepared and developed a new method to control metrics and functionality in an isoreticular series of eight ZIFs that gave desired gmelinite (GME) topology. Structural properties such as varying the pore size from 7.1 to 15.9 Å and changing the polarity of the link functionalities from polar to non-polar were found to affect the ZIFs CO<sub>2</sub> adsorption capacity. ZIF-78 was found to have the most superior adsorption capacity for CO<sub>2</sub> from a mixture of gases (CO<sub>2</sub>/CH<sub>4</sub>/N<sub>2</sub>/O<sub>2</sub>) in comparison to all the other ZIFs in the study.

In conclusion, ZIFs are good candidates for CO<sub>2</sub> capture from industrial flue gas as they possess good structural and chemical stability. The tailoring of structural attributes such as the nature of the imidazole organic linkers, were found to play a crucial role in the uptake and separation of CO<sub>2</sub> from gas mixtures. A lot of research still needs to be done in the field to fully understand the mechanisms of adsorption with ZIFs, whether experimentally or through simulation. In doing so ZIFs CO<sub>2</sub> capturing capabilities may be fully exploited.

### 2.2.7 Mesoporous materials

Mesoporous materials are defined as materials with pores in the diameter range of 2–50 nm according to the IUPAC nomenclature [105]. Mesoporous materials have an advantage over microporous (< 2 nm) materials in the sense that the application of these materials is based on the organic moieties used in synthesis that control thermal stability, shapes of cages or channels formed during the synthesis step, which in effect restricts their ability to be used for a wide variety of applications [106]. The

size of microporous materials consequently excludes them from size specific processes that involve larger molecules.

Mesoporous materials generally are composed of a wide range of oxide materials including silica ( $\text{SiO}_2$ ), alumina [107], carbon [108] as well as transition metal oxides like  $\text{TiO}_2$ ,  $\text{ZnO}_2$ ,  $\text{Fe}_2\text{O}_3$  [109-110].

Mesoporous materials have been used in a wide range of applications due to their structural properties. Applications include catalysis, drug delivery control, biosensors, biofuel, sorption and membrane separation [111].

#### **2.2.7.1 Ordered mesoporous silica (OMS)**

Mesoporous silica is synthesized using silica as the main building block, due to its cheapness, thermal stability, the ability of being chemically inert, its relative harmlessness and having a massive abundance in the earth's crust [112-113].

The synthesis of OMS was first patented in 1969, but due to a lack of deeper understanding through lack of analysis, its wide range of applicability and versatility could not be realized. The realization only came about when a group of researchers at the Mobil Corporation, through further inspection, unravelled the extraordinary attributes of these materials. In 1992 the researchers at the Mobil Corporation reported a new way of synthesizing these materials. The researchers came up with an amazing idea of using supramolecular surfactant templates to prepare OMS materials. The material was named Mobil composition of Matter number 41 commonly known as MCM-41. The concept of using these surfactants in the synthesis of ordered mesoporous silica materials led to a more compact way of controlling the morphology and the pore size of the materials by simply manipulating the synthetic protocol. The preparation of these materials only required three

straightforward ingredients, i.e. surfactant, silica source and solvent. Depending on the aggregation and packing of these micelles during synthesis, the three structures may be obtained.

In general the mesophase is synthesized through either hydrothermal, microwave, assisted hydrothermal synthesis or the sol gel method. The hydrothermal method is the most commonly employed, as it allows crystallization of substances from aqueous solutions at modest temperatures. Microporous to mesoporous materials synthesis has been reported using hydrothermal synthesis [114-115].

Microwave assisted hydrothermal synthesis has also shown to be an effective route for synthesizing porous materials. Microwave synthesis offers swift heating for crystallization, similar nucleation and quicker crystallization times [116-117]. Microwave assisted hydrothermal synthesis thus allows for the control, crystallinity and morphology of mesoporous materials [118].

The sol-gel process occurs through the hydrolysis and condensation of precursors to form a colloidal sol, which results in the formation of porous inorganic materials [119]. The sol-gel route has been used to synthesize inorganic materials with controlled meso and micro porosity with excellent thermal and chemical stability. The further additives to the synthetic protocol of mesoporous silica have included reagents such as acids, bases, expander molecules and co-solvents.

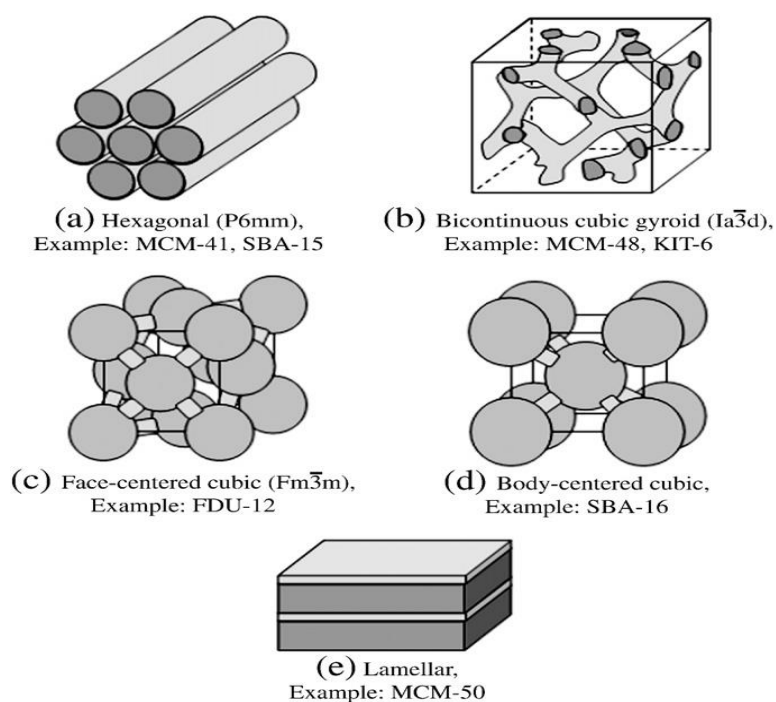
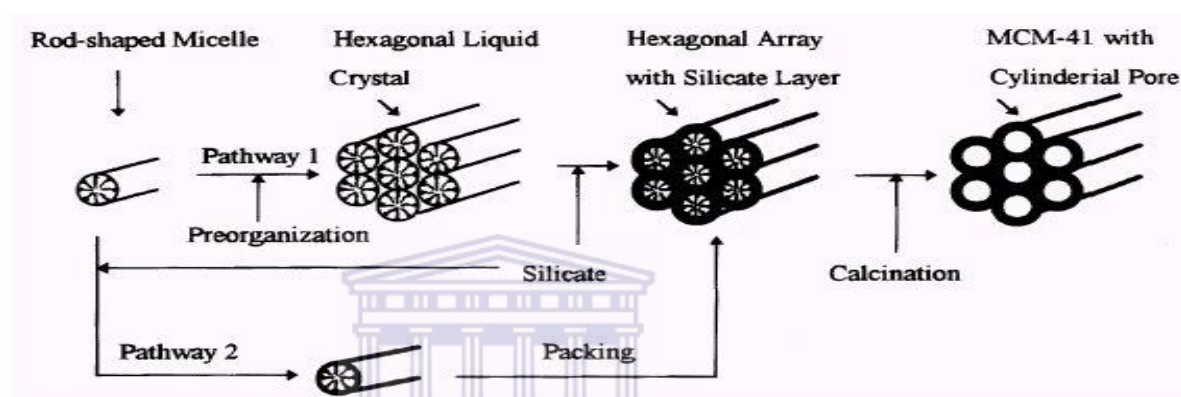


**Figure 4:** Structure of OMS

Recently these OMS were easily prepared under a broad range of pH as well as temperature ranging from room temperature to 150 °C. Synthesis includes using cationic, anionic, neutral, zwitterionic, bolaamphiphile, gemini, and divalent surfactants including a variety of polymers that are commercially available. Mesoporous silica materials synthesized to date include SBA-1 and SBA-6 ( $Pm3n$ ), SBA-2 and SBA-12 ( $P63/mmc$ ), SBA-11 ( $Pm3m$ ), SBA-16 ( $Im3m$ ), SBA-8 ( $cmm$ ), and disordered HMS, MSU-n, MSU-V, as well as KIT-1 [120-122].

MCM-41 is a member of the M41S family that is constructed of hexagonal arrays of non-intersecting channels that have a narrow pore size distribution. MCM-41 has a hexagonal packed rod shape micelle structure [123]. Initially M41S was carried out through an electrostatic templating route. This route utilizes cationic quaternary ammonium micelles that act as structure directing agents to direct mesostructure formation from anionic inorganic precursors [124-125]. Beck and co-workers were the first to prepare MCM 41 and proposed that these materials were formed through

a liquid crystal ‘templating’ mechanism whereby the silicate material forms inorganic walls between the surfactant micelles that arrange themselves in an orderly manner. The same authors further investigated the formation of MCM-41 materials in order to understand the mechanism, as the micelle formations were very sensitive to reaction conditions. Beck and co-workers justified the liquid mechanism and showed that the structure as well as the pore dimensions was closely linked to the surfactants properties, such as chain length and the chemistry of solutions [126].



**Scheme 1:** Reaction pathway for the synthesis of MCM-41.

MCM-41 since then has been prepared under a wide variety of conditions such as using molecular and non-molecular silica as a silica source. Silica sources include TEOS, fumed silica and tetramethylorthosilicate etc. The nature of the silica source predicts the nature of crystallization depending on the temperature during synthesis [127].

Synthesis of MCM-41 often commonly uses CTABr as a surfactant. During synthesis, bromide from CTABr is exchanged with the anionic silicate species [128]. Alkyltrimethyl ammonium chloride has also been used in the synthesis of MCM-41 materials, and depending on reaction conditions, they would give rise to hexagonal, cubic and lamellar structures. Gemini surfactants cetyldimethyl ammonium bromide, expressed by the formula  $C_nH_{2n+1}N^+(CH_3)_2(CH_2)_2N^+(CH_3)_3$ , was used by the Sayari

group to investigate the effect which the length of surfactant chains would have on the structures when synthesized under basic conditions. Sayari concluded that when using the odd numbered surfactants, hexagonal phases were obtained, and when even numbered surfactants were used, lamellar phases were obtained [129]. Grun and co-workers reported that the porosity and morphology of MCM-41 could effectively be controlled through two novel techniques. TEOS and tetra-n-propoxysilane were used as silica sources that were added to solutions containing surfactants with ammonia as a catalyst. The study showed that the addition of alcohols (ethanol or isopropanol) during synthesis yielded MCM-41 particles with spherical morphology. The procedure was then later modified as it was found that post synthetic treatment through aging the mother liquor at 90 °C for several days enhanced the structural ordering of MCM-41 materials [130].

In another study performed by Sayari and co-workers, the pore size of MCM-41 silica were expanded by using amines as expanders during both direct and post synthesis. It was concluded that using N,N-dimethylhexadecylamine (DMHA) expanded the pores of MCM-41 materials in mild conditions. The expanding agent increased the pore size of MCM-41 materials up to 7.7 nm in diameter, having a large primary mesopore volume and narrow pore size distribution, but at the same time the structural order was compromised with an increasing amount of expanding agent added. Other amines like trioctylamine, tridodecylamine, dimethyldecylamine (DMDA), dimethyloctylamine (DMOA), and small trialkylamines, were also used in the study. Trioctylamine and tridodecylamine also formed large pores whereas DMDA, DMOA and the small trialkylamines did not increase the pore size but instead decreased the ordering as well as the growth of microporosity [131].

Jana *et al.* prepared a MCM-41 molecular sieve by using a surfactant which had different alkyl chain lengths and using organic auxiliary chemicals. Surfactants with different alkyl chain lengths ( $C_8$  to  $C_{22}$ ) were found to increase the pore size from 1.6-4.2 nm when using one or a mixture of surfactants. Organic auxiliary compounds such as 1, 3, 5 trimethylbenzene, isopropylbenzene and tridecane increased the BJH pore size to 12.0 nm [132].

Recently Ghoshal and co-workers reported a novel synthesis of pore expanded MCM-41 materials without the use of swelling agents or using different surfactant alkyl chain lengths, but through a simple adjustment of the pH. MCM-41 materials were synthesized obtaining average pore sizes of up to approximately 30 nm in diameter [133].

Since the introduction of SBA materials in 1998 by Stucky [124], SBA-15 has become a famous member of the Santa Barbara Amorphous family of materials. Zhao *et al.* synthesized SBA-15 materials using a triblock copolymer, typically a non-ionic triblock copolymer as a structure directing agent and TMOS, TEOS or tetrapropyl Orthosilicate (TPOS) as a silica source [134]. The as-prepared SBA -15 template is then removed either through calcination, washing, reflux extraction, using acid,  $H_2O_2$  treatment, extraction with supercritical  $CO_2$  or microwave digestion. SBA-15 possesses uniform hexagonal pores that have narrow pore size distribution and their porosity may be tailored up to 30 nm. The thickness of the framework walls can range from 3.1 to 6.4 nm, and this gives rise to higher hydrothermal and mechanical stability than other ordered mesoporous silica's e.g. MCM-41[135-137]. SBA-15 materials have large surface areas and pore volumes of  $2.5 \text{ cm}^3/\text{g}$ . The pore size distribution of SBA-15 is bimodal whereby the larger pores are interconnected by micropores through the silica walls [138]. The surface of SBA-15 when dry

consists largely of isolated silanol groups and the smaller regions consist of geminal and hydrogen-bonded silanols [139].

SBA-15 has been viewed as a promising material for a variety of applications such as adsorption and separation, catalysis, bio-sensing, and controlled drug release as well as for the production of nanostructured carbon or platinum replicas [140].

### 2.3 OMS (MCM-41 and SBA-15) CO<sub>2</sub> adsorbents

OMS have been used for the CO<sub>2</sub> adsorption process. This is due to their structural properties such as large surface area, range of pore sizes from micro to mesopores, inertness as well as mechanical strength. OMS materials like MCM-41, MCM-48 and SBA-15 were found to be good adsorbents for CO<sub>2</sub> from a mixture of gases that include CH<sub>4</sub> and N<sub>2</sub> [73]. CO<sub>2</sub> adsorption studies on SBA-15 from a mixture of gases containing CH<sub>4</sub> and N<sub>2</sub> were performed by Liu *et al.* SBA-15 showed a considerable selectivity towards CO<sub>2</sub> over N<sub>2</sub> with considerable selectivity towards CO<sub>2</sub> over N<sub>2</sub> and CH<sub>4</sub>. SBA-15 displayed adsorption selectivities of 4.70 for  $n_{\text{CO}_2} : n_{\text{CH}_4}$  and 9.60 for  $n_{\text{CO}_2} : n_{\text{N}_2}$  at 0/5 MPa, where  $n$  is the number of moles [141-142]. Macario *et al.* studied the CO<sub>2</sub> uptake of pure silica MCM-41 and MCM-48 from gas mixtures of CO<sub>2</sub>/N<sub>2</sub>. MCM-41 and MCM-48 showed CO<sub>2</sub> selectivities over N<sub>2</sub> of 8.6-22.2 and 9.2 respectively [143]. MCM-41 and MCM-48 were reported to have CO<sub>2</sub> adsorption capacities of approximately 0.7-1.5 mmol/g and 0.8 mmol/g, respectively. The higher adsorption of CO<sub>2</sub> of MCM-41 compared to MCM-48 was reported as a result of the channel system which MCM-48 possesses.

Belmabkhout *et al.* prepared MCM-41 samples using the surfactant template method, with CTABr as a structure directing agent, and investigated their adsorption capacity

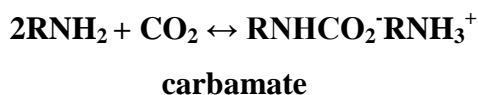


in the temperature range between 60-120 °C [144]. Adsorption experiments were carried out in a range of temperatures and pressures of up to 45 bar using a magnetic suspension balance. The adsorption capacity was found to be dependent on surface area and structural ordering, reflected by the (100) peak from the X-Ray diffraction patterns. The most promising sorbent in terms of adsorption capacity was found to be MCM-41-100 (where 100 denoted the temperature) prepared at 100 °C, and the sorbent displayed higher volumetric capacity when compared to other solid adsorbents such as activated carbons and zeolite 13X .

#### 2.4 Functionalization of OMS

OMS have shown to be promising adsorbents for CO<sub>2</sub>, nevertheless for OMS to be competitive with current systems used in industry; the adsorption capacity has to be equal to or greater than 3.0 mmol/g as estimated by Gray *et al.* [145]. Ho *et al.* mentioned similar adsorption capacity ranges, stating that for solid adsorbents to be competitive with current liquid systems, the adsorption capacity should be in the range of 2-4 mmol/g [146]. Many efforts have been devoted to increasing the adsorption capacity of OMS by functionalization of the surface with various amine functional groups in order to increase its adsorption capacity. The silanol groups on the surfaces of OMS afforded the opportunity for many chemical reactions as the hydroxyl groups are very reactive.

The affinity of CO<sub>2</sub> to amine groups arises from the weak chemical interaction between slightly acidic CO<sub>2</sub> which is attracted to the basic amine groups. The reaction that occurs is thus an acid base reaction type of reaction. The reaction pathway that occurs between the amine groups and CO<sub>2</sub> may be explained using the following Scheme 1 [147-148].



**Scheme 2:** The reaction pathway between CO<sub>2</sub> and amine groups under dry and humid conditions.

## 2.5 Methods used to functionalize OMS

- Physical impregnation
- Co-condensation
- Anionic templating template method
- Post synthesis chemical grafting



### 2.5.1 Physical impregnation

Physical impregnation of OMS involves the introduction of amine molecules onto the support. The affinity of the amine containing molecules and the supports arises from van der Waal's interactions. Impregnation results in the amine's group being physically absorbed onto the surface and in the pores of the support. Impregnation is carried out through suspending the adsorbent in a mixture of amine molecules and volatile solvent. The loading of amine molecules are achieved through stoichiometric additions of amine molecules during mixing, the solvent is then removed through evaporation.

Song and co-workers investigated the effect of humidity on the CO<sub>2</sub> adsorption capacity of PEI impregnated MCM-41 (MCM-41-PEI) [149]. The study concluded

that the presence of moisture when having a molar concentration of less than or equal to that of CO<sub>2</sub>, was found to increase the adsorbents' CO<sub>2</sub> adsorption capacity, and when the molar concentration of moisture was increased above CO<sub>2</sub> molar concentration, no increase in adsorption capacity was observed. An increase from 2.01 mmol/g under dry conditions to 2.84 mmol/g from a stream containing 10 % moisture, was observed.

Zhao and co-workers prepared amine impregnated SBA-15 sorbents for CO<sub>2</sub> capture impregnated with tetraethylenepentamine (TEPA). The study investigated the adsorption capacity of the amine impregnated sorbents from both an experimental and theoretical point of view. The sorbents showed reversible CO<sub>2</sub> adsorption/desorption with quick adsorption kinetics. The optimal temperature for CO<sub>2</sub> adsorption was found to be 75 °C using SBA-15 sorbents loaded with 60 wt% of TEPA and the highest adsorption capacity was (5.22 mmol/g) in dry and humid conditions. Various kinetic models were used to investigate the experimental data obtained for the CO<sub>2</sub> adsorption measurements. The Fractional Order kinetic model was found to be a good model for the adsorption region of interest, having maximum absolute deviation of 2.42 % between experimentally obtained CO<sub>2</sub> uptake and CO<sub>2</sub> uptake which was calculated using the model [150]. Novel solid adsorbents impregnated with pentaethylenehexamine (PEHA) on SBA-15 by a wet impregnation method were prepared by Wei and co-workers [151]. A fixed system was used to determine the adsorption capacity of the novel solid sorbents by studying the factors which have an effect on the adsorption capacity such as temperature, PEHA loading, and height/diameter ratio of the fixed bed. SBA -15 sorbents loaded with 70 and 50 wt% of PEHA achieved CO<sub>2</sub> adsorption capacities of 201.7 mg of CO<sub>2</sub>/(g of adsorbent) and 308.3 mg of CO<sub>2</sub>/(g of PEHA), respectively. A model was used to

analyse the CO<sub>2</sub> adsorption performance, namely a two amine layer adsorption model. Consecutive adsorption/desorption cycles showed that the novel sorbents remained stable [151]. PEI was also impregnated onto a variety of ordered mesoporous silica. Ahn's group investigated the CO<sub>2</sub> adsorption capacity of these supports loaded with the same amount of PEI [152]. The results obtained different CO<sub>2</sub> uptake for PEI impregnated sorbents, which demonstrated that the type of support also played a role in the adsorption capacity of PEI impregnated sorbents. In fact the adsorption capacity was found to be dependent on pore size, when the sorbents were investigated under the same operating conditions. KIT-6 type silica with a pore diameter of 6 nm loaded with 50 wt% of PEI adsorbed 3.07 mmol/g in a stream of pure CO<sub>2</sub> at 75 °C, in comparison with MCM-41 with similar PEI loading that had a pore diameter of 2.8 nm, and which adsorbed 2.52 mmol/g. The pore size was also found to affect the adsorption kinetics of the PEI impregnated sorbents.

Following the trend observed from this study Ahn and his co-workers decided to impregnate silica monoliths with hierarchical pore structure, having pore diameters of 3, 17 and 120 nm with PEI. PEI impregnated silica monoliths displayed the highest adsorption capacity of 3.75 mmol/g when exposed to a stream of 5% CO<sub>2</sub> in N<sub>2</sub> at 75 °C [152-153]. Silica aerogel was impregnated with tetraethylenepentamine (TEPA) as an adsorbent for CO<sub>2</sub> by Linneen and co-workers. The TEPA silica aerogel sorbents were prepared using two methods namely; evaporative precipitation and wet-impregnation. The evaporative precipitation method was found to distribute TEPA on silica aerogel more than wet impregnation, resulting in enhanced CO<sub>2</sub> adsorption in comparison to the impregnated silica aerogels. Nevertheless the difference in adsorption capacity was small [154]. Mesoporous alumina (MA) was also impregnated using diisopropanolamine, triethanolamine, 2-amino-2-methyl- 1,3-

propanediol, diethylenetriamine (DETA) and PEI. Their CO<sub>2</sub> adsorption capacity was evaluated by Plaza *et al.* [155]. PEI and DETA impregnated MA with 40 wt% loading showed high CO<sub>2</sub> at room temperature and increasing the adsorption temperature gave rise to an increase in CO<sub>2</sub> adsorption capacity. PEI-MA and DETA-MA exhibited CO<sub>2</sub> adsorption capacities of 1.4 mmol/g and 1.14 mmol/g respectively, in the presence of pure CO<sub>2</sub>, at 57 °C. Physical impregnation is a suitable technique for introducing amine moieties on mesoporous silica supports for CO<sub>2</sub> adsorption processes. The literature has shown that it is possible to introduce large polymers onto mesoporous silica supports with considerable ease, and that one is able to achieve high loadings of these polymers. The presence of high loading increased the adsorption capacity of mesoporous silica. The disadvantage of the impregnation method is that although high loading is achieved, diffusional resistance increases. Changes in adsorption temperature combat this problem, as the increase of adsorption temperature increases the adsorption capacity. In light of the fact that the amine moieties are physically bound to the supports, the stability of these sorbents comes into question when exposed to cyclic use.

The attachment of aminosilanes on mesoporous supports offers a more attractive route for the functionalization of sorbents for CO<sub>2</sub> capture. The advantage over physical impregnation is that chemical bonds are formed between the supports and the silylating agent, resulting in a much stronger interaction between the support and the functional group. There are two methods used to synthesize these functionalized supports namely;

### 2.5.2 Co-condensation

The co-condensation method, also known as “one-pot synthesis”, involves the direct condensation of the desired functional group to be introduced onto the support in conjunction with the silica source during the synthesis of the mesoporous silica. The method involves stirring moderate quantities of aminosilanes and the silica source, including a structure directing agent. The silica source and aminosilane, polymerize in the presence of the structure directing agent, and amino functionalized mesoporous silica are then produced. The structure-directing agent is generally removed through solvent extraction. Substitution of the desired silica source with an aminosilane during synthesis results in simultaneous condensation up to the mesophase assembly step. The co-condensation method allows for the incorporation of aminosilanes on the surface as well as within the walls of the silica framework [156-157].

Kim *et al.* prepared mesoporous silica using the co-condensation method and compared that to the anhydrous grafting method. The findings showed that the sorbents prepared using the co-condensation method yielded higher amine content in comparison to the anhydrous grafting method. Sorbents denoted as TRI-MS and AP-MS obtained adsorption capacities of 1.74 mmol/g and 1.14 mmol/g for pure CO<sub>2</sub> at 25 °C respectively, whereas the AP-MS sample with a CO<sub>2</sub>/N ratio of 0.43 was found to be the most efficient [158]. Yokoi *et al.* performed a similar study; comparing amine functionalized MCM-41 synthesized using direct co-condensation as well as post synthesis grafting. Elemental analysis and argentometric synthesis showed that 18% of the amino silane was unexposed when using the co-condensation method [159]. Hao and co-workers prepared amino-functionalized silica nanospheres with centrosymmetric radial mesopores using the co-condensation method. The amino

functionalized sorbents were prepared using anionic surfactant N-lauroylsarcosine sodium (Sar-Na) as the template and APS as the co-structure directing agent. The findings concluded that the amino amino-functionalized silica nanospheres treated with MEA-ethanol solution to remove the surfactant showed the highest CO<sub>2</sub> in comparison to the functionalized silica treated with acidic-acetonitrile [160].

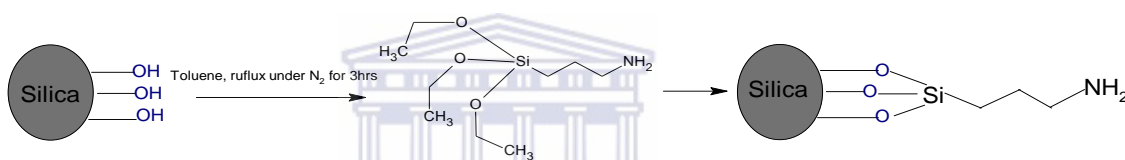
The co-condensation method is an effective way of incorporating amine groups into the pores as well as the surfaces of mesoporous silica. In spite of this the method does have some drawbacks, e.g. the aminosilanes can compromise the structural integrity and not all of the aminosilanes may be accessible as active sites when large quantities of these silanes are used.

### **2.5.3 Anionic surfactant template method**

The anionic surfactant template method involves using aminosilane or quaternized aminosilanes as co-structure directing agents and functional groups for CO<sub>2</sub> adsorption processes at the same time. Anionic surfactant template mesoporous silica (AMS) were synthesized by first dissolving an anionic surfactant in a solvent, followed by the addition of TEOS. The solution is then treated at a desired temperature and time under static conditions. Anionic surfactant template method involves the condensation of aminosilane or quaternized aminosilanes with the inorganic precursors, resulting in the ammonium sites attaching themselves to silicon atoms that are situated in walls. The electrostatic interaction between these ammonium sites with the anionic surfactants gives rise to well-ordered AMS.

### 2.5.4 Post synthesis chemical grafting

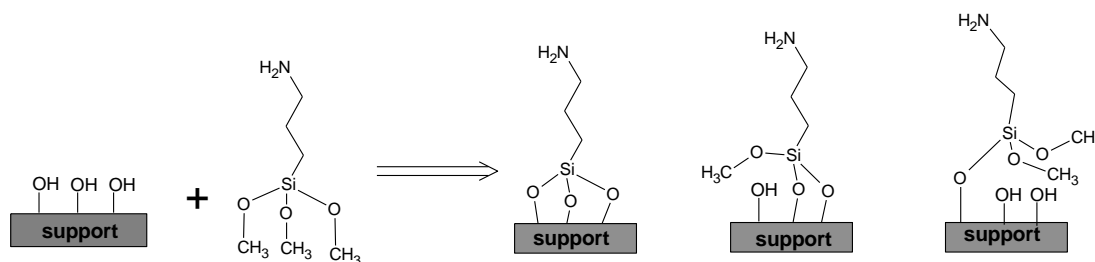
Chemical grafting of amine groups on the surfaces of mesoporous silica have become an attractive means to attach aminosilanes to a support. The interest arises from the simple approach. Through simple stirring the support in an anhydrous solvent with the addition of the desired molar ratio of aminopropylalkoxysilane under reflux, amines can be tethered to mesoporous supports. The first synthesis of amine grafted silica materials was done by refluxing APMS with silica in 1978 by Knözinger and Rumpf [161]. The reaction occurs between the alkoxy part of the silane and the surface of mesoporous.



**Scheme 3:** Reaction between surface silanol groups of silica support with the alkoxy.

The reaction allows the silane to be grafted on the surface of mesoporous supports through a covalent bond which is formed through the oxygen atom from the surface of the support. These oxygen atoms which take part in the reaction are either the silanol or siloxane bridge atoms from the supports. Therefore it is clear that depending on the oxygen atom involved in the reaction, a variety of linkages may arise. In fact three tethering linkages come forth from the reaction [162].





**Scheme 4:** The different tethering linkages obtained through post grafting of aminosilanes on mesoporous supports.

Post synthesis grafting of the aminosilane linker onto mesoporous supports gives rise to three different modes of binding, i.e. mono dentate, bi dentate and tridentate (Scheme 4). As seen from the various linkage modes that can be obtained, researchers have focused on ways to enhance the loading of aminosilanes. Research has shown that the addition of water to create a type of wet silica surface is one such method to increase the loading. The alkoxy silane reacts with water to form the corresponding  $R-Si(OR)_2-OH$ , which subsequently reacts with the silanol surface groups of the support to form covalent bonds. This method increases the loading but the disadvantage is that the aminosilane can oligomerize uncontrollably in the presence of water.

Another method for increasing the loading of aminosilanes on mesoporous supports was through the addition of a strong base e.g. triethylamine which was discovered by Tripp and co-workers. It was proposed that the amine groups of the base form hydrogen bonds with the surface silanol groups, which in turn activates the silanols to react with an alkoxy silane that is in close proximity. The advantage that this method has over the addition of water is that oligomerization does not occur as water is not present; however, the disadvantage of this method is that it gives rise to the formation of multiple types of amine sites on the surface with different reactivities.

## 2.6 Factors influencing CO<sub>2</sub> adsorption capacity of amine modified mesoporous silica

Mesoporous silica have poor hydrothermal stability. In the presence of humid streams mesoporous silica's structural integrity diminishes. The structural weakness is caused by the hydrolysis of thin pore walls which consists of [SiO<sub>4</sub>]. This was confirmed through studies performed by Cassiers *et al.* [163] and Guo *et al.* [164]. Both investigations subjected OMS (SBA-15, SBA-16 and MCM-48) to steam treatment and in both cases the structures of the OMS were compromised to a certain extent through a reduction in primary mesopore volume and surface area. As a result, the research focus has investigated a method to combat the hydrothermal stability of mesoporous sorbents. Pore-wall thickening through varying synthesis conditions, forming composites as well as silanol group modification, has shown to improve the hydrothermal stability.

Silylation of silanol groups reduce the number of silanol groups, reducing the number of Si-O-Si bonds which might undergo hydrolysis when exposed to water. Park *et al.* confirmed this through silylating the MCM-48 and MCM-41 trimethylchlorosilane and hydrophobic methyl group and the chloropropyl groups respectively. The structure of the silylated sorbents were maintained after hydrothermal treatment [165].

## 2.7 Amine grafted mesoporous silica for CO<sub>2</sub> capture

Leal *et al.* were the first to study amine grafted materials for CO<sub>2</sub> adsorption. In this study silica gel was grafted with APS under anhydrous conditions. The adsorbent had an adsorption capacity of 0.41 mmol/g when exposed to a 100 % CO<sub>2</sub> stream at 23 °C [166].

The initial study sparked considerable interest in using solid adsorbents for CO<sub>2</sub> capture as an alternative to the liquid amine systems. In fact Huang *et al.* performed a comparative study between propyl amine grafted MCM-48 and silica xerogel. MCM-48-AP displayed the higher adsorption capacity of 1.42 mmol/g in comparison to 0.58 mmol/g for silica xerogel-AP when exposed to a 10% CO<sub>2</sub> in N<sub>2</sub> at room temperature. The increase in adsorption capacity was found to be directly proportional to the amine loading which was 2.3 and 1.7 mmol/g for MCM-48 and silica xerogel respectively. It was therefore very clear that the amine grafted mesoporous silica increased the adsorption capacity, and that an increase in amine loading increased the adsorption capacity [167].

In another study Chaffee's group functionalized HMS with a series of aminosilanes. HMS was chosen due to its high porosity, which is an attribute needed for adsorbents that would be used to capture CO<sub>2</sub>, and which would then further be enhanced by grafting HMS with amino propyl silanes [168].

Delaney *et al.* developed HMS grafted with APS, aminoethyl- aminopropyl-trimethoxysilane (AEAPTS), N-[3-(trimethoxysilyl) propyl] diethylenetriamine (DAEAPTS), ethylhydroxyl- aminopropyl-trimethoxysilane (EHAPTS) as well as diethylhydroxyl- aminopropyl-trimethoxysilane (DEHAPTS). The aminosilane grafted HMS displayed different amine loadings depending on the surface area as well as the nature of bonding with the surface silanol groups. The grafted HMS showed an increase in CO<sub>2</sub> adsorption capacity as well as showing good reversibility. In fact the sorbents displayed CO<sub>2</sub> adsorption and reversibility that was higher than that reported by Leal [169-172].

Chang's group also prepared SBA-15 grafted with APS- and 2N-APS for CO<sub>2</sub> capture [173]. The group managed to obtain CO<sub>2</sub> adsorption capacities of less than 1

mmol/g. The group justified the low adsorption capacity as a result of supports with low surface areas of approximately 200 m<sup>2</sup>/g. The group also used in situ infrared spectroscopy coupled with mass spectrometry to investigate the effect that the nature of the amine groups, adsorbed CO<sub>2</sub>, as well SO<sub>2</sub>, would have on the CO<sub>2</sub> adsorption capacity of amine grafted sorbents. The study concluded that the nature of the amine determined the desorption temperature and that carbonate species is the primary species formed and that the rate of carbamate formation was higher than that of bicarbonate species.

In order to further investigate the nature of the amines, pre-treatment of supports as well as the effect of moisture on the CO<sub>2</sub> adsorption capacity, Yogo's group [174] prepared 3N-APS-SBA-15 to study the aforementioned factors influencing the adsorption capacity. The groups revealed that SBA-15, pre-treated with boiling water, gave rise to higher amine density upon the grafting step, which resulted in an increase in adsorption capacity. The higher amine density i.e. N atoms per nm<sup>2</sup>, also displayed good stability when subjected to cyclic use at 60 °C. Wei *et al.* confirmed the study by reporting that indeed upon SBA-15 being pre-treated with boiling water, the hydrolysed surface Si-O-Si bonds, which in effect increased the number of Si-OH groups which lead to higher amine densities [175].

Zelenak and co-workers showed that when using OMS with different pore sizes and when it is grafted with aminopropyl silane groups, the CO<sub>2</sub> adsorption capacity was dependant on both pore size and amine density [176]. The CO<sub>2</sub> adsorption capacities of MCM-41, SBA-12 and SBA-15 were 0.57, 1.04 and 1.54 mmol g<sup>-1</sup>, respectively. Knowles and his group prepared mono-, di- and triaminosilanes grafted on hexagonal mesoporous silica substrates in an attempt to investigate the effect which the number of amines has on CO<sub>2</sub> adsorption capacity. The study revealed that the adsorbed

amount of CO<sub>2</sub> increased with the increasing number of amines introduced, i.e. the triaminosilane > diaminosilane > monosilane. Ko *et al* .synthesized primary (1°), secondary (2°), and tertiary (3°) amines grafted on SBA-15 to study the effect of the nature of the amine group on CO<sub>2</sub> adsorption capacity [171]. The study showed that the maximum adsorption capacity of SBA-15-NH<sub>2</sub>, SBA-15-NH-CH<sub>3</sub> and SBA-15-N(CH<sub>2</sub>CH<sub>3</sub>)<sub>2</sub> were found to be 0.95, 0.75, 0.17 mmol CO<sub>2</sub> g<sup>-1</sup> adsorbent, respectively. Many researchers concluded that CO<sub>2</sub> was easily desorbed from the adsorbent in the order 3°, 2° and 1° amines, whereas the reverse order was observed for the adsorption of CO<sub>2</sub> [177-178].

Sayari and co-workers have been viewed as pioneers in the field of amine modified solid adsorbents for CO<sub>2</sub> capture. Sayari and co-workers have made considerable strides in preparing novel mesoporous adsorbents as well as investigating the effects of amine grafted mesoporous silica for capturing CO<sub>2</sub> from flue gas [178].

Pore expanded MCM-41 sorbents were prepared via post synthetic hydrothermal treatment with swelling agents, to generate MCM-41 materials with high surface area and pore diameters of up to 20 nm and pore volume of 3.5 cm<sup>3</sup>/g, without compromising the structural ordering associated with MCM-41 type materials. Harlick and Sayari prepared pore expanded MCM-41 and grafted the support with N-(3-trimethoxysilylpropyl)diethylenetriamine (DEAPTES). The amine loading was comparable due to the fact that both MCM-41 and PE-MCM-41 had similar surface areas. DAEAPTS grafted PE-MCM-41 displayed an adsorption capacity of 2.05 mmol/g at 25 °C and 1.0 atm when exposed to a dry stream of CO<sub>2</sub> in N<sub>2</sub>. The adsorption capacity of the PE-MCM-41-DAEAPTS was found to be 50 % higher in comparison to MCM-41- DAEAPTS and that PE-MCM-41- DAEAPTS desorbed CO<sub>2</sub> 30 % faster than MCM-41- DAEAPTS [179]. Harlick and Sayari also optimized

the grafting conditions of DAEAPTS on PE-MCM-41. The optimal conditions for grafting DAEAPTS was found to be 0.3 ml of water and 3 ml of aminosilane per gram of support at 85 °C. An increase from 6.11 to 7.98 mmol/g aminosilane loading was obtained when using the optimized reaction conditions in comparison with the conventional grafting. As a result of the optimized grafting method, an unprecedented increase of 70% in adsorption capacity was observed, i.e. from 1.55 mmol/g using conventional dry grafting to 2.65 mmol/g using the optimized method. In the presence of a moist stream (5% CO<sub>2</sub> in N<sub>2</sub> with 27 % ) the adsorption capacity of PE-MCM-41- DAEAPTS increased to 2.94 mmol/g whereas a substantial drop in adsorption capacity down to 0.09 mmol/g was observed for zeolite 13X as a comparison. The adsorption rate was also found to be higher for PE-MCM-41-DAEAPTS in comparison to zeolite 13X, which also justifies the fact that pore expansion, as well as grafting aminosilanes onto the surface, improves adsorption capacity as well as kinetics [179].

Sayari and co-workers have done further investigations of the amine grafted sorbents' long term stability using substantial adsorption/desorption cycles under various conditions. The sorbent exposed to numerous cycles under dry conditions showed a drop in sorption capacity under moderate conditions. The drop in sorption capacity was due to the formation of urea groups on the surface of the amine grafted sorbents. Humid streams combated the formation of urea and the stability of the sorbent remained constant, even after 700 adsorption/desorption cycles.

**Amine group expansion or hyperbranched aminosilicas**

Chaffee *et al.* [180] synthesized a step-wise polymerization of melamine dendrons with aminosilane grafted SBA-15 (G0) for high amine content silica support for CO<sub>2</sub> capture. The expansion was carried out up until the fourth generations (G4). G0 to G4 had amine loadings of 0.52, 2.88, 4.51, 6.75, and 7.49 mmol N g<sup>-1</sup>, respectively. Chaffee and co-workers also prepared melamine-type dendrimers that were grafted onto mesocellular siliceous foam (MCF). MCF poses ultra large mesopores that make them ideal sorbents for adsorption processes. MCF was grafted with the stepwise growth of 2,4,6-trichlorotriazine and ethylenediamine on the surface up to the 4<sup>th</sup> generation. The study showed that it was possible to achieve high organic loadings as high as 55 wt% up to the 4<sup>th</sup> generation. Although high organic content was achieved, CO<sub>2</sub> adsorption studies inferred that only primary amine groups of the melamine dendrimers structures took part in CO<sub>2</sub> chemisorption. Nevertheless the grafted MCF displayed a higher CO<sub>2</sub> adsorption compared to the unfunctionalized MCF [181]. Bhagiyalakshmi *et al.* synthesized SBA-15 utilizing rice husk ash (RHA) as a silica source [182]. SBA-15 was then grafted with 2,4,6-trichlorotriazine and tris(2-aminoethyl)amine (TREN) dendrimers generation via stepwise growth. Characterization techniques such as the nitrogen adsorption/desorption showed that dendrimers grew inside the mesopores of SBA-15. CO<sub>2</sub> adsorption measurements revealed that 2<sup>nd</sup> and 3<sup>rd</sup> generation sorbents displayed the highest capacity with a dendrimer loading of 5-6 and 7-8 wt % respectively. CO<sub>2</sub> chemisorption was hindered due to steric hindrances of dendrimer growth which resulted in adsorption capacities less than the anticipated values. The TREN dendrimer grafted SBA-15 sorbents showed good thermal stability of up to 350 °C, and upon seven adsorption/desorption cycles, the adsorption capacity remained the same.

Jones and his group also prepared an adsorbent with high amine content through the polymerization of aziridine by ring opening inside the pores of SBA15 that produced covalently tethered HAS. The HAS displayed CO<sub>2</sub> adsorption capacity of 3.11 mmolg<sup>-1</sup> under humid flow of 10% CO<sub>2</sub>/Ar, with high CO<sub>2</sub> of 0.44 at room temperature. At an elevated temperature of 75 °C the HAS proved to be stable when exposed to a flow of 10% CO<sub>2</sub>/Ar for over 12 cycles with a CO<sub>2</sub> adsorption capacity of 1.98 mmol/g. Further studies showed that a higher loading of hyper-branched amines gave rise to better adsorption capacities, and that the best had an amine loading of 9.78 mmol/g. The HAS adsorbed 4 mmol/g when exposed to a humid stream consisting of 10% CO<sub>2</sub>/N<sub>2</sub> at 75 °C [183-185].

In conclusion OMS have been viewed as an alternative sorbent for capturing CO<sub>2</sub> from post combustion flue streams. OMS have been shown to separate CO<sub>2</sub> from a mixture of gases. This shows the selectivity which these sorbents possess. Sorption capacities were not nearly close to the commercial benchmark, which led to the functionalization with amine groups. A variety of functionalization techniques have been put forward to introduce amine groups onto OMS, with post-synthesis grafted seemingly the most attractive route. Post-synthesis grafting allows for amine groups to be covalently bonded to OMS surfaces which improving stability to a certain extent, when exposed to harsh flue gas conditions. The grafting route also allows for the attachment of various amino groups through silylation chemistry, and it is for this reason that the focus of this research was based upon the functionalization of mesoporous silica with novel amino functionalities for the capturing of CO<sub>2</sub>.



**References:**

1. A new solvent for CO<sub>2</sub> capture. [Online]. Available: <http://www.combustion-institute.it/proceedings/XXXVI-ASICI/papers/36proci2013.X5.pdf>
2. Olajire, A.A. 2010. "CO<sub>2</sub> Capture and Separation Technologies for End-of-pipe Applications-A review". *Energy* 35: 2610–2628.
3. Resnik, K.P. 2004, "Aqua Ammonia Process for Simultaneous Removal of CO<sub>2</sub>, SO<sub>2</sub> and NO<sub>x</sub>", *Int. J. Environ. Technol. Manage.* 4: 89–104.
4. Yu, C., Huang, C. & Tan, C. 2012, "A review of CO<sub>2</sub> capture by absorption and adsorption", *Aerosol and Air Quality Research*, vol. 12, no. 5, pp. 745-769.
5. Hikita, H. & Asai, S. & Katsu, Y. & Ikuno, S. 1979, "Absorption of carbon dioxide into aqueous monoethanolamine solutions", *AIChE J.*, vol. 25, p.793-800.
6. Ma'mun, S., Dindore, V.Y. & Svendsen, H.F. 2007, "Kinetics of the reaction of carbon dioxide with aqueous solutions of 2-((2-aminoethyl)amino)ethanol", *Industrial and Engineering Chemistry Research*, vol. 46, no. 2, pp. 385-394.
7. Bishnoi, S. & Rochelle, G.T. 2000, "Absorption of carbon dioxide into aqueous piperazine: Reaction kinetics, mass transfer and solubility", *Chemical Engineering Science*, vol. 55, no. 22, pp. 5531-5543.
8. Bishnoi, S. & Rochelle, G.T. 2002, "Absorption of carbon dioxide in aqueous piperazine/methyldiethanolamine", *AIChE Journal*, vol. 48, no. 12, pp. 2788-2799.
9. Xiao, J., Li, C.-. & Li, M.-. 2000, "Kinetics of absorption of carbon dioxide into aqueous solutions of 2-amino-2-methyl-1-propanol + monoethanolamine", *Chemical Engineering Science*, vol. 55, no. 1, pp. 161-175.
10. Hartono, A., da Silva, E.F. & Svendsen, H.F. 2009, "Kinetics of carbon dioxide absorption in aqueous solution of diethylenetriamine (DETA)", *Chemical Engineering Science*, vol. 64, no. 14, pp. 3205-3213.
11. Mandal, B.P., Guha, M., Biswas, A.K. & Bandyopadhyay, S.S. 2001, "Removal of carbon dioxide by absorption in mixed amines: Modelling of

- absorption in aqueous MDEA/MEA and AMP/MEA solutions", *Chemical Engineering Science*, vol. 56, no. 21-22, pp. 6217-6224.
12. Cullinane, J.T. & Rochelle, G.R. 2004, "Carbon dioxide absorption with aqueous potassium carbonate promoted by piperazine", *Chemical Engineering Science*, vol. 59, no. 17, pp. 3619-3630.
  13. Pani, F., Gaunand, A., Cadours, R., Bouallou, C. & Richon, D. 1997, "Kinetics of absorption of CO<sub>2</sub> in concentrated aqueous methyldiethanolamine solutions in the range 296 K to 343 K", *Journal of Chemical and Engineering Data*, vol. 42, no. 2, pp. 353-359.
  14. Alper, E. 1990, "Reaction mechanism and kinetics of aqueous solutions of 2-amino-2-methyl-1-propanol and carbon dioxide", *Industrial and Engineering Chemistry Research*, vol. 29, no. 8, pp. 1725-1728.
  15. Songolzadeh, M., Ravanchi, M. T., Soleimani M, 2012. "Carbon Dioxide Capture and Storage: A General Review on Adsorbents", *The Scientific World Journal Volume*, vol. 2014, pp. 1-34.
  16. Tarka, T. J.; Ciferno, J. P.; Gray, M. L.; Fauth, D. CO<sub>2</sub> capture systems using amine enhanced solid sorbents. Presented at the Fifth Annual Conference on Carbon Capture & Sequestration, Alexandria, VA, USA, May 8-11, 2006; Paper No. 152, 30 pp. (Available via the Internet at <http://www.netl.doe.gov/publications/proceedings/06/carbon-seq/Tech%20Session%20152.pdf>.)
  17. Samanta, A., Zhao, A., Shimizu, G.K.H., Sarkar, P. & Gupta, R. 2012, "Post-combustion CO<sub>2</sub> capture using solid sorbents: A review", *Industrial and Engineering Chemistry Research*, vol. 51, no. 4, pp. 1438-1463.
  18. Choi, S., Drese, J.H. & Jones, C.W. 2009, "Adsorbent materials for carbon dioxide capture from large anthropogenic point sources", *ChemSusChem*, vol. 2, no. 9, pp. 796-854.
  19. Ruthven, D. M. 1984. *Principles of Adsorption and Adsorption Processes*; Wiley Interscience: New York.
  20. Rodríguez-Reinoso, F. & Molina-Sabio, M. 1992, "Activated carbons from lignocellulosic materials by chemical and/or physical activation: an overview", *Carbon*, vol. 30, no. 7, pp. 1111-1118.

21. Lopes, F.V.S., Grande, C.A., Ribeiro, A.M., Loureiro, J.M., Evaggelos, O., Nikolakis, V. & Rodrigues, A.E. 2009, "Adsorption of H<sub>2</sub>, CO<sub>2</sub>, CH<sub>4</sub>, CO, N<sub>2</sub> and H<sub>2</sub>O in activated carbon and zeolite for hydrogen production", *Separation Science and Technology*, vol. 44, no. 5, pp. 1045-1073.
22. Himeno, S., Komatsu, T. & Fujita, S. 2005, "High-pressure adsorption equilibria of methane and carbon dioxide on several activated carbons", *Journal of Chemical and Engineering Data*, vol. 50, no. 2, pp. 369-376.
23. Arenillas, A., Smith, K.M., Drage, T.C. & Snape, C.E. 2005, "CO<sub>2</sub> capture using some fly ash-derived carbon materials", *Fuel*, vol. 84, no. 17, pp. 2204-2210.
24. Na, B., Koo, K., Eum, H., Lee, H. & Song, H.K. 2001, "CO<sub>2</sub> Recovery from Flue Gas by PSA Process using Activated Carbon", *Korean Journal of Chemical Engineering*, vol. 18, no. 2, pp. 220-227.
25. Sircar, S., Golden, T.C. & Rao, M.B. 1996, "Activated carbon for gas separation and storage", *Carbon*, vol. 34, no. 1, pp. 1-12.
26. Cinke, M., Li, J., Bauschlicher Jr., C.W., Ricca, A. & Meyyappan, M. 2003, "CO<sub>2</sub> adsorption in single-walled carbon nanotubes", *Chemical Physics Letters*, vol. 376, no. 5-6, pp. 761-766.
27. Yong, Z., Mata, V. & Rodrigues, A.E. 2000, "Adsorption of carbon dioxide on basic alumina at high temperatures", *Journal of Chemical and Engineering Data*, vol. 45, no. 6, pp. 1093-1095.
28. Baltrusaitis, J., Jensen, J.H. & Grassian, V.H. 2006, "FTIR spectroscopy combined with isotope labeling and quantum chemical calculations to investigate adsorbed bicarbonate formation following reaction of carbon dioxide with surface hydroxyl groups on Fe<sub>2</sub>O<sub>3</sub> and Al<sub>2</sub>O<sub>3</sub>", *Journal of Physical Chemistry B*, vol. 110, no. 24, pp. 12005-12016.
29. Casarin, M., Falcomer, D. & Vittadini, A. 2004, "A theoretical study of the interaction of CO<sub>2</sub> with hydroxylated  $\alpha$ -alumina", *Surface Science*, vol. 566-568, no. 1-3 PART 2, pp. 890-894.
30. Pan, Y., Liu, C. & Ge, Q. 2008, "Adsorption and protonation of CO<sub>2</sub> on partially hydroxylated  $\gamma$ -Al<sub>2</sub>O<sub>3</sub> surfaces: A density functional theory study", *Langmuir*, vol. 24, no. 21, pp. 12410-12419.

31. Doskocil, E.J., Bordawekar, S.V. & Davis, R.J. 1997, "Alkali-support interactions on rubidium base catalysts determined by XANES, EXAFS, CO<sub>2</sub> adsorption, and IR spectroscopy", *Journal of Catalysis*, vol. 169, no. 1, pp. 327-337.
32. Tai, J, Ge, Q, Davis, R J., Neurock, M. 2004, "Adsorption of CO<sub>2</sub> on Model Surfaces of Cesium Oxides Determined from First Principles", *J. Phys. Chem. B*, vol. 108, pp. 16798-16805.
33. Kato, M., Yoshikawa, S. & Nakagawa, K. 2002, "Carbon dioxide absorption by lithium orthosilicate in a wide range of temperature and carbon dioxide concentrations", *Journal of Materials Science Letters*, vol. 21, no. 6, pp. 485-487.
34. Manovic, V. & Anthony, E.J. 2008, "Parametric study on the CO<sub>2</sub> capture capacity of CaO-based sorbents in looping cycles", *Energy and Fuels*, vol. 22, no. 3, pp. 1851-1857.
35. Miyata, S. 1983, "Anion-exchange properties of hydrotalcite-like compounds", *Clays & Clay Minerals*, vol. 31, no. 4, pp. 305-311.
36. Yong, Z., Mata, V. & Rodrigues, A.E. 2001, "Adsorption of carbon dioxide onto hydrotalcite-like compounds (HTLcs) at high temperatures", *Industrial and Engineering Chemistry Research*, vol. 40, no. 1, pp. 204-209.
37. Oliveira, E.L.G., Grande, C.A. & Rodrigues, A.E. 2008, "CO<sub>2</sub> sorption on hydrotalcite and alkali-modified (K and Cs) hydrotalcites at high temperatures", *Separation and Purification Technology*, vol. 62, no. 1, pp. 137-147.
38. Yong Z.; Rodrigues A.E. Hydrotalcite-Like Compounds as Adsorbents for Carbon Dioxide Energy Convers. & Manage. 2002, 43, 1865-1876.
39. Hufton, J.R., Mayorga, S. & Sircar, S. 1999, "Sorption-enhanced reaction process for hydrogen production", *AIChE Journal*, vol. 45, no. 2, pp. 248-256.
40. Hufton, J.R., Mayogra S.G., Gaffney T.R., Nataraj S., Rao M., Sircar S. 1996, "Sorption enhanced reaction process (SERP) for the production of hydrogen", *Proc. USDOE Hydrogen Program Rev. 2*, 693-705.
41. Ram Reddy, M.K., Xu, Z.P., Lu, G.Q. & Da Costa, J.C.D. 2006, "Layered double hydroxides for CO<sub>2</sub> capture: Structure evolution and regeneration",

- Industrial and Engineering Chemistry Research, vol. 45, no. 22, pp. 7504-7509.
42. Cundy, C.S. & Cox, P.A. 2003, "The hydrothermal synthesis of zeolites: History and development from the earliest days to the present time", *Chemical Reviews*, vol. 103, no. 3, pp. 663-701.
  43. The Micro-Porous Structure, Properties and Actions of Zeolites. [Online]. Available: [www.tren.net](http://www.tren.net).
  44. Dyer, A. 1988. *An Introduction to Zeolite Molecular Sieves*, John Wiley, New York, pp. 2-9.
  45. Yang, H., Xu, Z., Fan, M., Gupta, R., Slimane, R.B., Bland, A.E. & Wright, I. 2008, "Progress in carbon dioxide separation and capture: A review", *Journal of Environmental Sciences*, vol. 20, no. 1, pp. 14-27.
  46. Coriani, S., Halkier, A., Rizzo, A. & Ruud, K. 2000, "On the molecular electric quadrupole moment and the electric-field-gradient-induced birefringence of CO<sub>2</sub> and CS<sub>2</sub>", *Chemical Physics Letters*, vol. 326, no. 3-4, pp. 269-276.
  47. Hardie, S.M.L., Garnett, M.H., Fallick, A.E., Rowland, A.P. & Ostle, N.J. 2005, "Carbon dioxide capture using a zeolite molecular sieve sampling system for isotopic studies (<sup>13</sup>C and <sup>14</sup>C) of respiration", *Radiocarbon*, vol. 47, no. 3, pp. 441-451.
  48. Walton, K. S., Abney M. B. and LeVan, M. D., "CO<sub>2</sub> adsorption in Y and X zeolites modified by alkali metal cation exchange *Microporous Mesoporous Mater.*, 2006, 91, 78-84.
  49. Wang, Q., Luo, J., Zhong, Z. & Borgna, A. 2011, "CO<sub>2</sub> capture by solid adsorbents and their applications: Current status and new trends", *Energy and Environmental Science*, vol. 4, no. 1, pp. 42-55.
  50. Zhang, J., Singh, R. & Webley, P.A. 2008, "Alkali and alkaline-earth cation exchanged chabazite zeolites for adsorption based CO<sub>2</sub> capture", *Microporous and Mesoporous Materials*, vol. 111, no. 1-3, pp. 478-487.
  51. Barthomeuf, D. 1984, "Conjugate acid-base pairs in zeolites", *Journal of Physical Chemistry*, vol. 88, no. 1, pp. 42-45.
  52. Siriwardane, R., Shen, M., Fisher, E. & Poston, J. 2002, "CO<sub>2</sub> capture utilizing solid sorbents", *ACS Division of Fuel Chemistry, Preprints*, pp. 75.

53. Siriwardane, R.V., Shen, M.-. & Fisher, E.P. 2003, "Adsorption of CO<sub>2</sub>, N<sub>2</sub>, and O<sub>2</sub> on natural zeolites", *Energy and Fuels*, vol. 17, no. 3, pp. 571-576.
54. Delgado, J.A., Uguina, M.A., Gómez, J.M. & Ortega, L. 2006, "Adsorption equilibrium of carbon dioxide, methane and nitrogen onto Na- and H-mordenite at high pressures", *Separation and Purification Technology*, vol. 48, no. 3, pp. 223-228.
55. Shao, W., Zhang, L., Li, L. & Lee, R.L. 2009, "Adsorption of CO<sub>2</sub> and N<sub>2</sub> on synthesized NaY zeolite at high temperatures", *Adsorption*, vol. 15, no. 5-6, pp. 497-505.
56. Inui, T., Okugawa, Y. & Yasuda, M. 1988, "Relationship between properties of various zeolites and their CO<sub>2</sub>-adsorption behaviors in pressure swing adsorption operation", *Industrial and Engineering Chemistry Research*, vol. 27, no. 7, pp. 1103-1109.
57. Merel, J., Clause, M. & Meunier, F. 2008, "Experimental investigation on CO<sub>2</sub> post-combustion capture by indirect thermal swing adsorption using 13X and 5A zeolites", *Industrial and Engineering Chemistry Research*, vol. 47, no. 1, pp. 209-215.
58. Suzuki H., 1987, Aluminum or gallium, silicon or germanium oxides on porous support; separation or catalytic action, United States Patent 4, 699, 892.
59. McLeary, E.E., Jansen, J.C. & Kapteijn, F. 2006, "Zeolite based films, membranes and membrane reactors: Progress and prospects", *Microporous and Mesoporous Materials*, vol. 90, no. 1-3 SPEC. ISS, pp. 198-220.
60. Haag W.O., Tsikoyiannis J.G. 1991. Membrane composed of a pure molecular sieve. United States Patent 5,019,263, assigned to Mobil Oil Corp.
61. Geus, E.R., Den Exter, M.J. & Van Bekkum, H. 1992, "Synthesis and characterization of zeolite (MFI) membranes on porous ceramic supports", *Journal of the Chemical Society, Faraday Transactions*, vol. 88, no. 20, pp. 3101-3109.
62. Tavolaro, A. & Drioli, E. 1999, "Zeolite membranes", *Advanced Materials*, vol. 11, no. 12, pp. 975-996.

63. Anderson, M. & Lin, Y.S. 2010, "Carbonate-ceramic dual-phase membrane for carbon dioxide separation", *Journal of Membrane Science*, vol. 357, no. 1-2, pp. 122-129.
64. Merkel, T.C., Lin, H., Wei, X. & Baker, R. 2010, "Power plant post-combustion carbon dioxide capture: An opportunity for membranes", *Journal of Membrane Science*, vol. 359, no. 1-2, pp. 126-139.
65. Reif, M. & Dittmeyer, R. 2003, "Porous, catalytically active ceramic membranes for gas-liquid reactions: A comparison between catalytic diffuser and forced through flow concept", *Catalysis Today*, vol. 82, no. 1-4, pp. 3-14.
66. Kusakabe, K., Kuroda, T., Murata, A. & Morooka, S. 1997, "Formation of a Y-Type Zeolite Membrane on a Porous  $\alpha$ -Alumina Tube for Gas Separation", *Industrial and Engineering Chemistry Research*, vol. 36, no. 3, pp. 649-655.
67. Poshusta, J.C., Noble, R.D. & Falconer, J.L. 1999, "Temperature and pressure effects on CO<sub>2</sub> and CH<sub>4</sub> permeation through MFI zeolite membranes", *Journal of Membrane Science*, vol. 160, no. 1, pp. 115-125.
68. Hasegawa, Y., Tanaka, T., Watanabe, K., Jeong, B.-., Kusakabe, K. & Morooka, S. 2002, "Separation of CO<sub>2</sub>-CH<sub>4</sub> and CO<sub>2</sub>-N<sub>2</sub> Systems Using Ion-exchanged FAU-type Zeolite Membranes with Different Si/Al Ratios", *Korean Journal of Chemical Engineering*, vol. 19, no. 2, pp. 309-313.
69. Carreon, M.A., Li, S., Falconer, J.L. & Noble, R.D. 2008, "Alumina-supported SAPO-34 membranes for CO<sub>2</sub>/CH<sub>4</sub> separation", *Journal of the American Chemical Society*, vol. 130, no. 16, pp. 5412-5413.
70. Sebastián, V., Kumakiri, I., Bredesen, R. & Menéndez, M. 2006, "Zeolite membrane for CO<sub>2</sub> removal: operating at high pressure", *Desalination*, vol. 199, no. 1-3, pp. 464-465.
71. Li, S., Falconer, J.L. & Noble, R.D. 2006, "Improved SAPO-34 membranes for CO<sub>2</sub>/CH<sub>4</sub> separations", *Advanced Materials*, vol. 18, no. 19, pp. 2601-2603.
72. Caro, J. & Noack, M. 2008, "Zeolite membranes - Recent developments and progress", *Microporous and Mesoporous Materials*, vol. 115, no. 3, pp. 215-233.
73. Figueroa, J.D., Fout, T., Plasynski, S., McIlvried, H. & Srivastava, R.D. 2008, "Advances in CO<sub>2</sub> capture technology-The U.S. Department of

- Energy's Carbon Sequestration Program", *International Journal of Greenhouse Gas Control*, vol. 2, no. 1, pp. 9-20.
74. James, S.L. 2003, "Metal-organic frameworks", *Chemical Society Reviews*, vol. 32, no. 5, pp. 276-288.
75. Long, J.R. & Yaghi, O.M. 2009, "The pervasive chemistry of metal-organic frameworks", *Chemical Society Reviews*, vol. 38, no. 5, pp. 1213-1214.
76. Eddaoudi, M., Moler, D.B., Li, H., Chen, B., Reineke, T.M., O'Keeffe, M. & Yaghi, O.M. 2001, "Modular chemistry: Secondary building units as a basis for the design of highly porous and robust metal-organic carboxylate frameworks", *Accounts of Chemical Research*, vol. 34, no. 4, pp. 319-330.
77. Tranchemontagne, D.J., Mendoza-Cortés, J.L., O'Keeffe, M. & Yaghi, O.M. 2009, "Secondary building units, nets and bonding in the chemistry of metal-organic frameworks", *Chemical Society Reviews*, vol. 38, no. 5, pp. 1257-1283.
78. Li, J, Kuppler, R.J. & Zhou, H.-. 2009, "Selective gas adsorption and separation in metal-organic frameworks", *Chemical Society Reviews*, vol. 38, no. 5, pp. 1477-1504.
79. Mueller, U., Schubert, M., Teich, F., Puetter, H., Schierle-Arndt, K. & Pastré, J. 2006, "Metal-organic frameworks - Prospective industrial applications", *Journal of Materials Chemistry*, vol. 16, no. 7, pp. 626-636.
80. Lee, Y., Kim, J. & Ahn, W.-. 2013, "Synthesis of metal-organic frameworks: A mini review", *Korean Journal of Chemical Engineering*, vol. 30, no. 9, pp. 1667-1680.
81. Klinowski, J., Almeida Paz, F.A., Silva, P. & Rocha, J. 2011, "Microwave-assisted synthesis of metal-organic frameworks", *Dalton Transactions*, vol. 40, no. 2, pp. 321-330.
82. Jung, D., Yang, D., Kim, J., Kim, J. & Ahn, W. 2010, "Facile synthesis of MOF-177 by a sono chemical method using 1-methyl-2-pyrrolidinone as a solvent", *Dalton Transactions*, vol. 39, no. 11, pp. 2883-2887.
83. Sumida, K., Rogow, D.L., Mason, J.A., McDonald, T.M., Bloch, E.D., Herm, Z.R., Bae, T.-. & Long, J.R. 2012, "Carbon dioxide capture in metal-organic frameworks", *Chemical Reviews*, vol. 112, no. 2, pp. 724-781.



84. Haque, E., Lee, J.E., Jang, I.T., Hwang, Y.K., Chang, J., Jegal, J. & Jung, S.H. 2010, "Adsorptive removal of methyl orange from aqueous solution with metal-organic frameworks, porous chromium-benzenedicarboxylates", *Journal of Hazardous Materials*, vol. 181, no. 1-3, pp. 535-542.
85. Rowsell, J.L.C., Spencer, E.C., Eckert, J., Howard, J.A.K. & Yaghi, O.M. 2005, "Chemistry: Gas adsorption sites in a large-pore metal-organic framework", *Science*, vol. 309, no. 5739, pp. 1350-1354.
86. Férey, G., Latroche, M., Serre, C., Millange, F., Loiseau, T. & Percheron-Guégan, A. 2003, "Hydrogen adsorption in the nanoporous metal-benzenedicarboxylate  $M(OH)(O_2C-C_6H_4-CO_2)$  ( $M = Al^{3+}, Cr^{3+}$ ), MIL-53", *Chemical Communications*, vol. 9, no. 24, pp. 2976-2977.
87. Sabouni, R., Kazemian, H. & Rohani, S. 2014, "Carbon dioxide capturing technologies: A review focusing on metal organic framework materials (MOFs)", *Environmental Science and Pollution Research*, vol. 21, no. 8, pp. 5427-5449.
88. Ramsahye, N.A., Maurin, G., Bourrelly, S., Llewellyn, P., Loiseau, T. & Férey, G. 2007, "Charge distribution in metal organic framework materials: Transferability to a preliminary molecular simulation study of the  $CO_2$  adsorption in the MIL-53 (Al) system", *Physical Chemistry Chemical Physics*, vol. 9, no. 9, pp. 1059-1063.
89. D'Alessandro, D.M., Smit, B. & Long, J.R. 2010, "Carbon dioxide capture: Prospects for new materials", *Angewandte Chemie - International Edition*, vol. 49, no. 35, pp. 6058-6082.
90. Millward, A.R. & Yaghi, O.M. 2005, "Metal-organic frameworks with exceptionally high capacity for storage of carbon dioxide at room temperature", *Journal of the American Chemical Society*, vol. 127, no. 51, pp. 17998-17999.
91. Banerjee, R., Phan, A., Wang, B., Knobler, C., Furukawa, H., O'Keeffe, M. & Yaghi, O.M. 2008, "High-throughput synthesis of zeolitic imidazolate frameworks and application to  $CO_2$  capture", *Science*, vol. 319, no. 5865, pp. 939-943.
92. Banerjee, R., Furukawa, H., Britt, D., Knobler, C., O'Keeffe, M. & Yaghi, O.M. 2009, "Control of pore size and functionality in isoreticular zeolitic

- imidazolate frameworks and their carbon dioxide selective capture properties", *Journal of the American Chemical Society*, vol. 131, no. 11, pp. 3875-3877.
93. Britt, D., Furukawa, H., Wang, B., Glover, T.G. & Yaghi, O.M. 2009, "Highly efficient separation of carbon dioxide by a metal-organic framework replete with open metal sites", *Proceedings of the National Academy of Sciences of the United States of America*, vol. 106, no. 49, pp. 20637-20640.
94. Bourrelly, S., Llewellyn, P.L., Serre, C., Millange, F., Loiseau, T. & Férey, G. 2005, "Different adsorption behaviors of methane and carbon dioxide in the isotypic nanoporous metal terephthalates MIL-53 and MIL-47", *Journal of the American Chemical Society*, vol. 127, no. 39, pp. 13519-13521.
95. Yazaydin, A.Ö., Benin, A.I., Faheem, S.A., Jakubczak, P., Low, J.J., Richard R. Willis & Snurr, R.Q. 2009, "Enhanced CO<sub>2</sub> adsorption in metal-organic frameworks via occupation of open-metal sites by coordinated water molecules", *Chemistry of Materials*, vol. 21, no. 8, pp. 1425-1430.
96. Kizzie, A.C., Wong-Foy, A.G. & Matzger, A.J. 2011, "Effect of humidity on the performance of microporous coordination polymers as adsorbents for CO<sub>2</sub> capture", *Langmuir*, vol. 27, no. 10, pp. 6368-6373.
97. An, J., Geib, S.J. & Rosi, N.L. 2010, "High and selective CO<sub>2</sub> uptake in a cobalt adeninate metal-organic framework exhibiting pyrimidine- and amino-decorated pores", *Journal of the American Chemical Society*, vol. 132, no. 1, pp. 38-39.
98. Bae, Y., Hauser, B.G., Farha, O.K., Hupp, J.T. & Snurr, R.Q. 2011, "Enhancement of CO<sub>2</sub>/CH<sub>4</sub> selectivity in metal-organic frameworks containing lithium cations", *Microporous and Mesoporous Materials*, vol. 141, no. 1-3, pp. 231-235.
99. Sumida, K., Horike, S., Kaye, S.S., Herm, Z.R., Queen, W.L., Brown, C.M., Grandjean, F., Long, G.J., Dailly, A. & Long, J.R. 2010, "Hydrogen storage and carbon dioxide capture in an iron-based sodalite-type metal-organic framework (Fe-BTT) discovered via high-throughput methods", *Chemical Science*, vol. 1, no. 2, pp. 184-19
100. Phan, A., Doonan, C.J., Uribe-Romo, F.J., Knobler, C.B., Okeeffe, M. & Yaghi, O.M. 2010, "Synthesis, structure, and carbon dioxide capture

- properties of zeolitic imidazolate frameworks", *Accounts of Chemical Research*, vol. 43, no. 1, pp. 58-67.
101. Cravillon, J., Nayuk, R., Springer, S., Feldhoff, A., Huber, K. & Wiebcke, M. 2011, "Controlling zeolitic imidazolate framework nano- and microcrystal formation: Insight into crystal growth by time-resolved in situ static light scattering", *Chemistry of Materials*, vol. 23, no. 8, pp. 2130-2141.
  102. Amrouche, H., Aguado, S., Pérez-Pellitero, J., Chizallet, C., Siperstein, F., Farrusseng, D., Bats, N. & Nieto-Draghi, C. 2011, "Experimental and computational study of functionality impact on sodalite-zeolitic imidazolate frameworks for CO<sub>2</sub> separation", *Journal of Physical Chemistry C*, vol. 115, no. 33, pp. 16425-16432.
  103. Park, K.S., Ni, Z., Côté, A.P., Choi, J.Y., Huang, R., Uribe-Romo, F.J., Chae, H.K., O'Keeffe, M. & Yaghi, O.M. 2006, "Exceptional chemical and thermal stability of zeolitic imidazolate frameworks", *Proceedings of the National Academy of Sciences of the United States of America*, vol. 103, no. 27, pp. 10186-10191.
  104. Wang, B., Côté, A.P., Furukawa, H., O'Keeffe, M. & Yaghi, O.M. 2008, "Colossal cages in zeolitic imidazolate frameworks as selective carbon dioxide reservoirs", *Nature*, vol. 453, no. 7192, pp. 207-211.
  105. McCusker, L.B., Liebau, F. & Engelhardt, G. 2001, "Nomenclature of structural and compositional characteristics of ordered microporous and mesoporous materials with inorganic hosts: (IUPAC recommendations 2001)", *Pure and Applied Chemistry*, vol. 73, no. 2, pp. 381-394.
  106. Morey, M.S., Davidson, A. & Stucky, G.D. 1998, "Silica-Based, Cubic Mesostructures: Synthesis, Characterization and Relevance for Catalysis", *Journal of Porous Materials*, vol. 5, no. 3-4, pp. 195-204.
  107. Xu, B., Long, J., Tian, H., Zhu, Y. & Sun, X. 2009, "Synthesis and characterization of mesoporous  $\gamma$ -alumina templated by saccharide molecules", *Catalysis Today*, vol. 147, no. SUPPL., pp. S46-S50.
  108. Chen, J., N. Xia, T. Zhou, S. Tan and F. Jiang. 2009, "Mesoporous carbon spheres: synthesis, characterization and super capacitance", *Int. J. Electrochem. Sci.*, vol. 4, pp. 1063-1073.

109. Jiao, F. & Bruce, P.G. 2004, "Two- and three-dimensional mesoporous iron oxides with microporous walls", *Angewandte Chemie - International Edition*, vol. 43, no. 44, pp. 5958-5961.
110. Rao, Y. & Antonelli, D.M. 2009, "Mesoporous transition metal oxides: Characterization and applications in heterogeneous catalysis", *Journal of Materials Chemistry*, vol. 19, no. 14, pp. 1937-1944.
111. Nandiyanto, A.B.D., Kim, S, Iskandar, F. & Okuyama, K. 2009, "Synthesis of spherical mesoporous silica nanoparticles with nanometer-size controllable pores and outer diameters", *Microporous and Mesoporous Materials*, vol. 120, no. 3, pp. 447-453.
112. Draggan, S., 2008. Silicon. [Online]. Available: <http://www.eoearth.org/article/Silicon>.
113. Chew, T., Ahmad, A.L. & Bhatia, S. 2010, "Ordered mesoporous silica (OMS) as an adsorbent and membrane for separation of carbon dioxide (CO<sub>2</sub>)", *Advances in Colloid and Interface Science*, vol. 153, no. 1-2, pp. 43-57.
114. Cundy, C.S. & Cox, P.A. 2005, "The hydrothermal synthesis of zeolites: Precursors, intermediates and reaction mechanism", *Microporous and Mesoporous Materials*, vol. 82, no. 1-2, pp. 1-78.
115. Kim, T, Ryoo, R, Kruk, M, Gierszal, K. P, Jaroniec, M, Kamiya, S, Terasaki. 2004, "Tailoring the Pore Structure of SBA-16 Silica Molecular Sieve through the Use of Copolymer Blends and Control of Synthesis Temperature and Time", *Journal of Physical Chemistry B*, vol. 108, pp. 11480.
116. Newalkar, B.L. & Komarneni, S. 2001, "Control over microporosity of ordered microporous-mesoporous silica SBA-15 framework under microwave-hydrothermal conditions: Effect of salt addition", *Chemistry of Materials*, vol. 13, no. 12, pp. 4573-4579.
117. Park S-E, Kim DS, Chang J-S, Kim WY. 1998, "Synthesis of MCM-41 using microwave heating with ethylene glycol", *Catalysis Today*, vol. 44, no.1-4, pp. 301-308.
118. Brinker, C.J., Sehgal, R., Hietala, S.L., Deshpande, R., Smith, D.M., Loy, D. & Ashley, C.S. 1994, "Sol-gel strategies for controlled porosity inorganic materials", *Journal of Membrane Science*, vol. 94, pp. 85-102.

119. Sayari, A. & Hamoudi, S. 2001, "Periodic mesoporous silica-based organic-inorganic nanocomposite materials", *Chemistry of Materials*, vol. 13, no. 10, pp. 3151-3168.
120. Huo, Q., Leon, R., Petroff, P.M. & Stucky, G.D. 1995, "Mesostructure design with gemini surfactants: Supercage formation in a three-dimensional hexagonal array", *Science*, vol. 268, no. 5215, pp. 1324-1327.
121. Zhao, D., Huo, Q., Feng, J., Chmelka, B.F. & Stucky, G.D. 1998, "Nonionic triblock and star diblock copolymer and oligomeric surfactant syntheses of highly ordered, hydrothermally stable, mesoporous silica structures", *Journal of the American Chemical Society*, vol. 120, no. 24, pp. 6024-6036.
122. Tanev, P.T. & Pinnavaia, T.J. 1995, "A neutral templating route to Mesoporous molecular sieves", *Science*, vol. 267, no. 5199, pp. 865-867.
123. Vartuli, J.C.; Roth, W.J.; Degnan, T.F. 2008, *Mesoporous materials (M41S): From discovery to application*. In *Dekker Encyclopedia of Nanoscience and Nanotechnology*; Schwarz, J.A., Contescu, C.I., Putyera, K., Eds.; Taylor and Francis: New York, NY, USA; pp. 1797-1811.
124. Ralf Kohn. 2001, *Synthesis, Characterization, and Modification of various mesoporous silica phases*. University of Hamburg.
125. Huo, Q., Margolese, D.I., Ciesla, U., Demuth, D.G., Feng, P., Gier, T.E., Sieger, P., Firouzi, A., Chmelka, B.F., Schüth, F. & Stucky, G.D. 1994, "Organization of organic molecules with inorganic molecular species into nanocomposite biphasic arrays", *Chemistry of Materials*, vol. 6, no. 8, pp. 1176-1191.
126. Beck, J.S., Vartuli, J.C., Roth, W.J., Leonowicz, M.E., Kresge, C.T., Schmitt, K.D., Chu, C.T.-., Olson, D.H., Sheppard, E.W., McCullen, S.B., Higgins, J.B. & Schlenker, J.L. 1992, "A new family of mesoporous molecular sieves prepared with liquid crystal templates", *Journal of the American Chemical Society*, vol. 114, no. 27, pp. 10834-10843.
127. Edler, K.J. & White, J.W. 1999, "Preparation dependent stability of pure silica MCM-41", *Journal of Materials Chemistry*, vol. 9, no. 10, pp. 2611-2615.

128. Cheng, C, Luan, Z. & Klinowski, J. 1995, "The role of surfactant micelles in the synthesis of the mesoporous molecular sieve MCM-41", *Langmuir*, vol. 11, no. 7, pp. 2815-2819.
129. Sayari, A., Karra, V.R., Reddy, J.S. & Moudrakovski, I.L. 1996, "Synthesis of mesostructured lamellar aluminophosphates", *Chemical Communications*, no. 3, pp. 411-412.
130. Grün, M., Unger, K.K., Matsumoto, A. & Tsutsumi, K. 1999, "Novel pathways for the preparation of mesoporous MCM-41 materials: Control of porosity and morphology", *Microporous and Mesoporous Materials*, vol. 27, no. 2-3, pp. 207-216.
131. Sayari, A., Yang, Y., Kruk, M. & Jaroniec, M. 1999, "Expanding the pore size of MCM-41 silicas: Use of amines as expanders in direct synthesis and post synthesis procedures", *Journal of Physical Chemistry B*, vol. 103, no. 18, pp. 3651-3658.
132. Jana, S.K., Mochizuki, A. & Namba, S. 2004, "Progress in pore-size control of mesoporous MCM-41 molecular sieve using surfactant having different alkyl chain lengths and various organic auxiliary chemicals", *Catalysis Surveys from Asia*, vol. 8, no. 1, pp. 1-13.
133. Loganathan, S., Tikmani, M. & Ghoshal, A.K. 2013, "Novel pore-expanded MCM-41 for CO<sub>2</sub> capture: Synthesis and characterization", *Langmuir*, vol. 29, no. 10, pp. 3491-3499.
134. Zhao, D., Feng, J., Huo, Q., Melosh, N., Fredrickson, G.H., Chmelka, B.F. & Stucky, G.D. 1998, "Triblock copolymer syntheses of mesoporous silica with periodic 50 to 300 angstrom pores", *Science*, vol. 279, no. 5350, pp. 548-552.
135. Zhao, D., Sun, J., Li, Q. & Stucky, G.D. 2000, "Morphological control of highly ordered mesoporous silica SBA-15", *Chemistry of Materials*, vol. 12, no. 2, pp. 275-279.
136. Yang, C., Zibrowius, B., Schmidt, W. & Schüth, F. 2004, "Stepwise removal of the copolymer template from mesopores and micropores in SBA-15", *Chemistry of Materials*, vol. 16, no. 15, pp. 2918-2925.
137. Van Grieken, R., Calleja, G., Stucky, G.D., Melero, J.A., García, R.A. & Iglesias, J. 2003, "Supercritical fluid extraction of a nonionic surfactant

- template from SBA-15 materials and consequences on the porous structure", *Langmuir*, vol. 19, no. 9, pp. 3966-3973.
138. Kleitz F. 2002, Ordered mesoporous materials, template removal, frameworks and morphology. University of Bochum.
139. Van Der Meer, J., Bardez-Giboire, I., Mercier, C., Revel, B., Davidson, A. & Denoyel, R. 2010, "Mechanism of metal oxide nanoparticle loading in SBA-15 by the double solvent technique", *Journal of Physical Chemistry C*, vol. 114, no. 8, pp. 3507-3515.
140. Vinh-Thang, H., Huang, Q., Eić, M., Trong-On, D. & Kaliaguine, S. 2005, "Adsorption of C7 hydrocarbons on biporous SBA-15 mesoporous silica", *Langmuir*, vol. 21, no. 11, pp. 5094-5101.
141. Liu, X., Li, J., Zhou, L., Huang, D. & Zhou, Y. 2005, "Adsorption of CO<sub>2</sub>, CH<sub>4</sub> and N<sub>2</sub> on ordered mesoporous silica molecular sieve", *Chemical Physics Letters*, vol. 415, no. 4-6, pp. 198-201.
142. Sun, Y., Liu, X.-., Su, W., Zhou, Y. & Zhou, L. 2007, "Studies on ordered mesoporous materials for potential environmental and clean energy applications", *Applied Surface Science*, vol. 253, no. 13 SPEC. ISS., pp. 5650-5655.
143. Macario A, Katovic A, Giordano G, Iucolano F, Caputo D. 2005, "Synthesis of mesoporous materials for carbon dioxide sequestration", *Microporous and Mesoporous Materials*, vol. 81, no. 1, pp. 139-147.
144. Belmabkhout, Y., Serna-Guerrero, R. & Sayari, A. 2009, "Adsorption of CO<sub>2</sub> from dry gases on MCM-41 silica at ambient temperature and high pressure. 1: Pure CO<sub>2</sub> adsorption", *Chemical Engineering Science*, vol. 64, no. 17, pp. 3721-3728.
145. Gray, M.L., Champagne, K.J., Fauth, D., Baltrus, J.P. & Pennline, H. 2008, "Performance of immobilized tertiary amine solid sorbents for the capture of carbon dioxide", *International Journal of Greenhouse Gas Control*, vol. 2, no. 1, pp. 3-8.
146. Ho, M.T., Allinson, G.W. & Wiley, D.E. 2008, "Reducing the cost of CO<sub>2</sub> capture from flue gases using pressure swing adsorption", *Industrial and Engineering Chemistry Research*, vol. 47, no. 14, pp. 4883-4890.

147. da Silva, E.F. & Svendsen, H.F. 2007, "Computational chemistry study of reactions, equilibrium and kinetics of chemical CO<sub>2</sub> absorption", *International Journal of Greenhouse Gas Control*, vol. 1, no. 2, pp. 151-157.
148. Kizzie. A.C. 2012, *Synthesis and Characterization of Microporous Coordination Polymers as adsorbents for CO<sub>2</sub> capture*. The University of Michigan.
149. Xu, X., Song, C., Miller, B.G. & Scaroni, A.W. 2005, "Influence of moisture on CO<sub>2</sub> separation from gas mixture by a nanoporous adsorbent based on polyethylenimine-modified molecular sieve MCM-41", *Industrial and Engineering Chemistry Research*, vol. 44, no. 21, pp. 8113-8119.
150. Zhao, A., Samanta, A., Sarkar, P. & Gupta, R. 2013, "Carbon dioxide adsorption on amine-impregnated mesoporous SBA-15 sorbents: Experimental and kinetics study", *Industrial and Engineering Chemistry Research*, vol. 52, no. 19, pp. 6480-6491.
151. Wei, L., Gao, Z., Jing, Y. & Wang, Y. 2013, "Adsorption of CO<sub>2</sub> from simulated flue gas on pentaethylenhexamine-loaded mesoporous silica support adsorbent", *Industrial and Engineering Chemistry Research*, vol. 52, no. 42, pp. 14965-14974.
152. Son. W.J, Choi. J.S, Ahn. W.S. 2008, "Adsorptive removal of carbon dioxide using polyethylenimine-loaded mesoporous materials", *Microporous Mesoporous Materials*, vol. 113, pp. 31-40.
153. Chen, C., Yang, S., Ahn, W. & Ryoo, R. 2009, "Amine-impregnated silica monolith with a hierarchical pore structure: Enhancement of CO<sub>2</sub> capture capacity", *Chemical Communications*, no. 24, pp. 3627-3629.
154. Linneen, N.N., Pfeffer, R. & Lin, Y.S. 2013, "Amine distribution and carbon dioxide sorption performance of amine coated silica aerogel sorbents: Effect of synthesis methods", *Industrial and Engineering Chemistry Research*, vol. 52, no. 41, pp. 14671-14679.
155. Plaza, M.G., Pevida, C., Arias, B., Feroso, J., Arenillas, A., Rubiera, F. & Pis, J.J. 2008, "Application of thermogravimetric analysis to the evaluation of aminated solid sorbents for CO<sub>2</sub> capture", *Journal of Thermal Analysis and Calorimetry*, vol. 92, no. 2, pp. 601-606.



156. Gargiulo, N., Pepe, F. & Caputo, D. 2014, "CO<sub>2</sub> adsorption by functionalized nanoporous materials: A Review", *Journal of Nanoscience and Nanotechnology*, vol. 14, no. 2, pp. 1811-1822.
157. J.C. Hicks. 2007, *Organic/Inorganic hybrid amine and sulfonic acid tethered silica materials: Synthesis, Characterization and application*. Georgia Institute of Technology.
158. Kim, S., Son, W., Choi, J. & Ahn, W. 2008, "CO<sub>2</sub> adsorption using amine-functionalized mesoporous silica prepared via anionic surfactant-mediated synthesis", *Microporous and Mesoporous Materials*, vol. 115, no. 3, pp. 497-503.
159. Yokoi, T., Yoshitake, H. & Tatsumi, T. 2003, "Synthesis of Anionic-Surfactant-Templated Mesoporous Silica Using Organoalkoxysilane-Containing Amino Groups", *Chemistry of Materials*, vol. 15, no. 24, pp. 4536-4538.
160. Hao, S., Xiao, Q., Yang, H., Zhong, Y., Pepe, F. & Zhu, W. 2010, "Synthesis and CO<sub>2</sub> adsorption property of amino-functionalized silica nanospheres with centrosymmetric radial mesopores", *Microporous and Mesoporous Materials*, vol. 132, no. 3, pp. 552-558.
161. Knözinger, H. & Rumpf, E. 1978, "Stabilization of hexarhodiumhexadecacarbonyl by attachment to chemically modified silica surfaces", *Inorganica Chimica Acta*, vol. 30, no. C, pp. 51-58.
162. Che, S., Garcia-Bennett, A.E., Yokoi, T., Sakamoto, K., Kunieda, H., Terasaki, O. & Tatsumi, T. 2003, "A novel anionic surfactant templating route for synthesizing mesoporous silica with unique structure", *Nature Materials*, vol. 2, no. 12, pp. 801-805.
163. Cassiers K, Linssen T, Mathieu M, Benjelloun M, Schrijnemakers K, Van der Voort P, "A Detailed Study of Thermal, Hydrothermal, and Mechanical Stabilities of a Wide Range of Surfactant Assembled Mesoporous Silicas", *Chemistry of Materials* 2002; 14: 2317-2324.
164. Guo W, Li X, Zhao XS. "Understanding the hydrothermal stability of large-pore periodic mesoporous organosilicas and pure silicas", *Microporous Mesoporous Materials*, 2006; 93: 285-293.

165. Park, D, Nishiyama, N., Egashira, Y. & Ueyama, K. 2001, "Enhancement of hydrothermal stability and hydrophobicity of a silica MCM-48 membrane by silylation", *Industrial and Engineering Chemistry Research*, vol. 40, no. 26, pp. 6105-6110.
166. Leal, O., Bolívar, C., Ovalles, C., García, J.J. & Espidel, Y. 1995, "Reversible adsorption of carbon dioxide on amine surface-bonded silica gel", *Inorganica Chimica Acta*, vol. 240, no. 1-2, pp. 183-189.
167. Huang, H.Y., Yang, R.T., Chinn, D. & Munson, C.L. 2003, "Amine-grafted MCM-48 and silica xerogel as superior sorbents for acidic gas removal from natural gas", *Industrial and Engineering Chemistry Research*, vol. 42, no. 12, pp. 2427-2433.
168. Delaney, S.W., Knowles, G.P. & Chaffee, A.L. 2002, "Hybrid mesoporous materials for carbon dioxide separation", *ACS Division of Fuel Chemistry, Preprints*, pp. 65.
169. Knowles, G.P., Delaney, S.W. & Chaffee, A.L. 2005, "Amine-functionalised mesoporous silicas as CO<sub>2</sub> adsorbents", vol. 156, pp. 887-896.
170. Knowles, G.P., Graham, J.V., Delaney, S.W. & Chaffee, A.L. 2005, "Aminopropyl-functionalized mesoporous silicas as CO<sub>2</sub> adsorbents", *Fuel Processing Technology*, vol. 86, no. 14-15, pp. 1435-1448.
171. Chaffee, A.L. 2005, "Molecular modeling of HMS hybrid materials for CO<sub>2</sub> adsorption", *Fuel Processing Technology*, vol. 86, no. 14-15, pp. 1473-1486.
172. Knowles, G.P., Delaney, S.W. & Chaffee, A.L. 2006, "Diethylenetriamine[propyl(silyl)]-functionalized (DT) mesoporous silicas as CO<sub>2</sub> adsorbents", *Industrial and Engineering Chemistry Research*, vol. 45, no. 8, pp. 2626-2633.
173. Chang, A.C.C., Chuang, S.S.C., Gray, M. & Soong, Y. 2003, "In-situ infrared study of CO<sub>2</sub> adsorption on SBA-15 grafted with  $\gamma$ -(aminopropyl)triethoxysilane", *Energy and Fuels*, vol. 17, no. 2, pp. 468-473.
174. Hiyoshi, N., Yogo, K. & Yashima, T. 2005, "Adsorption characteristics of carbon dioxide on organically functionalized SBA-15", *Microporous and Mesoporous Materials*, vol. 84, no. 1-3, pp. 357-365.

175. Wei, J., Shi, J., Pan, H., Zhao, W., Ye, Q. & Shi, Y. 2008, "Adsorption of carbon dioxide on organically functionalized SBA-16", *Microporous and Mesoporous Materials*, vol. 116, no. 1-3, pp. 394-399.
176. Zeleňák, V., Badaničová, M., Halamová, D., Čejka, J., Zukal, A., Murafa, N. & Goerigk, G. 2008, "Amine-modified ordered mesoporous silica: Effect of pore size on carbon dioxide capture", *Chemical Engineering Journal*, vol. 144, no. 2, pp. 336-342.
177. Ko, Y.G., Shin, S.S. & Choi, U.S. 2011, "Primary, secondary, and tertiary amines for CO<sub>2</sub> capture: Designing for mesoporous CO<sub>2</sub> adsorbents", *Journal of Colloid and Interface Science*, vol. 361, no. 2, pp. 594-602.
178. Harlick, P.J.E. & Sayari, A. 2006, "Applications of pore-expanded mesoporous silicas. 3. Triamine silane grafting for enhanced CO<sub>2</sub> adsorption", *Industrial and Engineering Chemistry Research*, vol. 45, no. 9, pp. 3248-3255.
179. Harlick, P.J.E. & Sayari, A. 2007, "Applications of pore-expanded mesoporous silica. 5. triamine grafted material with exceptional CO<sub>2</sub> dynamic and equilibrium adsorption performance", *Industrial and Engineering Chemistry Research*, vol. 46, no. 2, pp. 446-458.
180. Liang, Z., Fadhel, B., Schneider, C.J. & Chaffee, A.L. 2008, "Stepwise growth of melamine-based dendrimers into mesopores and their CO<sub>2</sub> adsorption properties", *Microporous and Mesoporous Materials*, vol. 111, no. 1-3, pp. 536-543.
181. Liang, Z., Fadhel, B., Schneider, C.J. & Chaffee, A.L. 2009, "Adsorption of CO<sub>2</sub> on mesocellular siliceous foam iteratively functionalized with dendrimers", *Adsorption*, vol. 15, no. 5-6, pp. 429-437.
182. Bhagiyalakshmi, M., Park, S.D., Cha, W.S. & Jang, H.T. 2010, "Development of TREN dendrimers over mesoporous SBA-15 for CO<sub>2</sub> adsorption", *Applied Surface Science*, vol. 256, no. 22, pp. 6660-6666.
183. Jones, C.W., Hicks, J.C., Fauth, D.J., Gray, M. 2007, Structures for capturing CO<sub>2</sub>, methods of making the structures and methods of capturing CO<sub>2</sub>, US Patent Application No. US2007/0149398.
184. Hicks, J.C., Drese, J.H., Fauth, D.J., Gray, M.L., Qi, G. & Jones, C.W. 2008, "Designing adsorbents for CO<sub>2</sub> capture from flue gas-hyperbranched

aminosilicas capable of capturing CO<sub>2</sub> reversibly", *Journal of the American Chemical Society*, vol. 130, no. 10, pp. 2902-2903.

185. Drese, J.H., Choi, S., Lively, R.P., Koros, W.J., Fauth, D.J., Gray, M.L. & Jones, C.W. 2009, "Synthesis-structure-property relationships for Hyperbranched aminosilica CO<sub>2</sub> adsorbents", *Advanced Functional Materials*, vol. 19, no. 23, pp. 3821-3832.



## CHAPTER 3

Chapter 3 discusses the materials used to prepare the sorbents investigated during this study. All the techniques used to characterize the adsorbents are discussed in detail in this chapter. A detailed description of the synthetic protocols used to prepare the adsorbents is also documented in this chapter.

### 3.1 Materials and methods

#### Chemicals:

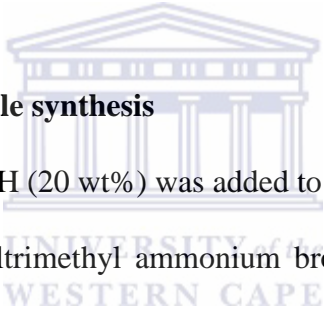
Chemical	Supplier
Amorphous silica gel, Davisal	Sigma Aldrich
Tetradecyltrimethylammonium bromide	Sigma Aldrich
Hexadecyltrimethylammonium bromide	Sigma Aldrich
Trimethyloctadecylammonium bromide	Sigma Aldrich
P123 Pluronic acid polymer	Sigma Aldrich
Tetraethyl orthosilicate	Alfa Aeser
Ammonium hydroxide	VWR
Toluene 99 %	Sigma Aldrich
Anhydrous acetonitrile	VWR
3-(Aminopropyl)triethoxysilane 99 %	Sigma Aldrich
N-[3-(trimethoxysilyl)propyl]ethylenediamine 97 %	Sigma Aldrich
3-Chloropropyl)-trimethoxysilane 97 %	Sigma Aldrich
Tris(2-aminoethyl) amine 96 %	Sigma Aldrich
Ethyl 2-bromopropanoate 99 %	Sigma Aldrich
Cyanuric chloride 99 %	Sigma Aldrich
Guandine hydrochloride 98 %	Sigma Aldrich
Absolute ethanol	Sigma Aldrich
Potassium carbonate	Merck
Potassium iodide	Merck

### 3.2 Methodology

#### 3.2.1 MCM-41 synthesis (C<sub>14</sub>TABr, C<sub>16</sub>TABr and C<sub>18</sub>TABr)

- 280 ml of NH<sub>4</sub>OH (20 wt%) was added to 275 ml of distilled water
- 1.85, 2 and 2.2 g of C<sub>14</sub>TABr, C<sub>16</sub>TABr and C<sub>18</sub>TABr was added to solution, respectively and thoroughly stirred until the surfactants dissolved.
- 10 ml of TEOS is then added drop-wise and solution is stirred for 2 hours.
- Solution is then filtered and product thoroughly washed with distilled water until excess ammonia was removed.
- Template removal was performed at 550 °C in air for 6 hours.

#### 3.2.2 C<sub>18</sub>MCM-41 upscale synthesis

- 
- 1536 ml of NH<sub>4</sub>OH (20 wt%) was added to 1650 ml of distilled water.
  - 12 g of hexacetyltrimethyl ammonium bromide was added to solution and thoroughly stirred until surfactant dissolved.
  - 60 ml of TEOS is then added drop-wise and solution is stirred for 2 hours.
  - Solution is then filtered and product thoroughly washed with distilled water until excess ammonia was removed.
  - Template removal was performed at 550 °C in air for 6 hours.

### 3.2.3 SBA-15 synthesis

4 g of Pluronic P123 dissolved in 125 ml of 2M HCl at 40 °C. Mixture was stirred until the polymer was completely dissolved. Upon complete dissolution of the polymer, 8.4 g of tetraethyl orthosilicate was added to the reaction mixture drop-wise and the reaction was stirred at 40 °C for 24 hours. The gel was then transferred into autoclaves and aged at 90 °C for 24 hours without stirring. Template removal was performed at 540 °C for 4 hours in air [2].

### 3.2.4 Modified mesoporous silica with APS (1<sup>st</sup> generation G1 adsorbents)

#### Silica gel

1 g of silica gel was suspended in 50 ml of dry toluene. To the reaction mixture 4 ml of APS was added and the reaction was left to stir overnight at 70 °C under reflux. The solid was collected and thoroughly washed with toluene, and the sample was placed in a convection oven and dried at 75 °C.

#### C<sub>18</sub>MCM-41

1 g of C<sub>18</sub>MCM-41 was suspended in 50 ml of dry toluene. To the reaction mixture 2 ml of APS was added and the reaction was left to stir overnight at 70 °C under reflux. The solid was collected and thoroughly washed with toluene, and the sample was placed in a convection oven and dried at 75 °C.

#### SBA-15

1 g of SBA 15 was suspended in 50 ml of dry toluene. To the reaction mixture 5 ml of APS was added and the reaction was left to stir overnight at 70 °C under reflux. The solid was collected and thoroughly washed with toluene, and the sample was placed in a convection oven and dried at 75 °C.

### 3.2.5 TPED modified mesoporous silica's (G1)

#### **Silica gel-TPED**

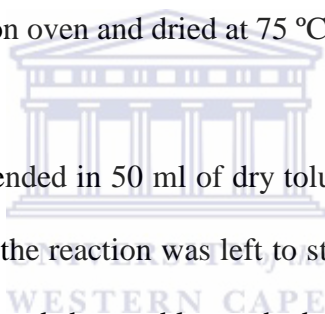
1 g of silica gel was suspended in 50 ml of dry toluene. To the reaction mixture 1 ml of TPED was added and the reaction was left to stir overnight at 70 °C under reflux. The solid was collected and thoroughly washed with toluene, and the sample was placed in a convection oven and dried at 75 °C.

#### **C<sub>18</sub>MCM-41-TPED**

1 g of C<sub>18</sub>MCM-41 was suspended in 50 ml of dry toluene. To the reaction mixture 2 ml of TPED was added and the reaction was left to stir overnight at 70 °C under reflux. The solid was collected and thoroughly washed with toluene, and the sample was placed in a convection oven and dried at 75 °C.

#### **SBA-15-TPED**

1 g of SBA 15 was suspended in 50 ml of dry toluene. To the reaction mixture 3 ml of TPED was added and the reaction was left to stir overnight at 70 °C under reflux. The solid was collected and thoroughly washed with toluene, and the sample was placed in a convection oven and dried at 75 °C.





### 3.2.6 TREN modified mesoporous silica's (2<sup>nd</sup> generation G2 adsorbents)

1 g of silica gel, C<sub>18</sub>MCM-41 and SBA-15 was dispersed in 50ml of dry toluene respectively. To the reaction mixtures of silica gel, C<sub>18</sub>MCM-41 and SBA-15, 3.6 ml, 3 ml and 5 ml of CPS was added respectively. The reactions were left to stir for 24 hours at 70 °C under reflux. The solid was collected, placed in a convection oven and dried at 75 °C. The products were denoted as silica gel-CPS, C<sub>18</sub>MCM-41-CPS and SBA-15-CPS.

Silica gel-CPS, C<sub>18</sub>MCM-41-CPS and SBA-15-CPS were re dispersed in 50 ml of dry toluene. To the reaction mixture containing silica gel-CPS, C<sub>18</sub>MCM-41-CPS and SBA-15-CPS, 1 ml, 2 ml and 3 ml of TREN were added respectively. The reactions were left to stir for 24 hours at 70 °C under reflux. The solid was collected and thoroughly washed with toluene, and the sample was placed in a convection oven and dried at 75 °C.

### 3.2.7 Guanidine grafted mesoporous silica's (G2)

1 g of C<sub>n</sub>MCM-41 (n = 14-18) was dispersed in 50 ml of dry toluene. 3 ml of CPS was added to the reaction mixtures which were stirred under reflux at 70 °C for 24 hours. The solid products were filtered and thoroughly washed with toluene. The products were denoted as C<sub>14</sub>MCM-41-CPS, C<sub>16</sub>MCM-41-CPS and C<sub>18</sub>MCM-41-CPS. In three separate reaction vessels containing C<sub>14</sub>MCM-41-CPS, C<sub>16</sub>MCM-41-CPS and C<sub>18</sub>MCM-41-CPS and 3.32 g of KI, were added to solutions containing 0.42 g of guanidine hydrochloride and 2.76 g of K<sub>2</sub>CO<sub>3</sub> in 100 ml of acetonitrile. The reaction mixtures were left to stir under reflux for 5 hours. The obtained solids were copiously washed with water/ethanol followed by drying using a convection oven at 75 °C.

### 3.2.8 Expansion of 1<sup>st</sup> generation adsorbents (G3)

#### **C<sub>18</sub>MCM-41-TPED-TREN**

Approximately 1 g of C<sub>18</sub>MCM 41-TPED was placed in 50 ml of dry toluene and allowed to stir until the reaction mixture became homogenous. To this mixture 2 ml of ethyl-2 bromopropanoate was added and the reaction was allowed to stir under reflux at 70 °C for 24 hours. The solid product was then filtered and thoroughly washed with toluene to remove any unreacted species. The product was denoted C<sub>18</sub>MCM-41-TPED-Br.

C<sub>18</sub>MCM-41-TPED -Br was re dispersed in 50 ml of dry toluene and 2 ml of TREN was added to the reaction mixture. The reaction was carried out under reflux at 70 °C for 24 hours. The solid product was then filtered and thoroughly washed with toluene. The product was denoted as C<sub>18</sub>MCM-41-TPED-TREN.

#### **SBA 15-TPED-TREN**

Approximately 1 g of SBA-15-TPED was placed in 50 ml of dry toluene and allowed to stir. To this mixture 3 ml of ethyl-2-bromopropanoate was added and the reaction was allowed to stir under reflux at 70 °C for 24 hours. The solid product was then filtered and thoroughly washed with toluene to remove any unreacted species. The product was denoted as SBA 15-TPED-Br.

SBA15-TPED-Br was re dispersed in 50 ml of dry toluene and 4 ml of TREN was added to the reaction mixture. The reaction was carried out under reflux at 70 °C for 24 hours. The solid product was then filtered and thoroughly washed with toluene. The product was denoted as SBA 15-TPED-TREN.

### 3.3 Characterization

#### 3.3.1 XRD

A diffraction experiment involves an incident wave that is directed through a material, and a detector is normally moved around on an axis to record the intensities of the diffracted waves. Depending on the nature of the scattering, constructive or destructive interference happens in different directions as the scattered waves are emitted by atoms occupying different positions. Crystals and molecules have interatomic distances that amount to 0.15–0.4 nm. The interatomic distance amount corresponds to the electromagnetic spectrum which x-ray photons have with an energy of between 3 and 8 keV. It can therefore be envisaged that the incident waves should have wavelengths that are similar to the spacing between the atoms. One of these waves was devised by von Laue and Bragg. The Bragg's wave consists of an oscillating electric field of an incident X-ray which causes the electrons in the atoms to accelerate, and the acceleration produces the outgoing wave.

The Bragg condition states that selective reflections that have an intensity represented by  $I$  that are reflected off planes  $hkl$ , which will give rise to diffractograms when then glancing angles satisfies Braggs equation 3.1.

$$n \lambda = 2d \sin\theta \quad (3.1)$$

Where **n**: Integer number of wavelengths

**$\lambda$** : wavelength

**d**: Distance between reflecting planes

**$\theta$** : Glancing angle

Mesoporous silica display regular hexagonal XRD patterns. The unit-cell parameter denoted as  $a_0$  may be obtained from the d spacing from the Bragg's equation 3.2 [3].

$$a_0 = d \cdot 2/\sqrt{3} \quad (3.2)$$

XRD is the most commonly used x-ray technique for the characterization of a variety of materials. Powdered samples mean that the crystalline domains are non-specifically positioned in the sample. The orientation of these domains give rise to 2-D diffraction patterns which display concentric rings of scattering peaks that relate to various d-spacing's in the material. The positioning of these peaks is used to interpret the structure of the material.

The wall thickness of mesoporous silica materials may also be calculated using the unit cell parameter (3.2) and the pore diameter value that is obtained from N<sub>2</sub> Physisorption experiments, using the equation 3.3;

$$W = a_0 - D_{\text{pore}} \quad (3.3)$$

In addition, one can determine factors such as the orientation of single crystals, or measure the size and shape of crystalline regions [4].

A study of XRD patterns of samples was carried out under an air atmosphere at room temperature on a Bruker A8 advance instrument operating at 40 kV and 40 mA using Cu K $\alpha$  ( $\lambda = 1.5406 \text{ \AA}$ ) radiation. The diffraction data were recorded in the  $2\theta$  range of  $0.5\text{--}8^\circ$  at a scanning rate of  $0.01^\circ \text{ s}^{-1}$  with a sampling time of 1 second per step.

### 3.3.2 SAXS

SAXS is an extremely useful technique for studying the structure of materials. SAXS usually involves studying materials with a size in the order of 1 nm to several hundreds of nm. Small angle scattering also includes light scattering, small angle x-ray and neutron scattering. SAXS is usually recorded at very low angles, typically in the range of  $0.1-10^\circ$  [5-6].

The scattered waves arising from this technique give information concerning the size, shape of the material to some extent which may be due to particles or pores, as well as the ordering of the material [7].

SAXS measures the changes in geometrical arrangements in the scattering density, and this is averaged over the time scale of the measurement [3].

In respect to the materials investigated during this study the SAXS measurement was required for SBA-15 materials. In general mesoporous materials display long range ordering, but in some cases their pore walls are amorphous. During wide angle measurement such materials may be viewed as semicrystalline solids. SAXS therefore affords the opportunity of conducting measurements at lower angles where conventional X-ray diffraction measurements cannot, and porous structures in the nanometer range can be studied more in-depth [8-10, 3].

### 3.3.3 Transmission Electron Microscopy (TEM)

The transmission electron microscope (TEM) operates on the same basic principles as the light microscope but uses electrons instead of light. A TEM forms images by using transmitted electrons as a light source and this makes it more efficient than the conventional light microscope since it facilitates much better resolution. The TEM allows one to see objects to the order of a few angstroms ( $10^{-10}$  m) [11]. As a consequence one is able to extract key information with regards to morphology (size, shape and arrangement of particles which make up the sample), crystallography (arrangement of atoms) and compositional information viz., the elemental make-up of the sample in question. TEM is used to determine the structure of mesoporous silica.



#### Sample preparation

A spatula tip of samples was sonicated for approximately 30 minutes to ensure efficient dispersion. A micro pipette is then used to extract some of the sample from the solution and then placed on holey carbon film or 400 mesh copper grids. The grid was then left to air dry.

#### Instrument setup

HRTEM Technai G2 F20 X-Twin MAT 200kV Field Emission Transmission Electron Microscope

**Gunlens used:** Gunlens 1, **Spot size:** 3, **C2 aperture:** 3, **Objective aperture:** 1

**Accelerating voltage:** 200kV

### 3.3.4 Scanning Electron Microscopy (SEM)

SEM is used to study the morphology of materials. SEM produces images through an electron beam that is focused into an extremely fine probe, which scans across the surface of the materials. A beam of accelerated electrons from the fine probe strikes the materials, which in turn emit secondary and backscattered electrons that are collected by a detector and recorded as a signal. The difference in height between the probe and the sample determines the contrast of the images. SEM requires samples to be conductive. It is for this reason that non-conductive samples are coated with conductive material such as carbon, gold or an alloy of conductive metals. The coating ensures that there is not a build-up of static electric charge as the probe traverses across the sample [12-13, 3].

Scanning Electron Micrographs (SEM) were recorded on a field-emission scanning Electron microscopy (Auriga Zeiss SEM) with accelerating voltage: 5 keV. The samples were coated with gold/palladium alloy using a Quorum Q150TES sputter coater to prevent surface changes and to protect the surface material from thermal damage by the electron beam.

### 3.3.5 Nitrogen (N<sub>2</sub>) physisorption measurements

Nitrogen physisorption is one of the most powerful techniques used to determine textural properties such as specific surface area and porosity of mesoporous materials. The technique makes use of gas solid phase interaction, and uses a variety of complex adsorption isotherm models to determine the aforementioned properties of mesoporous materials. During surface area measurements, nitrogen isotherms are the most commonly used methods, as nitrogen with its low boiling point easily accesses micropores as well as mesopores of porous materials [3].

During  $N_2$  physisorption experiments the accumulated data is normally represented as sorption isotherms where the quantity of gas adsorbed onto the material is plotted versus the relative pressure change. Various materials have different textural properties giving rise to several isotherms.

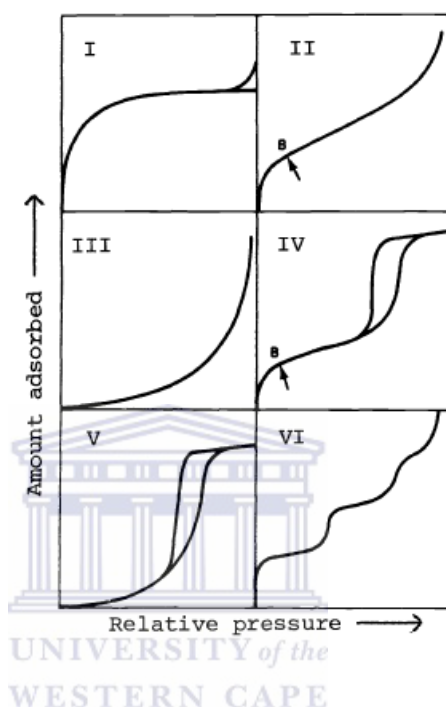


**Figure 5:** Different types of hysteresis loops according to the IUPAC classification [14].

Mesoporous materials give rise to type IV isotherms. This type of isotherm is associated with capillary adsorption that takes place in the mesopores. The initial part of the isotherm is due to monolayer and multilayer adsorption [14].

The most commonly method used to determine the specific surface area of porous materials is by using the Brunauer-Emmett-Teller (BET) method [15]. The BET method stems from the conventional Langmuir theory with multilayer corrections [16].



The BET method is governed by the following assumptions:

- Adsorbent surface is uniform and all adsorption sites are equivalent
- the adsorbed molecules do not interact
- Adsorption mechanism is the same
- When maximum adsorption is reached only a monolayer is formed, i.e. the molecules of the adsorbate do not deposit onto other adsorbed molecules of the adsorbate, only on the free surface of the adsorbent

The resulting BET equation is:

$$\frac{P}{V_a(p-p_0)} = \frac{(C-1)}{V_m C} \frac{p}{p_0} + \frac{1}{V_m C} \quad (3.4)$$

Where:

$p$ : equilibrium pressure of adsorbates at the temperature of adsorption.

$p_0$ : saturation pressure of adsorbates at the temperature of adsorption.

$V_a$ : volume of gas adsorbed at pressure  $p$ .

$V_m$ : volume of gas required to form a monolayer.

$C$ : BET constant related to energy of adsorption of the first layer.

The BET surface area is then evaluated by means of the equation:

$$S_{BET} = \frac{V_m N s}{V_a} \quad (3.5)$$

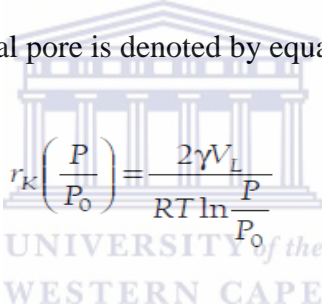
Where;

$N$ , Avogadro's number and

$s$ , the adsorption cross section.

**Pore size determination**

Several methods have been employed to determine the pore sizes of materials. The methods include BJH [17], Broekhoff and de Boer (BdB) [18-21], Kruk–Jaroniec–Sayari (KJS) [22-23] as well as methods (Non Localized Density Functional Theory) NLDFT [24-27]. In the pore size determination of the materials prepared in this work, the Barrett-Joyner Halenda BJH method was employed. The BJH method assumes that all pores are cylindrical, and when applying the simple Kelvin equation [ref], the pores would have a hemispherical meniscus with  $\theta = 0$ . The BJH method also assumes that the correction for multilayers is valid. The equation for the Kelvin radius as a function of relative pressure, when the capillary condensation in cylindrical pore is denoted by equation 3.6



$$r_K \left( \frac{P}{P_0} \right) = \frac{2\gamma V_L}{RT \ln \frac{P}{P_0}} \quad (3.6)$$

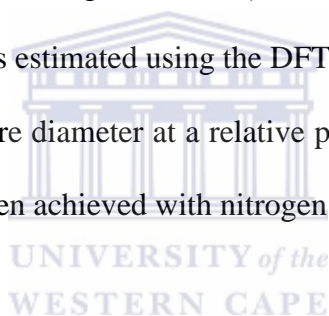
By adding the adsorbed layer thickness,  $t$ , to  $r_K$  the pore width may be obtained through equation

$$r_P = 2 \cdot (r_K + t). \quad (3.7)$$

By using the difference in core volume and volume of a cylinder with the radius  $r_P$  the total length of pores with its radius may be calculated. If all the steps of the complete isotherms are calculated in this manner the total PSD may be obtained.

**Pore volume estimation: Density functional theory (DFT)**

DFT describes the gas adsorption process that takes place at the fluid solid interface. The DFT is employed for analyzing pore size distributions of silica materials. The method allows the total isotherm to be used in determining both the micro as well as the mesoporosity as a continuous distribution of pore volume with regards to the pore size [28]. Nitrogen physisorption measurements were conducted on a Quantachrome Quadrasorb SI instrument. The different MCM-41 materials were degassed at 180 °C for 12 h prior to N<sub>2</sub> adsorption and desorption measurements. The specific surface area was calculated from the BET (Brunauer–Emmett–Teller) model. The pore size distribution was obtained through the BJH (Barrett–Joyner–Halenda) approach, and the total pore volume was estimated using the DFT cumulative pore volume for pores between 2 and 50 nm pore diameter at a relative pressure of 0.99, assuming that full surface saturation had been achieved with nitrogen.

**3.3.6 Thermogravimetric analysis (TGA)**

TGA is a technique which is used to study the thermal decomposition of various materials. In general samples are subjected to a temperature ramp, and mass loss of the material occurs due to changes in temperature. TGA, in conjunction with differential thermal analysis (DTA), allows for the simultaneous weight loss of material with respect to temperature changes as well as detecting enthalpic changes.

Thermogravimetric analysis (TGA) was performed on SDT 2960 Simultaneous SDT-TGA (TA Instruments) with a thermal ramp of 10 °C/min up to 900 °C. Initially the sample was heated from room temperature to 150 °C with a thermal ramp of

10 °C/min. The sample was then subjected to isothermal treatment at 150 °C for 30 minutes, thereafter heating up to 900 °C with a thermal ramp of 10 °C/min.

### 3.3.7 Fourier transform infrared (FTIR)

IR spectroscopy is a technique based on the vibration of the atoms of a molecule. IR spectrum is obtained by passing radiation through a sample and determining what fraction of the incident radiation is absorbed at a particular energy. The energy at which any peak in an absorption spectrum appears corresponds to the frequency of a vibration of a part of a sample molecule [29].

When an infrared light interacts with matter the chemical bonds will stretch, contract and bend. This implies that functional groups tend to adsorb infrared radiation in a specific wavenumber range regardless of the structure of the rest of the molecule. The correlation of the band wavenumber position with the chemical structure is then used to identify a functional group in a sample.

Fourier transform infrared (FTIR) was performed on a Jasco FT/IR-4100 spectrometer with a resolution of 4 cm<sup>-1</sup>.

### 3.3.8 Elemental analysis

Elemental analysis (EA) is a technique used to determine the elemental composition of materials. In the present study EA was used to determine the nitrogen content of the functionalized mesoporous silica materials.

### 3.3.9 Nuclear magnetic resonance (NMR)

NMR is viewed as one of the most important tools to study the structure as well as the dynamics of a variety of compounds. Essentially NMR may be defined as studying the properties of molecules that contain magnetic nuclei through applying a magnetic field to these nuclei and observing frequency of the resonant magnetic field [30, 3].

If nuclei have a spin quantum number of  $I > 0$ , it would have a constant magnitude of  $2I + 1$  variations with respect to its rotation on an axis. Nuclei have their own spin angular moment, and when an external magnetic field is applied to these nuclei it causes these nuclei to momentarily align themselves with the external magnetic field. Depending on the frequency of the radio frequency (rf) that may be applied, the orientation of the spin vectors of these nuclei may be changed, only when in a resonance state. The rf at which the resonance occurs is called the Larmor frequency, which is strongly dependent on the applied field strength, the type of nuclei and minimal contribution as a result of local interactions.

This gives rise to what is known as a chemical shift. Chemical shift interaction may be viewed as an anisotropic interaction. The term comes about due to the fact that the electron arrangement of electrons in the molecule is said to be ellipsoid. Chemical shift arises from the effect of the degree to which extent the electron density affects the resonance frequency of nuclei, and this would be dependent on the orientation of the electron cloud in respect to the applied magnetic field.

**Solid state NMR**

Solid state NMR (SSNMR) in a sense is different to conventional NMR of various molecules that are dissolved in liquids, whereas SSNMR uses the solid material directly for analysis. In SSNMR the signals that are generated are affected by isotropic as well as anisotropic interaction. This inevitably gives rise to complications when generating signals for interpretation. Solution NMR spectra usually display extremely sharp transitions that are generated due to anisotropic NMR interactions by rapid random tumbling. On the other hand SSNMR generates broad peaks caused by both types of NMR interactions as mentioned above, i.e. both isotropic and anisotropic interactions [3].

Broad peaks generated from SSNMR may be resolved by manipulating the spin interactions. By simply rotating the sample about an angle toward the magnetic field, a better resolution is obtained. The technique used to reduce the line width when performing high resolution SSNMR is the magic angle spinning method. This is achieved through spinning the sample at a high speed and at an angle of  $54.74^\circ$ . Spinning of the sample is done at high speed at the magic angle and relative to the applied magnetic field. The magic angle is related to the Legendre polynomial  $x = \arccos(1/\sqrt{3})$ . If the spinning frequency is increased at the magic angle, dipole dipole interactions as well as chemical shift anisotropy is averaged to zero, which results in higher resolution of peaks. The magic angle technique, in combination with other techniques such as multiple pulse sequences and cross polarization, may also be used to reduce peak broadening of SSNMR spectra [30].

### 3.3.10 Temperature Programmed Desorption (TPD)

TPD technique was first introduced by Amenomiya and Cvetanovic in 1963 [31]. In general there are two methods used by temperature desorption technique. The first being where the temperature is increased very quickly, and- this method is known as flash desorption. The second method is where the temperature is raised slowly, and- this method is known as TPD.

TPD is a technique that is used to determine kinetic and thermodynamic parameters of desorption processes or decomposition reactions. TPD uses thermal energy to desorb molecules that were previously adsorbed to the surface of the adsorbate through pre-treatment. The adsorbed molecules then desorb from the surface when sufficient energy is applied and is usually detected using a thermal conductivity detector (TCD) or by mass spectrometry. TPD experiments primarily involves heating a sample with a temperature programmer  $\beta(t) = dT/dt$ .

TPD is a useful technique used to determine acidic or basic sites of catalysts. TPD is also used to determine to which extent the interaction of the adsorbed molecules interacts with the adsorbate, whether it is physically or chemically adsorbed, which would be dependent on the energy required to desorb the adsorbed species [32-34]. In this study CO<sub>2</sub>-TPD was used to determine to which extent the prepared mesoporous adsorbents adsorbed CO<sub>2</sub> molecules, and to determine whether these contributions were as a result of physisorbed or chemisorbed CO<sub>2</sub>.

Temperature Programmed Desorption (TPD) studies were performed on a Thermo Electron TPD/R/O 1100. Sample cell was loaded with 130 mg of sorbent and heated in flowing helium to 160 °C for 2 hours. The cell was then cooled to 25 and a CO<sub>2</sub> flow rate of 30 ml/min was then introduced into the sample cell for 40 min. The

weakly adsorbed CO<sub>2</sub> was removed by flowing helium with a rate of 30 ml/min at 25 °C for 1 h. The TPD experiment was then carried out by flowing helium at a rate of 30 ml/min from 25 to 160 °C with a ramp of 3 °C/min.





**References**

1. Zeleňák, V., Badaničová, M., Halamová, D., Čejka, J., Zukal, A., Murafa, N. & Goerigk, G. 2008, "Amine-modified ordered mesoporous silica: Effect of pore size on carbon dioxide capture", *Chemical Engineering Journal*, vol. 144, no. 2, pp. 336-342.
2. Zhao, D., Feng, J., Huo, Q., Melosh, N., Fredrickson, G.H., Chmelka, B.F. & Stucky, G.D. 1998, "Triblock copolymer syntheses of mesoporous silica with periodic 50 to 300 angstrom pores", *Science*, vol. 279, no. 5350, pp. 548-552.
3. Kailasam, K. 2008, "Synthesis and Characterization of Mesoporous Silica and Metal Oxide Based Stationary Phase Materials, PhD thesis, University of Stuttgart.
4. Introduction to X-ray Diffraction (XRD) Learning Activity Basic Theory. [Online]. Available: [http://www.asdlib.org/onlineArticles/ecourseware/Bullen\\_XRD/LearningActivity\\_Diffraction\\_BraggsLaw.pdf](http://www.asdlib.org/onlineArticles/ecourseware/Bullen_XRD/LearningActivity_Diffraction_BraggsLaw.pdf)
5. Lindner, P., Zemb Th. 2002. *Neutrons, X-rays and Light: Scattering Methods Applied to Soft Condensed Matter*, North-Holland, Elsevier.
6. Small-angle scattering and data analysis. [Online]. Available: [www.soft-matter.uni-tuebingen.de/teaching/SASTutorial.pdf](http://www.soft-matter.uni-tuebingen.de/teaching/SASTutorial.pdf).
7. Small-angle scattering (SAXS), Synchrotron Radiation Course. [Online]. Available: [www.ifm.liu.se/edu/coursescms/SYNCRAD/project-reports-2008/saxs.pdf](http://www.ifm.liu.se/edu/coursescms/SYNCRAD/project-reports-2008/saxs.pdf).
8. Kailasam, K. & Müller, K. 2008, "Physico-chemical characterization of MCM-41 silica spheres made by the pseudomorphic route and grafted with octadecyl chains", *Journal of Chromatography A*, vol. 1191, no. 1-2, pp. 125-135.
9. Selvam, P., Bhatia, S.K. & Sonwane, C.G. 2001, "Recent advances in processing and characterization of periodic mesoporous MCM-41 silicate molecular sieves", *Industrial and Engineering Chemistry Research*, vol. 40, no. 15, pp. 3237-3261.
10. Lin, H. & Mou, C. 1999, "Studies on Mesoporous Self-Organizing Aluminosilica", *Journal of Cluster Science*, vol. 10, no. 2, pp. 271-293.
11. Transmission electron microscope. [Online]. Available: [nobelprize.org/educational/physics/microscopes/tem/index.html](http://nobelprize.org/educational/physics/microscopes/tem/index.html).

12. Johansson, E. M. (2010). Controlling the Pore Size and Morphology of Mesoporous Silica. PhD thesis. Linköping University.
13. Brief introduction to scanning electron microscopy (SEM). [Online]. Available: <http://micron.ucr.edupublicmanualsSem-intro.pdf>.
14. Sing, K.S.W. 1984, "Reporting physisorption data for gas/solid systems" pp. 567.
15. Grosso, D., Cagnol, F., Soler-Illia, G.J.D.A.A., Crepaldi, E.L., Amenitsch, H., Brunet-Bruneau, A., Bourgeois, A. & Sanchez, C. 2004, "Fundamentals of mesostructuring through evaporation-induced self-assembly", *Advanced Functional Materials*, vol. 14, no. 4, pp. 309-322.
16. Langmuir, I. 1916, "The constitution and fundamental properties of solids and liquids. Part I. Solids", *The Journal of the American Chemical Society*, vol. 38, no. 2, pp. 2221-2295.
17. Broekhoff, J.C.P. & de Boer, J.H. 1967, "Studies on pore systems in catalysts. IX. Calculation of pore distributions from the adsorption branch of nitrogen sorption isotherms in the case of open cylindrical pores A. Fundamental equations", *Journal of Catalysis*, vol. 9, no. 1, pp. 8-14.
18. Broekhoff, J.C.P. & de Boer, J.H. 1967, "Studies on pore systems in catalysts. IX. Calculation of pore distributions from the adsorption branch of nitrogen sorption isotherms in the case of open cylindrical pores B. Fundamental equations", *Journal of Catalysis*, vol. 9, no. 1, pp. 15-27.
19. Broekhoff, J.C.P. & De Boer, J.H. 1968, "Studies on pore systems in catalysts. XI. Pore distribution calculations from the adsorption branch of a nitrogen adsorption isotherm in the case of "ink-bottle" type pores", *Journal of Catalysis*, vol. 10, no. 2, pp. 153-165.
20. Lukens Jr., W.W., Schmidt-Winkel, P., Zhao, D., Feng, J. & Stucky, G.D. 1999, "Evaluating pore sizes in mesoporous materials: a simplified standard adsorption method and a simplified Broekhoff-de Boer method", *Langmuir*, vol. 15, no. 16, pp. 5403-5409.
21. Kruk, M., Jaroniec, M. & Sayari, A. 1997, "Application of large pore MCM-41 molecular sieves to improve pore size analysis using nitrogen adsorption measurements", *Langmuir*, vol. 13, no. 23, pp. 6267-6273.

22. Jaroniec, M. & Solovyov, L.A. 2006, "Improvement of the Kruk-Jaroniec-Sayari method for pore size analysis of ordered silicas with cylindrical mesopores", *Langmuir*, vol. 22, no. 16, pp. 6757-6760.
23. Neimark, A.V. 2002, "Colloids and Surfaces A: Physicochemical and Engineering Aspects: Foreword", vol. 206, no. 1-3, pp. 1-2.
24. Neimark, A.V. & Ravikovitch, P.I. 2001, "Capillary condensation in MMS and pore structure characterization", *Microporous and Mesoporous Materials*, vol. 44-45, pp. 697-707.
25. Ravikovitch, P.I. & Neimark, A.V. 2002, "Density functional theory of adsorption in spherical cavities and pore size characterization of templated nanoporous silicas with cubic and three-dimensional hexagonal structures", *Langmuir*, vol. 18, no. 5, pp. 1550-1560.
26. Ogbuka, C.P. 2012, Development of solid adsorbent materials for CO<sub>2</sub> capture. MSc thesis. The University of Nottingham.
27. Ritter, H.T.K. 2009, Synthesis and Analysis of Amino-Functionalised Mesoporous Silica. PhD thesis. University of Zurich.
28. Ravikovitch, P.I., Domhnaill, S.C.Ó., Neimark, A.V., Schüth, F. & Unger, K.K. 1995, "Capillary hysteresis in nanopores: Theoretical and experimental studies of nitrogen adsorption on MCM-41", *Langmuir*, vol. 11, no. 12, pp. 4765-4772.
29. George, S., and McIntyre. 1996, *Modern Infrared spectroscopy*. 2nd Edition.
30. Aziz. B. 2012, Synthesis and modification of potential CO<sub>2</sub> adsorbents. PhD thesis. Stockholm University.
31. Amenomiya, Y. & Cvetanovic, R.J. 1963, "Application of flash-desorption method to catalyst studies. I. Ethylene-alumina system", *Journal of Physical Chemistry*, vol. 67, no. 1, pp. 144-147.
32. Kleitz, F. 2002, Ordered mesoporous materials, template removal, framework and morphology. PhD Thesis. The University of Bochum.
33. Temperature Programmed Desorption measurement. Measurement of energy of desorption and adsorption heat. 6 June 2003, Kazuyuki Nakai, Kaori Nakamura. [Online]. Available: [www.tdno.ru/files/file/CAT-APP-001%28E%29.pdf](http://www.tdno.ru/files/file/CAT-APP-001%28E%29.pdf).

34. Sven L.M. Schroeder, Gottfried. M. 2002. Temperature-Programmed Desorption (TPD) Thermal Desorption Spectroscopy (TDS). [Online]. Available: [www.academia.edu/262423/Temperature-Programmed\\_Desorption\\_TPD\\_Thermal\\_Desorption\\_Spectroscopy\\_TD](http://www.academia.edu/262423/Temperature-Programmed_Desorption_TPD_Thermal_Desorption_Spectroscopy_TD)



## CHAPTER 4

This chapter focuses on the characterization of mesoporous silica which were used in this study. All the supports were characterized by several techniques, and the data evaluation of these supports serves as a base for further modification with various amine groups to capture CO<sub>2</sub>.

### 4.1 Systematic study of MCM-41

Initially MCM-41 supports were synthesized using a low surfactant concentration method. The ease of the preparation of MCM-41 allowed for a systematic study of structural properties. The systematic study involved expanding the pore size of the MCM-41 materials using surfactants with different alkyl chain lengths.

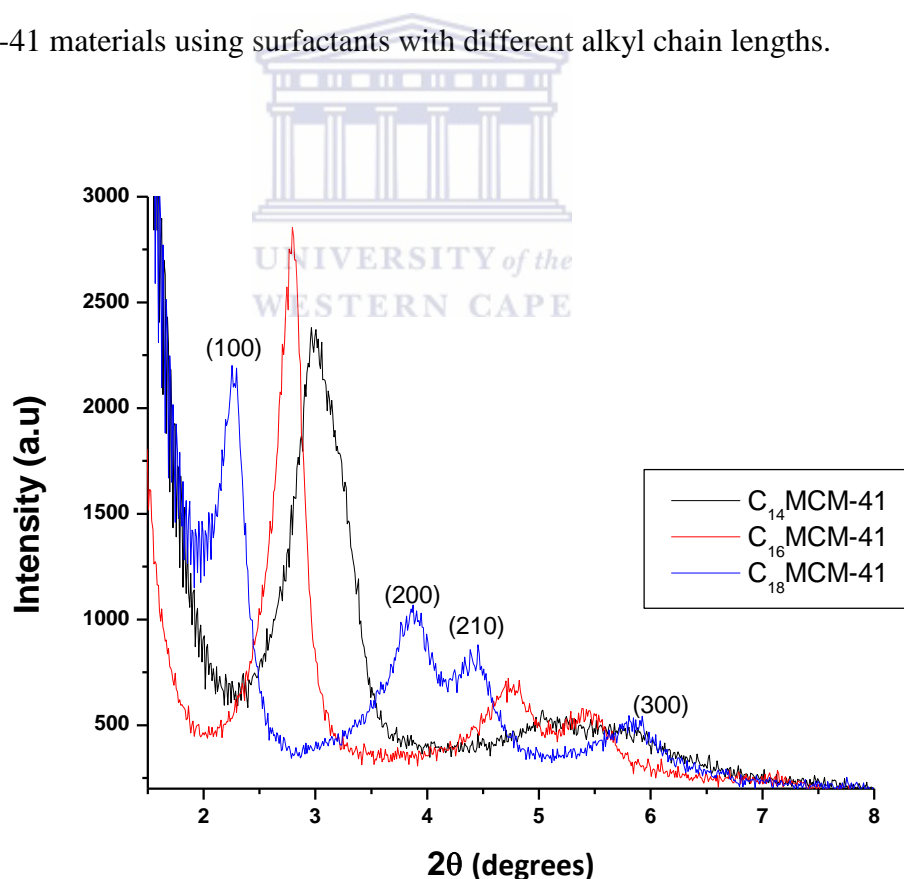


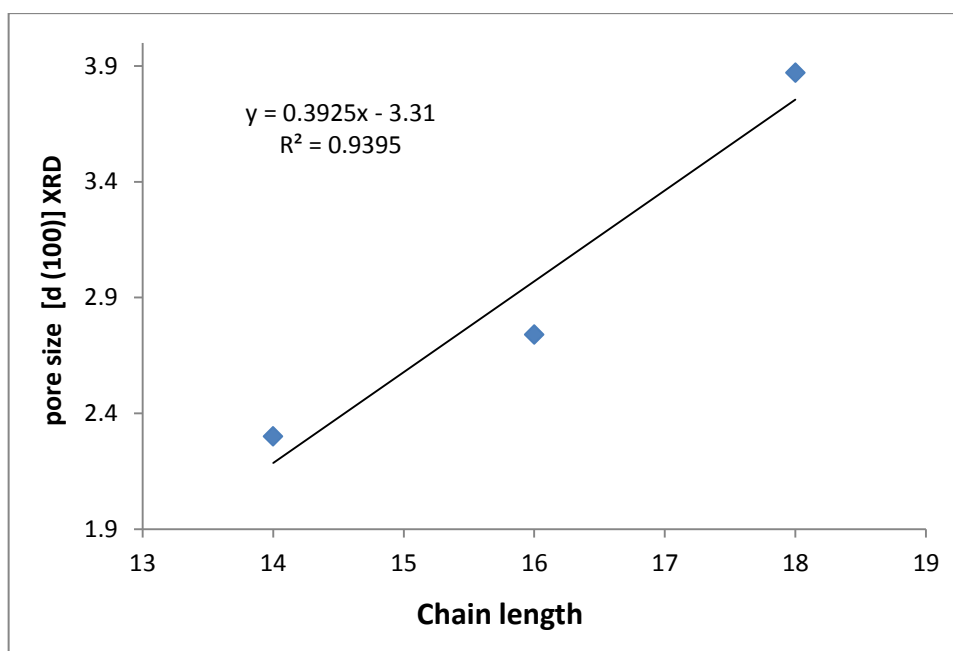
**Figure 6:** Powder XRD patterns of calcined MCM-41 synthesized with different alkyl chain lengths.

**Table 5:** Miller indices hkl,  $2\theta_{hkl}$ ,  $d_{hkl}$  values and calculated unit cell parameters ( $a_0$ ) of the first peak in the diffraction patterns of the calcined MCM 41 phases.

Sample	$2\theta_{hkl}$ (°)	$d_{hkl}$ <sup>a</sup> (nm)	$a_0$ <sup>b</sup> (nm)
C <sub>14</sub> MCM-41	3.1	3.0	3.5
C <sub>16</sub> MCM-41	2.7	3.2	3.7
C <sub>18</sub> MCM-41	2.3	3.8	4.4

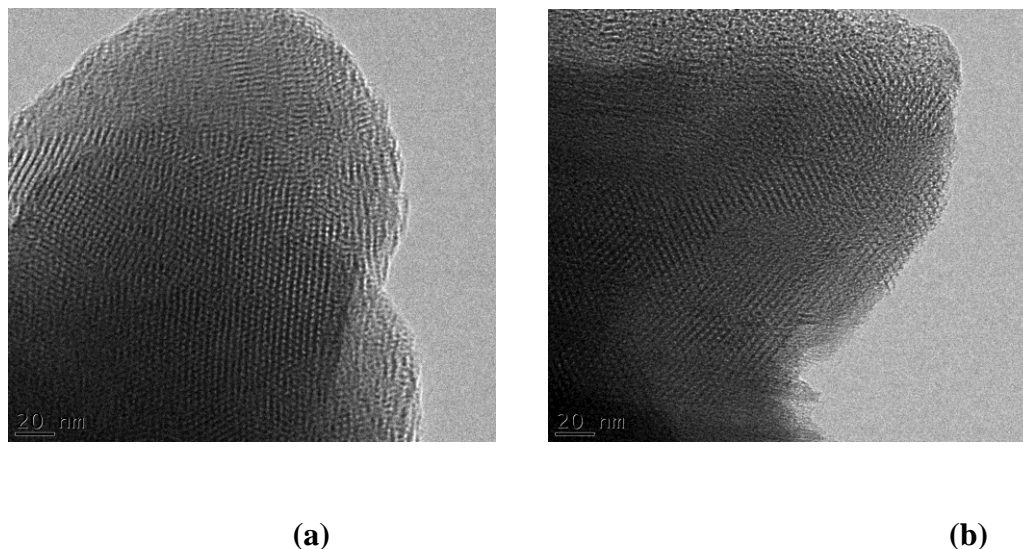
$$^a d(100) = n\lambda = 2d \sin\theta, \quad ^b a_0 = 2 \times d(100)/\sqrt{3}.$$

Figure 6 shows the powder XRD patterns of calcined MCM-41 materials synthesized with different surfactant alkyl chain lengths. MCM-41 materials synthesized with C<sub>14</sub>TABr, C<sub>16</sub>TABr and C<sub>18</sub>TABr exhibited XRD patterns displaying well-ordered mesoporous phases that can be indexed to a hexagonal lattice [1, 2]. The long-range ordering of the prepared MCM-41 materials are evident due to the observed peaks at  $2\theta$  values greater than 3. Table 5 shows the Miller indices hkl,  $2\theta_{hkl}$ ,  $d_{hkl}$  values and calculated unit cell parameters ( $a_0$ ) of the first peak in the diffraction patterns of the calcined MCM-41 phases. Increasing the surfactant chain length from C<sub>14</sub> to C<sub>18</sub> resulted in a shift in  $2\theta$  values to lower angles. The shift in  $2\theta$  values led to an increase in  $d$  spacing, which was consistent with the Bragg's equation. The increase in  $d$  spacing was accompanied with an increase in the unit cell parameter  $a_0$ , and this was found to be consistent with previously reported literature, i.e. the effect that surfactant template alkyl chain lengths have on the pore diameter and lattice parameter of the M41S mesoporous materials [3-4]. It is therefore clear that the pore size of the MCM-41 materials was controlled by changing the surfactant alkyl chain lengths.



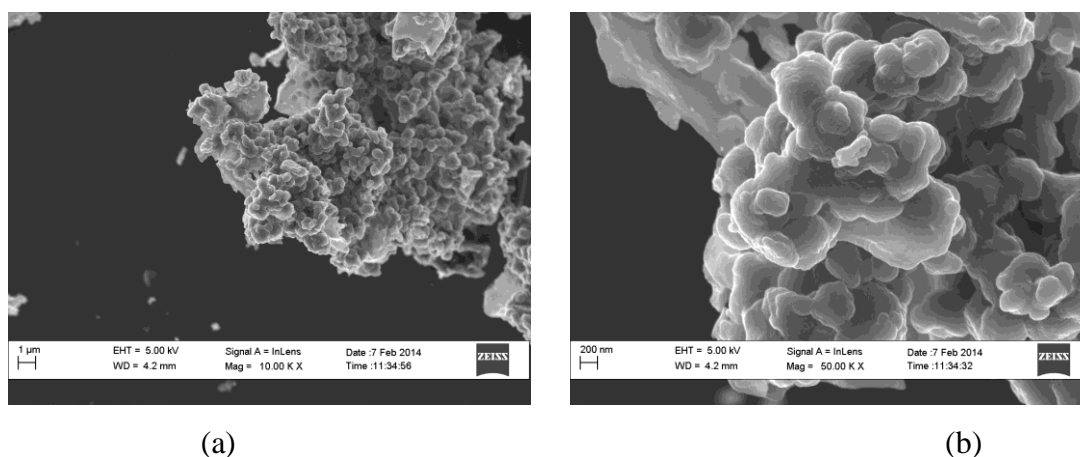
**Figure 7:** Effect of surfactant chain length on pore size.

Figure 7 displays the relationship between the carbon chain length of the surfactants  $C_{14}$ TABr,  $C_{16}$ TABr and  $C_{18}$ TABr and the approximated pore sizes using XRD. It shows a linear increase in pore size when increasing alkyl chain lengths of the surfactant. Figure 7 shows a linear fit across all the data points, with a slope of 0.39 nm. The increase in pore size was in good agreement with the geometrical aspects, as an increase in pore diameter of roughly 0.5 nm is expected. MCM-41 materials prepared using different surfactant alkyl chain lengths results in an average increase of 0.25 nm in the distance between the pore centers ( $a_0$ ). In the case of  $C_{14}$ -MCM-41 and  $C_{16}$ -MCM-41 (Table 5) an increase of 0.2 nm was achieved with the introduction of the  $-(CH_2)_2-$  group, and this is in good agreement with what was previously reported [4, 5].



**Figure 8:** TEM images of synthesized  $C_{18}MCM-41$ .

Figure 8 shows the TEM image of calcined  $C_{18}MCM-41$  which display pores that are unidirectional and arranged in a honeycomb like structure [6]. The TEM image of  $C_{18}MCM-41$  is in good agreement with the XRD patterns obtained, as the XRD patterns displayed well-ordered mesoporous phases that can be indexed to a hexagonal lattice. TEM in conjunction with XRD confirm the structure of  $C_{18}MCM-41$ .



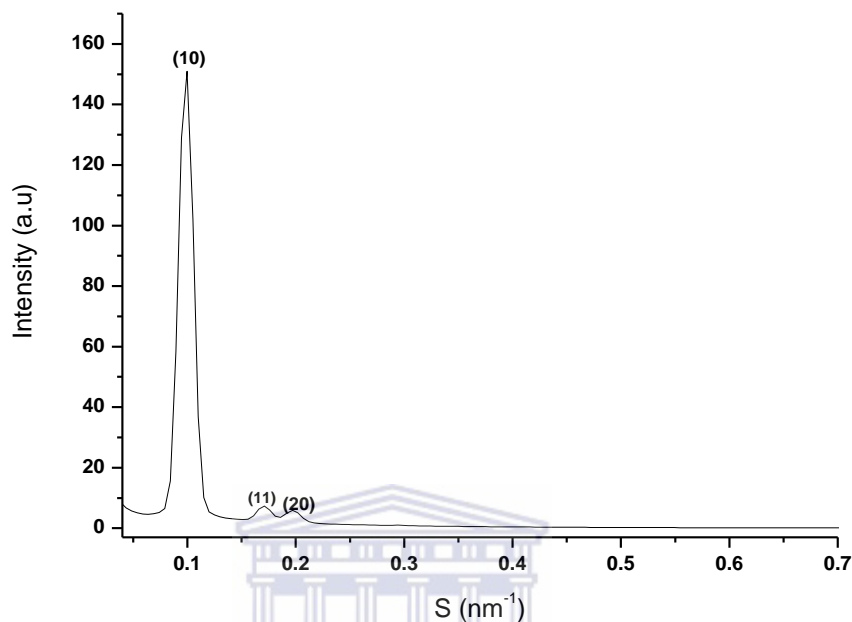
**Figure 9:** SEM images of  $C_{18}MCM-41$ .

Figure 9 shows the SEM images of  $C_{18}MCM-41$ .  $C_{18}MCM-41$  has clustered spheroidal particles morphology. The spheroidal particles are agglomerated which



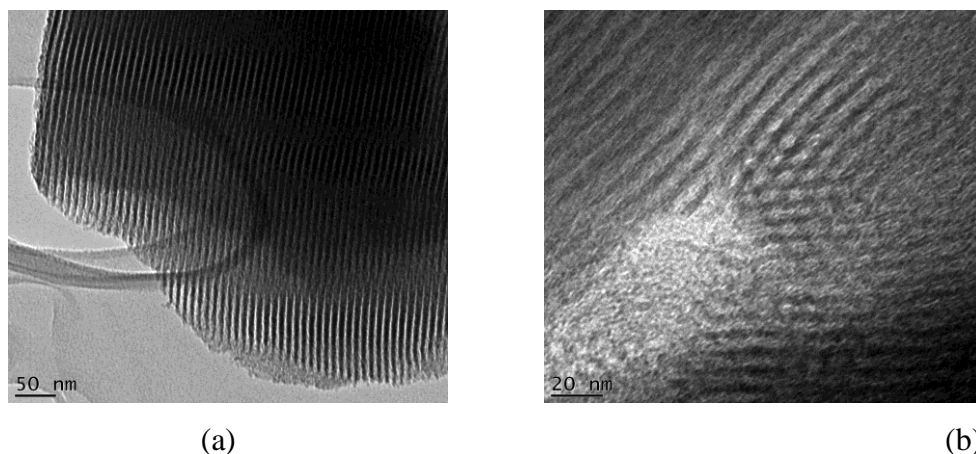
makes it difficult to determine the average size of the particles. Particle sizes ranged from 50-200 nm in diameter.

#### 4.2 SBA-15



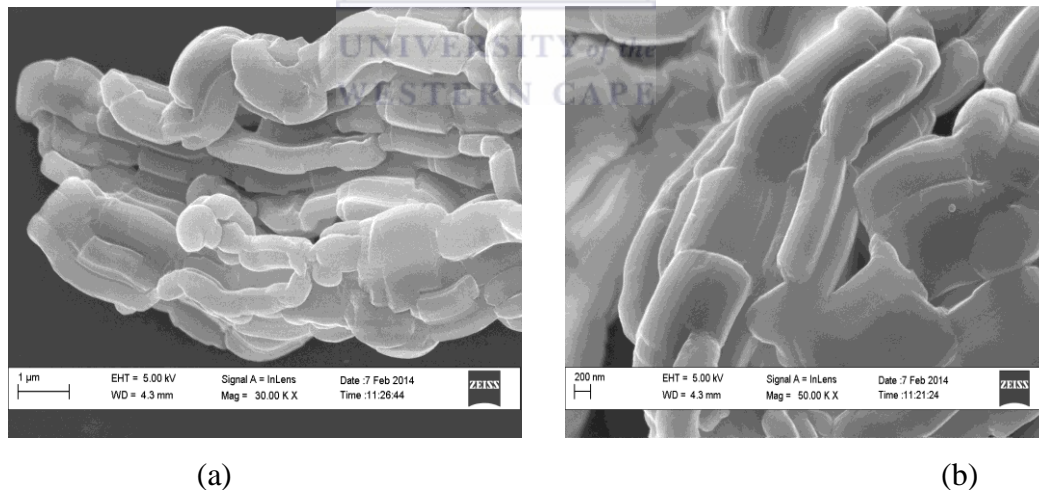
**Figure 10:** SAXS of calcined SBA-15.

Figure 10 shows the SAXS of calcined SBA-15 displaying three well resolved peaks that are indexed at (100), (110) and (200) reflections which are associated with P6mm hexagonal symmetry [7]. SBA-15 displayed a strong diffraction peak at  $q = 0.13 \text{ nm}^{-1}$ . The d spacing obtained from the reflective plane at (10), (11) and (20) were 10.1, 5.9 and 5.1 nm respectively. The unit cell parameter of calcined SBA-15 was calculated from the main (10) peak and was calculated to be 11.66 nm. The SAXS pattern confirmed that SBA-15 was prepared with a hexagonal structure.



**Figure 11:** TEM images of SBA-15.

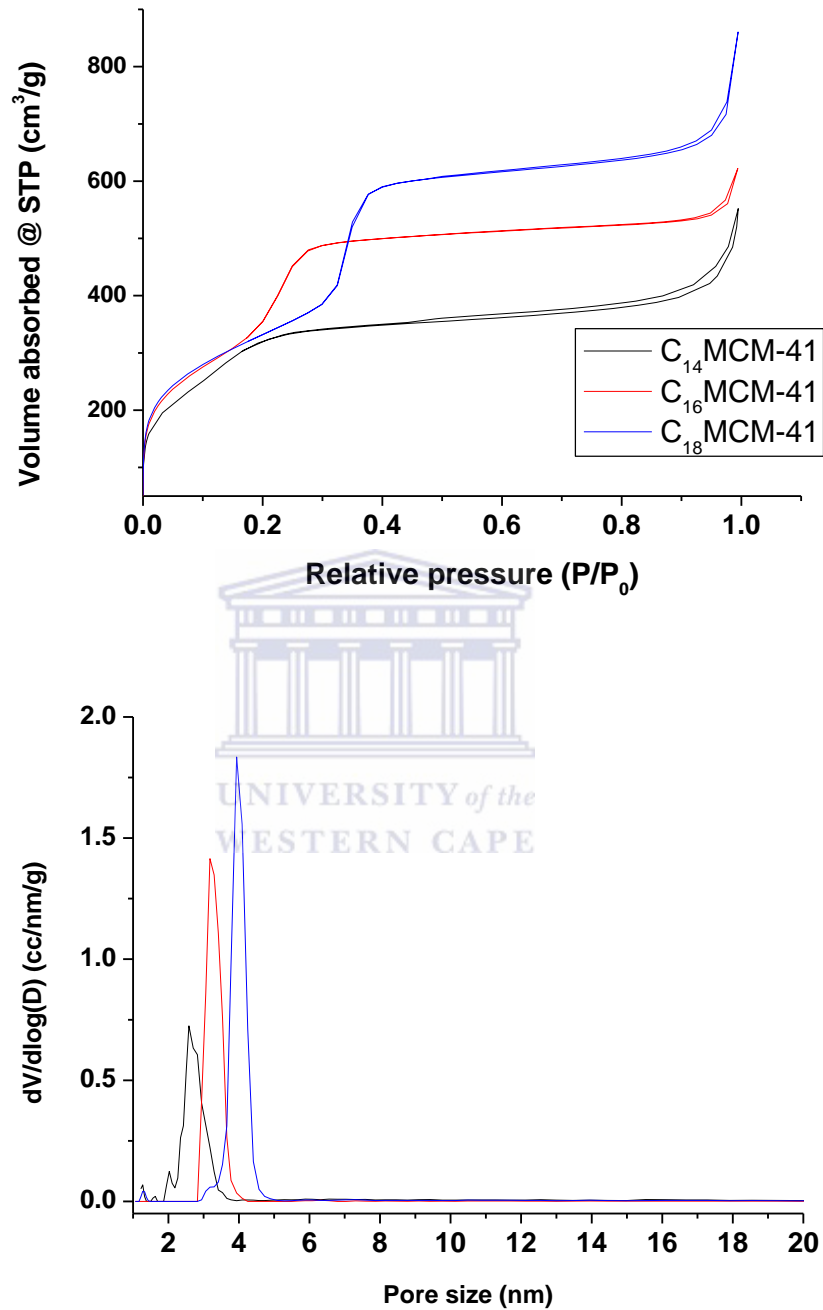
Figure 11 shows the TEM images of calcined SBA-15 which has well-ordered hexagonal arrays of mesopore channels and confirms that SBA-15 displays a 2D  $p6mm$  hexagonal structure [8]. TEM images obtained for SBA-15 was in good agreement with the SAXS measurement confirming the hexagonal symmetry, proving that SBA-15 was synthesized successfully [9].



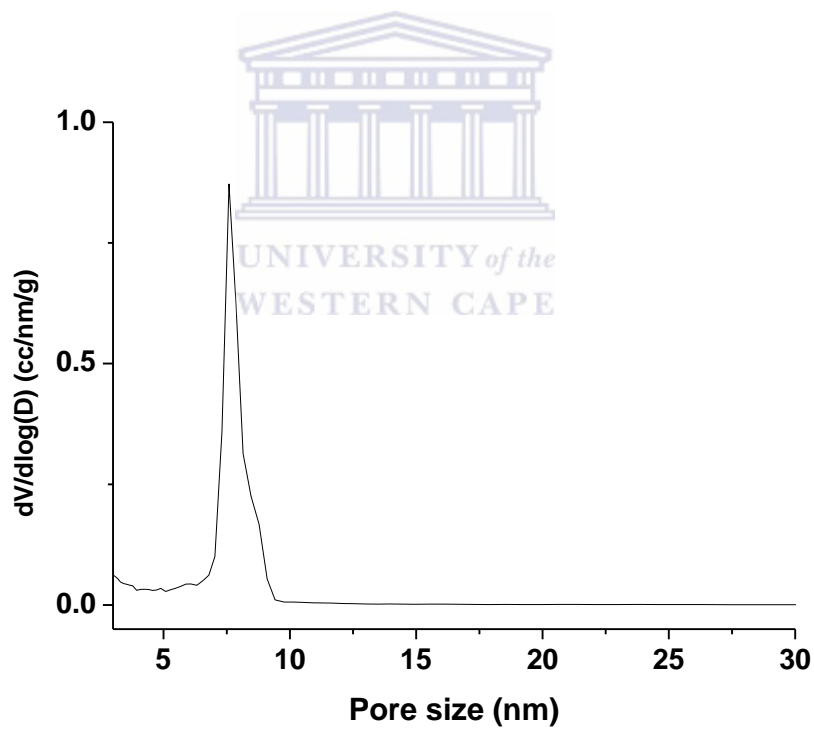
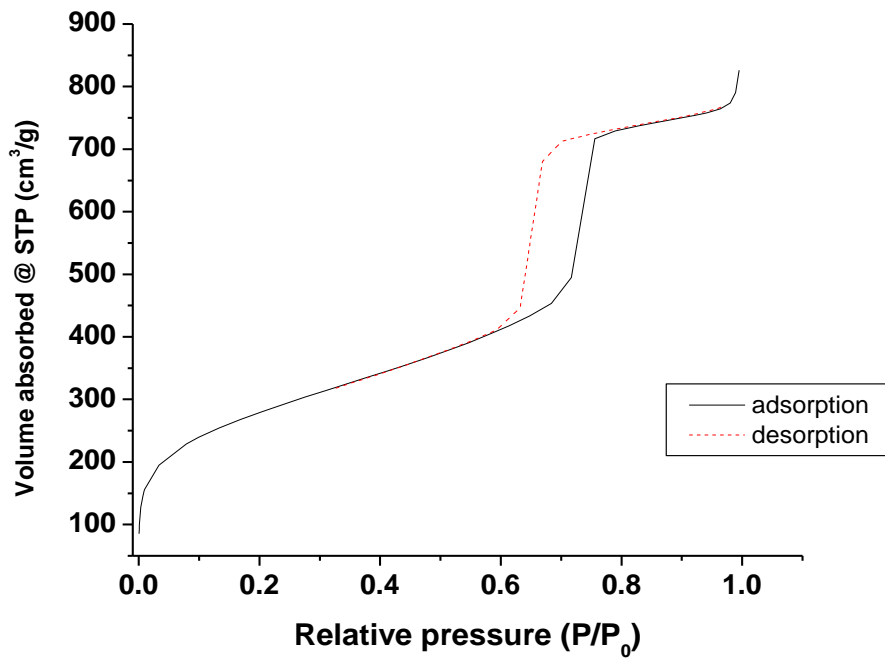
**Figure 12:** SEM images of calcined SBA-15.

Figure 12 shows the SEM images of SBA-15. SBA-15 displayed rod like structures with sizes ranging from 100-500 nm in diameter. The rod-like structures are aggregated together. Even after calcination of the rod-like

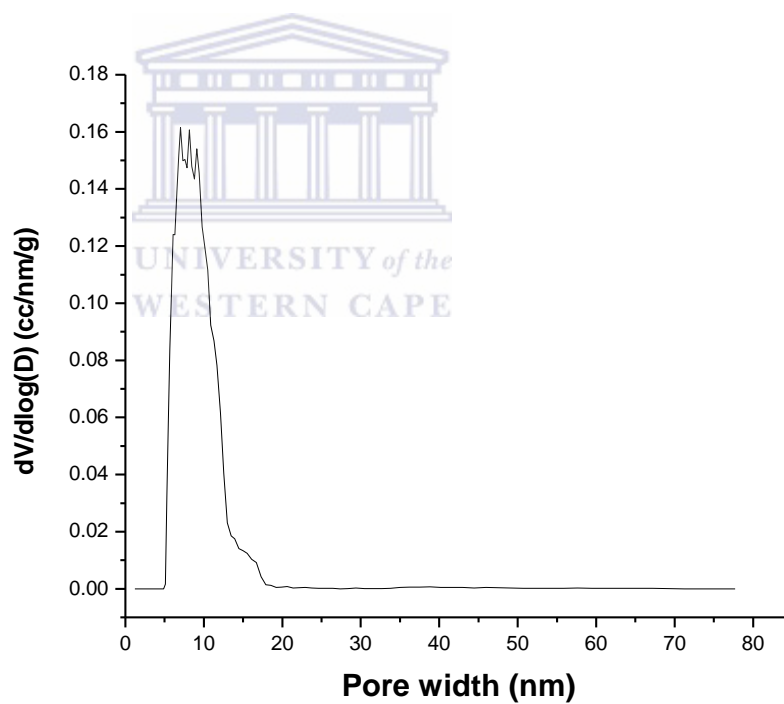
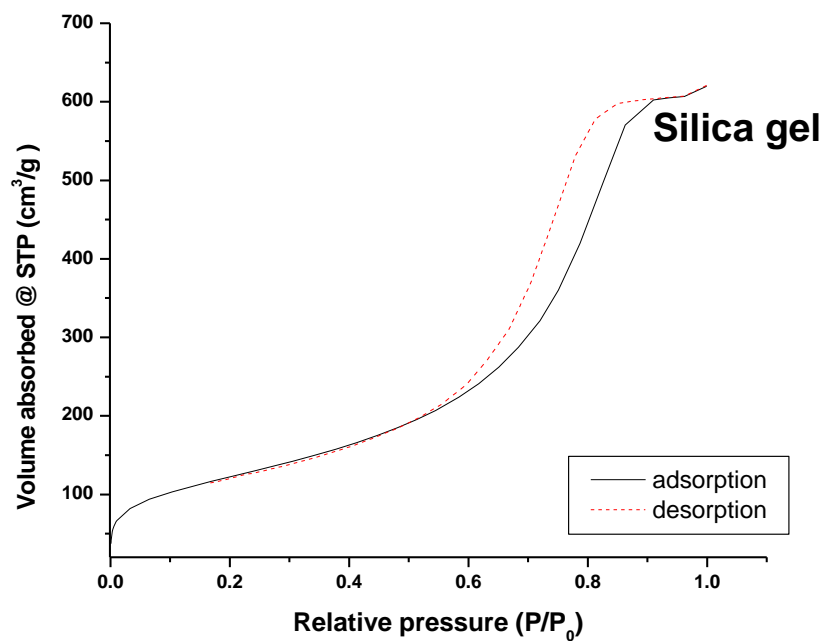
morphology displayed in figure 9 was retained, this indicated that the macroscopic structure of the prepared SBA-15 is thermally stable [8].



(a)



(b)



(c)

**Figure 13:** N<sub>2</sub> isotherms plots and pore size distributions calculated by DFT of (a) MCM 41 materials synthesized using C<sub>14</sub>TABr, C<sub>16</sub>TABr and C<sub>18</sub>TABr surfactants, (b) SBA-15 and (c) silica gel.

**Table 6:** Textural properties of MCM-41 materials synthesized using different alkyl chain lengths surfactants, SBA-15 and amorphous silica gel.

Sample	Surface area (m <sup>2</sup> /g)	Pore volume (cc/g)	Pore size (nm)	d spacing <sup>a</sup> (nm)	a <sub>0</sub> <sup>b</sup> (nm)	Wall thickness <sup>c</sup> W (nm)
C <sub>14</sub> MCM 41	1302	0.8	2.6	2.84	3.30	0.70
C <sub>16</sub> MCM 41	1186	0.9	3.2	3.23	3.74	0.54
C <sub>18</sub> MCM 41	1211	1.3	4.4	4.20	4.87	0.47
SBA-15	1024	1.3	7.6	10	11.5	3.9
Amorphous silica gel	446	0.9	8.6	-	-	-

MCM-41: <sup>a</sup> d spacing (d(100)) =  $n \lambda = 2d \sin$  <sup>b</sup> a<sub>0</sub> = 2 X d(100)/√3, <sup>c</sup> W = a<sub>0</sub> – Pore size

SBA-15: <sup>a</sup> d spacing (d(100)) = 1/S, <sup>b</sup> a<sub>0</sub> = 2 X d(100)/√3, <sup>c</sup> W = a<sub>0</sub> – Pore size

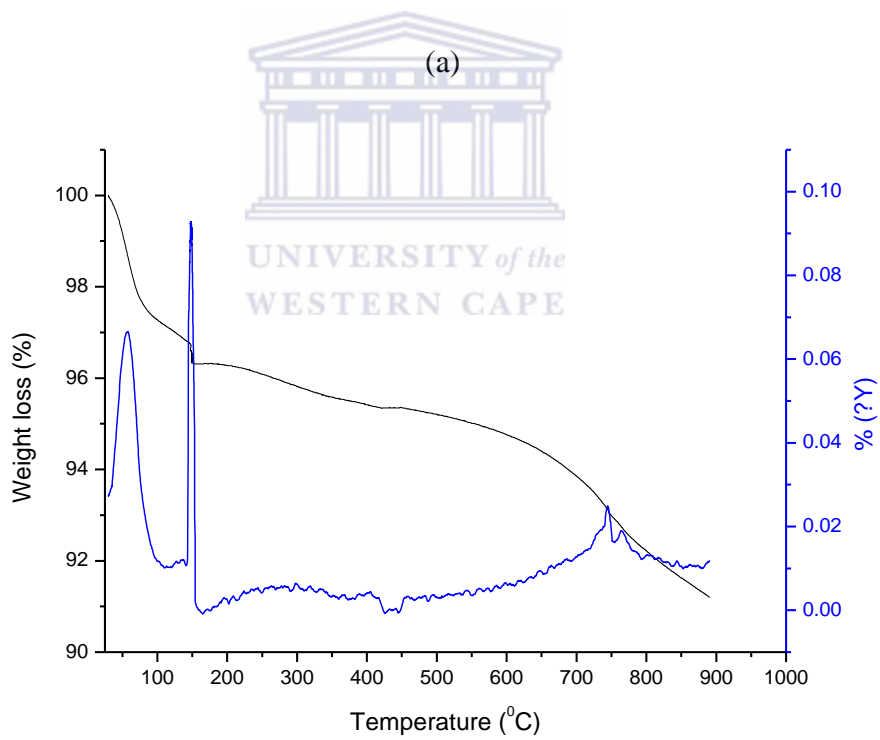
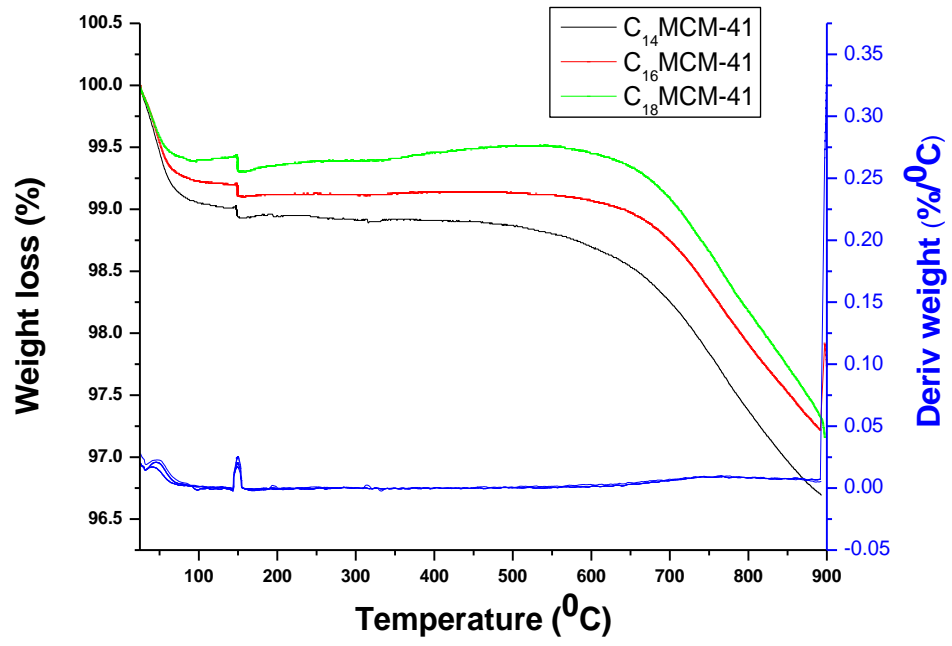
Figure 13 shows the N<sub>2</sub> isotherms and pore size distributions calculated by DFT of (a) MCM 41 silica prepared using different surfactants, (b) SBA-15 and (c) amorphous silica gel from Davisal. MCM-41 materials displayed type IV isotherm in the IUPAC classification. MCM-41 silica prepared displayed microporosity at low pressures (Figure 13a). C<sub>16</sub>MCM-41 and C<sub>18</sub>MCM-41 both displayed well resolved knees in the relative pressure ranges of  $P/P_0$  (0.17-0.3) and  $P/P_0$  (0.2-0.4) respectively, which is attributed to the capillary condensation of nitrogen in the mesopores. C<sub>14</sub>MCM-41, C<sub>16</sub>MCM-41 and C<sub>18</sub>MCM-41 displayed multilayer adsorption on the outer surface in the pressure range 0.5-1 (Figure 13a) [10]. SBA-15 (Figure 13b) exhibited a typical type IV isotherm with H1 hysteresis loops according to the IUPAC classification [11]. The steep increase observed in the relative pressure range of 0.6-0.8 may be attributed to the capillary condensation of N<sub>2</sub> into the mesopores of SBA-15. SBA-15 shows a hysteresis loop with parallel and almost vertical branches, which is characteristic

of materials with a well-defined cylindrical like shape. The sharpness of the adsorption branch is indicative of the narrow pore size distribution of mesopores that is evident in the pore size distribution plot (Figure 13b) [12-14]. Amorphous silica gel (Figure 13c) displayed a type IV  $N_2$  isotherm according to the IUPAC classification and had a hysteresis loop that was indicative of mesopores. The volume of  $N_2$  absorbed steadily increased at relative pressure ( $P/P_0$ ) indicating capillary condensation of  $N_2$  within the mesopores. The adsorption/desorption branches are almost parallel, indicating the uniformity of pores of silica gel [15]

The BET method was used to determine the surface area of the mesoporous silica. The pore size distribution (PSD) was calculated using the adsorption branch of the isotherm according to the DFT kernel method for cylindrical silica pores.

The high BET surface area (Table 6) observed for  $C_{14}$ MCM-41 may be due to the capillary condensation at low  $P/P_0$  [16].  $C_{16}$ MCM-41 and  $C_{18}$ MCM-41 also displayed comparably high BET surface areas. Figure 10a shows the PSD of  $C_{14}$ MCM-41,  $C_{16}$ MCM-41 and  $C_{18}$ MCM-41. MCM-41 materials displayed narrow pore size distribution which indicates the homogeneity of the pores. An increase in pore size as well as pore wall thickness (Table 6) was achieved through using surfactants with increasing alkyl chain lengths

SBA-15 also displayed a relatively high BET surface area (Table 6). In addition the BJH PSD was found to be centered on 8 nm (Table 6) (Figure 10b), having a narrow pore size distribution. Amorphous silica from Davisal had the lowest BET surface area. In contrast silica gel had the largest pore diameter of the mesoporous silica. Nevertheless the PSD (Figure 13c) was broad, owing to the irregularity of its amorphous structure.



(b)



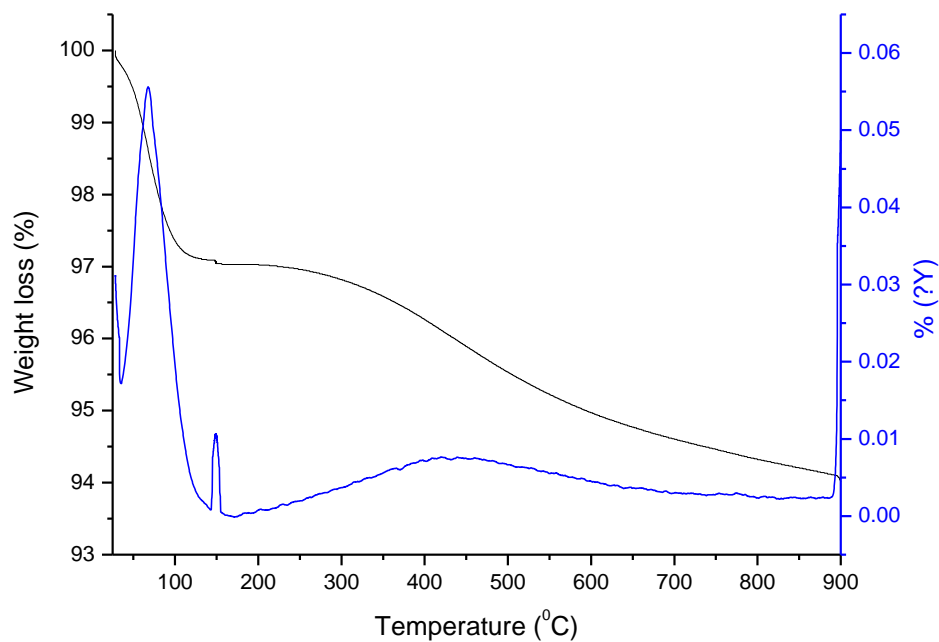


**Figure 14:** Thermogravimetric (TG) profiles of (a) MCM 41 silica synthesized using  $C_{14}TABr$ ,  $C_{16}TABr$  and  $C_{18}TABr$  surfactants, (b) SBA-15 and (c) silica gel.

**Table 7:** TG analysis of mesoporous silica.

Sample	% Weight loss		OH group (mmol/g $SiO_2$ )	OH number <sup>a</sup> (OH $nm^2$ )
	< 150 °C	500-900 °C		
$C_{14}MCM\ 41$	1.2	4.0	4.4	1.4
$C_{16}MCM\ 41$	0.8	2.5	2.8	1.1
$C_{18}MCM\ 41$	0.7	3.0	3.3	1.3
SBA-15	2.8	6	6.5	4.0
Silica gel	3.0	3	3.3	2.5

$$OH\ number\ (nm^2) = \frac{2 \times W(wt\%) \times 6.22141 \times 10^{23}}{100 \times S_{BET} \times MM\ H_2O} \quad (4.1)$$

Figure 14a shows the thermal gravimetric (TG) profiles of C<sub>14</sub>MCM-41, C<sub>16</sub>MCM-41 and C<sub>18</sub>MCM-41. The TG profiles show weight loss between 25-100 °C which is attributed to the loss of physisorbed water. Above 150 °C minimal losses were observed and this is due to water trapped inside the cavities of MCM-41 materials. The TG curves of all MCM-41 prepared materials displayed weight loss in the range of 500-900 °C, which is attributed to the condensation of surface hydroxyl groups. The number of OH groups on the surface is calculated from the condensation of surface hydroxyl group's weight loss (Table 7). Figure 14b shows the TGA/DTA profile of SBA 15. The initial weight loss was observed (25-150 °C) in Figure 11b was due to the evaporation of pre-adsorbed water on the surface of the mesoporous silica. Condensation of mesopores occurred in the temperature range of 500-900 °C. The weight loss in this region was also used to quantify the number of hydroxyl groups present in SBA 15. Table 7 shows the data obtained from the TG profiles. MCM-41 materials had similar weight losses in the temperature range 500-900 °C, and the OH group content (mmol/g SiO<sub>2</sub>) could be calculated. The silanol number which was obtained for MCM-41 materials was in good agreement with results which were previously reported, also using TG methods [17]. Filhou reported that the estimated number of groups per nm<sup>2</sup> accessible in silica surfaces is between four and five [18]. The -OH group per nm<sup>2</sup> of SBA-15 was calculated and was in good agreement with literature reported [11]. SBA-15 was found to have the highest number of OH groups per nm<sup>2</sup>.

### 4.3 FT-IR analysis

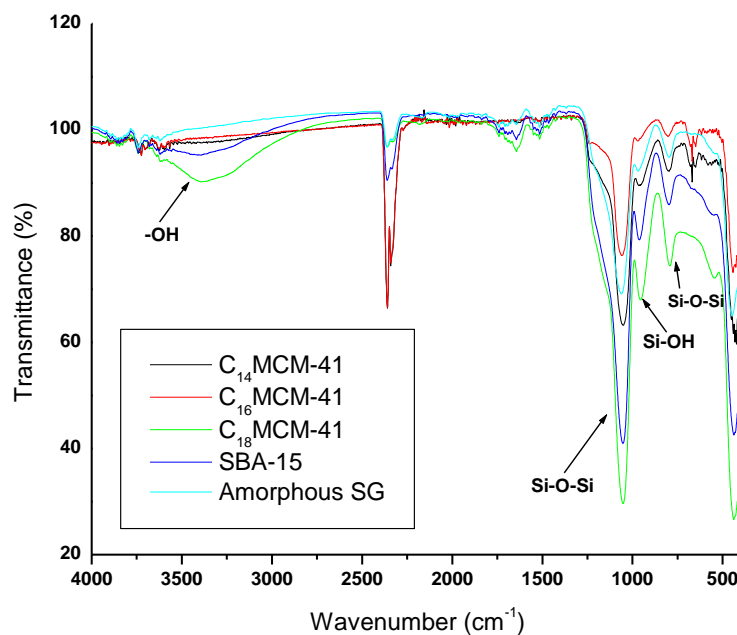


**Figure 15:** FT-IR spectra of mesoporous silica.

Figure 15 shows the FT-IR spectra of synthesized ordered mesoporous silica as well as commercial amorphous silica gel. FT-IR spectra of the mesoporous silica display characteristic peaks attributed to siliceous materials. Asymmetric Si-O-Si stretching was observed at 1234.3 cm<sup>-1</sup> and 1051.4 cm<sup>-1</sup>. Symmetric Si-O-Si stretching was observed at 787.7 cm<sup>-1</sup>. Characteristic bending of Si-O-Si was observed at 451.3 cm<sup>-1</sup>. Broad bands were observed in MCM-41 as well as SBA-15 materials, which may be due to surface silanol groups as well as pre-adsorbed water although samples were dried prior to measurements [19-20]. The presence of water shows the hygroscopic nature of these mesoporous materials although they were dried prior to FT-IR measurements being performed.

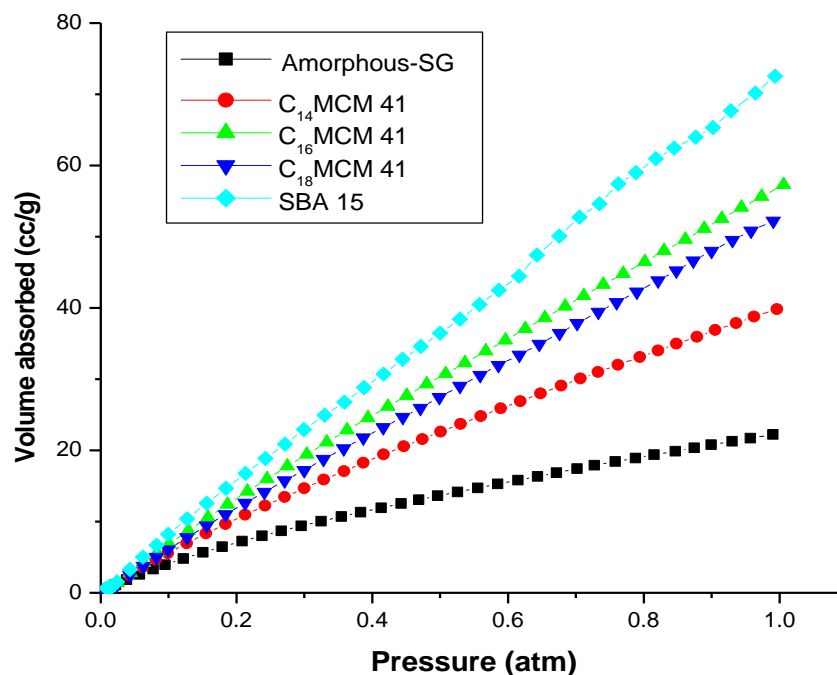


**Figure 16:** CO<sub>2</sub> isotherms of mesoporous silica performed at 0 °C.

The mesoporous materials show a linear increase in CO<sub>2</sub> uptake over the pressure range (Figure 16). At low pressure (0-0.2) atm the mesoporous silica displayed similar CO<sub>2</sub> uptake [21]. As the pressure is increased the difference of CO<sub>2</sub> uptake was observed across the relative pressure range (0-1) atm. At a relative pressure of 0.15 atm, the CO<sub>2</sub> concentration corresponds to the concentration of the effluent gases from a typical power plant. The absorption capacity of mesoporous silica used in this study at this pressure was 0.03, 0.04, 0.05, 0.04 and 0.05 mmol/g for amorphous silica gel, C<sub>14</sub>MCM-41, C<sub>16</sub>MCM-41, C<sub>18</sub>MCM-41, and SBA-15, respectively. The CO<sub>2</sub> uptake of the mesoporous silica at 1 atm was 0.1, 0.18, 0.26, 0.23 and 0.32 mmol/g for amorphous silica gel, C<sub>14</sub>MCM-41, C<sub>16</sub>MCM-41, C<sub>18</sub>MCM-41, and SBA-15, respectively. The CO<sub>2</sub> uptake proved to be dependent on the structural properties of the mesoporous silica. Initially CO<sub>2</sub> molecules come into contact with the mesoporous silica surfaces, and a monolayer of CO<sub>2</sub> is gradually formed. This implies that large surface area silica can adsorb

more CO<sub>2</sub> molecules. In raising the partial pressure of CO<sub>2</sub>, the CO<sub>2</sub> molecules then fill the micropores as bulk liquid, resulting in samples having larger microporosity to adsorb more CO<sub>2</sub>. As the pressure increases to relatively high pressures, mesopore adsorption takes precedence [22]. SBA-15 showed the highest uptake of CO<sub>2</sub> across the entire pressure range.

#### 4.4 CO<sub>2</sub>-TPD analysis

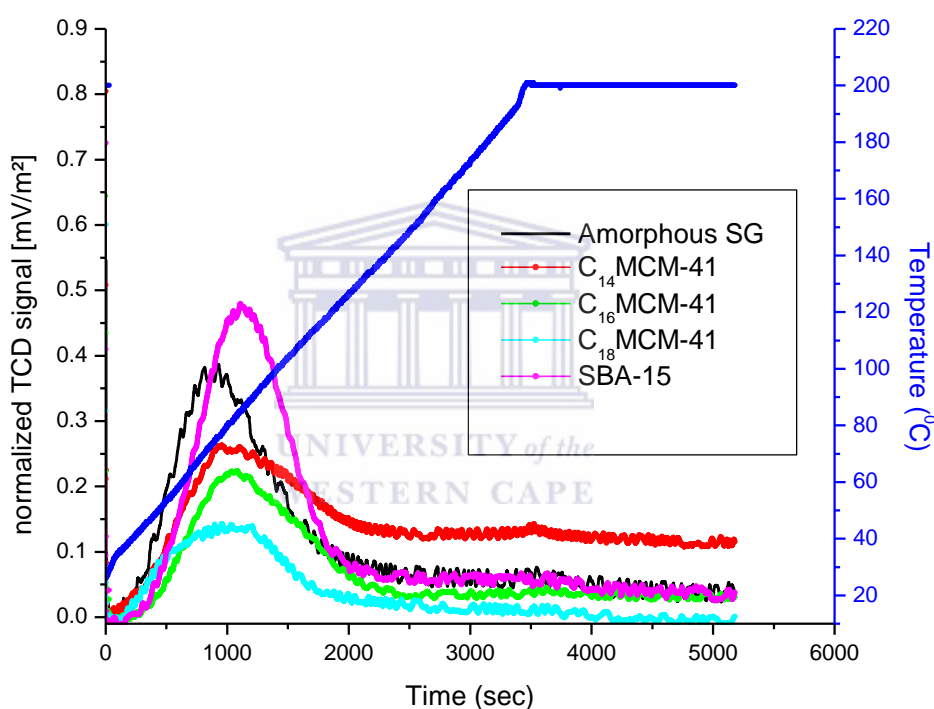


**Figure 17:** CO<sub>2</sub> TPD profiles of mesoporous silica at a rate of 3 °C min<sup>-1</sup> (flow rate = 30 ml/min).

**Table 8:** CO<sub>2</sub> uptake obtained from CO<sub>2</sub>-TPD.

Sample	Amount adsorbed (mmol/g)
C <sub>14</sub> MCM-41	0.19
C <sub>16</sub> MCM-41	0.16
C <sub>18</sub> MCM-41	0.11
SBA-15	0.26
Amorphous SG	0.09

Figure 17 shows the CO<sub>2</sub> TPD profiles of the adsorbents used in this study. The TCD signal was normalized taking into account that the mesoporous materials used in this study had different surface areas. It is clear from the profiles that there was only one maximum for all the sorbents visible between 500-2000 seconds in the temperature range 40-120 °C, which was due to the physisorbed CO<sub>2</sub>. In the range of 500-2500 sec and 120 °C almost all of the trapped CO<sub>2</sub> is desorbed from the sorbents used during this study. Interestingly, C<sub>14</sub>MCM-41 desorption profiles seem to deviate from the other sorbents due to the fact that even at high temperatures, residual CO<sub>2</sub> was still detected.

In conclusion, mesoporous silica were successfully synthesized and fully characterized. The structural information obtained through various characterization techniques provided important information that would assist in determining the extent of functionalization strategies that would follow during the various chemical modification of the as-prepared mesoporous materials. The CO<sub>2</sub> adsorption capacities of the as-prepared mesoporous silica gave a good indication as to which adsorbents would be ideal for adsorption processes. It is for this reason that C<sub>18</sub>MCM-41, SBA-15 and silica gel was chosen for this particular study after assessing all the structural properties obtained from the several characterization techniques.

**References**

1. Russo, P.A., Carrott, M.M.L.R. & Carrott, P.J.M. 2007, "Effect of hydrothermal treatment on the structure, stability and acidity of Al containing MCM-41 and MCM-48 synthesised at room temperature", *Colloids and Surfaces A: Physicochemical and Engineering Aspects*, vol. 310, no. 1-3, pp. 9-19.
2. Sayari, A. & Yang, Y. 2000, "Highly Ordered MCM-41 Silica Prepared in the Presence of Decyltrimethylammonium Bromide", *Journal of Physical Chemistry B*, vol. 104, no. 20, pp. 4835-4839.
3. Kresge, C.T., Leonowicz, M.E., Roth, W.J., Vartuli, J.C. & Beck, J.S. 1992, "Ordered mesoporous molecular sieves synthesized by a liquid-crystal template mechanism", *Nature*, vol. 359, no. 6397, pp. 710-712.
4. Beck, J.S., Vartuli, J.C., Roth, W.J., Leonowicz, M.E., Kresge, C.T., Schmitt, K.D., Chu, C.T.-., Olson, D.H., Sheppard, E.W., McCullen, S.B., Higgins, J.B. & Schlenker, J.L. 1992, "A new family of mesoporous molecular sieves prepared with liquid crystal templates", *Journal of the American Chemical Society*, vol. 114, no. 27, pp. 10834-10843.
5. Kruk, M., Jaroniec, M. & Sayari, A. 1997, "Adsorption study of surface and structural properties of MCM-41 materials of different pore sizes", *Journal of Physical Chemistry B*, vol. 101, no. 4, pp. 583-589.
6. Meynen, V., Cool P., Vansant E.F. 2009, "Verified syntheses of mesoporous materials," *Microporous and Mesoporous Materials* 125, 170–223.
7. Zhao, D., Feng, J., Huo, Q., Melosh, N., Fredrickson, G.H., Chmelka, B.F. & Stucky, G.D. 1998, "Triblock copolymer syntheses of mesoporous silica with periodic 50 to 300 angstrom pores", *Science*, vol. 279, no. 5350, pp. 548-552.
8. Zhao, D., Sun, J., Li, Q. & Stucky, G.D. 2000, "Morphological control of highly ordered mesoporous silica SBA-15", *Chemistry of Materials*, vol. 12, no. 2, pp. 275-279.
9. Klinthong, W., Huang, C.-. & Tan, C.-. 2013, "CO<sub>2</sub> capture by mesoporous SBA-15 grafted with 3-aminopropyl triethoxysilane in supercritical propane", *Energy Procedia*, pp. 175.

10. Jana, S.K., Mochizuki, A. & Namba, S. 2004, "Progress in pore-size control of mesoporous MCM-41 molecular sieve using surfactant having different alkyl chain lengths and various organic auxiliary chemicals", *Catalysis Surveys from Asia*, vol. 8, no. 1, pp. 1-13.
11. Li, Y., Sun, N., Li, L., Zhao, N., Xiao, F., Wei, W., Sun, Y. & Huang, W. 2013, "Grafting of amines on ethanol-extracted SBA-15 for CO<sub>2</sub> adsorption", *Materials*, vol. 6, no. 3, pp. 981-999.
12. Rouquerol F., Rouquerol J., Sing. K.S.K. 1999, "Adsorption by Powders and Porous Solids", San Diego Academic Press.
13. Lowell, S., Shields, J.E., Thomas, M.A., Thommes, M. 2004, "Characterization of Porous Solids and Powders: Surface Area, Pore Size and Density", Springer.
14. Kruk. M, Jaroniec. M. 2000, "Characterization of the Porous Structure of SBA-15", *Chemical Materials*, vol. 12, no. 7, pp. 1961-1968.
15. Yin, P., Tian, Y., Wang, Z., Qu, R., Liu, X., Xu, Q. & Tang, Q. 2011, "Synthesis of functionalized silica gel with poly(diethylenetriamine bis(methylene phosphonic acid)) and its adsorption properties of transition metal ions", *Materials Chemistry and Physics*, vol. 129, no. 1-2, pp. 168-175.
16. Jana, S.K., Mochizuki, A. & Namba, S. 2004, "Progress in pore-size control of mesoporous MCM-41 molecular sieve using surfactant having different alkyl chain lengths and various organic auxiliary chemicals", *Catalysis Surveys from Asia*, vol. 8, no. 1, pp. 1-13.
17. Ek, S., Root, A., Peussa, M. & Niinistö, L. 2001, "Determination of the hydroxyl group content in silica by thermogravimetry and a comparison with 1H MAS NMR results", *Thermochimica Acta*, vol. 379, no. 1-2, pp. 201-212.
18. Filho, N. L. D., 2002, "Adsorption at Surface-Modified Silicas Gels", *Encyclopedia of Surface and Colloid Science*. Pp. 191-201.
19. Liu, S, Hsiao, W. & Sie, W. 2012, "Tetraethylenepentamine-modified mesoporous adsorbents for CO<sub>2</sub> capture: Effects of preparation methods", *Adsorption*, vol. 18, no. 5-6, pp. 431-437.



20. Taib. N.I, Endud. S, Katun. M.N. 2011, "Functionalization of Mesoporous Si-MCM-41 by Grafting with Trimethylchlorosilane", International Journal of Chemistry Vol. 3, No. 3.
21. Belmabkhout, Y., Serna-Guerrero, R. & Sayari, A. 2010, "Amine-bearing mesoporous silica for CO<sub>2</sub> removal from dry and humid air", Chemical Engineering Science, vol. 65, no. 11, pp. 3695-3698.
22. Yan X, Komarneni S, Yan Z, 2013, "CO<sub>2</sub> adsorption on Santa Barbara Amorphous-15 (SBA-15) and amine-modified Santa Barbara Amorphous-15 (SBA-15) with and without controlled microporosity", Journal of Colloid and Interface Science, vol. 390, no. 1, pp. 217-224.

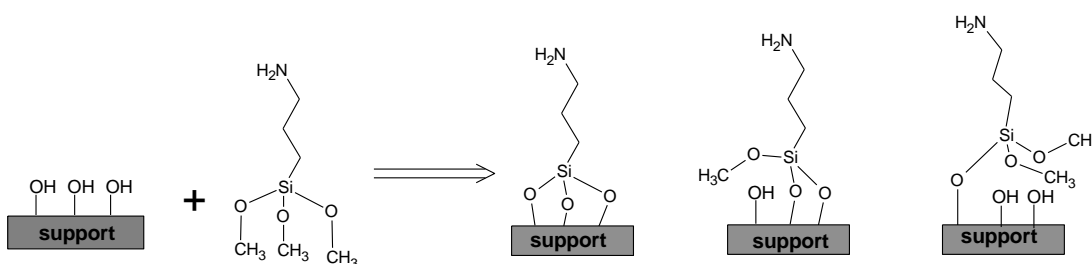


## CHAPTER 5: Functionalization of supports

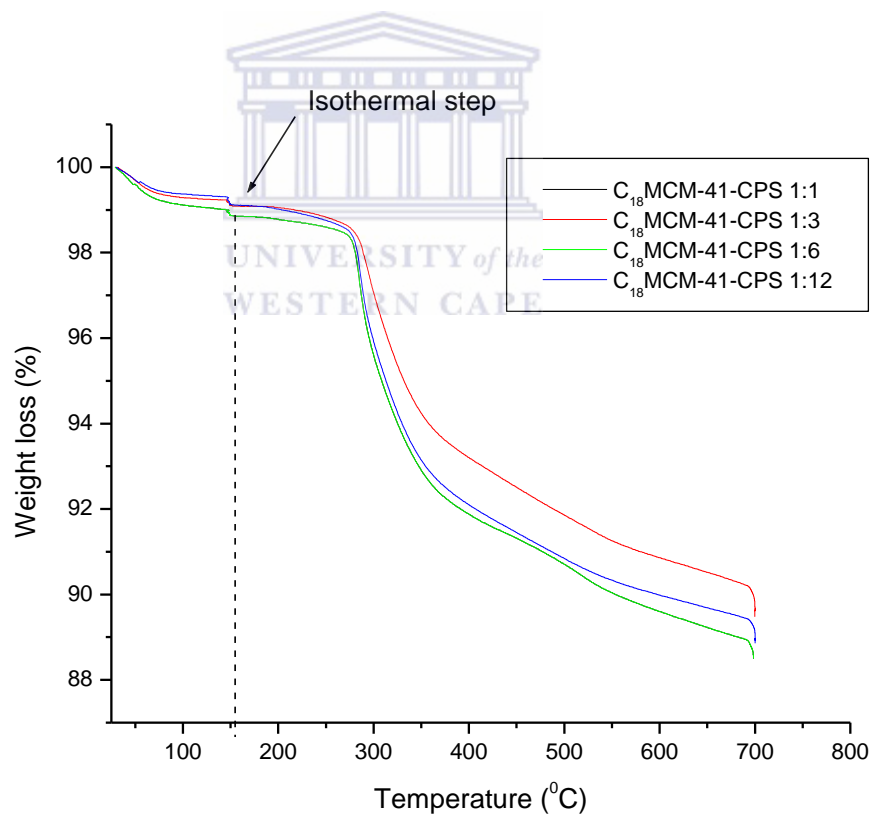
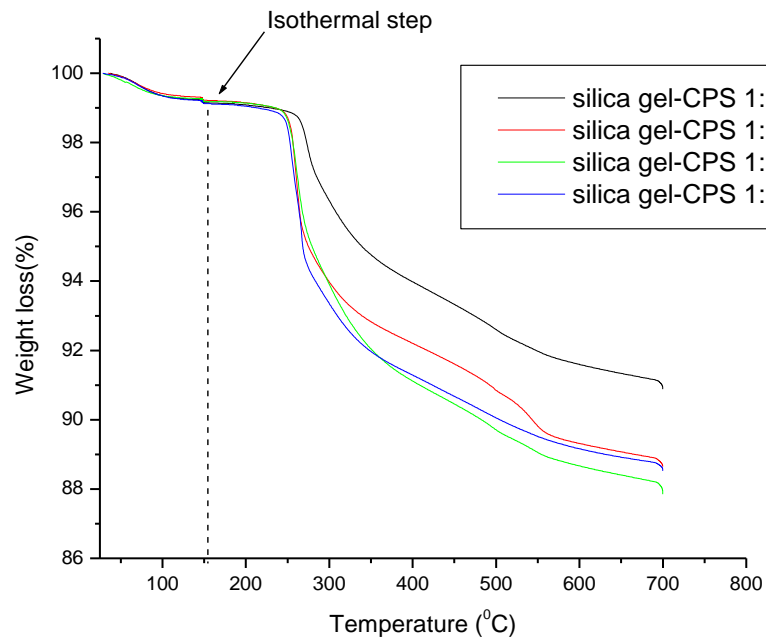
Chapter 5 discusses the functionalization of the mesoporous silica (used in this study), with amine groups to improve the CO<sub>2</sub> sorption capacities. This chapter includes the characterization of mesoporous silica functionalized with amine groups, and also investigates the effect structural properties of the support, the nature of the amine group (primary or secondary amines) and the number of amine groups has on the adsorption capacity of the prepared sorbents. Prior to functionalization with various amines, optimal loading of silanes used as the foundations for further modification, had to be undertaken. The silanes used for the optimization study was 3-aminopropyl)triethoxysilane (APS) and 3 chloropropyl trimethoxysilane (CPS).

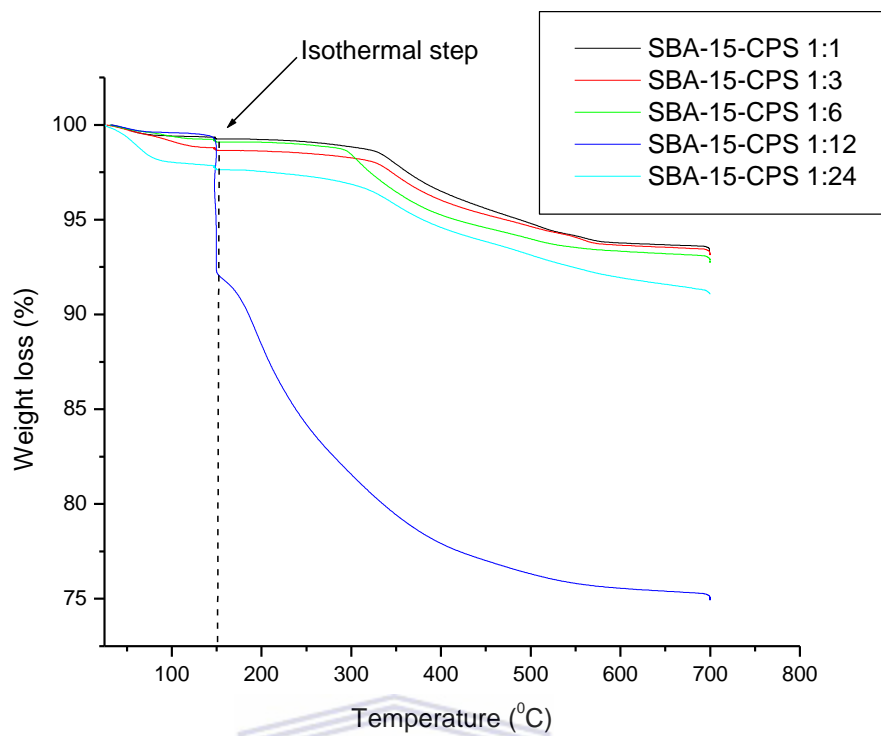
### 5.1 Systematic loading of amine linker onto support

Grafting of a silane linker onto mesoporous supports gives rise to three different modes of binding, i.e. tridentate, bidentate and monodentate. In light of this grafting silane linkers onto the supports with different silane loading/OH groups was investigated.

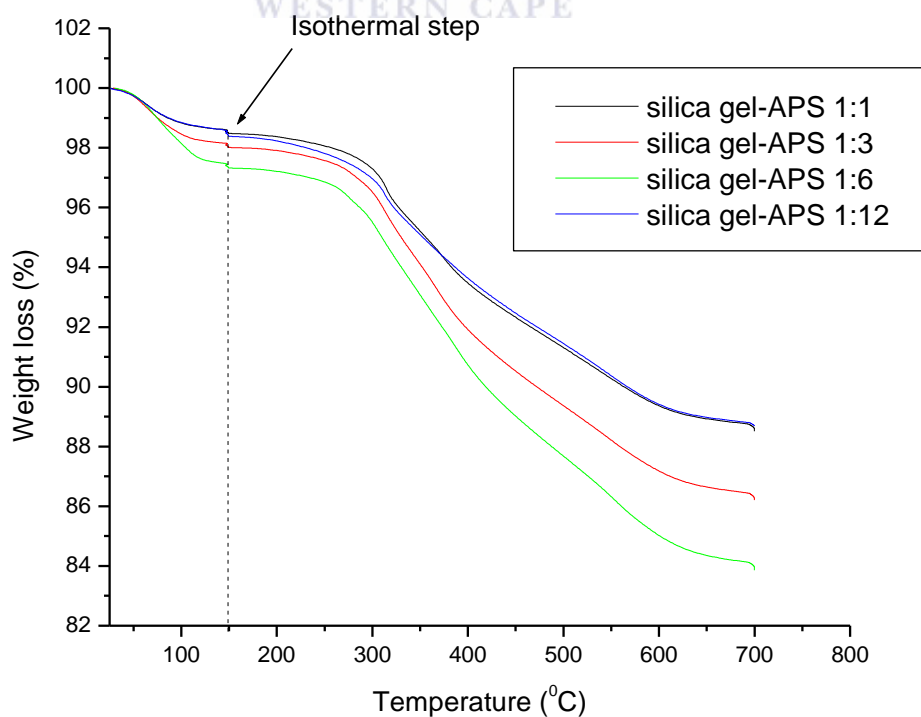


**Scheme 5:** Modes of bonding of silanes onto mesoporous supports.





**Figure 18:** TGA profile of mesoporous silica grafted with different molar ratios of CPS.



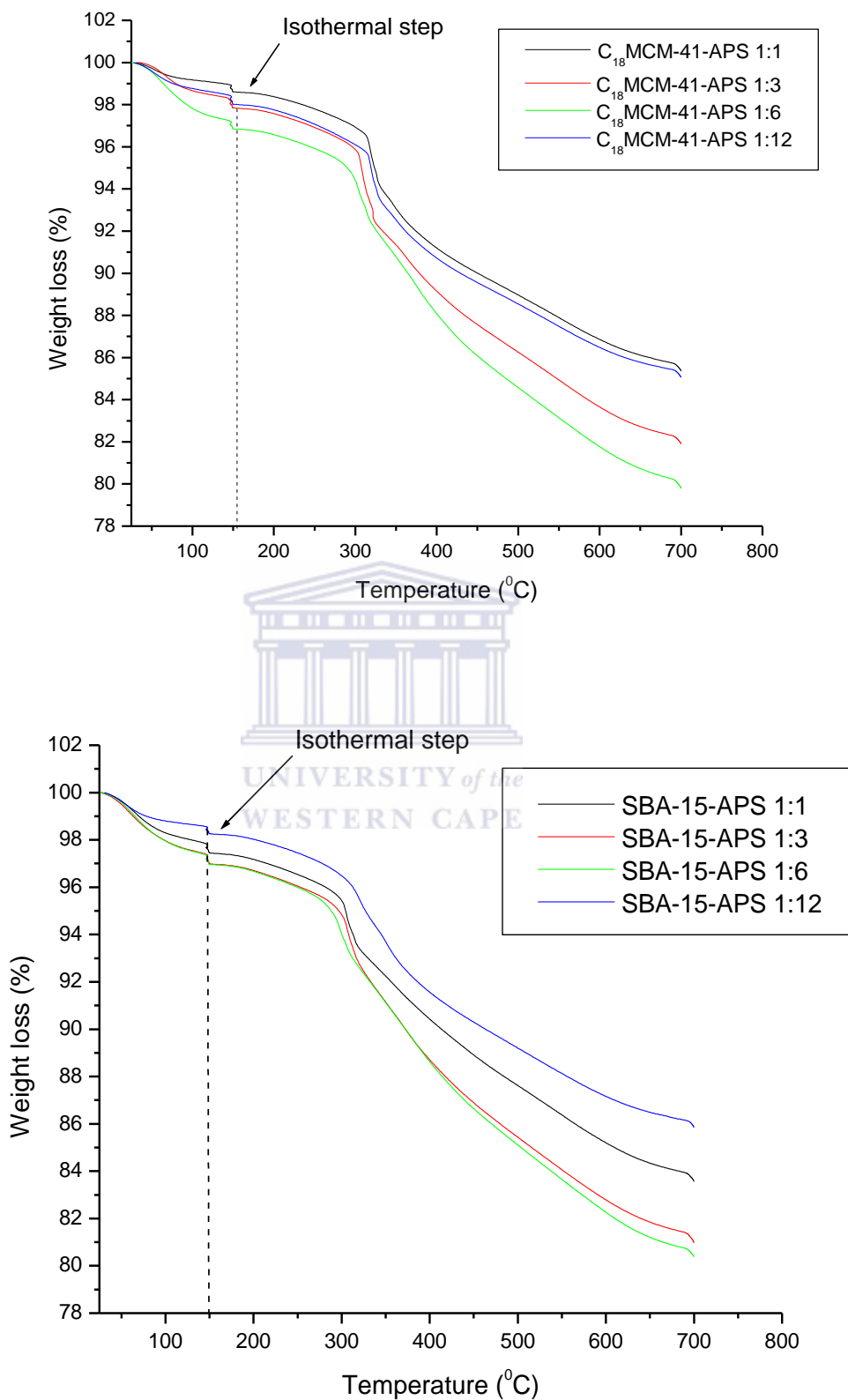


Figure 19: TGA profile of mesoporous silica grafted with different molar ratios of APS.

**Table 9:** Systematic study of CPD and APS loading using TGA.

Sample	Weight loss (°C)	Loading (wt%)
C <sub>18</sub> MCM-41-CPS 1:1	200-550	7.6
C <sub>18</sub> MCM-41-CPS 1:3	200-550	9.2
C <sub>18</sub> MCM-41-CPS 1:6	200-550	7.6
C <sub>18</sub> MCM-41-CPS 1:12	200-550	6.0
SBA 15-CPS 1:1	200-550	5.7
SBA 15-CPS 1:3	200-550	5.0
SBA 15-CPS 1:6	200-550	5.7
SBA 15-CPS 1:12	200-550	24.0
SBA 15-CPS 1:24	200-550	6.4
Amorphous SG-CPS 1:1	200-550	7.6
Amorphous SG-CPS 1:3	200-550	9.9
Amorphous SG-CPS 1:6	200-550	11.1
Amorphous SG-CPS 1:12	200-550	10.2
C <sub>18</sub> MCM-41-APS 1:1	200-550	13.3
C <sub>18</sub> MCM-41-APS 1:3	200-550	16.1
C <sub>18</sub> MCM-41- APS 1:6	200-550	17
C <sub>18</sub> MCM-41- APS 1:12	200-550	13.5
SBA 15- APS 1:1	200-550	14.1
SBA 15- APS 1:3	200-550	16.0
SBA 15- APS 1:6	200-550	16.7
SBA 15- APS 1:12	200-550	12.5
Amorphous SG-APS 1:1	200-550	9.6
Amorphous SG-APS 1:3	200-550	11.7
Amorphous SG-APS 1:6	200-550	13.4
Amorphous SG-APS 1:12	200-550	9.8

Figure 18 shows the various loading of CPS on the mesoporous silica used in this study. The loading was varied with respect to the number of OH groups /nm<sup>2</sup> calculated previously (Chapter 4, Table 7). The loading of CPS varied for each support. The loading was found to be dependent on surface area as well as pore size. Amorphous silica gel showed the highest loading, due to its large pores which could accommodate more CPS molecules as well as on the surface.

The number of OH groups in SBA-15 (Chapter 4, Table 7) was found to be relatively more than the other supports. The higher OH content was due to the contribution of both micro and mesoporosity. The micro pores of SBA-15 are relatively inaccessible for grafting. Therefore the micro porosity had to be subtracted from the total porosity, in order to obtain the amount of accessible OH groups for the grafting process.

SBA-15-CPS 1:12 (OH groups: CPS) ratio was found to be the optimal grafting of CPS. SBA-15-CPS 1:24 displayed a greater weight loss, but this was due to pre-adsorbed water, resulting in a considerable change in weight during the isothermal heating step.

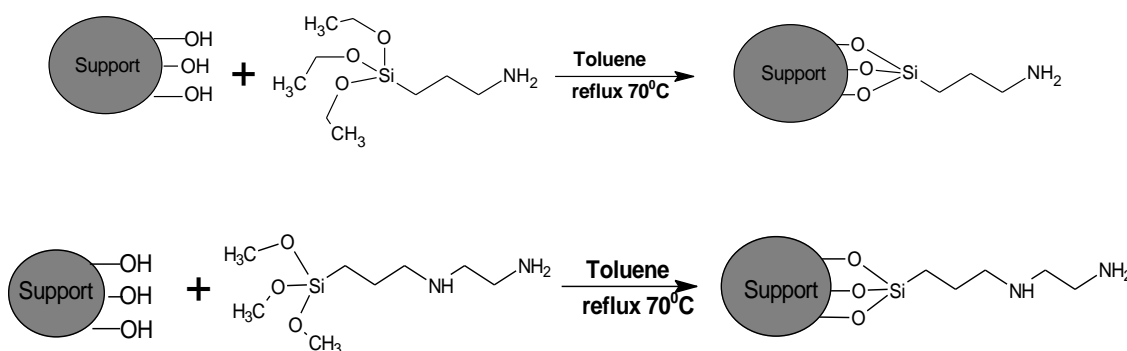
The optimum OH group: CPS ratio for C<sub>18</sub>MCM-41 was 1:6. The OH group content was less than SBA-15 and amorphous silica gel, which meant that the loading of CPS would also be less. This was evident through the TGA profiles obtained. The maximum loading at the optimal ratio of 1:6 was 9.3 wt %.

A systematic study of grafting mesoporous silica with APS is displayed in Figure 19. The optimal loading of APS on C<sub>18</sub>MCM-41, SBA-15 and amorphous silica gel was found to be 1:6, 1:6 and 1:3 OH groups/APS, respectively. In the case of SBA-15-APS 1:3 and 1:6 gave similar loadings, and therefore 1:3 was chosen in terms of an economical point of view.

The systematic study of grafting mesoporous silica with different molar ratios of CPS and APS allowed for the exploitation of OH groups available for reaction on the surface of the mesoporous silica's. The initial silylation step is crucial, as it serves as the foundation for further chemical modifications to expand the number of amine groups.

## 5.2 Functionalization with APS and TPED (G1)

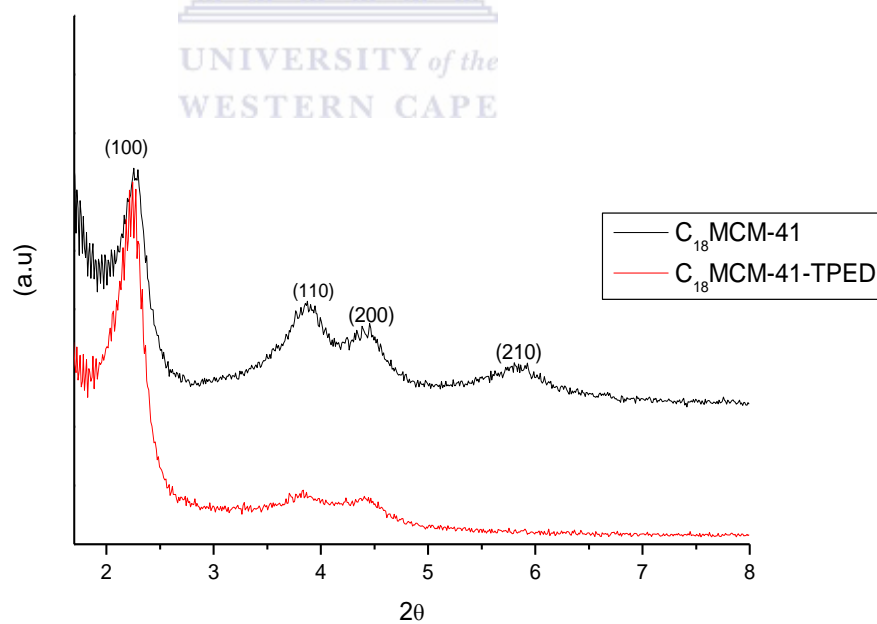
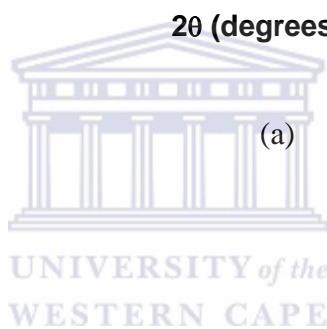
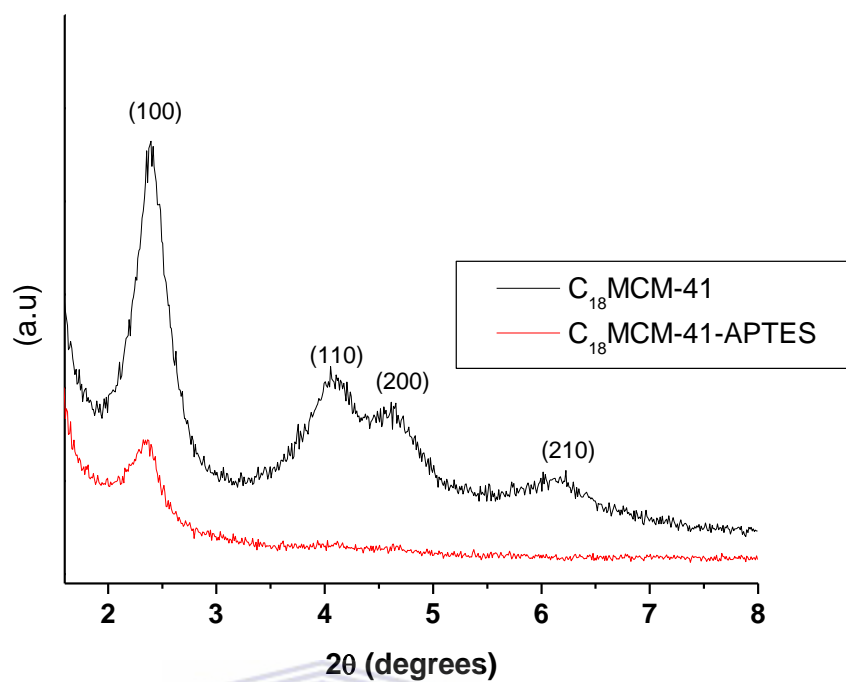
The characterization of APS and TPED grafted C<sub>18</sub>MCM-41, SBA-15 and amorphous silica gel is discussed in this chapter (section 5.2). Grafting of amine groups onto the supports provides a much stronger interaction with the amine species and the support material. The grafted amines are immobilized onto the surface of the OMS through a silylation reaction between the hydroxyl groups of the OMS and the ethoxy groups of the silane linkers. The chemical bonds formed gives rise to a much stronger interaction between support and amine species immobilized on the surface, and may be used at elevated temperatures [1]. Several studies have been reported on grafted mesoporous silica using amine groups for capturing CO<sub>2</sub> [2].



**Scheme 6:** APS and TPED grafted mesoporous silica.



## 5.3 XRD.

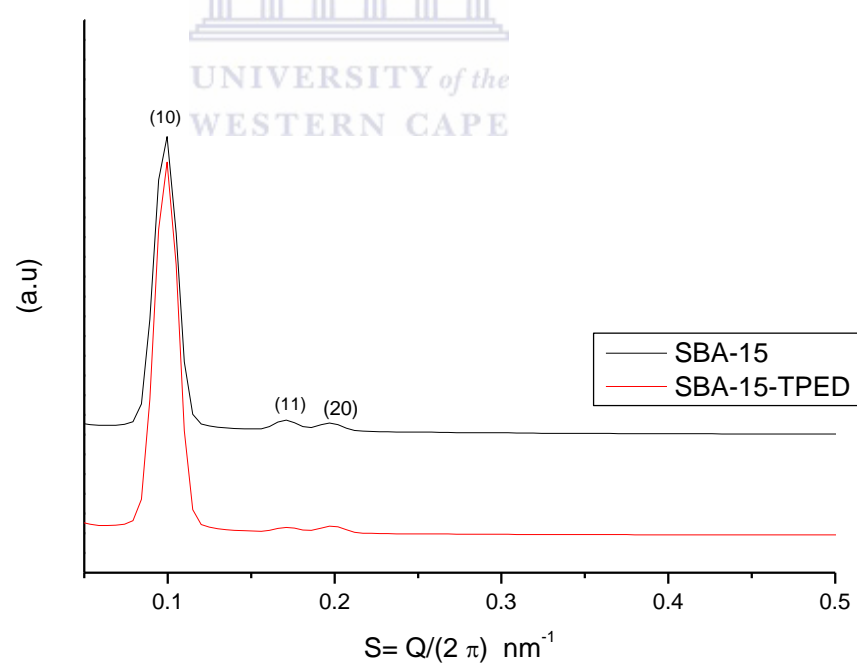
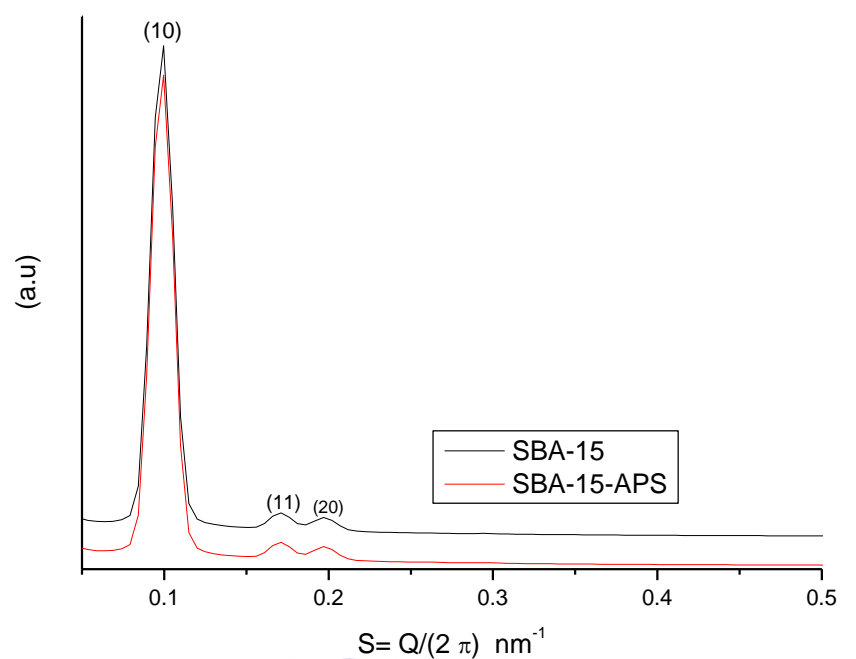


(b)

**Figure 20:** Powder XRD patterns of (a) APS and (b) TPED grafted  $C_{18}$ MCM-41.

Powder XRD was used to characterize the structure of C<sub>18</sub>MCM-41 before and after grafting with (a) APS and (b) TPED as shown in Figure 17. According to the Bragg equation ( $n\lambda = 2d \sin \theta$ ), the distribution  $1/d$  spacing has the ratio  $1:\sqrt{3}:2:\sqrt{7}$ , which corresponds to the planes indexed as (100), (110), (200), and (210), respectively. These indices have typical features of a hexagonal mesoporous structure [3]. The XRD pattern of the C<sub>18</sub>MCM-41 (Figures 20a and b) displayed four peaks that can be indexed to a two dimensional hexagonal lattice, indicating a good degree of structural ordering [4]. Upon grafting C<sub>18</sub>MCM-41 with APS and TPED, the intensity of the diffraction patterns decreased (Figure 20a and b). The higher order indices peaks (110, 200 and 210) intensity was reduced. The reduction in the intensity of the peaks was possibly caused by pore filling when grafted with APS and TPED [5]. This implies that after grafting C<sub>18</sub>MCM-41 with APS and TPED it gave rise to less ordering in comparison to the parent C<sub>18</sub>MCM-41. The d-spacing of APS and TPED grafted C<sub>18</sub>MCM-41 was 2.52 and 2.75 nm respectively. The d spacing remained unchanged, indicating that the grafting step did not cause any structural damage.

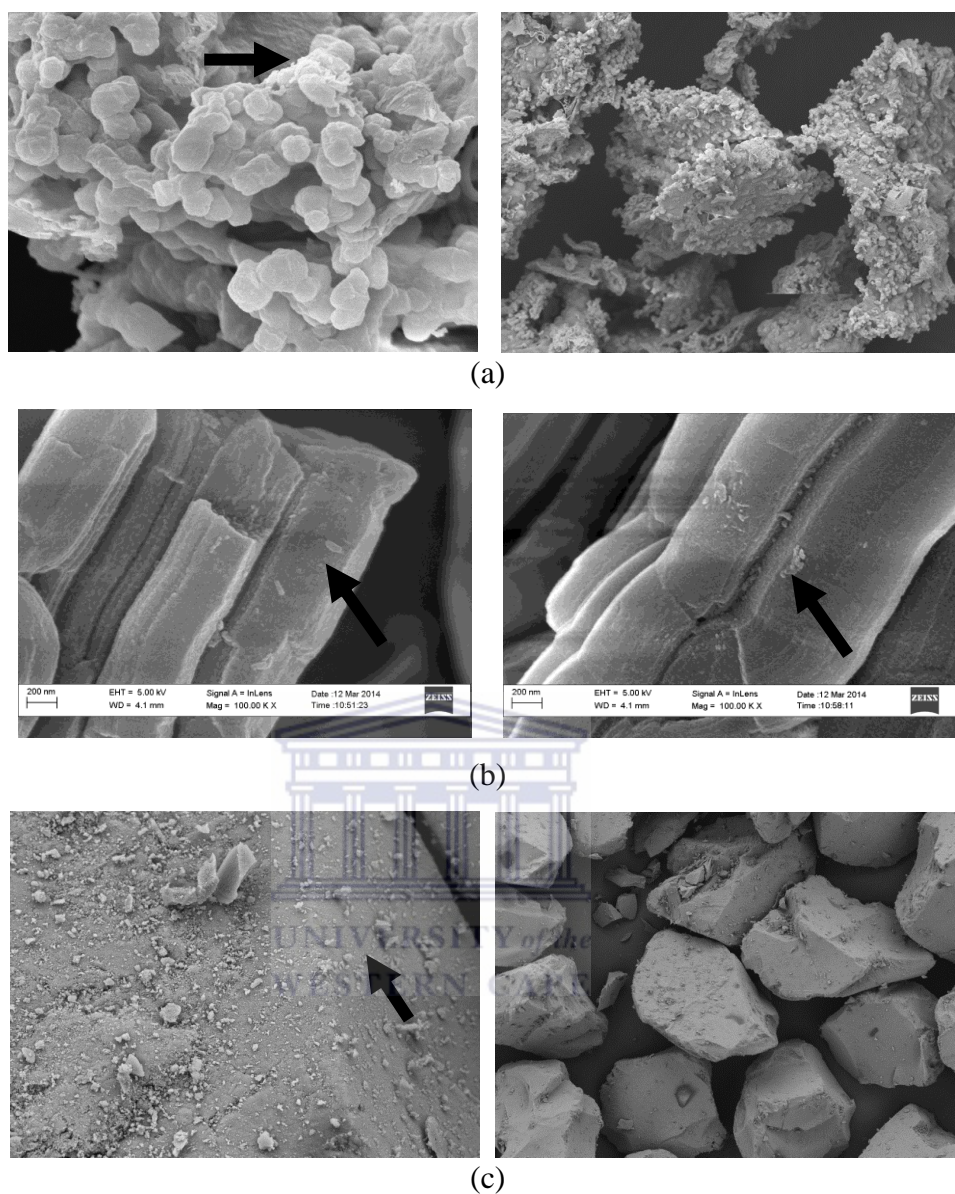
## 5.4 SAXS



**Figure 21:** SAXS of (a) APS and (b) TPED grafted SBA-15.

SAXS was used to monitor the stability of APS and TPED grafted SBA-15. SAXS patterns of SBA-15 showed three well resolved peaks that are indexed as (10), (11) and (20) and which are associated with p6mm 2D hexagonal periodicity of the cylindrical pore array in the SBA-15 (Figure 21 a and b) [6]. The scattering vector ( $S$ ) was used in this case to assign the diffraction peaks, as opposed to the conventional ( $q$ ). The scattering vector ( $s$ ) is simply  $Q/(2\pi)$ , and therefore  $s = 1/d$ , where  $S = 2/\lambda \sin(2\theta/2)$  with  $2\theta$  being the full scattering angle. The indices corresponded to a strong peak at  $s = 0.1 \text{ nm}^{-1}$  and weaker peaks at  $s = 0.17 \text{ nm}^{-1}$  and  $s = 0.2 \text{ nm}^{-1}$  respectively. Grafting SBA-15 with APS and TPED resulted in a decrease in intensity of higher order peaks indexed at (11) and (20). The d spacing of SBA-15-APS and SBA-TPED was 1.2 and 2.3 respectively. The d spacing remained unchanged after grafting SBA-15 with APS and TPED. The position of the main peak indexed at (10) remained unchanged indicating that the structure of SBA-15 was not compromised during the functionalization step [7].

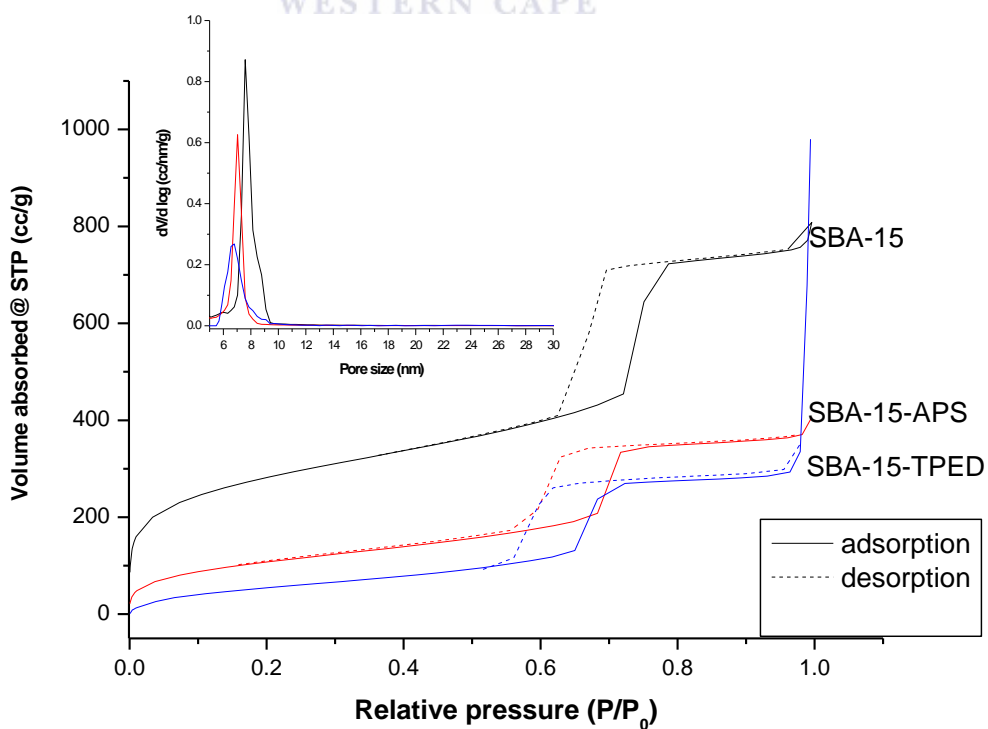
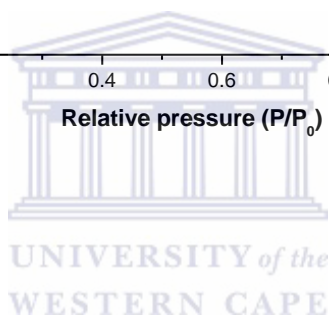
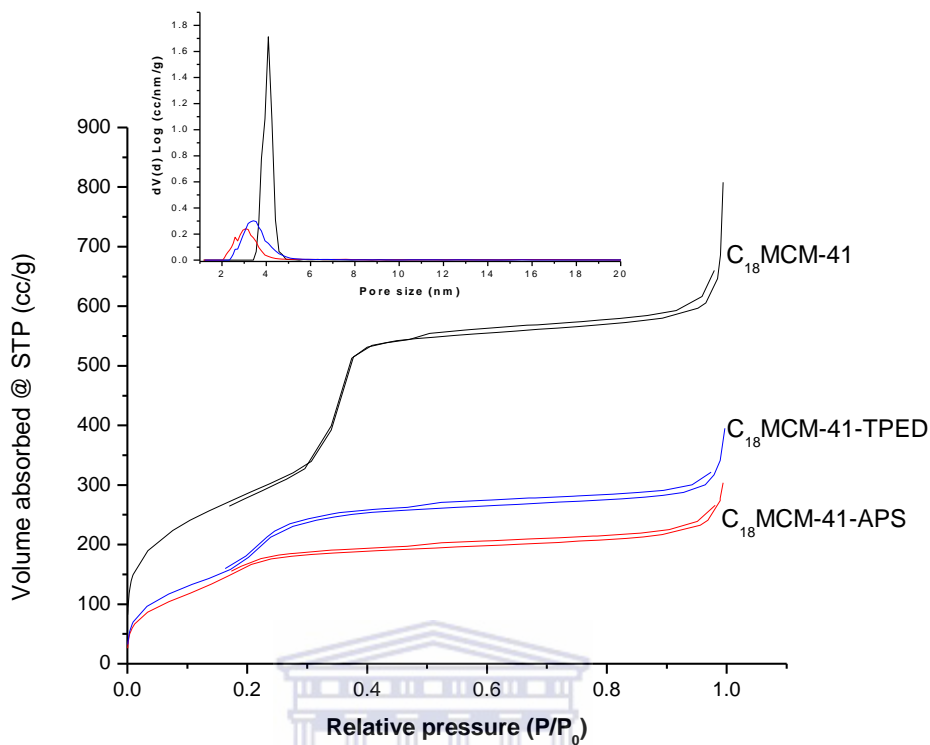
## 5.5 HRSEM



**Figure 22:** HRSEM images of APS grafted C<sub>18</sub>MCM-41 (a), SBA-15 (b) and amorphous SG (c).

Grafting with APS C<sub>18</sub>MCM-41, SBA-15 and amorphous SG displayed changes in morphology (Figure 22). The arrows indicated on Figures 22 a, b and c shows the possible introduction of organosilanes on the surface of the mesoporous materials used in this study. In contrast to SBA-15 and amorphous SG, C<sub>18</sub>MCM-41 morphology changed, where some spherical particles were covered with a layer of organic material in some regions, forming clusters as observed in Figure 22 a.

5.6 Textural properties.



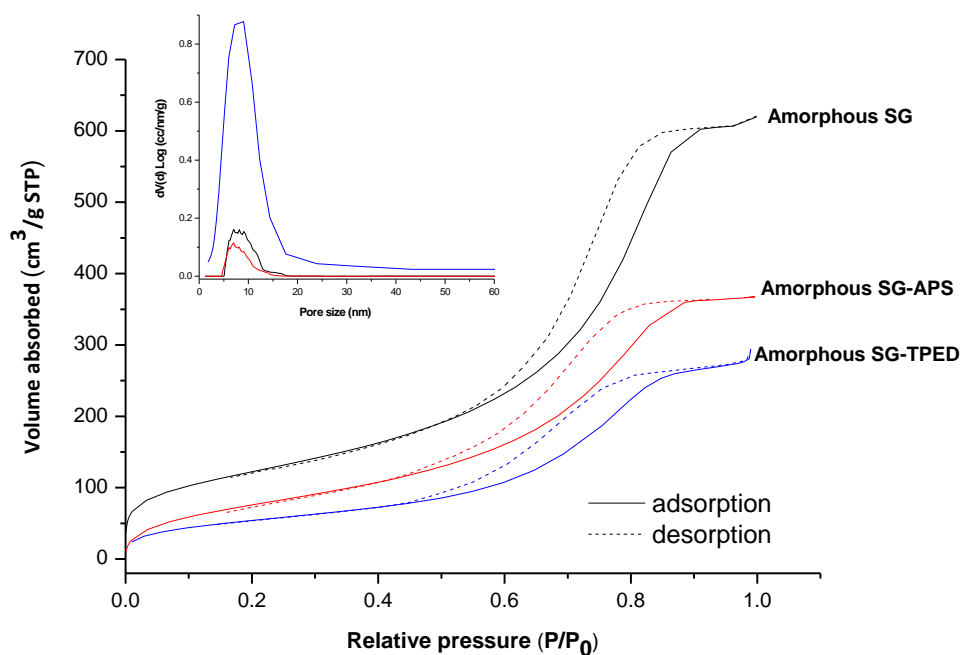


**Figure 23:** N<sub>2</sub> isotherms of APS and TPED grafted sorbents.

**Table 10:** Textural properties of silica gel, MCM-41 and SBA-15 as well as APS and TPED grafted sorbents.

Sample	Surface area (m <sup>2</sup> /g)	Pore volume (cm <sup>3</sup> /g)	Pore size (nm)	D spacing <sup>a</sup> (nm)	a <sub>0</sub> <sup>b</sup> (nm)	Wall thickness <sup>c</sup> (nm)	N content <sup>d</sup> (wt %)	Tether loading <sup>e</sup> (#tethers/nm <sup>2</sup> )
C <sub>18</sub> MCM-41	1211	1.3	4.4	2.75	3.31	1.09	-	-
C <sub>18</sub> MCM-41-APS	631	0.5	2.9	2.52	3.17	0.27	3.21	3.3
C <sub>18</sub> MCM-41-TPED	632	0.6	3.9	2.75	3.31	0.59	4.42	3.3
SBA-15	1024	1.3	7.6	10.01	11.56	3.96	-	-
SBA-15-APS	405	0.6	6.2	9.94	11.48	5.28	4.11	5.4
SBA-15-TPED	222	1.5	6.8	10.01	11.56	4.77	4.40	9.5
Amorphous SG	445	0.9	8.6	-	-	-	-	-
Amorphous SG-APS	405	0.6	6.2	-	-	-	2.52	3.7
Amorphous SG-TPED	202	0.4	7.0	-	-	-	3.61	9.5

MCM-41: <sup>a</sup>  $d(100) = n \lambda / 2 \sin q$ , <sup>b</sup>  $a_0 = 2 \times d(100) / \sqrt{3}$ , <sup>c</sup>  $W = a_0 - \text{Pore size}$

SBA-15: <sup>a</sup>  $d(10) = 1/s$ , <sup>b</sup>  $a_0 = 2 \times d(10) / \sqrt{3}$ , <sup>c</sup>  $W = a_0 - \text{Pore size}$

<sup>d</sup> N content: elemental analysis

e

$$\frac{\# \text{tethers}}{SA_{sub}} = \frac{N_{prod} (g \cdot g^{-1}) \times \frac{6.023 \times 10^{23} (\text{atoms} \cdot \text{mol}^{-1})}{\text{Atomic Wt}[N] \cdot (g \cdot \text{mol}^{-1})}}{SA_{prod} (m^2 \cdot g^{-1}) * 10^{18} (nm^2 \cdot m^2)} \cdot \frac{r_{prod}}{r_{sub}} \cdot \frac{\# \text{tethers}}{\# N}$$

Where:

( $r_{prod}$ ) is the BJH pore radius, ( $N_{prod}$ ) N content, ( $SA_{prod}$ ): surface area and ( $r_{sub}$ ) BJH pore radius of the substrate.

Figure 23 shows the N<sub>2</sub> isotherms of C<sub>18</sub>MCM-41 and C<sub>18</sub>MCM-41 grafted with APS and TPED. C<sub>18</sub>MCM-41 displayed a type IV isotherm with H1 hysteresis with a sharp increase in volume of nitrogen adsorbed at P/P<sub>0</sub> = 0.1–0.4, which is characteristic of highly ordered mesoporous materials [8]. The desorption branch of C<sub>18</sub>MCM-41 isotherm was found to coincide with the adsorption branch of C<sub>18</sub>MCM-41 indicating the order of the structure (Figure 23). Grafting of C<sub>18</sub>MCM-41 with APS and TPED showed a decrease in N<sub>2</sub> adsorbed. The extent of the decrease was found to be different with APS and TPED. The capillary condensation steps of APS and TPED grafted C<sub>18</sub>MCM-41 shifted to lower relative pressures (Figure 23), i.e. in the range of P/P<sub>0</sub> (0.1-0.3). Overall the shape of APS and TPED grafted C<sub>18</sub>MCM-41 remained the same. Capillary condensation in primary mesopores was still evident in APS and TPED grafted C<sub>18</sub>MCM-41, suggesting that the ordering of the C<sub>18</sub>MCM-41 support was not changed during the grafting step [9]. The specific surface area, total pore volume and pore sizes of APS and TPED grafted C<sub>18</sub>MCM-41 are shown in Table 10. The specific surface area decreased from 1211 m<sup>2</sup>/g for C<sub>18</sub>MCM-41 to 631 and 632 m<sup>2</sup>/g for C<sub>18</sub>MCM-41-APS and C<sub>18</sub>MCM-41-TPED respectively. The pore volume decreased from 1.3 cm<sup>3</sup>/g for C<sub>18</sub>MCM-41 to 0.5 and 0.6 cm<sup>3</sup>/g for C<sub>18</sub>MCM-41-APS and C<sub>18</sub>MCM-41-TPED respectively. The reduction



in pore volume suggests that the organic material was successfully grafted inside the pores of C<sub>18</sub>MCM-41 [10-12]. The PSD of APS and TPED grafted C<sub>18</sub>MCM-41 was broader in comparison to the parent C<sub>18</sub>MCM-41 (Figure 23 a, b and c). The PSD shifted to a smaller pore size in comparison to the parent C<sub>18</sub>MCM-41. Pore size decreased from 4.4 nm for C<sub>18</sub>MCM-41 to 2.9 and 3.9 nm for C<sub>18</sub>MCM-41-APS and C<sub>18</sub>MCM-41-TPED respectively. The broad PSD (Figure 23 a) was due to APS and TPED partially lining the pore walls of C<sub>18</sub>MCM-41.

SBA-15 (Figure 23) displayed a typical type IV isotherm with a well-defined hysteresis loop showing the existence of ordered mesopores in the framework. A sharp steepness and a H1 loop was observed for SBA-15 in the relative pressure range of 0.6-0.8, showing that SBA-15 possessed large pores with a narrow pore size distribution (Figure 23). Upon grafting SBA-15 with APS and TPED, the steepness of the hysteresis loops decreased, and a shift in the inflection point to lower relative pressure (i.e. approximately 0.55-0.7) was observed, resulting in a decrease in pore size and a broader pore PSD (Figure 23) [13]. The amount of N<sub>2</sub> absorbed also decreased after grafting with APS and TPED. A considerable decrease in the specific surface area, pore volume and pore size was observed for APS and TPED grafted SBA-15 in comparison to the parent SBA-15 (Table 10). The diminishing of the hysteresis loops of grafted SBA-15 may be attributed to APS and TPED grafted inside the mesopore channels that in turn gave rise to decreases in pore volume (Table 10) [14]. The mean pore diameters of APS and TPED grafted SBA-15 was lower than that of SBA-15 (Figure 20 b), which was a strong indication that the organosilanes (APS and TPED) was anchored on SBA-15 pore walls. PSD graph shows that the mean pore sizes were found to be in the order APS > TPED, and this was in accordance with the molecular sizes of the organosilanes. Nevertheless the

narrow pore size distribution was retained for APS and TPED grafted SBA-15, indicating even distribution of organosilanes on the pore walls [13].

Amorphous SG displayed type IV isotherm according to the IUPAC classification with a hysteresis loop (Figure 23). Amorphous SG displayed surface area, pore volume and pore size of  $445\text{m}^2/\text{g}$ ,  $0.9\text{ cm}^3/\text{g}$  and  $8.6\text{ nm}$  respectively. Figure 23 showed that the adsorption and desorption branches were almost identical for amorphous SG as APS and TPED grafted amorphous SG. The branches were found to almost be parallel, indicating uniformity of pores of silica gel. Amorphous SG showed capillary condensation of  $\text{N}_2$  into the mesopores at relative pressure  $P/P_0 = 0.55$ . APS and TPED displayed similar isotherms with the exception in the reduction of the total amount of  $\text{N}_2$  absorbed. The reduction in  $\text{N}_2$  absorbed was accompanied by a shift in capillary condensation to lower relative pressure [15]. Occupation of APS and TPED in the pores of amorphous silica gel may be attributed to the shift. This is justified by the fact that the pore volume of the parent material was reduced from  $0.9\text{ cm}^3/\text{g}$  to  $0.6\text{ cm}^3/\text{g}$  and  $0.4\text{ cm}^3/\text{g}$  for amorphous SG-APS and amorphous SG-TPED, respectively (Table 10). The reduction in pore volume amounted to 33 % for amorphous SG-APS and 55 % for amorphous SG-TPED. These are considerable decreases in pore volume, thus not absorbing as much  $\text{N}_2$  as in the parent material, due to the organic material grafted onto the surface as well as inside the pores. The PSD of APS and TPED grafted amorphous silica gel is shown in Figure 23. Amorphous SG had a wide pore size distribution which makes it difficult to see any changes in pore size after the grafting step [16].

Nitrogen content of APS and TPED functionalized mesoporous silica was obtained by elemental analysis shown in Table 10. The extent of amine surface coverage was expressed as tether loading as proposed by Knowles *et al.* Knowles proposed that the

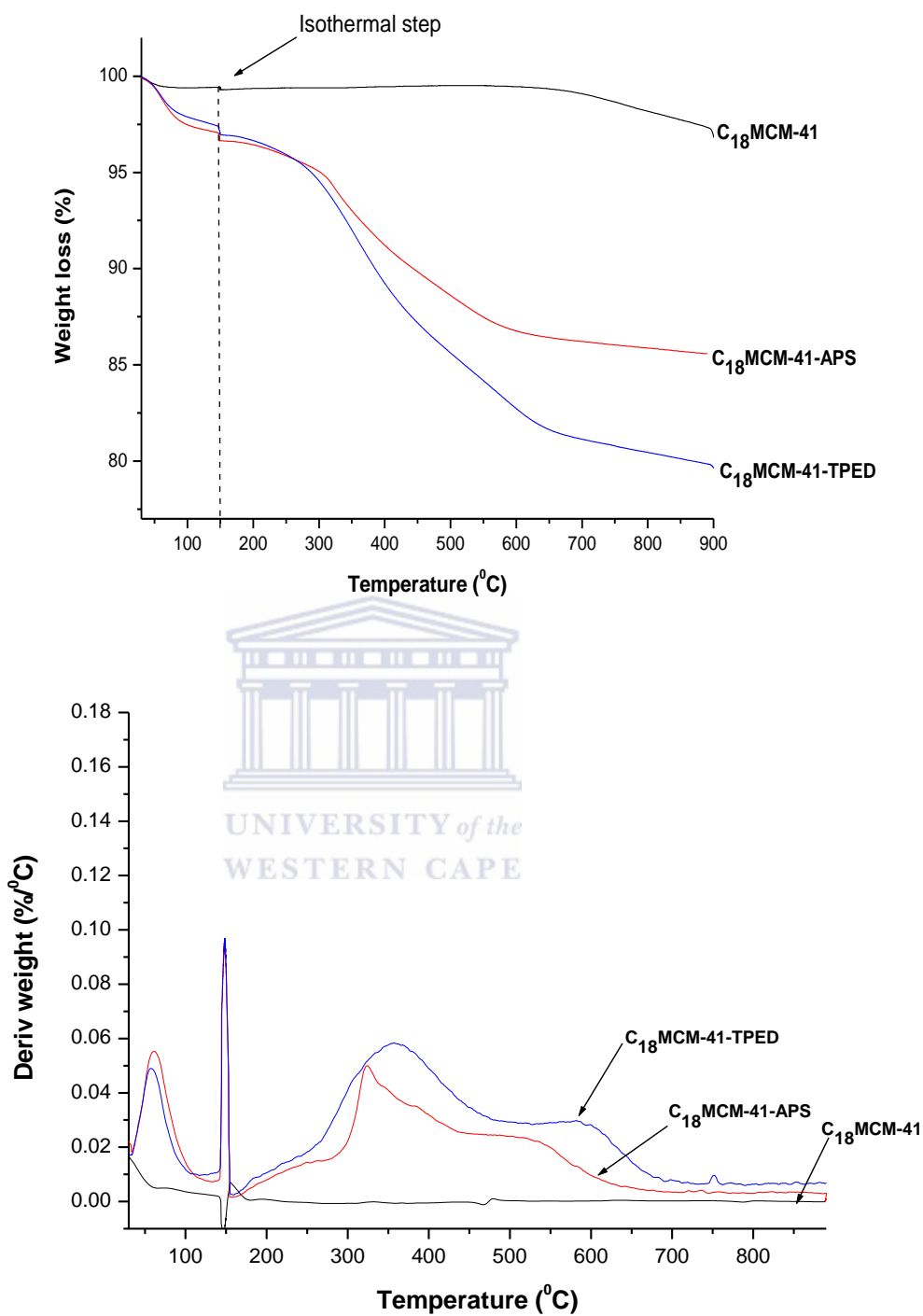
functionalization of different supports had to be compared using a common baseline, e.g. the surface area of the support, which may be expressed as number of tethers/nm<sup>2</sup><sub>sub</sub> [15].

Table 10 shows the nitrogen content for APS and TPED grafted mesoporous supports. As expected, the amine content of C<sub>18</sub>MCM-41, SBA-15 and amorphous silica gel were found to be in the following order, i.e. C<sub>18</sub>MCM-41-TPED > SBA-15-TPED > SBA-15-APS > amorphous SG-TPED > C<sub>18</sub>MCM-41-APS > amorphous SG-APS. The loading of the organosilanes grafted onto the supports varied with the structural properties of the supports used in this particular study. The tether loading is displayed in Table 10. The number of OH groups available was previously discussed (Chapter 4), and the number of tethered organosilanes suggests extensive coverage. The silanes are possibly covalently bonded in a mono- and bi- as well as a tridentate manner. The possibility of the alkoxy groups reacting with neighbouring OH groups of covalently bonded organosilanes may also be a contributing factor. The loading of organosilanes seems to vary with the surface area as well as pore size of the supports. In comparing the APS grafted mesoporous silica, it is observed that SBA-15 showed higher tether loading than C<sub>18</sub>MCM-41 and amorphous SG. Tether loading for SBA-15, C<sub>18</sub>MCM-41 and amorphous SG were 5.4, 3.3 and 3.7 tethers/nm<sup>-2</sup> respectively. The SBA-15 tether loading which was obtained points out that large pores and high surface area could accommodate more silanes, as they have a smaller degree of pore curvature, confirmed in a previous study conducted by Knowles. TPED grafted mesoporous supports followed similar trends owing to the structural properties of the supports. Surface coverage was relatively high for SBA-15 and amorphous SG (Table 10), which was to be expected, seeing as the silanes added were in excess of the amount of OH groups present on the supports used in

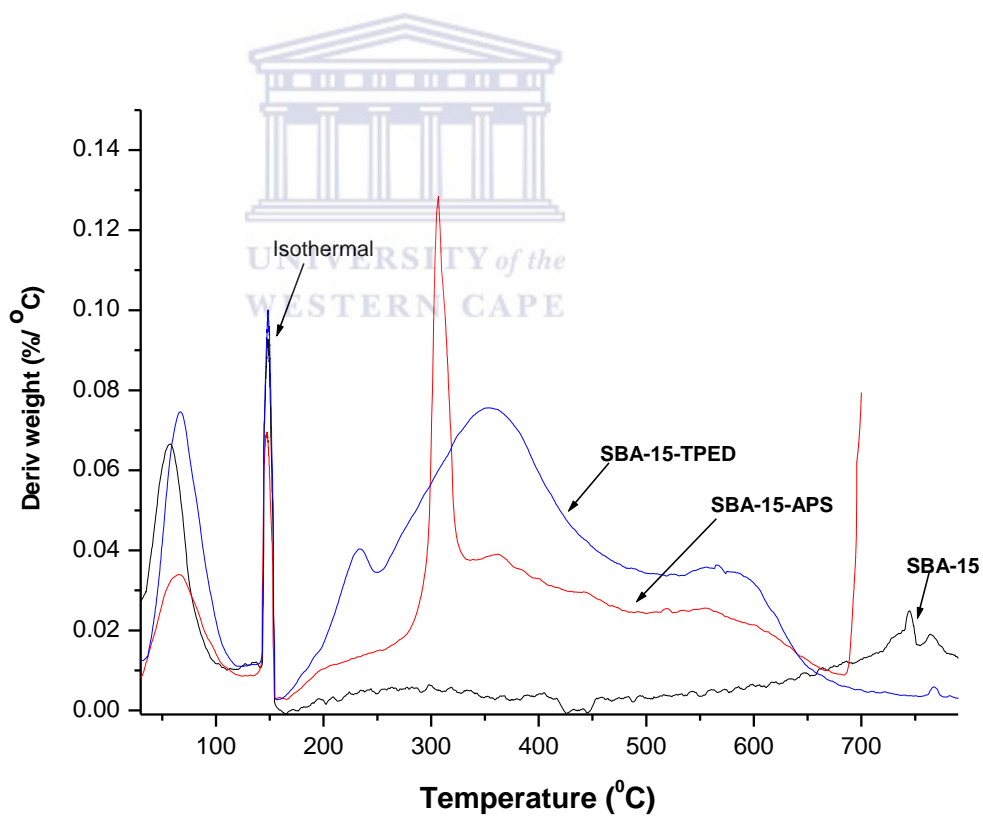
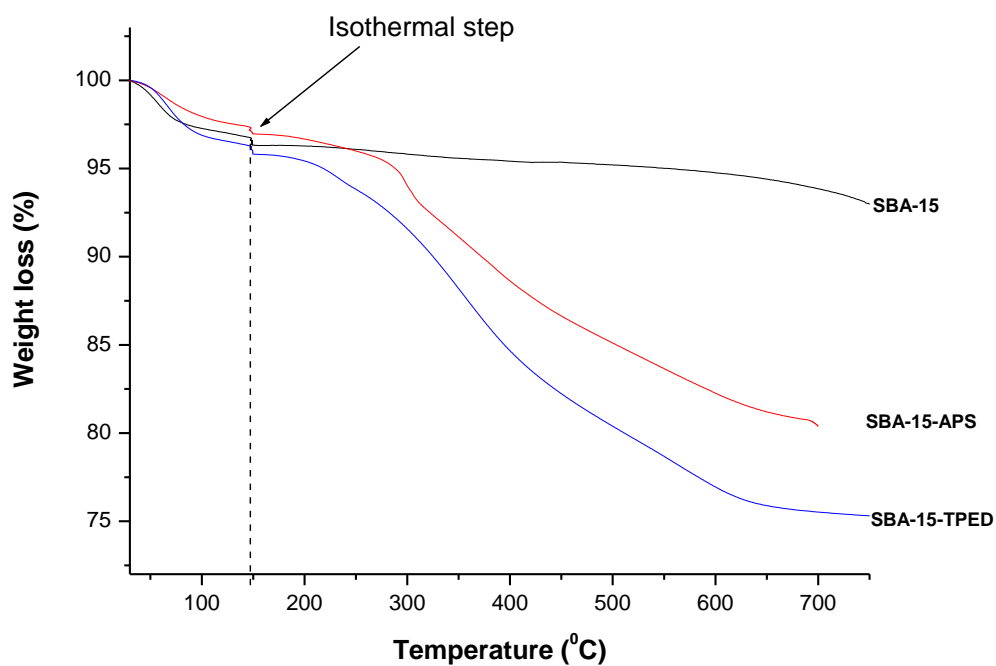
this study. Knowles and co-workers proposed that relatively high tether loading is attributed to the greater accessibility of mesopores and the larger average pore diameters of the support materials. The aforementioned factors allow greater entry and quicker diffusion of organic molecules into the supports. Performing the reaction for twelve hours instead of three hours could also be a contributing factor for the high tether loading of SBA-15 and amorphous SG. It is presumed that the extended time assists in overcoming diffusion limitations within the mesopores of SBA-15 and amorphous SG [17].



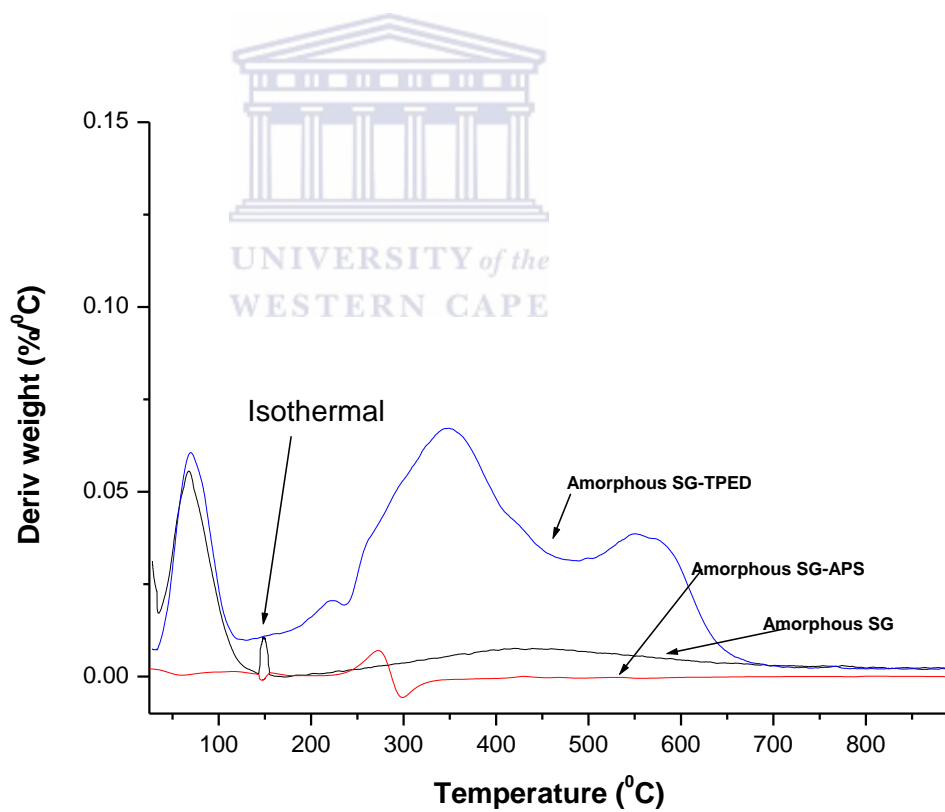
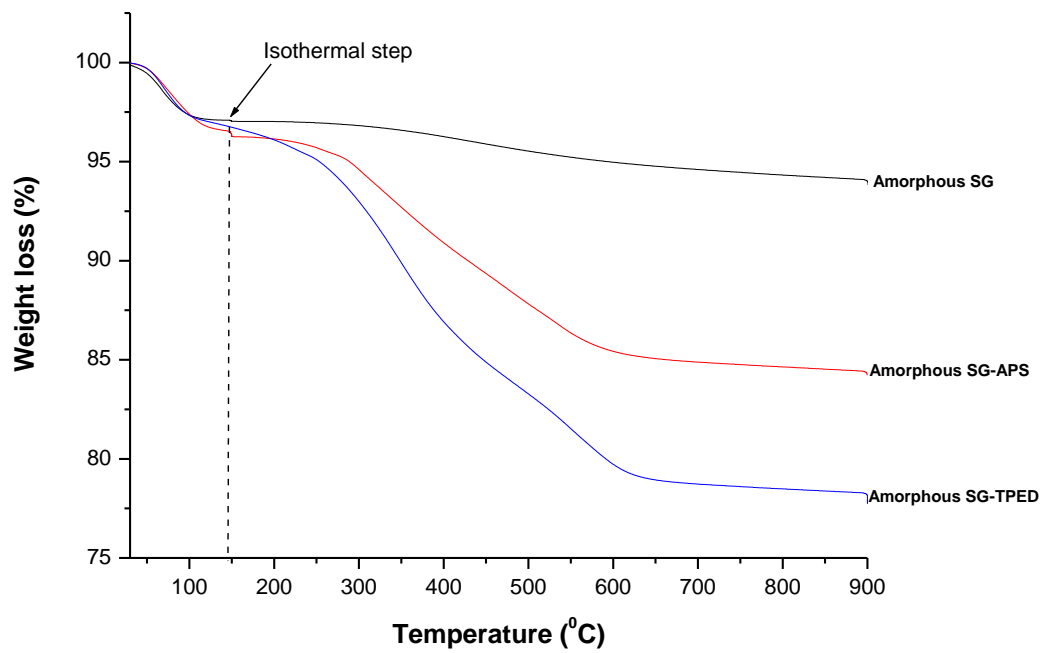
5.7 TG evaluation.



(a)



(b)



(c)

Figure 24: TG/DTA profiles of APS and TPED grafted sorbents.

**Table 11:** Summary of TG profiles of APS and TPED grafted sorbents.

Sample	%Weight loss at different temperatures	
	< 150 °C	150-600 °C
C <sub>18</sub> MCM-41-APS	2.8	11
C <sub>18</sub> MCM-41-TPED	2.3	15
SBA-15-APS	2.5	15
SBA-15-TPED	2.6	20
Amorphous SG-APS	3.7	12
Amorphous SG-TPED	2.9	16

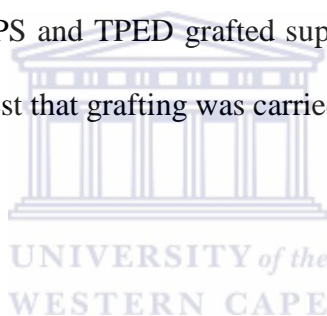
Figure 24 (a) shows the TG/DTA profiles of the parent C<sub>18</sub>MCM-41 as well as the APS and TPED modified mesoporous silica. The decomposition profile of C<sub>18</sub>MCM-41 changed considerably after grafting with APS and TPED. The initial weight loss observed in all the samples (Figure 24 a) was due to physisorbed water. The isothermal step (150 °C) ensured that the physisorbed water was removed, so that all the weight loss observed as the temperature ramp increases was due to the decomposition of the grafted organic molecules. Weight loss above 600 °C was attributed to the condensation of silanol groups (Chapter 1), which is then subtracted from the total weight loss, and the total weight loss due to the decomposition of organic material is then obtained (Table 11). Interestingly APS and TPED grafted C<sub>18</sub>MCM-41 displayed significant loss of physisorbed water in comparison with the parent material. This can be attributed to the aminopropyl ligands which are relatively small, and water molecules not only interact with the amine groups, but also react with the un-reacted ethoxy groups of the bonded organosilanes as well as silanols of C<sub>18</sub>MCM-41 [9]. This accounts for the loss observed for physisorbed water in C<sub>18</sub>MCM-41-APS and C<sub>18</sub>MCM-41-TPED. C<sub>18</sub>MCM-41-APS displayed decomposition of bonded APS of approximately 11 wt % (Table 11) accompanied by



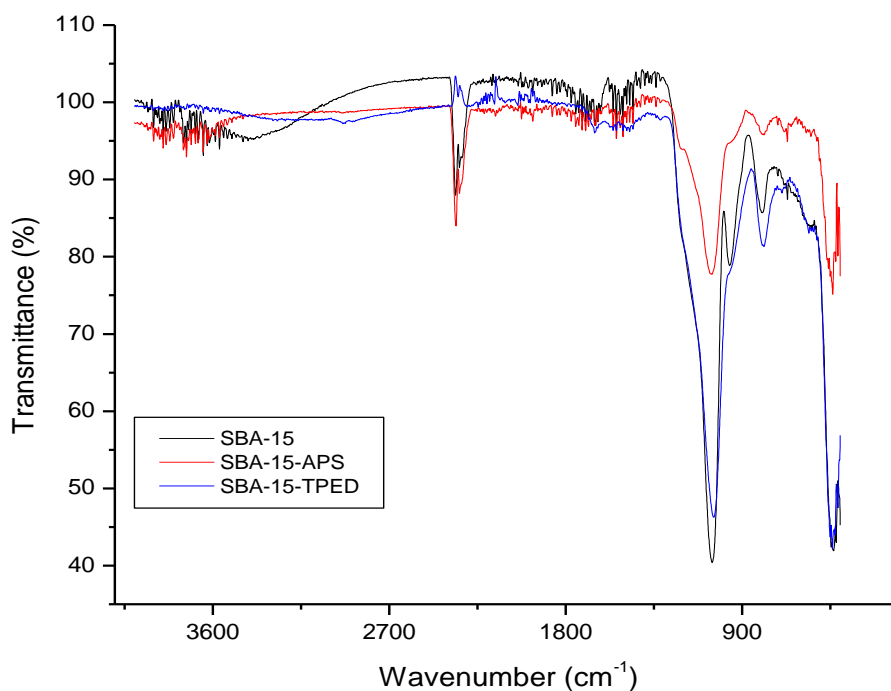
an exothermic peak at 323 °C [18]. C<sub>18</sub>MCM-41-TPED showed a loss of 15 % with 2 exothermic peaks at 357 and 592 °C. The two exothermic peaks may be attributed to the decomposition of the terminal primary amine groups of TPED, and further decomposition of the propyl chain. The position of the first exothermic peak, as well as another peak at a higher temperature, suggests this.

Similar trends were observed for SBA-15 and amorphous SG grafted with APS and TPED. The decomposition profiles were even more apparent and clear distinctions between the exothermic peaks were observed (Figure 24 b), suggesting the stepwise decomposition of TPED grafted mesoporous silica.

The distinct differences in the decomposition profiles (Figure 24) of the parent support materials and APS and TPED grafted support materials, combined with the textural properties, suggest that grafting was carried out successfully.



### 5.8 FT-IR analysis.



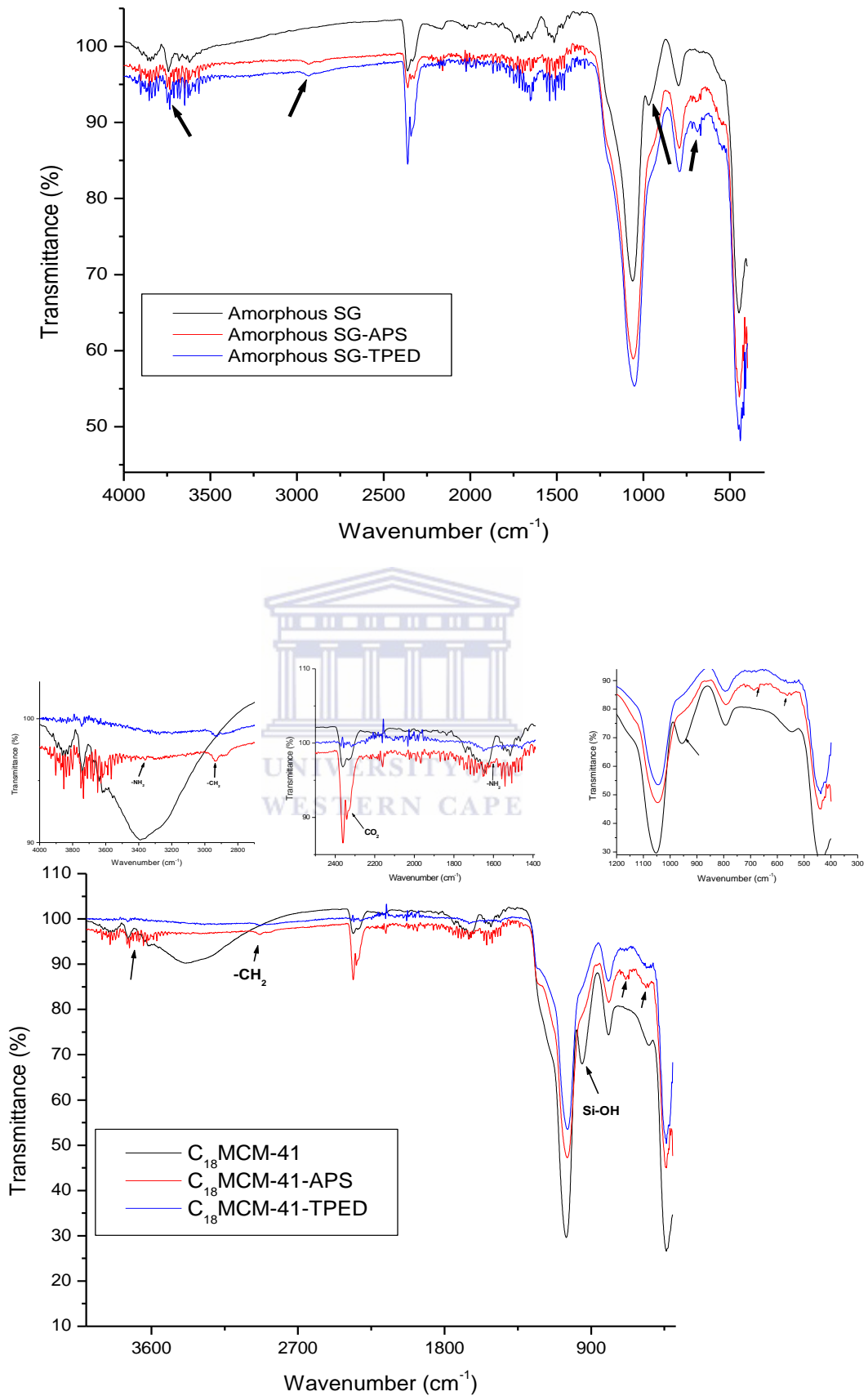


Figure 25: FT-IR spectra of APS and TPED grafted mesoporous silica

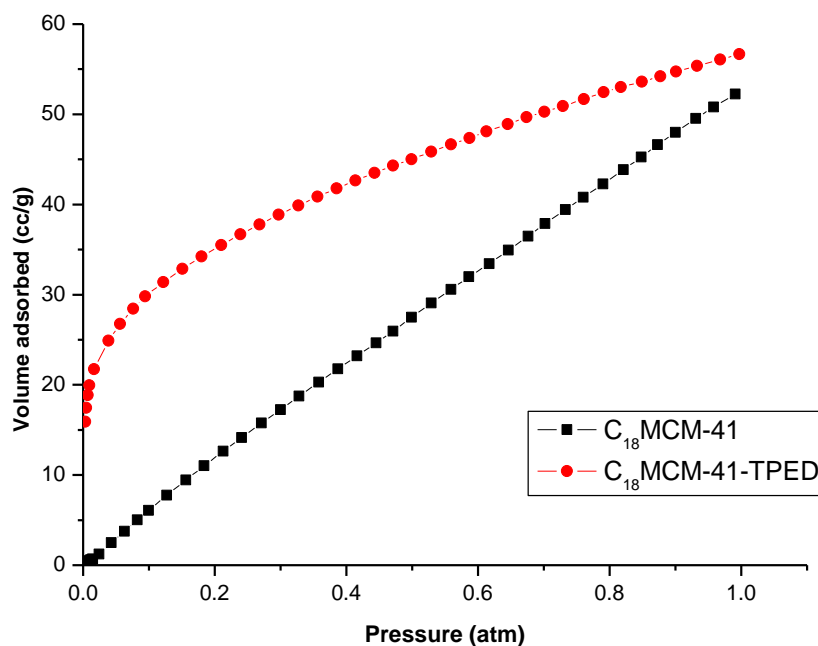
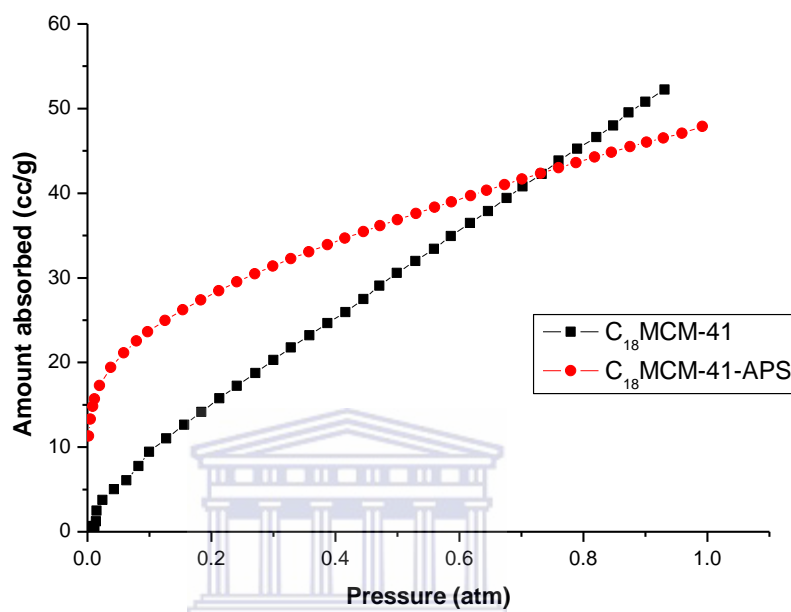
Figure 25 shows the FT-IR spectra of mesoporous silica grafted with APS and TPED. C<sub>18</sub>MCM-41, SBA-15 and amorphous SG displayed characteristic peaks attributed to mesoporous silica. A strong absorbance band was observed around 1080 cm<sup>-1</sup> which is due to the asymmetric stretching of Si-O-Si bonds. Absorption bands at 1150 and 940 cm<sup>-1</sup> correspond to the asymmetric stretching and bending of Si-OH groups on the silica surface. The deformation stretching frequency of Si-O-Si was also visible at 460 cm<sup>-1</sup>. The broad bands observed around 3500 cm<sup>-1</sup> are due to surface silanols and pre-adsorbed water indicating the silica framework is hydrophilic.

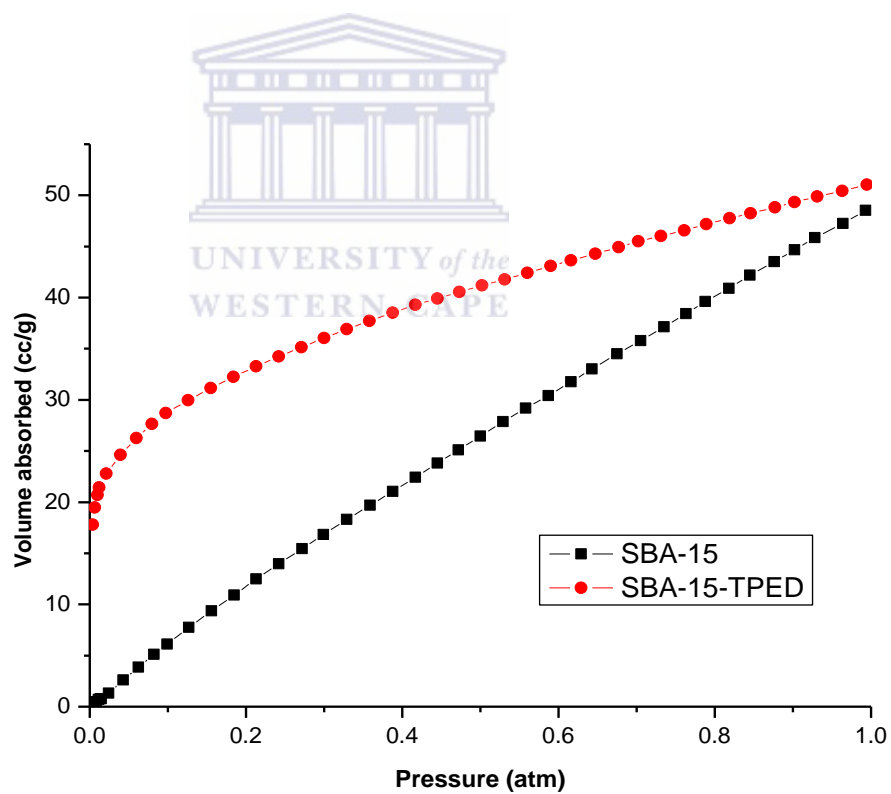
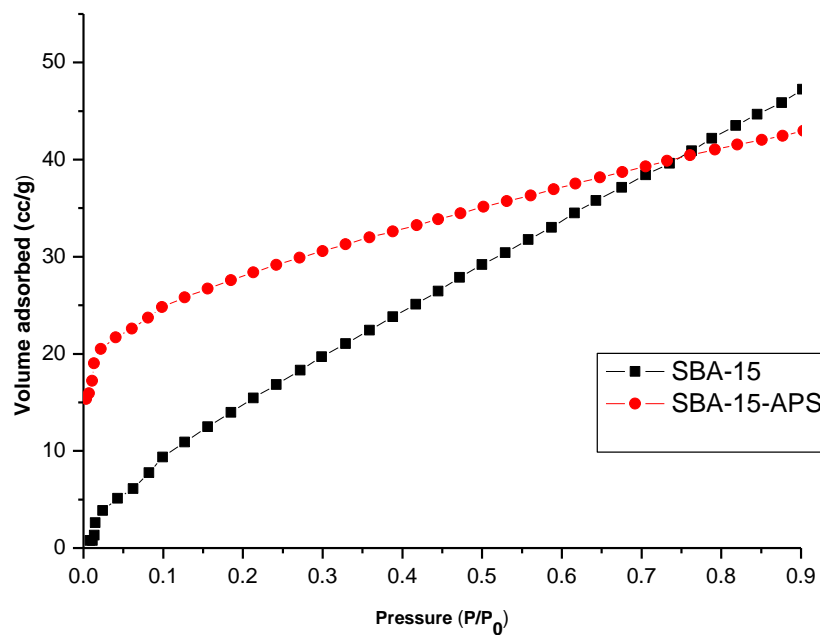
C<sub>18</sub>MCM-41 was shown to be a representative spectrum, with insets of certain sections of the FT-IR spectra that were magnified in order to show the differences in the spectra between the parent material as well as the grafted materials. After grafting C<sub>18</sub>MCM-41 with APS and TPED the intensity of Si-OH at 960 cm<sup>-1</sup> band decreased, suggesting that some of the silanol groups were involved in the reaction. The spectrum of C<sub>18</sub>MCM-41 grafted with APS and TPED also displayed absorption at 3362, 3314 and 1576 cm<sup>-1</sup>. These bands may be attributed to asymmetric NH<sub>2</sub> stretching, symmetric NH<sub>2</sub> stretching and NH<sub>2</sub> deformation of hydrogen bonded amino groups. C-H stretching at 2937 and 2935 cm<sup>-1</sup> of the propyl chain was also observed in the spectra of C<sub>18</sub>MCM-41-APS and C<sub>18</sub>MCM-41-TPED respectively [19-22]. A small band at 695 cm<sup>-1</sup> for C<sub>18</sub>MCM-41-APS was possibly due to Si-C bond stretching.

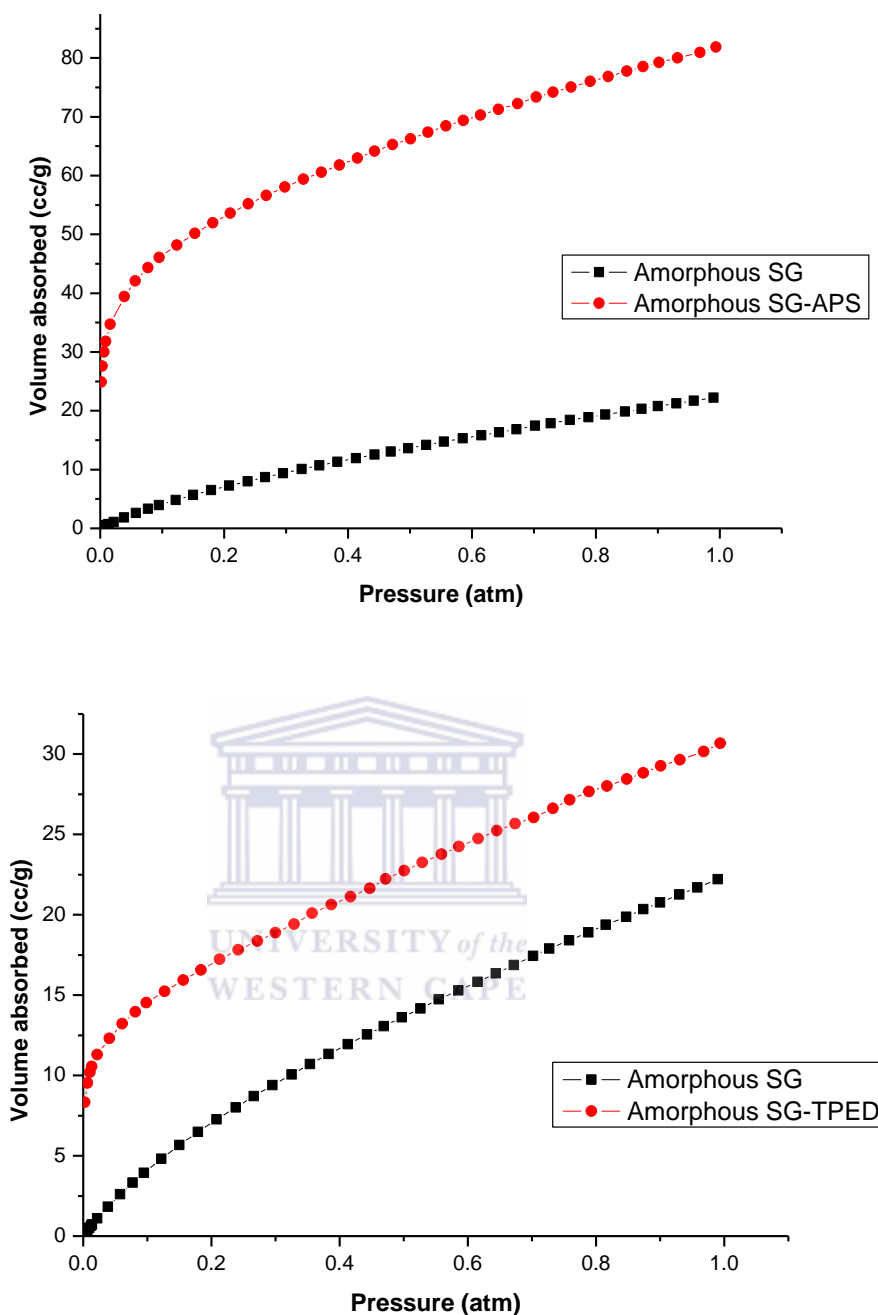
SBA-15 and amorphous SG grafted with APS and TPED showed similar adsorption bands in comparison with APS and TPED grafted C<sub>18</sub>MCM-41. SBA-15 showed an absorption band corresponding to C-H stretching frequency of 2928 and 2921 cm<sup>-1</sup> for SBA-15-APS and SBA-15-TPED respectively [23]. Symmetric and asymmetric

stretching of  $\text{NH}_2$  was also present in APS and TPED grafted SBA-15. The appearance of new absorption bands after functionalization confirms that APS and TPED were successfully grafted onto the mesoporous silica used in this study.

### 5.9 $\text{CO}_2$ isotherm studies.





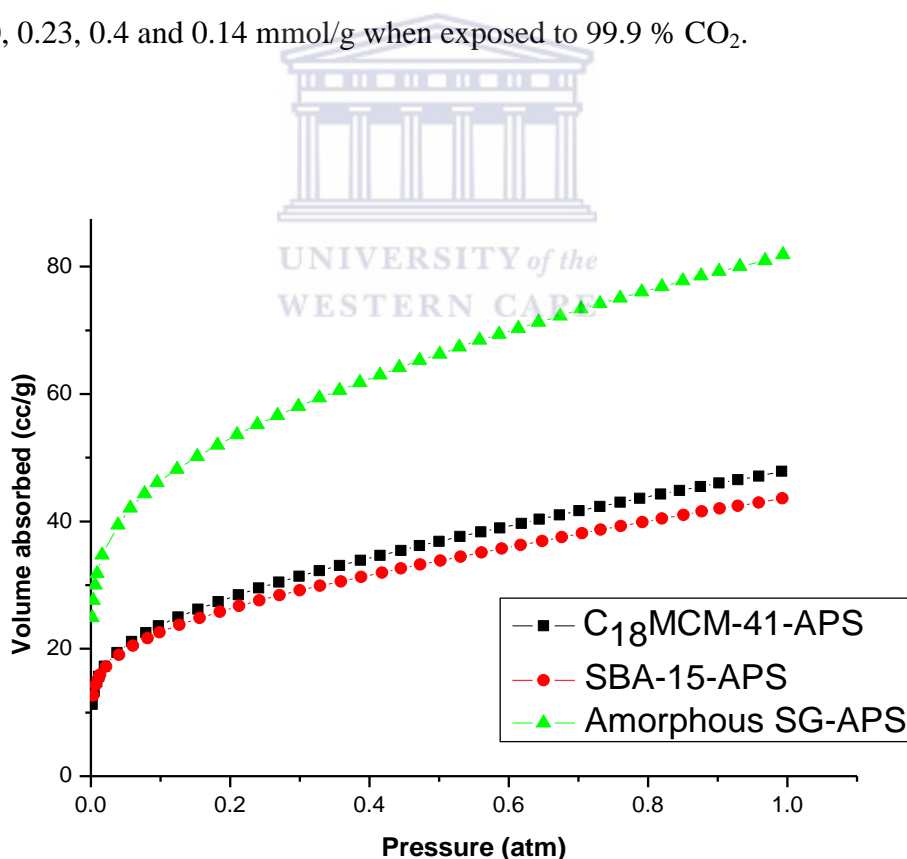


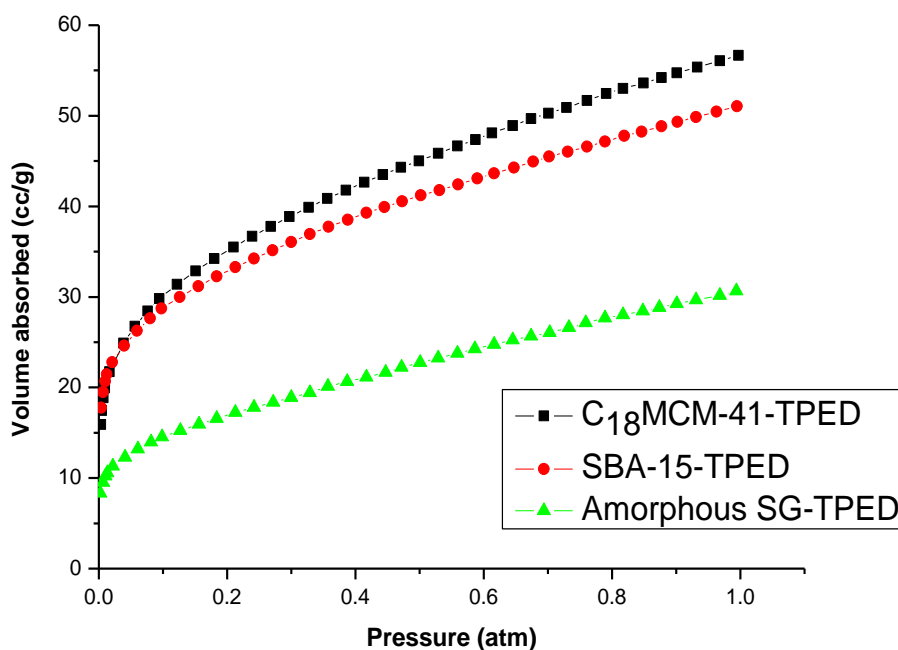
**Figure 26:** CO<sub>2</sub> isotherms of APS and TPED grafted mesoporous silica at 0 °C (99.9 % CO<sub>2</sub>).

Figure 26 shows the CO<sub>2</sub> isotherms of mesoporous silica and APS and TPED grafted mesoporous silica. All the CO<sub>2</sub> isotherms were performed at 0 °C. The shape of the isotherms obtained for APS and TPED grafted C<sub>18</sub>MCM-41, SBA-15 and amorphous

SG was found to be in good agreement with other isotherms reported in literature [24-26]. Steep uptake of CO<sub>2</sub> was observed at low pressure followed by a gradual but steady increase as the pressure increases.

The steep uptake of CO<sub>2</sub> experienced by the organosilane grafted mesoporous silica is caused by the chemical reaction with the amine groups and CO<sub>2</sub> molecules, resulting in chemisorbed CO<sub>2</sub>. CO<sub>2</sub> reacts with two amine groups that form a zwitterion carbamate (CO<sub>2</sub>/amine = 0.5). A further increase beyond the “knee” of the steep uptake region at low pressure, i.e. from 0.1-1 atm was due to physisorbed CO<sub>2</sub>. The amount of CO<sub>2</sub> adsorbed on C<sub>18</sub>MCM-41-APS, C<sub>18</sub>MCM-41-TPED, SBA-15-APS, SBA-15-TPED, amorphous SG-APS and amorphous SG-TPED was 0.14, 0.25, 0.20, 0.23, 0.4 and 0.14 mmol/g when exposed to 99.9 % CO<sub>2</sub>.





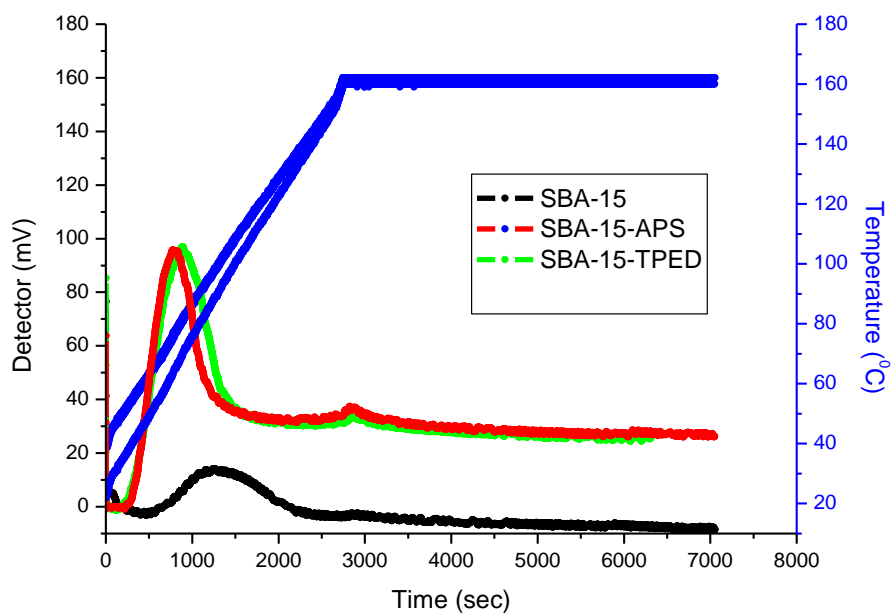
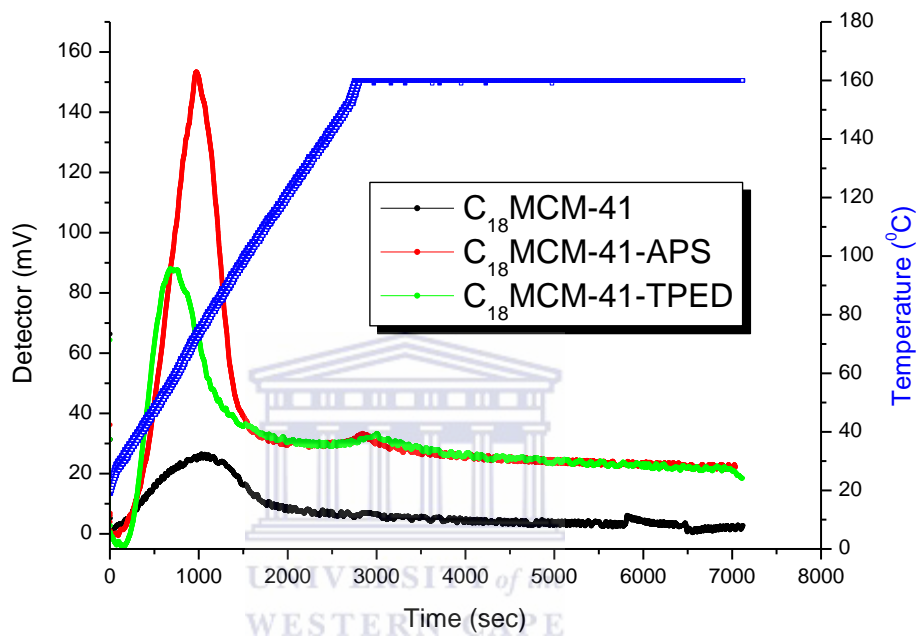
**Figure 27:** CO<sub>2</sub> isotherms of mesoporous silica grafted with APS and TPED at 0 °C.

Figure 27 shows the comparison of CO<sub>2</sub> isotherms of C<sub>18</sub>MCM-41, SBA-15 and amorphous SG grafted with APS and TPED at 0 °C with 99.9 % CO<sub>2</sub>. All the amine grafted supports displayed a steep increase in CO<sub>2</sub> uptake at low pressure, due to chemisorption. The steep increase in CO<sub>2</sub> uptake served as a good indicator as to whether or not the amine moieties were successfully grafted onto the support materials. The difference in CO<sub>2</sub> uptake of the amine grafted supports was apparent at low pressures. The onset capacity was different though, in the sense that C<sub>18</sub>MCM-41-TPED and SBA-15-TPED CO<sub>2</sub> uptake was higher in comparison to C<sub>18</sub>MCM-41-APS and SBA-15-APS. The increase in adsorption was due to more amine groups which chemisorb CO<sub>2</sub> molecules. Amorphous SG covalently grafted with APS had the superior adsorption capacity (0.4 mmol/g) across the entire pressure range of the adsorption experiment (Figure 27). C<sub>18</sub>MCM-41 and SBA-15 grafted with APS and TPED showed similar CO<sub>2</sub> isotherms, and as the pressure increased,



separation of the curves was observed. The separation was possibly caused by structural properties, carbamate formation in the pores and on the surface, causing diffusion limitations etc. In both cases  $C_{18}$ MCM-APS (0.14 mmol/g) and  $C_{18}$ MCM-41-TPED (0.25 mmol/g) showed higher  $CO_2$  uptake at 1 atm.

### 5.8 $CO_2$ -TPD measurements.



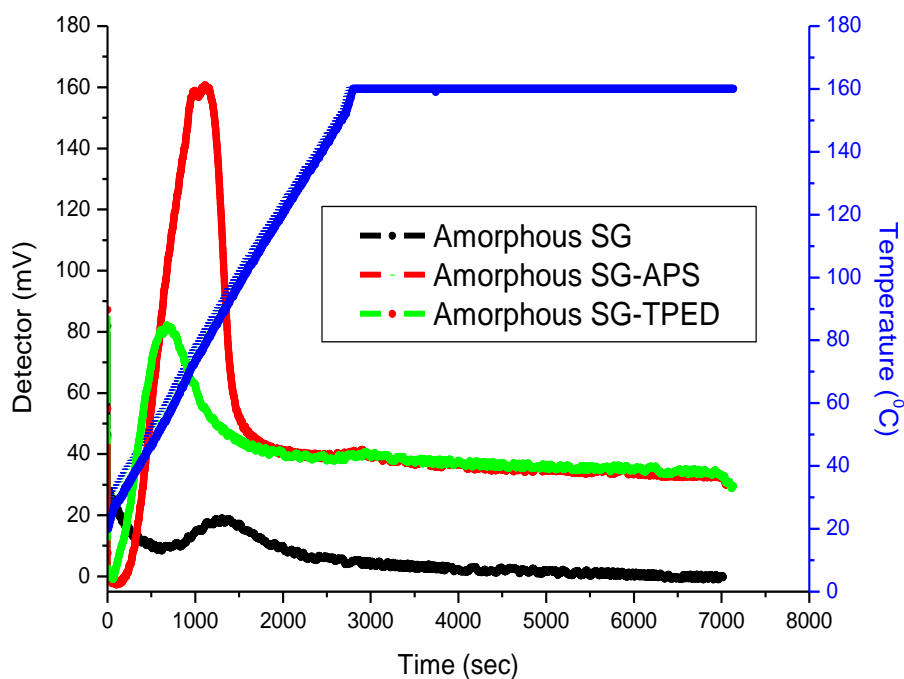


**Figure 28:** CO<sub>2</sub> TPD profiles of APS and TPED grafted sorbents.

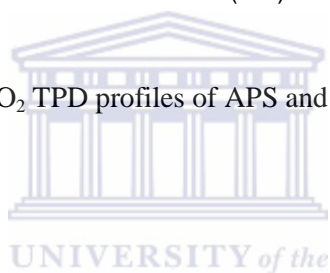


**Table 12:** CO<sub>2</sub> adsorption capacities of APS and TPED grafted sorbents.

Sample	CO <sub>2</sub> capacity (mmol/g)	N content (mmol/g)	N <sub>2</sub> efficiency(CO <sub>2</sub> /N <sub>2</sub> )
C <sub>18</sub> MCM-41	0.11	-	-
C <sub>18</sub> MCM-41-APS	0.5	2.30	0.2
C <sub>18</sub> MCM-41-TPED	0.5	3.07	0.2
SBA-15	0.08	-	-
SBA-15-APS	0.55	2.94	0.1
SBA-15-TPED	0.46	3.14	0.2
Amorphous SG	0.05	-	-
Amorphous SG -APS	0.68	1.8	0.4
Amorphous SG -TPED	0.47	2.58	0.2

Adsorption capacities of chemically grafted sorbents are shown in Table 12. The desorption peaks maxima of APS and TPED grafted sorbents was higher than the parent materials (Figure 28), indicating that the adsorption capacity was enhanced through grafting with amine groups. APS and TPED grafted supports had an additional desorption peak at 160 °C, which was due to chemisorbed CO<sub>2</sub> on the basic sites. Desorption of CO<sub>2</sub> was completed in a temperature range from 60-120 °C, and higher desorption temperatures were observed for APS grafted supports. CO<sub>2</sub>/N efficiency of APS and TPED grafted mesoporous silica are tabulated in Table 12. CO<sub>2</sub>/N ratios were slightly lower than 0.5 with the exception of amorphous SG-APS, which was close to 0.5. The lower efficiency observed is possibly attributed to the loss of porosity due to the grafting step, which may cause inaccessible amine functionalities or it might also give rise to diffusion limitations due to pore blocking [27]. Amorphous SG-APS efficiency was consistent with the carbamate formation under dry conditions, where two neighboring amine groups are required to react with one CO<sub>2</sub> molecule. For this reason amorphous SG-APS have the highest CO<sub>2</sub> adsorption capacity. CO<sub>2</sub> TPD profiles indeed further justify that the amine groups were successfully grafted onto the mesoporous silica used in this study.

In conclusion APS and TPED grafted mesoporous silica were prepared and several characterization proved that amine functionalities was successfully grafted onto C<sub>18</sub>MCM-41, SBA-15 and amorphous SG. The extent of functionalization was determined through the structural characteristics of the support materials, such as surface area, pore size and number of OH groups. The nature of amine groups (primary and secondary amines) gave rise to sorbents having different adsorption capacities. The conclusion drawn from the CO<sub>2</sub> adsorption capacities obtained for

APS and TPED grafted sorbents, showed that amorphous SG-APS had the highest adsorption capacity of all APS and TPED grafted mesoporous silica. The superior adsorption capacity was due to the large pores of silica gel that permits sufficient gas diffusion, as well as the proximity of neighbouring amine groups that are required for carbamate formation. In the case of primary and secondary amines, carbamate formation may inhibit gas diffusion as well as steric hindrances that make some amine groups inaccessible.



**References**

1. Harlick, P.J.E. & Sayari, A. 2007, "Applications of pore-expanded mesoporous silica. 5. triamine grafted material with exceptional CO<sub>2</sub> dynamic and equilibrium adsorption performance", *Industrial and Engineering Chemistry Research*, vol. 46, no. 2, pp. 446-458.
2. Yu, C., Huang, C. & Tan, C. 2012, "A review of CO<sub>2</sub> capture by absorption and adsorption", *Aerosol and Air Quality Research*, vol. 12, no. 5, pp. 745-769.
3. Zhao, H., Ma, Y., Tang, J., Hu, J. & Liu, H. 2011, "Influence of the solvent properties on MCM-41 surface modification of aminosilanes", *Journal of Solution Chemistry*, vol. 40, no. 4, pp. 740-749.
4. Russo, P.A., Carrott, M.M.L.R. & Carrott, P.J.M. 2007, "Effect of hydrothermal treatment on the structure, stability and acidity of Al containing MCM-41 and MCM-48 synthesised at room temperature", *Colloids and Surfaces A: Physicochemical and Engineering Aspects*, vol. 310, no. 1-3, pp. 9-19.
5. Mello, M.R., Phanon, D., Silveira, G.Q., Llewellyn, P.L. & Ronconi, C.M. 2011, "Amine-modified MCM-41 mesoporous silica for carbon dioxide capture", *Microporous and Mesoporous Materials*, vol. 143, no. 1, pp. 174-179.
6. X. Yan, S. Komarneni, Z. Yan. 2013, "CO<sub>2</sub> adsorption on Santa Barbara Amorphous-15 (SBA-15) and amine-modified Santa Barbara Amorphous-15 (SBA-15) with and without controlled microporosity", *Journal of Colloid and Interface Science*, vol.390, no 1, pp. 217-224
7. Maria Chong, A.S. & Zhao, X.S. 2003, "Functionalization of SBA-15 with APTES and Characterization of Functionalized Materials", *Journal of Physical Chemistry B*, vol. 107, no. 46, pp. 12650-12657.
8. Shang, F., Liu, H., Sun, J., Liu, B., Wang, C., Guan, J. & Kan, Q. 2011, "Synthesis, characterization and catalytic application of bifunctional catalyst: Al-MCM-41-NH<sub>2</sub>", *Catalysis Communications*, vol. 12, no. 8, pp. 739-743.

9. Jaroniec, C.P., Kruk, M., Jaroniec, M. & Sayari, A. 1998, "Tailoring surface and structural properties of MCM-41 silicas by bonding organosilanes", *Journal of Physical Chemistry B*, vol. 102, no. 28, pp. 5503-5510.
10. Manzano, M., Aina, V., Areán, C.O., Balas, F., Cauda, V., Colilla, M., Delgado, M.R. & Vallet-Regí, M. 2008, "Studies on MCM-41 mesoporous silica for drug delivery: Effect of particle morphology and amine functionalization", *Chemical Engineering Journal*, vol. 137, no. 1, pp. 30-37.
11. Balas, F., Manzano, M., Horcajada, P. & Vallet-Regí, M. 2006, "Confinement and controlled release of bisphosphonates on ordered mesoporous silica-based materials", *Journal of the American Chemical Society*, vol. 128, no. 25, pp. 8116-8117.
12. Muñoz, B., Rámila, A., Pérez-Pariente, J., Díaz, I. & Vallet-Regí, M. 2003, "MCM-41 organic modification as drug delivery rate regulator", *Chemistry of Materials*, vol. 15, no. 2, pp. 500-503.
13. Huang, C., Klinthong, W. & Tan, C.-. 2013, "SBA-15 grafted with 3-aminopropyl triethoxysilane in supercritical propane for CO<sub>2</sub> capture", *Journal of Supercritical Fluids*, vol. 77, pp. 117-126.
14. Liu, Z., Wu, C., Lee, H. & Liu, S. 2010, "Highly stable amine-modified mesoporous silica materials for efficient CO<sub>2</sub> capture", *Topics in Catalysis*, vol. 53, no. 3-4, pp. 210-217.
15. Knowles, G.P., Graham, J.V., Delaney, S.W. & Chaffee, A.L. 2005, "Aminopropyl-functionalized mesoporous silicas as CO<sub>2</sub> adsorbents", *Fuel Processing Technology*, vol. 86, no. 14-15, pp. 1435-1448.
16. Mahitti, P. Fuangfa. U. 2008, "Preparation and use of chemically modified MCM-41 and silica gel as selective adsorbents for Hg(II) ions", *Hazardous Materials*, vol 154, pp. 578-587.
17. Knowles, G.P., Graham, J.V., Delaney, S.W. & Chaffee, A.L. 2004, "Aminopropyl-functionalised silicas as high capacity CO<sub>2</sub> adsorbents", *ACS National Meeting Book of Abstracts*, pp. FUEL.
18. Klinthong, W., Chao, K. & Tan, C. 2013, "CO<sub>2</sub> capture by as-synthesized amine-functionalized MCM-41 prepared through direct synthesis under basic condition", *Industrial and Engineering Chemistry Research*, vol. 52, no. 29, pp. 9834-9842.

19. Hiyoshi, N., Yogo, K. & Yashima, T. 2005, "Adsorption characteristics of carbon dioxide on organically functionalized SBA-15", *Microporous and Mesoporous Materials*, vol. 84, no. 1-3, pp. 357-365.
20. White, L. D., Tripp, C. P. 2000, "Reaction of (3-Aminopropyl)dimethylethoxysilane with Amine Catalysts on Silica Surfaces", *Journal of Colloid and Interface Science*, vol 232, no.2, pp. 400-407.
21. Vrancken, K.C., Van Der Voort, P., Gillis-D'Hamers, I., Vansant, E.F. & Grobet, P. 1992, "Influence of water in the reaction of  $\gamma$ -aminopropyltriethoxysilane with silica gel. A Fourier-transform infrared and cross-polarisation magic-angle-spinning nuclear magnetic resonance study", *Journal of the Chemical Society, Faraday Transactions*, vol. 88, no. 21, pp. 3197-3200.
22. Okabayashi, H., Shimizu, I., Nishio, E. & O'Connor, C.J. 1997, "Diffuse reflectance infrared Fourier transform spectral study of the interaction of 3-aminopropyltriethoxysilane on silica gel. Behavior of amino groups on the surface", *Colloid and Polymer Science*, vol. 275, no. 8, pp. 744-753.
23. Chiang, C, Ishida, H. & Koenig, J.L. 1980, "The structure of  $\gamma$ -aminopropyltriethoxysilane on glass surfaces", *Journal of colloid and interface science*, vol. 74, no. 2, pp. 396-404.
24. Serna-Guerrero, R., Belmabkhout, Y. & Sayari, A. 2010, "Modeling CO<sub>2</sub> adsorption on amine-functionalized mesoporous silica: 1. A semi-empirical equilibrium model", *Chemical Engineering Journal*, vol. 161, no. 1-2, pp. 173-181.
25. Huang, H.Y., Yang, R.T., Chinn, D. & Munson, C.L. 2003, "Amine-grafted MCM-48 and silica xerogel as superior sorbents for acidic gas removal from natural gas", *Industrial and Engineering Chemistry Research*, vol. 42, no. 12, pp. 2427-2433.
26. Liu, X., Zhou, L., Fu, X., Sun, Y., Su, W. & Zhou, Y. 2007, "Adsorption and regeneration study of the mesoporous adsorbent SBA-15 adapted to the capture/separation of CO<sub>2</sub> and CH<sub>4</sub>", *Chemical Engineering Science*, vol. 62, no. 4, pp. 1101-1110.

27. Serna-Guerrero, R., Da'na, E. & Sayari, A. 2008, "New insights into the interactions of CO<sub>2</sub> with amine-functionalized silica", *Industrial and Engineering Chemistry Research*, vol. 47, no. 23, pp. 9406-9412.



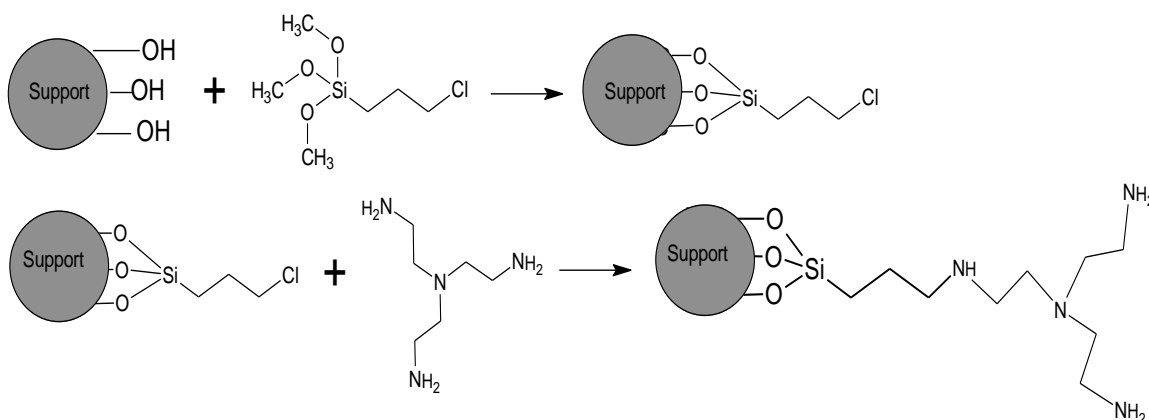


## CHAPTER 6: Supports functionalized with TREN

### 6.1 TREN grafted mesoporous silica

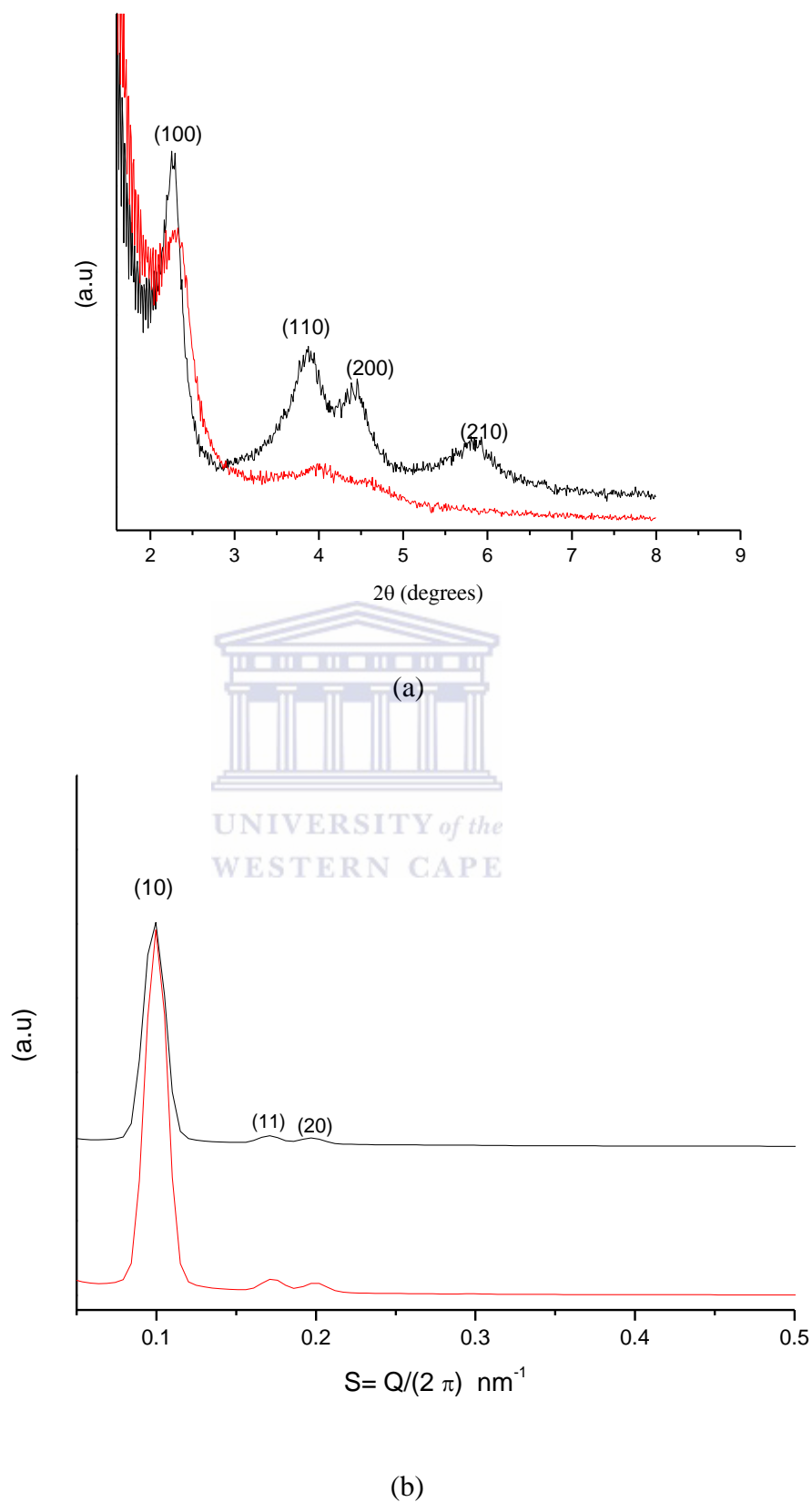
This chapter focuses on the chemical modification of supports with tris(2-aminoethyl) amine (TREN). Immobilization of these amine moieties are achieved through initially grafting a chlorosilane linker onto the surface of the supports.

Scheme 7 shows the synthetic protocol employed to graft TREN onto the mesoporous silica supports. Initially the supports are grafted with CPS. The resultant CPS grafted mesoporous silica have terminal Cl groups on the surface that creates reactive sites for substitution reactions. The  $-Cl$  groups are then displaced with the amine groups, in this case TREN, through a substitution reaction. In doing so terminal amine groups are introduced onto the surface. Terminal amine groups are required for carbamate formation through the reaction of the slightly acidic  $CO_2$  and basic amine groups.



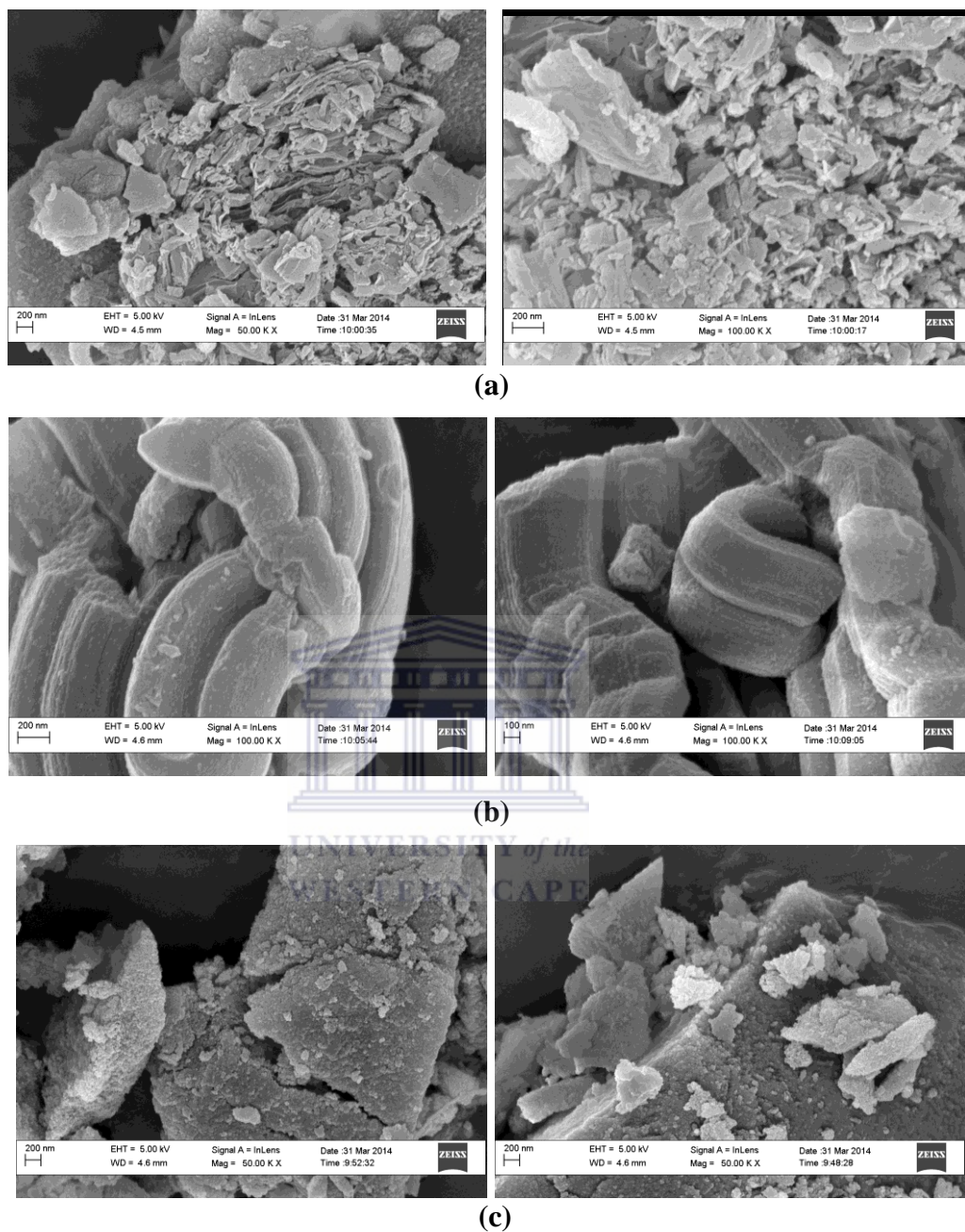
**Scheme 7:** Synthetic protocol for TREN grafted ordered mesoporous silica.

## 6.2 Structural properties of TREN grafted mesoporous silica



**Figure 29:** Powder X-ray diffraction patterns of TREN grafted (a) C<sub>18</sub>MCM-41 and (b) SAXS of TREN grafted SBA-15.

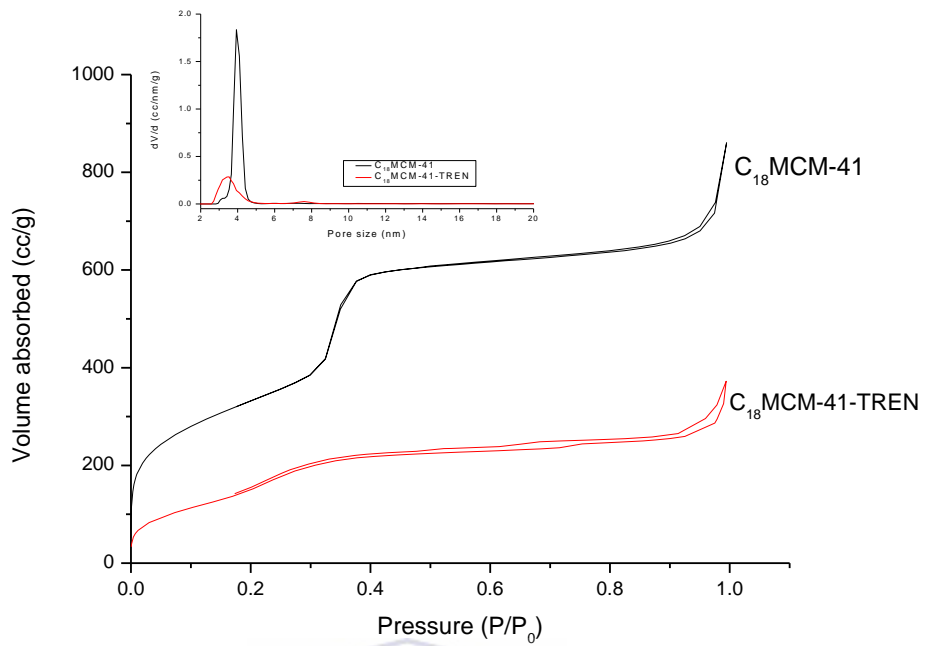
The XRD pattern of C<sub>18</sub>MCM-41 (Figure 29a) displayed a sharp peak at  $2\theta = 2.3^\circ$  and three peaks at  $3.9^\circ$ ,  $4.4^\circ$  and  $5.8^\circ$  that can be assigned to (100), (110), (200) and (210) faces of p6mm structure of C<sub>18</sub>MCM-41 [1-2]. A SAXS pattern of SBA-15 (Figure 29b) showed three resolved peaks at 0.09, 0.17 and  $0.2 \text{ nm}^{-1}$  that can be indexed as (10), (11) and (20) and which are associated with hexagonal symmetry, which is in good agreement with what was reported previously in literature [3-5]. Grafting the supports with TREN reduced the intensity of the higher ordering indices. This was an indication that TREN was incorporated into the siliceous framework. TREN was possibly situated inside the pore wall of the supports after the grafting step. The main peak at (100) shifted to slightly higher  $2\theta$  for C<sub>18</sub>MCM-41. The d-spacing calculated from the (100) and (10) peaks for C<sub>18</sub>MCM-41-TREN and SBA-15-TREN was 2.6 and 10.0 nm respectively. The unit cell parameter for C<sub>18</sub>MCM-41-TREN and SBA-15-TREN was 3.24 and 11.59 respectively. Interplanar spacing for SBA-15 inferred that the regularity of the hexagonal symmetry was maintained in post grafting. The presence of the (100) for C<sub>18</sub>MCM-41-TREN and (10) peak for SBA-15-TREN prove that the structure of the support material was not destroyed during the grafting process.

**6.3 HRSEM images of TREN grafted mesoporous silica**

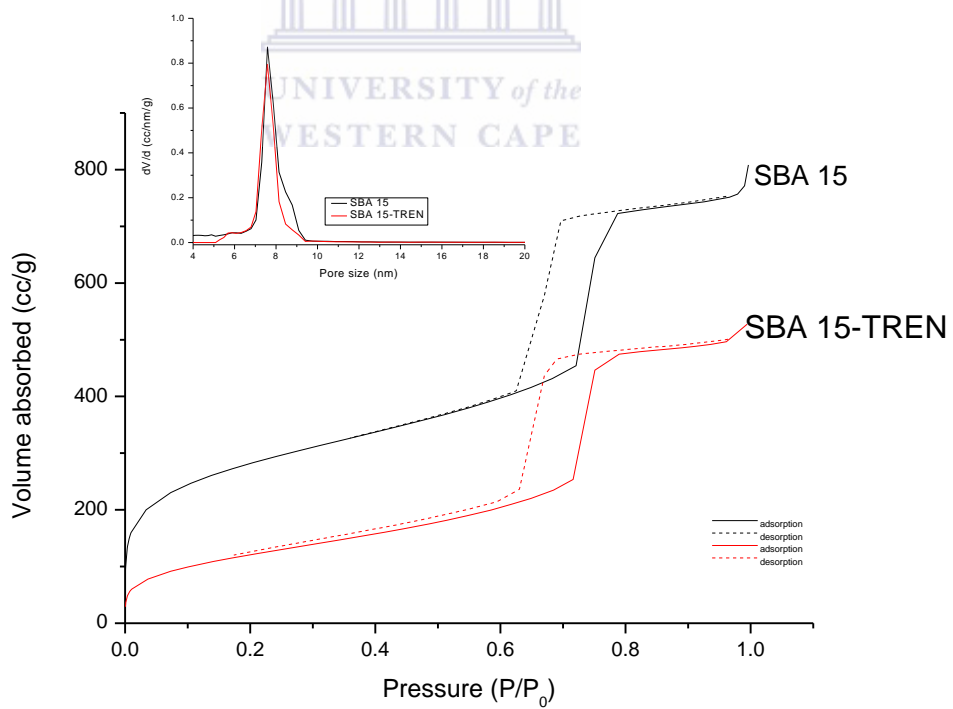
**Figure 30:** HRSEM of (a)  $C_{18}$ MCM-TREN, (b) SBA-15-TREN and (c) amorphous SG-TREN.

The morphology of TREN grafted mesoporous silica were observed using HRSEM. Figure 30 shows the HRSEM of C<sub>18</sub>MCM-41, SBA-15 and amorphous SG post grafting with TREN. Figure 30a shows the morphology of TREN grafted C<sub>18</sub>MCM-41 to be non-spherical, compared to the parent material (Chapter 3 Figure 9). The layers of flake like structures are due to the organic molecules that have been grafted onto C<sub>18</sub>MCM-41. The sizes of the particles were difficult to estimate. The layered material changed the structure of C<sub>18</sub>MCM-41, and this is in good accordance with the powder XRD patterns in Figure 29a. Figure 30b shows that SBA-15-TREN retained its rod like structure post modification. SBA-15-TREN images showed that the organic material was situated on the walls of SBA-15 supports. This was a good indication that TREN was successfully grafted onto SBA-15. Amorphous silica gel surface was also modified post TREN grafting (Figure 30c). Spherical particles that were agglomerated were found to be on the surface of amorphous silica gel. All the above mentioned changes in the morphology of the supports used in this study indicate that TREN was successfully grafted onto the supports.

6.4 Textural properties of TREN grafted mesoporous silica



(a)



(b)

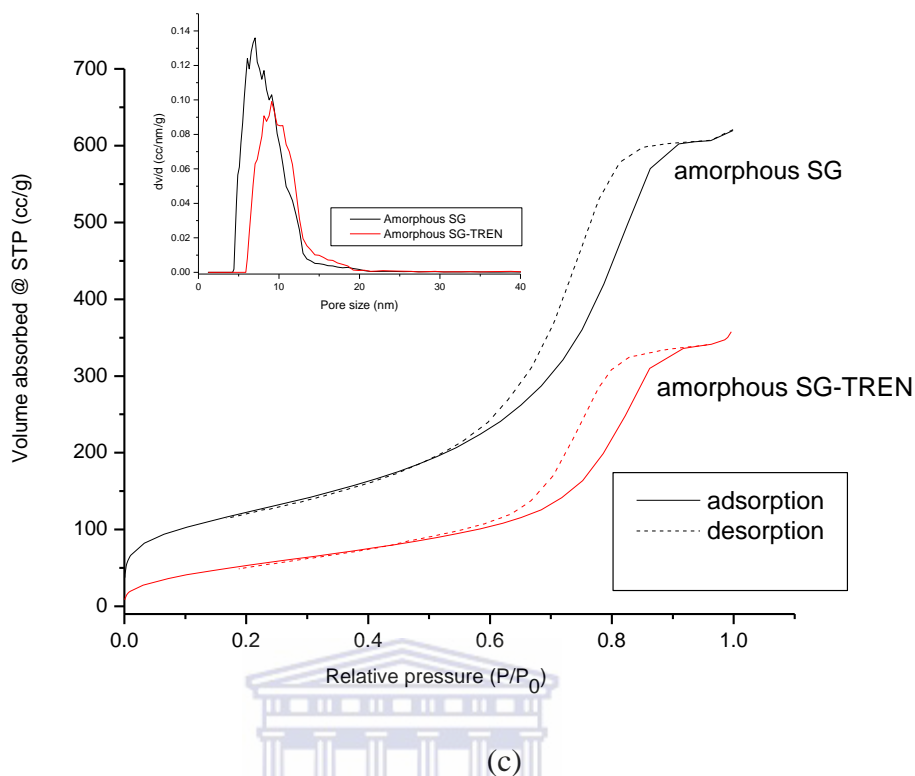


Figure 31: N<sub>2</sub> physisorption isotherms of TREN grafted mesoporous silica.

UNIVERSITY of the  
WESTERN CAPE

Table 13: Textural properties of mesoporous silica grafted with TREN.

Sample	Surface area (m <sup>2</sup> /g)	Pore volume (cc/g)	Pore size (nm)	D spacing (nm)	a <sub>0</sub> (nm)	Wall thickness (nm)	N content (wt %)
C <sub>18</sub> MCM-41	1211	1.3	4.4	2.7	3.3	1.1	-
C <sub>18</sub> MCM-41-TREN	558	0.6	4.1	2.6	3.2	0.9	6.76
SBA-15	1024	1.3	7.6	10.0	11.5	4.0	-
SBA-15-TREN	444	0.8	7.3	10.0	11.6	4.3	4.35
Silica gel	445	0.9	8.6	-	-	-	-
Silica gel-TREN	213	0.6	9	-	-	-	6.91

Figure 31a shows the N<sub>2</sub> physisorption isotherms of TREN grafted C<sub>18</sub>MCM-41. C<sub>18</sub>MCM-41-TREN absorbed less N<sub>2</sub> across the relative pressure range. Capillary condensation of N<sub>2</sub> into the mesopores in the relative pressure range  $P/P_0$  (0.2-0.4) was not as well pronounced compared to the parent material. This indicates that TREN was grafted inside the mesopores of C<sub>18</sub>MCM-41. The hysteresis of the isotherms almost overlay each other indicating homogeneous grafting of the functional group onto C<sub>18</sub>MCM-41. Specific surface area, pore volume and pore size of C<sub>18</sub>MCM-41-TREN are shown in Table 13. More than 50 % of the specific area was used up after grafting C<sub>18</sub>MCM-41 with TREN, accompanied by a reduction in pore volume and pore size of 0.6 cm<sup>3</sup>/g and 4.1 nm respectively. After grafting with TREN the PSD changed. A broad PSD was obtained post grafting, indicating the inhomogeneous pores of C<sub>18</sub>MCM-41 grafted with TREN.

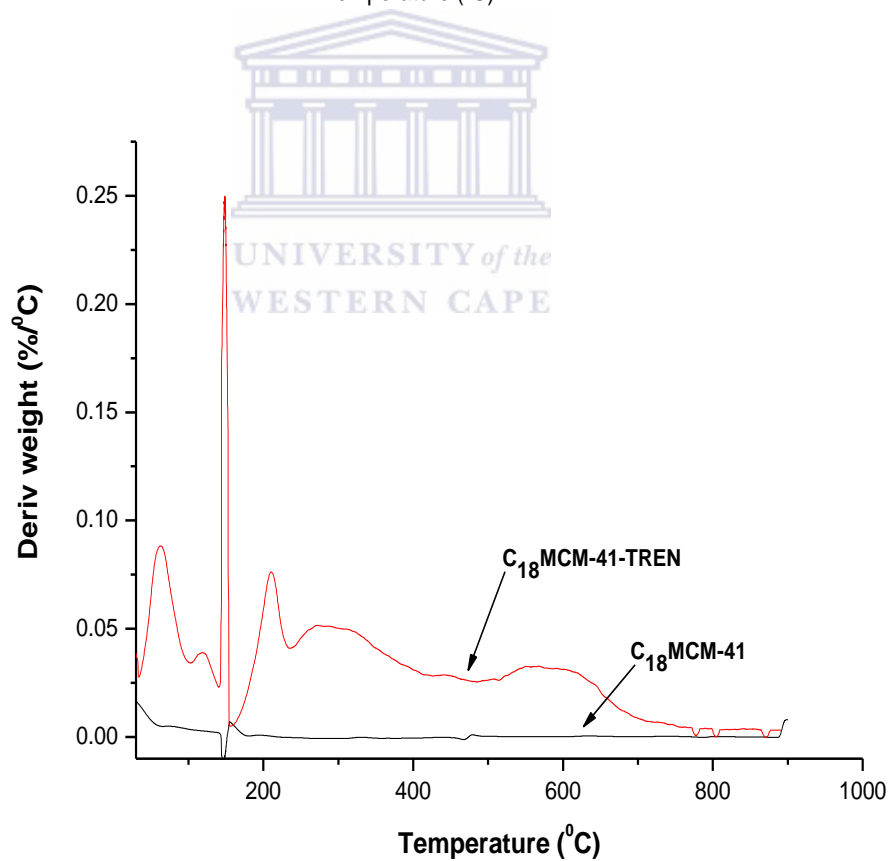
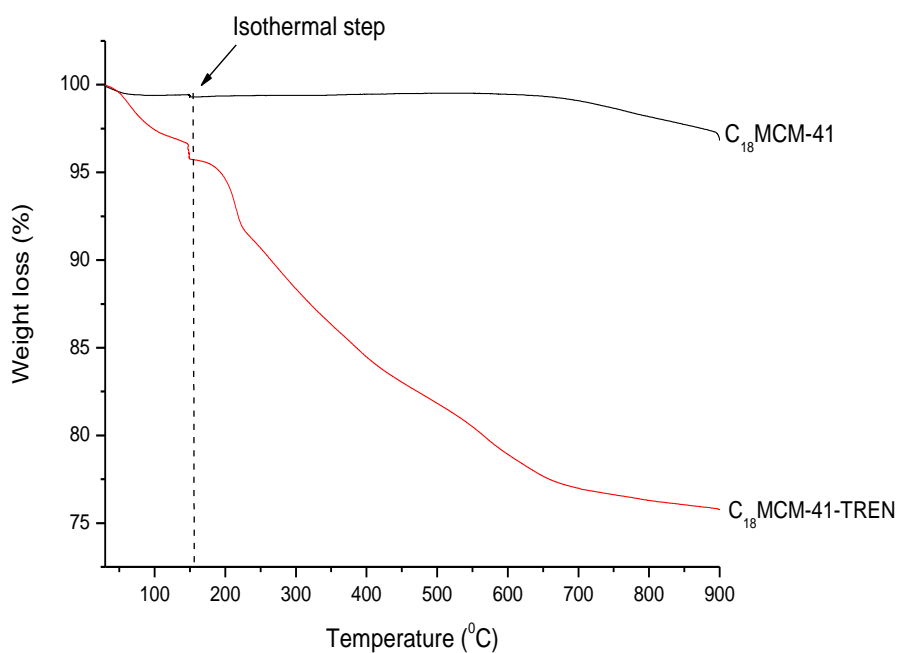
SBA-15 grafted with TREN isotherms are shown in Figure 31 b. SBA-15 as well as TREN and grafted SBA-15 displayed type IV isotherms with a well-defined hysteresis loop. The parallel loops suggest that the structure of the parent and grafted material has ordered mesoporous structure. All the SBA-15 sorbents displayed a steep increase in N<sub>2</sub> uptake in the relative pressure range  $P/P_0$  (0.6-0.75), caused by the condensation of N<sub>2</sub> into the mesopores that is indicative of mesoporous silica materials with large pores. TREN grafted SBA-15 N<sub>2</sub> uptake was less than SBA-15 across the relative pressure range. Nitrogen content obtained for C<sub>18</sub>MCM-41-TREN and SBA-TREN (Table 13) seems to suggest this. The decrease in the amount of N<sub>2</sub> absorbed was due to a decrease in specific surface, accompanied by a reduction in pore volume and pore sizes (Table 13). This was due to the grafting of organic molecules on the surface as well as inside the pore walls of SBA-15, which is in agreement with the SAXS patterns (Figure 29), as the intensity of the patterns



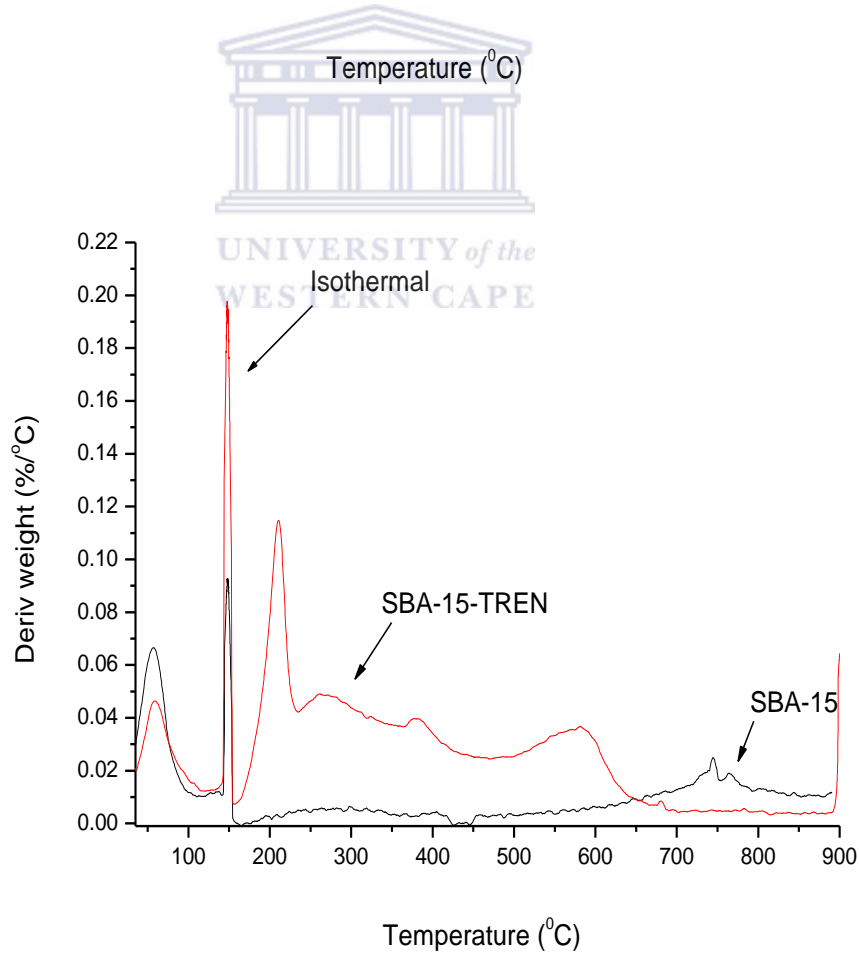
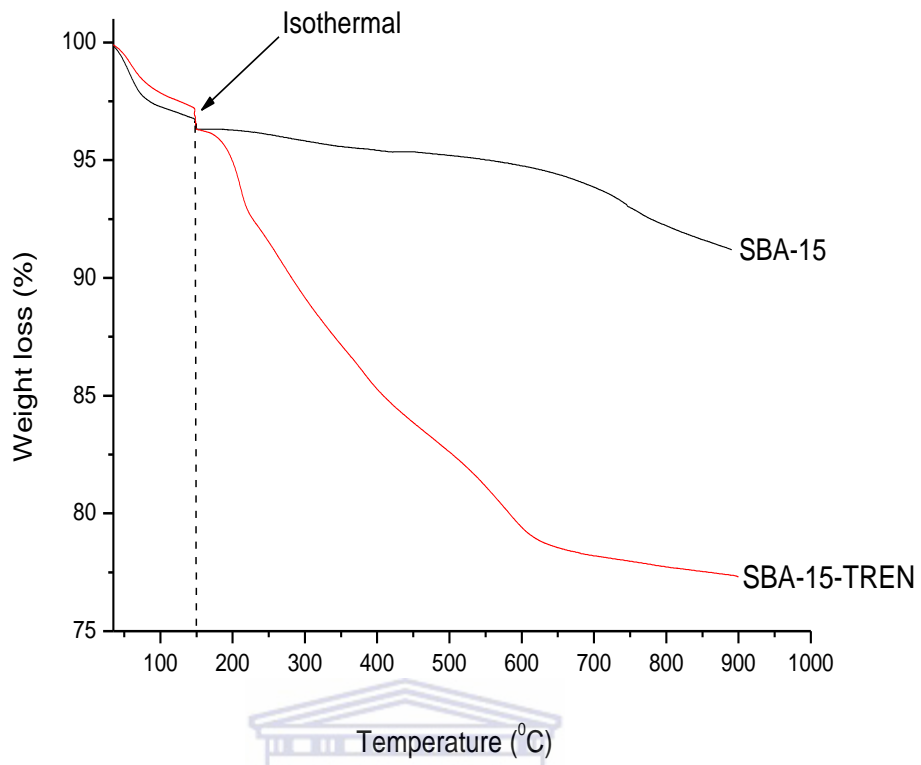
decreased after the grafting step [6-8]. PSD of TREN grafted SBA-15 are shown in Figure 31b. The graph shows a narrow pore size distribution post grafting, with average pore size between 6-10 nm. The narrow pore size distribution obtained was a good indication of even pore filling with the amine moieties. This confirms again that the grafting method is a simple and effective method for anchoring amine functionalities onto the surfaces and inside the pores of mesoporous silica.

Silica gel grafted with TREN (Figure 31c) showed type IV isotherm according to the IUPAC classification with a hysteresis loop. Amorphous SG sorbents showed a sharp increase in the relative pressure range  $P/P_0$  (0.6-0.9). This steep increase is due to the condensation of  $N_2$  into the mesopores, and the relative pressure range in which the condensation occurs, gives an indication of the mesoporosity of amorphous SG materials. The  $N_2$  isotherms of TREN grafted silica gel clearly show that the mesoscopic character was preserved during the grafting process, although it was accompanied with a decrease in surface area, pore volume and pore size (Figure 31c). Silica gel and silica gel- show broad PSD (Figure 31c) that is characteristic of amorphous silica materials, and makes it difficult to observe the effect grafting had on the pore size distribution.

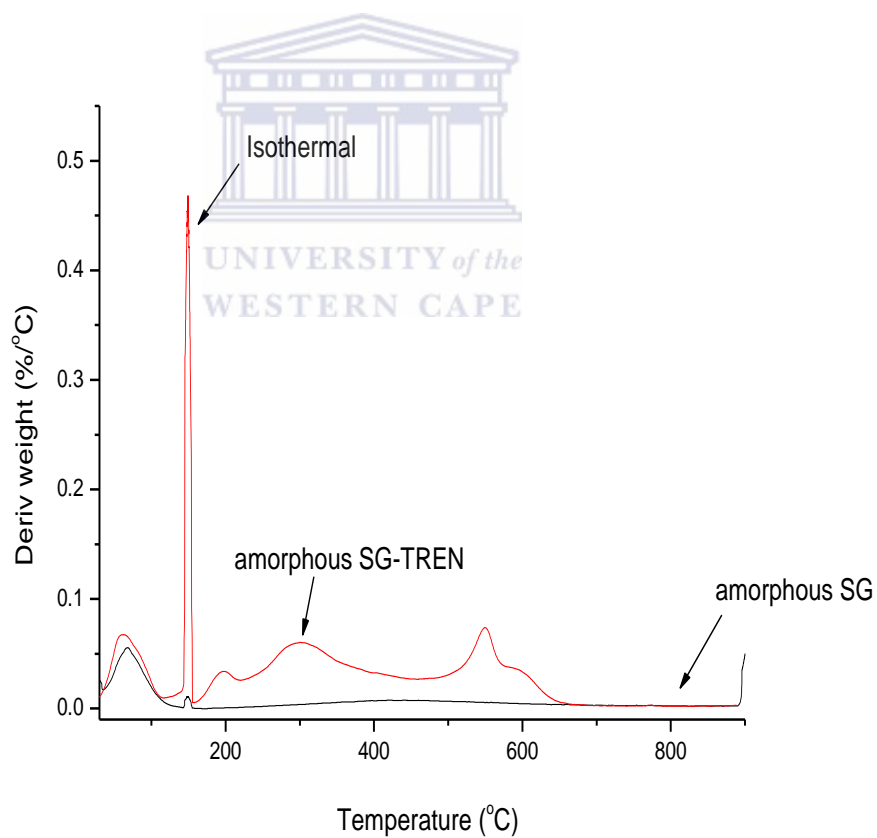
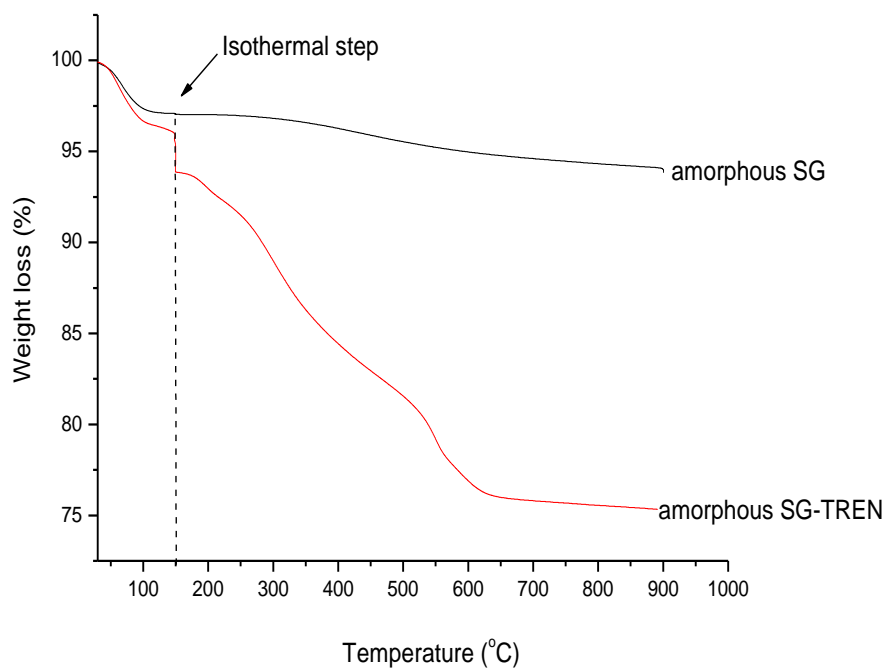
6.6. TG analysis



(a)



(b)



(c)

**Figure 32:** TGA/DTA profiles of TREN grafted mesoporous silica.

**Table 14:** Summary of TG profiles of TREN grafted modified mesoporous

Sample	(% Weight loss)			
	< 150 °C	150-300 °C	300-600 °C	600-900 °C
C <sub>18</sub> MCM-41-TREN	4.0	4.3	8.7	3.0
SBA-15-TREN	3.7	9.6	8.3	2
Amorphous SG –TREN	3.6	4.0	9.5	6.8

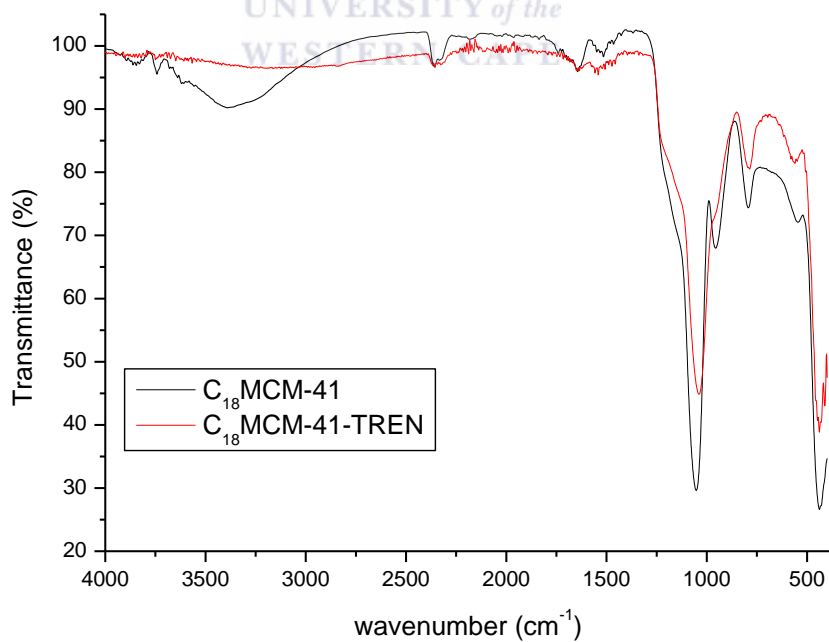
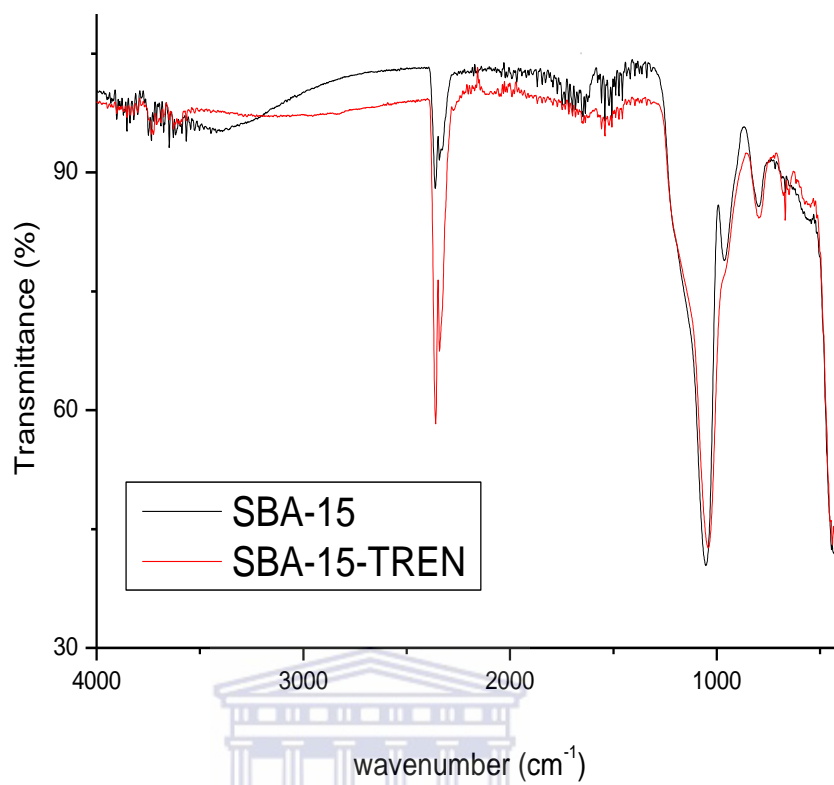
The organic loading of TREN on the mesoporous silica was estimated using TGA/DTA analysis. Figure 32 shows the TGA/DTA profiles of TREN grafted mesoporous silica supports. All of the decomposition profiles displayed weight loss below 150 °C that was due to pre-adsorbed water and some residual solvents (Figure 32). C<sub>18</sub>MCM-41 and SBA-15-TREN (Figure 32a and b) weight loss was more in this region in comparison to the other sorbents, and was due to the hydrophilic nature of the TREN groups. All the TREN grafted materials displayed considerably different TGA/DTA profiles in comparison to the parent materials [9].

C<sub>18</sub>MCM-41-TREN showed weight loss between 250-600 °C, this was attributed to the decomposition of organic moieties on the surface of the C<sub>18</sub>MCM-41. In order to determine the total amount of organic material grafted onto the support, weight loss attributed to the dehydroxylation of the silica framework, as well as water loss, was subtracted from the total weight loss. The weight loss (%) of TREN grafted C<sub>18</sub>MCM-41 is listed in Table 14. DTA profiles of C<sub>18</sub>MCM-41-TREN (Figure 32a) showed a number of peaks attributed to the step-wise decomposition of the organic linker, which was possibly due to the TREN groups, and the subsequent loss of the chloropropyl linker in the range of 200-700 °C. The decompositions profiles also showed that TREN grafted C<sub>18</sub>MCM-41 was stable up to 200 °C.

SBA-15 grafted with TREN displayed a similar decomposition profile (Figure 32b) to that of C<sub>18</sub>MCM-41-TREN. The total organic loading of TREN was estimated to be approximately 18 %. Amorphous silica gel was also grafted with TREN (Figure 32c). The trend in decomposition profiles of amorphous silica gel-TREN was similar to that obtained for SBA-15-TREN, in the sense that the materials underwent similar decomposition steps. Decomposition of amorphous silica gel-TREN displayed weight loss of 13.5 and 7.7 % in the temperature range of 200-600 °C respectively. Further confirmation that TREN was grafted onto amorphous SG was shown in the DTA profiles as numerous peaks were observed. This was attributed the stepwise decomposition of organic material.



## 6.7 FT-IR



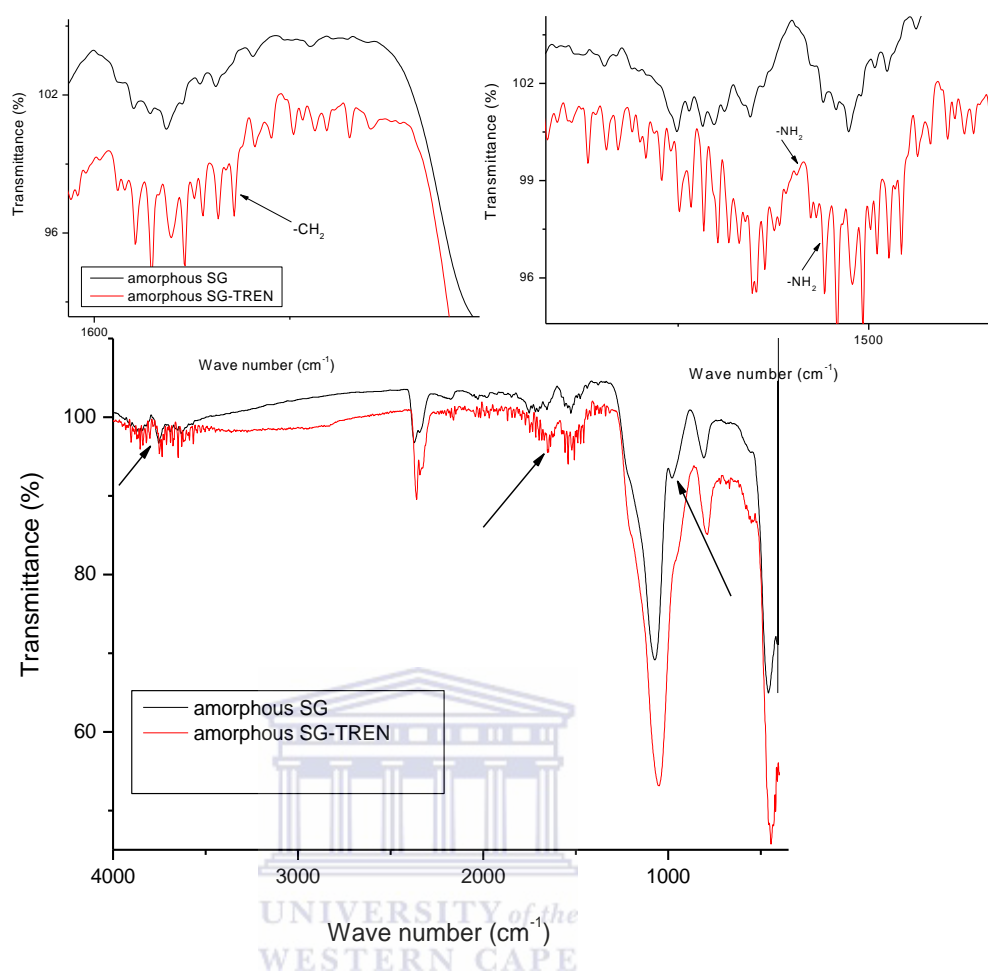


**Figure 33:** FT-IR spectra of TREN grafted mesoporous silica.

FT-IR was used to validate whether or not TREN was chemically bonded to the mesoporous supports used in this study. The parent materials displayed characteristic bands attributed to siliceous materials.  $C_{18}MCM-41$ , SBA-15 and amorphous SG displayed a strong absorption band at 1052, 1053 and 1072  $cm^{-1}$  which is due to the asymmetric stretching of Si-O-Si bonds (Figure 33). Absorption bands at 956, 963 and 979  $cm^{-1}$  correspond to the bending of Si-OH groups on  $C_{18}MCM-41$ , SBA-15 and amorphous SG respectively. Deformation of Si-O-Si stretching was also visible

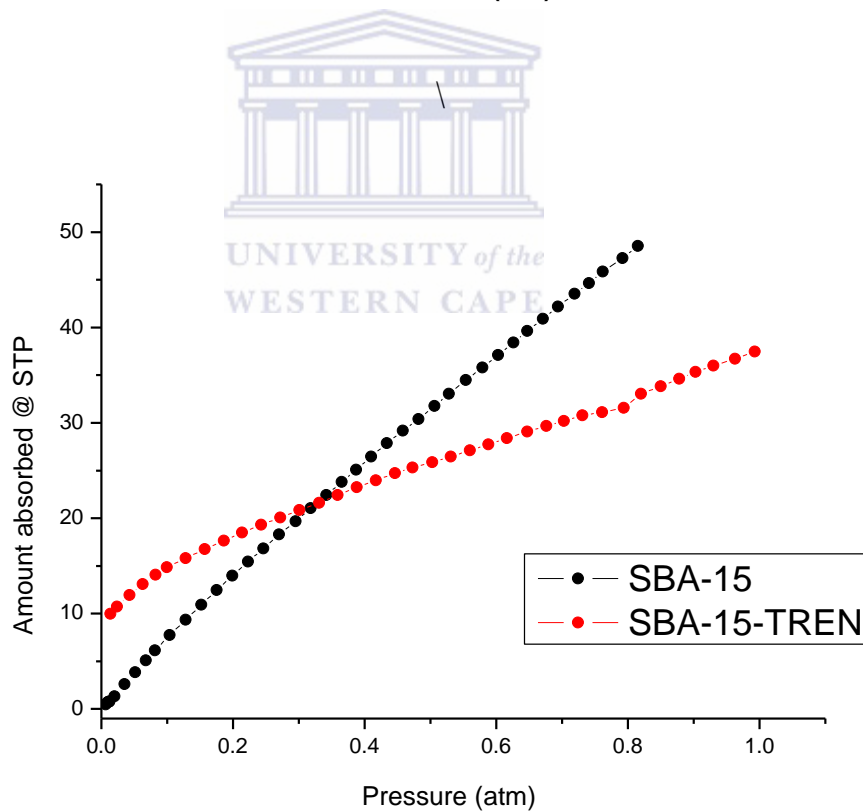
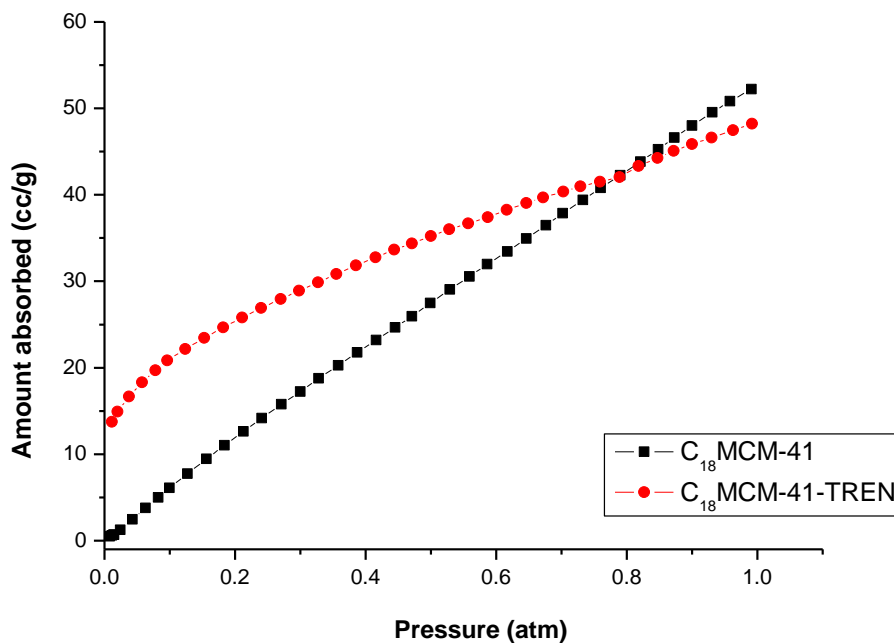


at 439, 446 and 458  $\text{cm}^{-1}$  for  $\text{C}_{18}\text{MCM-41}$ , SBA-15 and amorphous SG respectively [6].

Upon grafting the FT-IR spectra of TREN, the modified mesoporous silica materials changed (Figure 33). The intensity of the Si–OH band decreased, indicating that some of the surface silanol groups were used up during the grafting step. The band at 1457  $\text{cm}^{-1}$  for amorphous SG-TREN can be assigned to the  $-\text{CH}_2$  bending vibration. The appearance of this band confirms that the methylene groups of the aliphatic chain were anchored on the supports surface. A weak  $-\text{CH}$  bending frequency of ethyl chain in TREN was observed at 761  $\text{cm}^{-1}$  for amorphous SG-TREN (Figure 33 inset). The C-N stretching frequency of TREN is found approximately at 1050  $\text{cm}^{-1}$ , but was not visible due to the overlapping of Si-O-Si bands in this region. Amorphous SG-TREN showed bands at 1592 and 1558  $\text{cm}^{-1}$  - this could be attributed to the asymmetric and symmetric bending of primary amines, respectively. All of the aforementioned appearance of new absorbance bands post grafting proves that TREN was successfully grafted onto amorphous SG as well as  $\text{C}_{18}\text{MCM-41}$  and SBA-15 as similar absorbance bands were obtained [10].

All of the above mentioned absorbance peaks as well as XRD, SAXS and textural properties confirms that TREN was grafted on mesoporous silica used in the study.

6.8 CO<sub>2</sub> isotherm studies



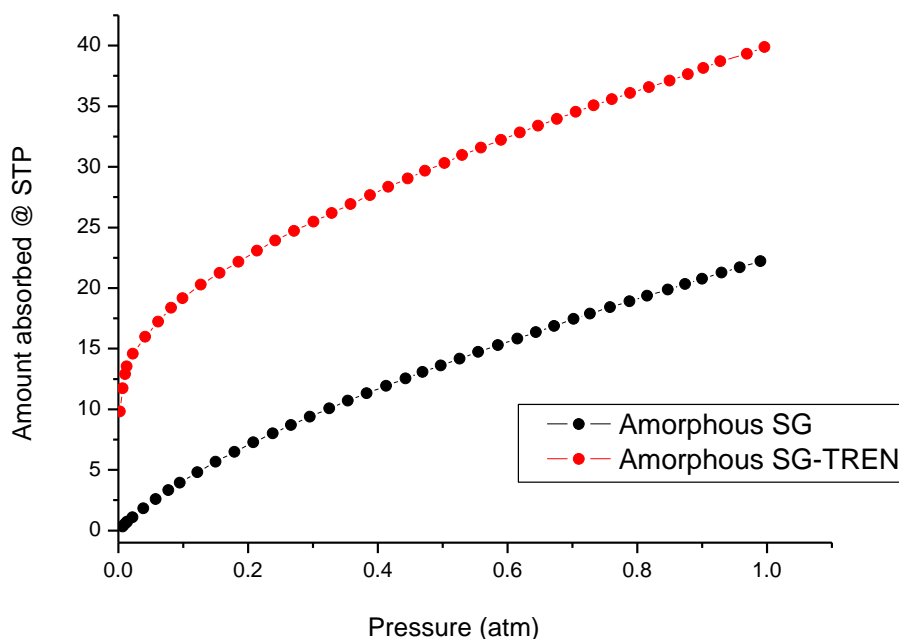
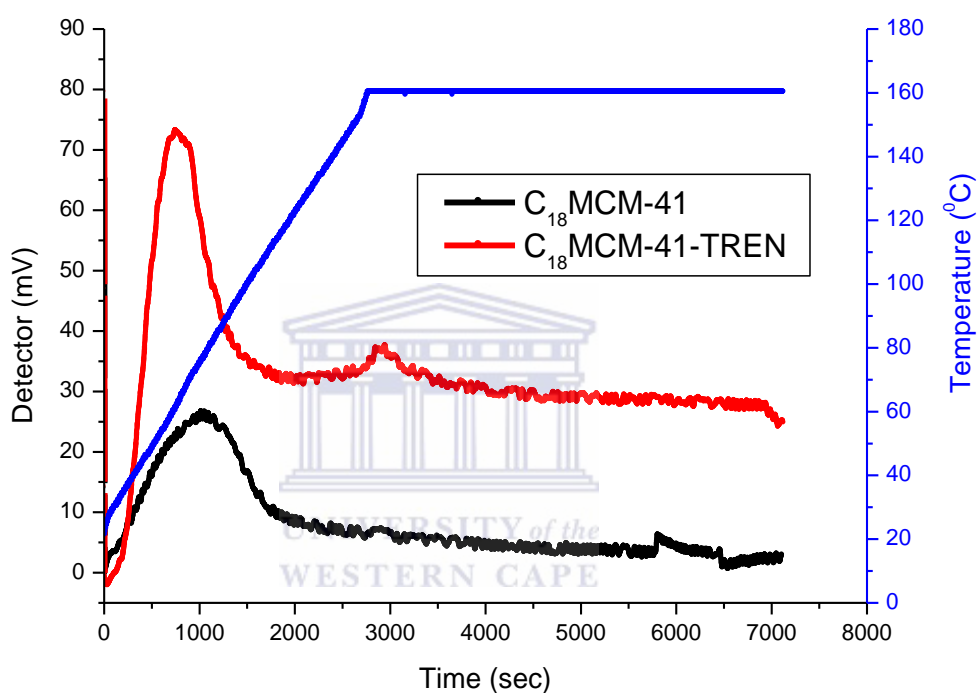


**Figure 34:** CO<sub>2</sub> isotherms of TREN and guanidine grafted mesoporous silica.

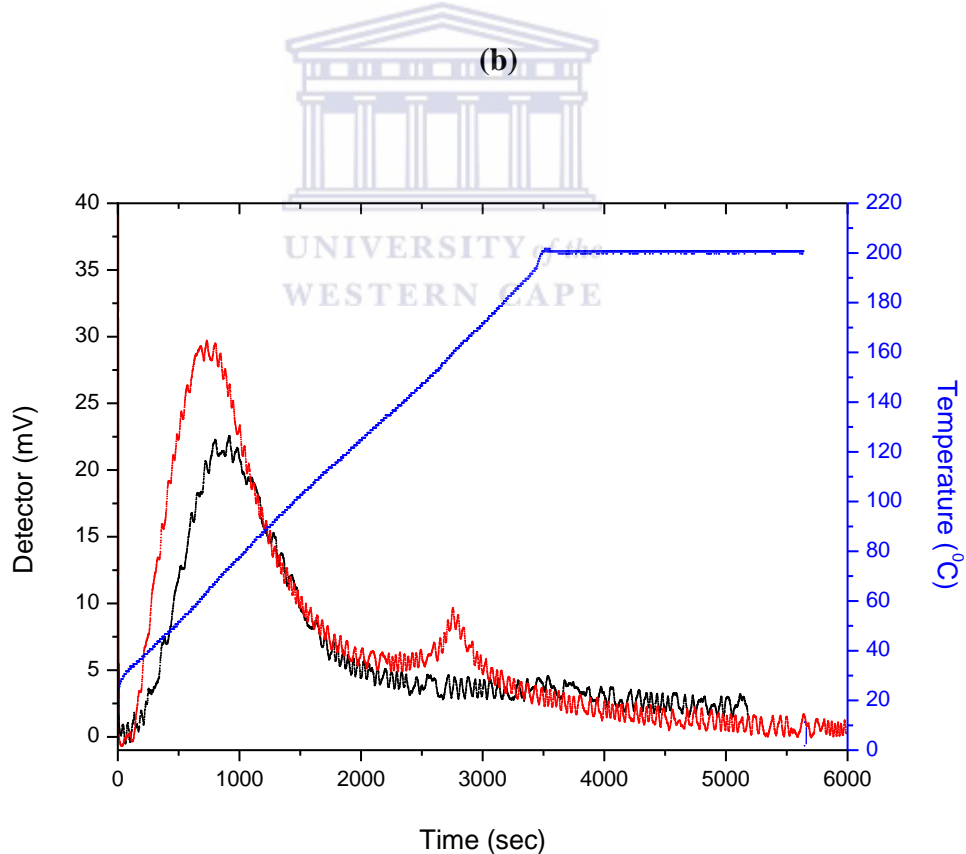
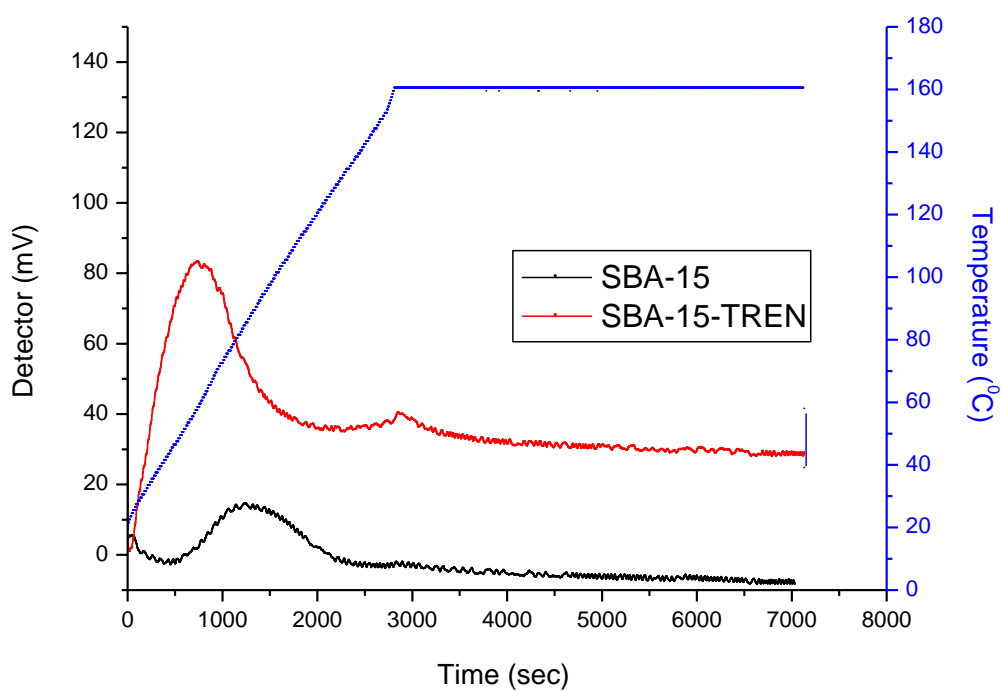
The CO<sub>2</sub> isotherms of parent materials, and TREN grafted mesoporous silica, showed considerable differences (Figure 34). All TREN grafted supports showed a steep increase in CO<sub>2</sub> uptake below 0.1 atm. The enhanced CO<sub>2</sub> capacity at low pressure may be attributed to chemisorbed CO<sub>2</sub> due to the amine moieties grafted on mesoporous silica supports. The strong interaction between CO<sub>2</sub> and an increased number of adsorption sites of TREN was noted to be the driving force for the change in CO<sub>2</sub> uptake. The absorption capacity of 1.0 atm for C<sub>18</sub>MCM-41, SBA-15-TREN and amorphous silica gel was 0.22, 0.17 and 0.18 mmol/g measured at 0 °C. Initially chemisorption is prominent and as the pressure is increased, physisorption takes precedence. The absorption capacity at higher pressure is thus dependent on the available surface area and porosity, which may explain the absorption capacities obtained for TREN grafted supports. A fair comparison of adsorption capacity would ideally be in the region where both contribution of chemisorbed and physisorbed

CO<sub>2</sub> would be prevalent. Interestingly amorphous SG-TREN absorption capacity was superior to the parent material across the entire pressure range. This is likely due to the large pores that facilitate gas diffusion. Even after carbamate formation, sufficient absorption sites were still available through diffusion into the silica matrix of amorphous SG.

### 6.9 CO<sub>2</sub> TPD



(a)



(c)

**Figure 35:** CO<sub>2</sub> TPD profiles of (a) C<sub>18</sub>MCM-41 TREN, (b) SBA-15-TREN and (c) AM SG-TREN.

**Table 15:** CO<sub>2</sub> adsorption capacities of TREN and guanidine grafted mesoporous silica.

Sample	CO <sub>2</sub> capacity (mmol/g)	N content (mmol/g)	N <sub>2</sub> efficiency(CO <sub>2</sub> /N <sub>2</sub> )
C <sub>18</sub> MCM-41-TREN	0.42	3.60	0.11
SBA-15-TREN	0.51	3.11	0.16
Amorphous SG-TREN	0.27	4.94	0.10

Figure 35 shows the CO<sub>2</sub> TPD profiles of TREN grafted mesoporous silica. TPD profiles of TREN grafted supports desorbed more CO<sub>2</sub>, proving that grafting mesoporous silica with amine groups enhances the CO<sub>2</sub> uptake. Desorption peaks observed for grafted supports show a peak maxima in the range of 500- 2000 sec, which is due to physisorbed and loosely adsorbed CO<sub>2</sub> molecules. Additional small peaks (Figure 35a, b and c) were observed at temperatures higher than 100 °C, which may possibly be due to chemisorbed CO<sub>2</sub>. The adsorption capacities were obtained through integrating the area under the desorption curves as tabulated in Table 15. TREN grafted supports showed superior capacity in comparison to the parent and guanidine grafted sorbents. The enhanced adsorption may be attributed to the high surface area of supports as well as the number of amine groups available on the surface and inside the pores providing sufficiently more adsorption sites. This was confirmed previously in the textural and thermogravimetric properties of the grafted materials.

In conclusion MCM-41 with larger pore size (C<sub>18</sub>MCM-41), SBA-15 and amorphous SG was grafted with TREN. TREN grafted onto the supports proved to increase the adsorption capacity of the sorbents, which was evident in the sorption studies performed. Amine groups (terminal) increase the adsorption capacity; hence the increased number of amine groups increases the adsorption capacity.

**Reference:**

1. Kamarudin, K.S.N., Alias. N., 2013, "Adsorption performance of MCM-41 impregnated with amine for CO<sub>2</sub> removal", *Fuel Processing Technology*, vol. 106, pp. 332-337.
2. Beck, J.S., Vartuli, J.C., Roth, W.J., Leonowicz, M.E., Kresge, C.T., Schmitt, K.D., Chu, C.T., Olson, D.H., Sheppard, E.W., McCullen, S.B., Higgins, J.B. & Schlenker, J.L. 1992, "A new family of mesoporous molecular sieves prepared with liquid crystal templates", *Journal of the American Chemical Society*, vol. 114, no. 27, pp. 10834-10843.
3. Wang, L. & Yang, R.T. 2011, "Increasing selective CO<sub>2</sub> adsorption on amine-grafted SBA-15 by increasing silanol density", *Journal of Physical Chemistry C*, vol. 115, no. 43, pp. 21264-21272.
4. Zhao, D., Feng, J., Huo, Q., Melosh, N., Fredrickson, G.H., Chmelka, B.F. & Stucky, G.D. 1998, "Triblock copolymer syntheses of mesoporous silica with periodic 50 to 300 angstrom pores", *Science*, vol. 279, no. 5350, pp. 548-552.
5. Kruk, M., Jaroniec, M., Ko, C.H. & Ryoo, R. 2000, "Characterization of the porous structure of SBA-15", *Chemistry of Materials*, vol. 12, no. 7, pp. 1961-1968.
6. Bhagiyalakshmi, M., Park, S.D., Cha, W.S. & Jang, H.T. 2010, "Development of TREN dendrimers over mesoporous SBA-15 for CO<sub>2</sub> adsorption", *Applied Surface Science*, vol. 256, no. 22, pp. 6660-6666.
7. Kumar, P., Kim, S., Ida, J. & Gulians, V.V. 2008, "Polyethyleneimine-modified MCM-48 membranes: Effect of water vapor and feed concentration on N<sub>2</sub>/CO<sub>2</sub> selectivity", *Industrial and Engineering Chemistry Research*, vol. 47, no. 1, pp. 201-208.
8. Xu, X., Song, C., Andrésen, J.M., Miller, B.G. & Scaroni, A.W. 2003, "Preparation and characterization of novel CO<sub>2</sub> "molecular basket" adsorbents based on polymer-modified mesoporous molecular sieve MCM-41", *Microporous and Mesoporous Materials*, vol. 62, no. 1-2, pp. 29-45.
9. Shahbazi, A., Younesi, H. & Badiei, A. 2014, "Functionalized nanostructured silica by tetradentate-amine chelating ligand as efficient heavy metals adsorbent: Applications to industrial effluent treatment", *Korean Journal of Chemical Engineering*, vol. 175, no. 1, pp. 928-938.

10. Bhagiyalakshmi, M., Yun, L.J., Anuradha, R. & Jang, H.T. 2010, "Utilization of rice husk ash as silica source for the synthesis of mesoporous silicas and their application to CO<sub>2</sub> adsorption through TREN/TEPA grafting", *Journal of hazardous materials*, vol. 175, no. 1-3, pp. 928-938.

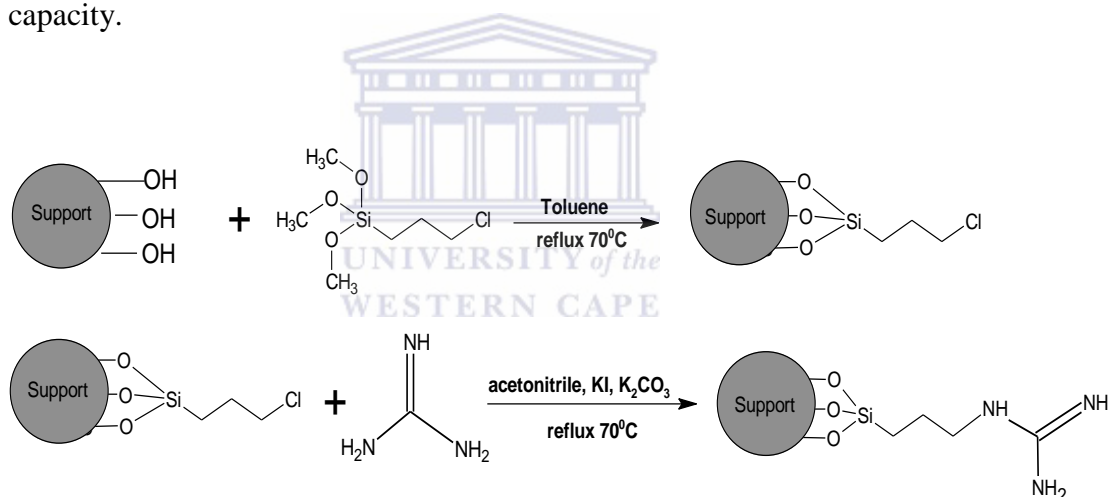




## CHAPTER 7: Systematic study of guanidine grafted MCM-41

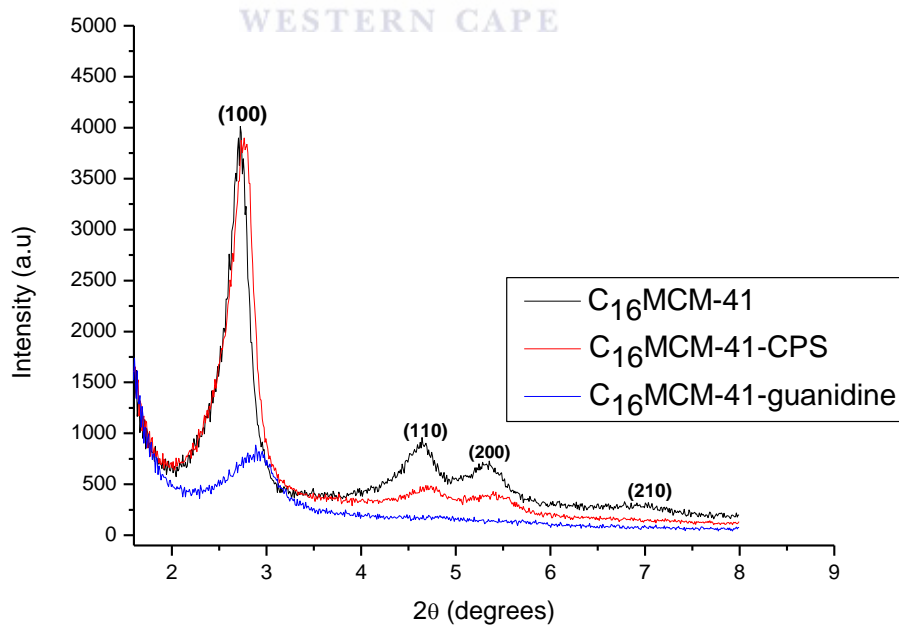
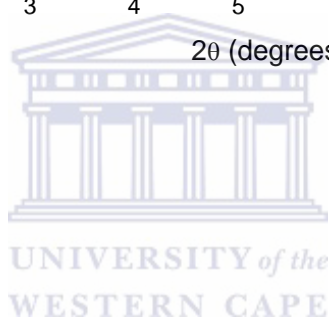
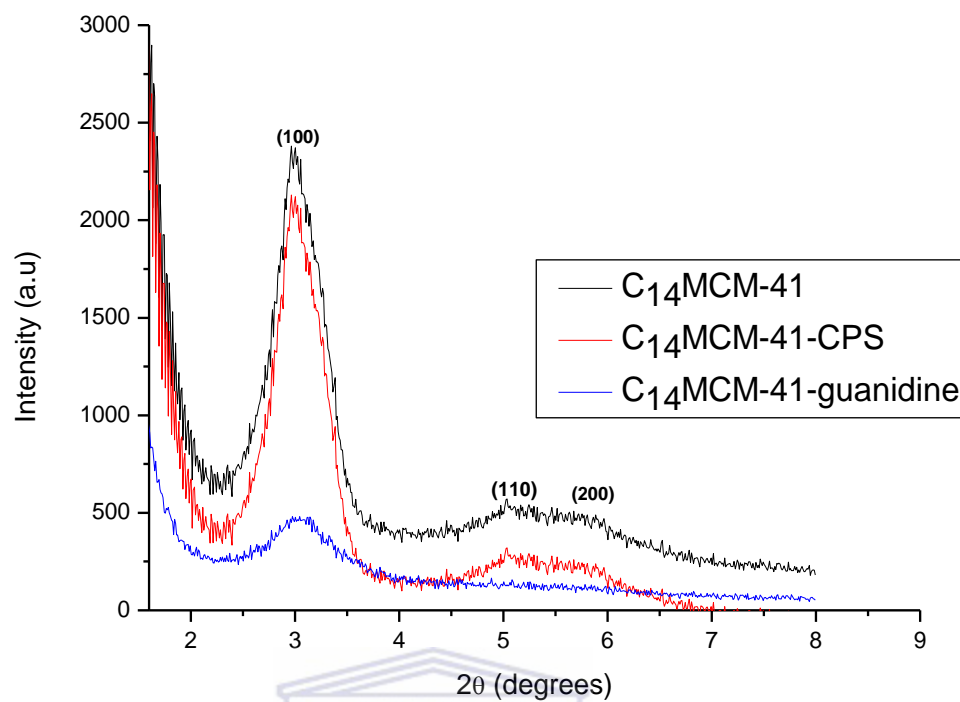
### 7.1 Systematic study of guanidine grafted MCM-41 with different pore sizes

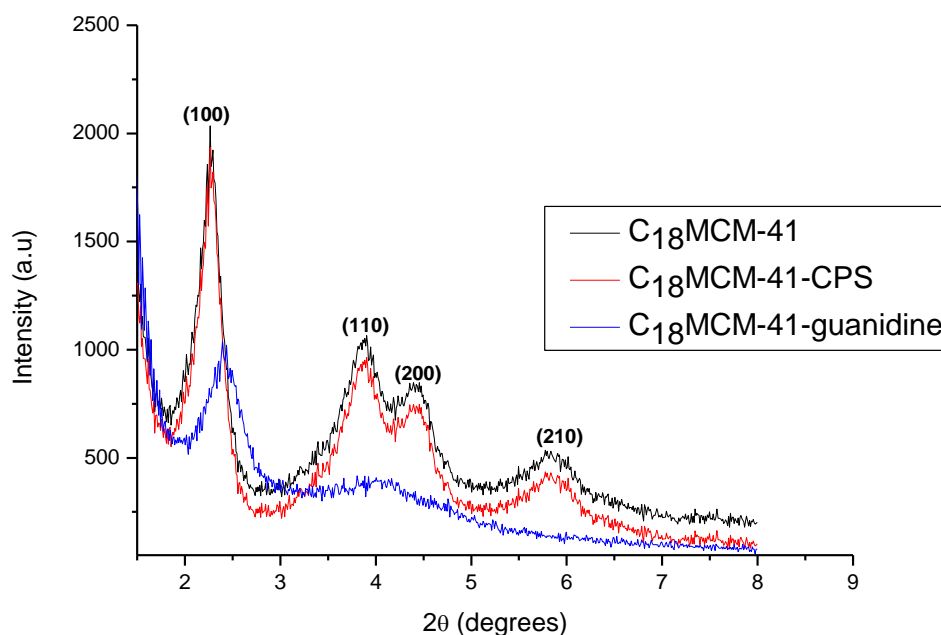
In this chapter a systematic study of guanidine grafted MCM-41 materials that was prepared with surfactant with varying chain lengths (Chapter 1) was undertaken. Guanidine has been chosen as an amine moiety that may be grafted onto MCM-41 materials due to its basic character. Guanidine is also bio-degradable that makes it ideal amine functionality and promotes the concept of “green chemistry”. In essence the aim of this study was to investigate the effect of variation in pore size coupled to guanidine grafted onto MCM-41 materials would have on the CO<sub>2</sub> adsorption capacity.



**Scheme 8:** Synthetic route to guanidine grafted MCM-41 supports.

## 7.2 Systematic XRD study

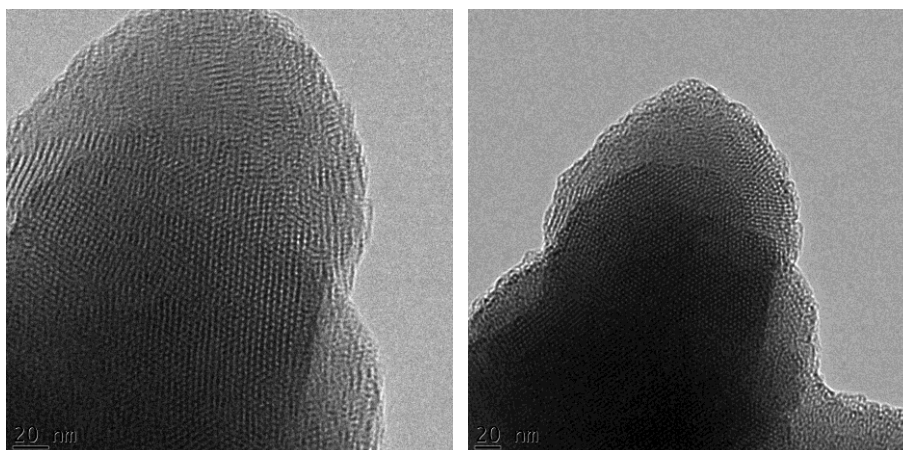




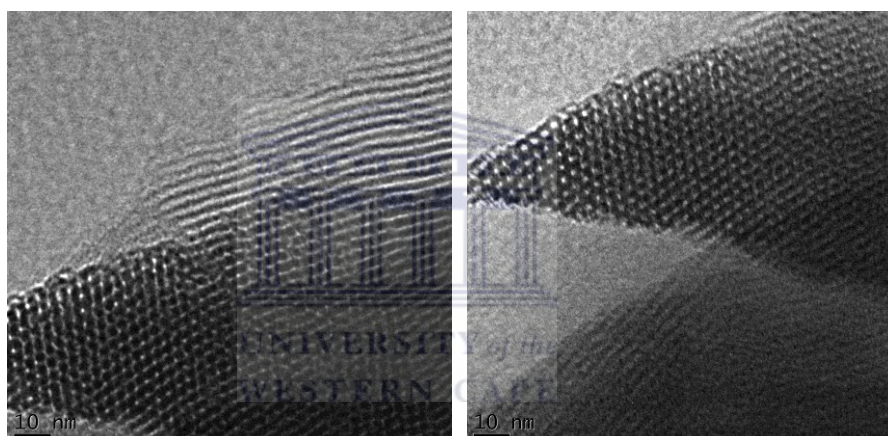
**Figure 36:** Powder X-ray diffractions guanidine grafted MCM-41.

Calcined  $C_{16}$ MCM-41 and  $C_{18}$ MCM-41 exhibited four peaks (Figure 36) that can be indexed to a two dimensional hexagonal lattice, indicating a good degree of structural ordering [1].  $C_{14}$ MCM-41 displayed three peaks, two of which were not that well resolved, indicating that not a high degree of ordering (Figure 36) was obtained. Previously it has been reported that shorter surfactant chain lengths experience difficulty in self-organization, resulting in less ordering compared to  $C_{16}$  and  $C_{18}$  [2]. Nevertheless it has been documented that silica based sorbents for  $CO_2$  adsorption does not necessarily need long range ordering [3-5]. The d-spacing of  $C_{14}$ MCM-41,  $C_{16}$ MCM-41 and  $C_{18}$ MCM-41 was 2.8, 3.2 and 4.2 nm respectively. The d-spacing increased with increasing surfactant chain length. XRD patterns after functionalization with CPS (Figure 36) showed that the long range ordering of MCM-41 materials was preserved. A slight decrease in the intensity of the diffraction

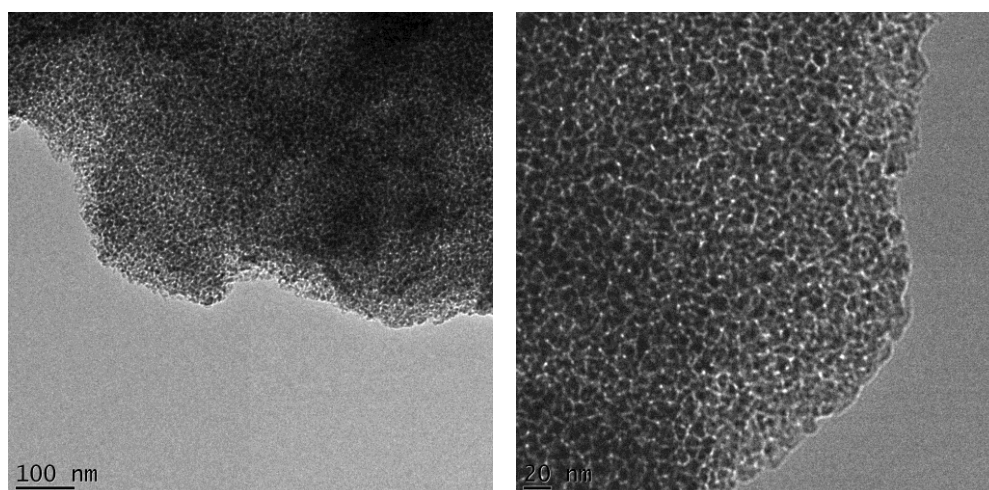
patterns was observed [6]. The width of the main (100) peaks of C<sub>14</sub>MCM-41-CPS and C<sub>18</sub>MCM-41-CPS narrowed, which seem to indicate a homogeneous pore structure after the functionalization with CPS. The d-spacing of C<sub>14</sub>MCM-41-CPS, C<sub>16</sub>MCM-41-CPS and C<sub>18</sub>MCM-41-CPS was comparable to the parent materials, with the exception of C<sub>16</sub>MCM-41-CPS that displayed a slight shift to higher 2 $\theta$  having a d-spacing of 2.2 nm. Upon functionalization with guanidine the long range orderings peaks intensity decreased substantially (Figure 36). The intensity of the main (100) was also reduced but the presence of the peak indicated that the structure was not completely destroyed during the functionalization step. A shift in 2 $\theta$  for the main (100) peak was observed for C<sub>16</sub>MCM-41-guanidine and C<sub>18</sub>MCM-41-guanidine, but not in C<sub>14</sub>MCM-41-guanidine. It is known that organic residual present in MCM-41 materials occlude inside the pores and have a significant impact on the intensity and possibly a shift in the (100) peak observed for C<sub>16</sub>MCM-41-guanidine and C<sub>18</sub>MCM-41-guanidine (Figure 36) [7]. The d-spacing of C<sub>14</sub>MCM-41-guanidine, C<sub>16</sub>MCM-41-guanidine and C<sub>18</sub>MCM-41-guanidine was 2.0, 2.1 and 2.5 nm respectively.

**7.3 HRSTEM and HRSEM images**

(a)

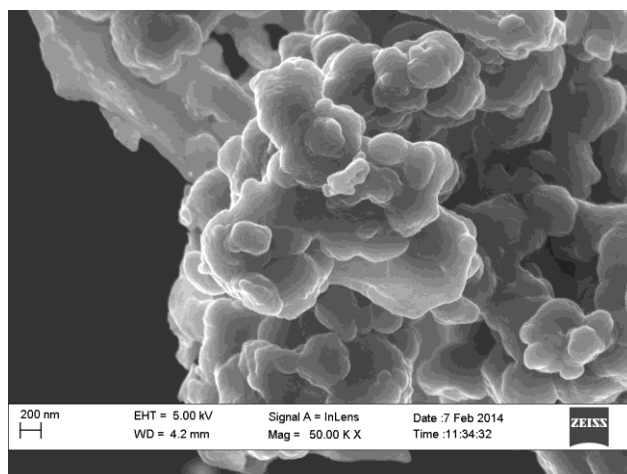


(b)

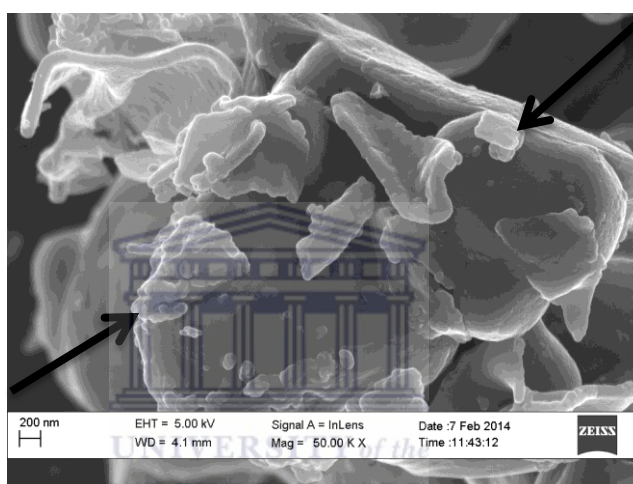


(c)

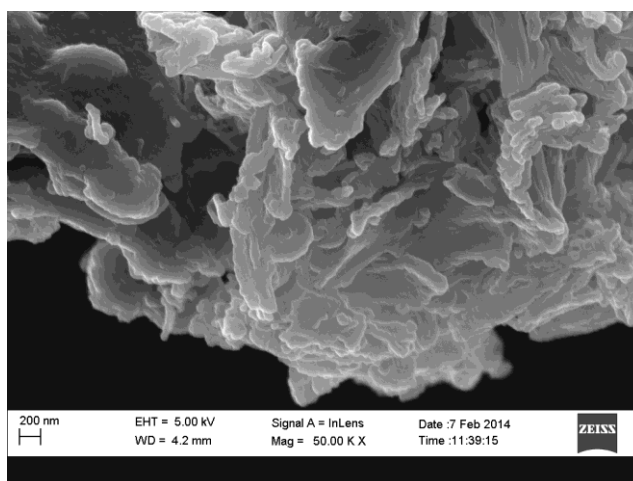
**Figure 37:** TEM images of (a)  $C_{18}MCM-41$ , (b)  $C_{18}MCM-41-CPS$  and (c)  $C_{18}MCM-41$ -guanidine.



(a)



(b)



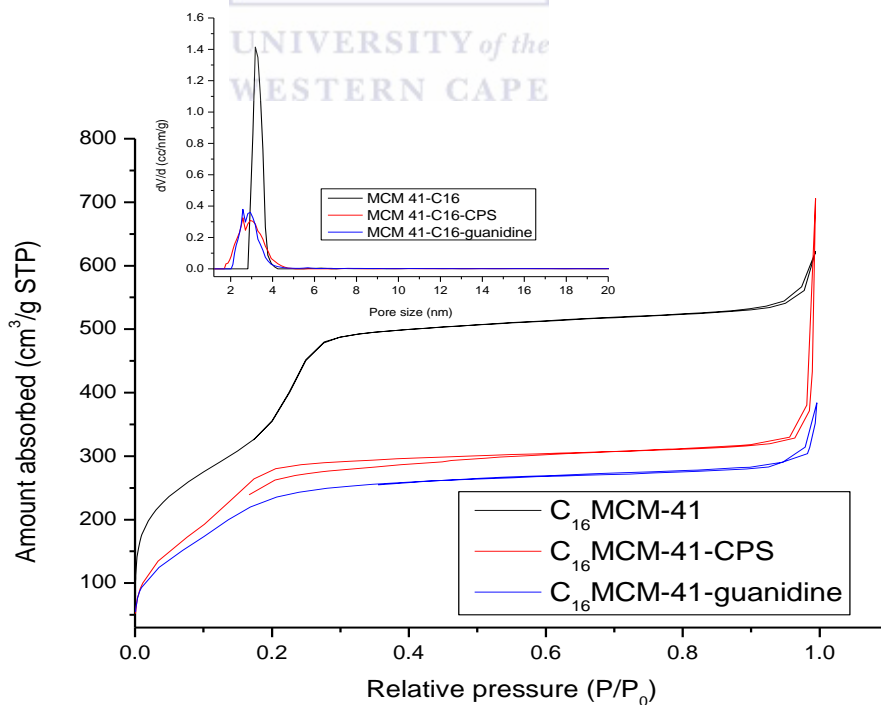
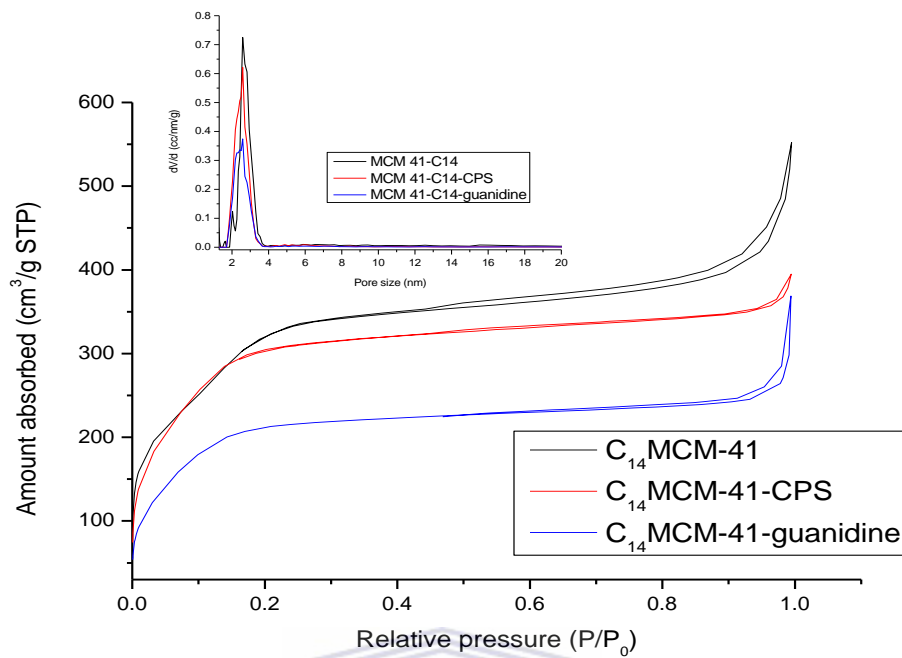
(c)

**Figure 38:** HRSEM images of (a)  $C_{18}MCM-41$ , (b)  $C_{18}MCM-41-CPS$  and (c)  $C_{18}MCM-41$ -guanidine.

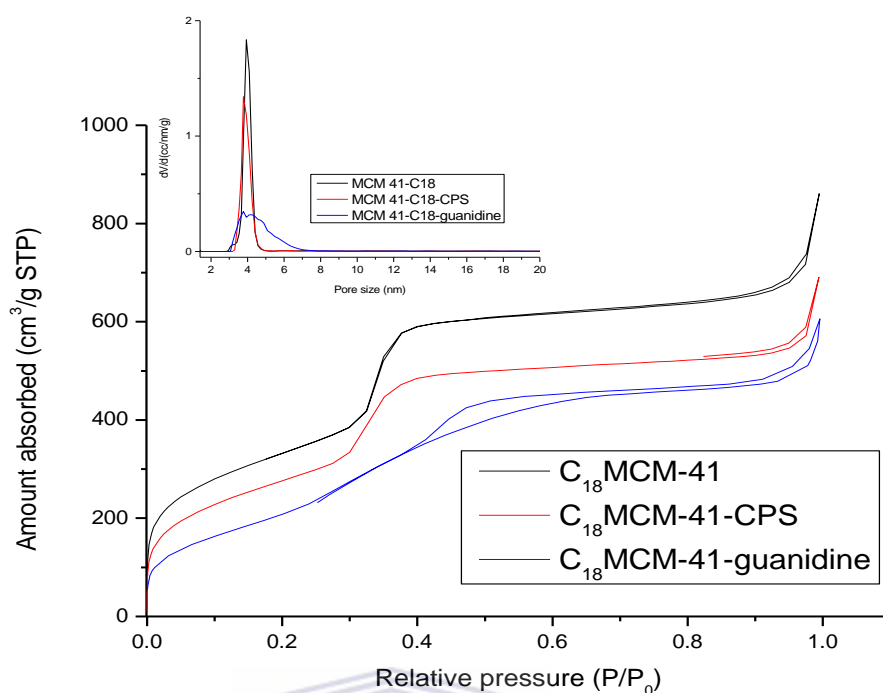
Figure 37a shows the HRTEM images of C<sub>18</sub>MCM-41, C<sub>18</sub>MCM-41-CPS and C<sub>18</sub>MCM-41-guanidine. The HRTEM images confirm the structure of C<sub>18</sub>MCM-41 materials to be highly ordered hexagonal structure. Figure 37b shows the HRTEM images of C<sub>18</sub>MCM-41 grafted with CPS. It can be seen that even after C<sub>18</sub>MCM-41 was grafted with CPS the hexagonal structure was maintained. This implied that grafting C<sub>18</sub>MCM-41 with CPS did not compromise the structure of C<sub>18</sub>MCM-41. This was also consistent with the XRD patterns of C<sub>18</sub>MCM-41-CPS (Figure 36). Guanidine grafted C<sub>18</sub>MCM-41 images are shown in Figure 2c. It can clearly be observed that the structure of C<sub>18</sub>MCM-41 post grafting with guanidine changed the structural properties. The well-ordered hexagonal structure was not as clear as before (Figure 37a and b). The XRD patterns coincide with the HRTEM images, showing that the periodicity of the structure was altered during the attachment of guanidine, indicated by the shift in the (100) peak to higher 2θ values.

Figure 38a shows the HRSEM image of C<sub>18</sub>MCM-41. The image shows that C<sub>18</sub>MCM-41 is spherical in shape with average particle sizes of 50-200 nm in diameter. The spherical particles appear to be agglomerated. Upon grafting with guanidine the morphology of the spherical particles changed, which was in accordance with XRD and HRTEM (Figure 37). Platelet like structures (Figure 38b) were found to be situated on the C<sub>18</sub>MCM-41 particles. Attachment of guanidine is believed to be the platelets that are observed on the spherical particles. The morphology changed from the agglomerated spherical particles to layers or sheet like structures forming clusters (Figure 38c).

7.4 Textural properties of guanidine grafted MCM-41 supports







**Figure 39:**  $N_2$  isotherms of CPS and guanidine grafted MCM-41 ( $C_{14}$ TABr,  $C_{16}$ TABr and  $C_{18}$ TABr).

**Table 16:** Textural properties of guanidine modified MCM-41 materials.

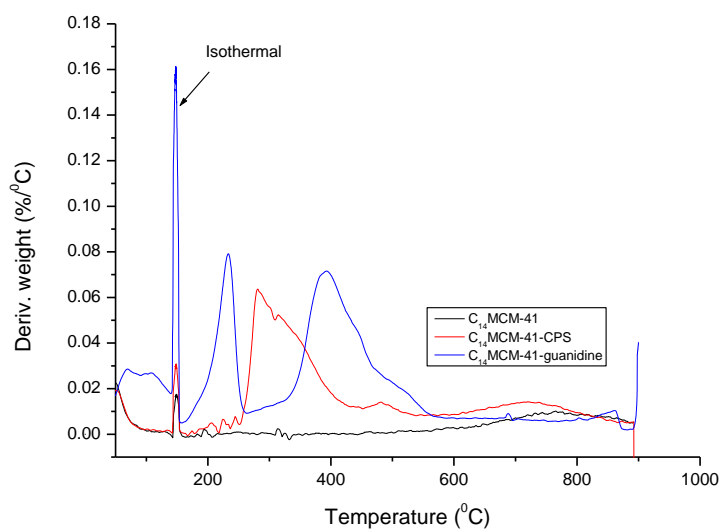
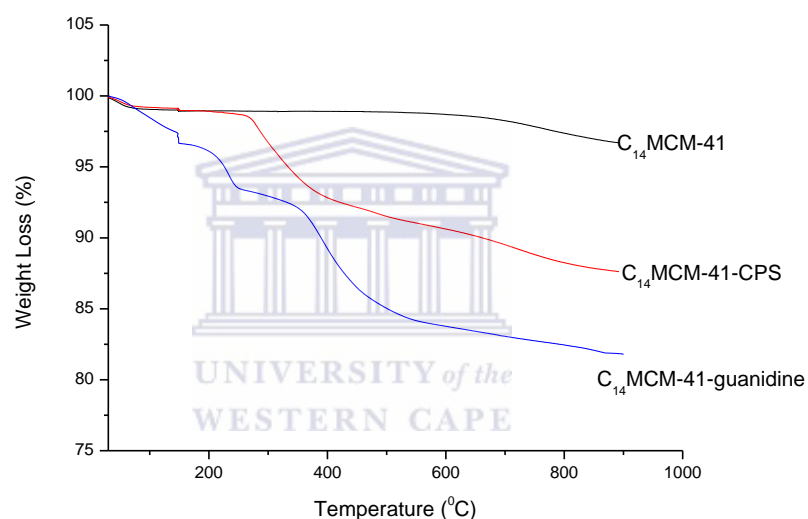
Sample	Surface area ( $m^2/g$ )	Pore volume ( $cm^3/g$ )	Pore size (nm)
$C_{14}$ MCM-41	1302	0.8	2.6
$C_{16}$ MCM-41	1186	0.9	3.2
$C_{18}$ MCM-41	1211	1.3	4.4
$C_{14}$ MCM-41-CPS	1245	0.6	2.6
$C_{16}$ MCM-41-CPS	1280	0.7	2.6
$C_{18}$ MCM-41-CPS	1021	1.1	3.8
$C_{14}$ MCM-41-guanidine	992	0.6	2.5
$C_{16}$ MCM-41-guanidine	986	0.5	2.6
$C_{18}$ MCM-41-guanidine	819	1.5	4.0

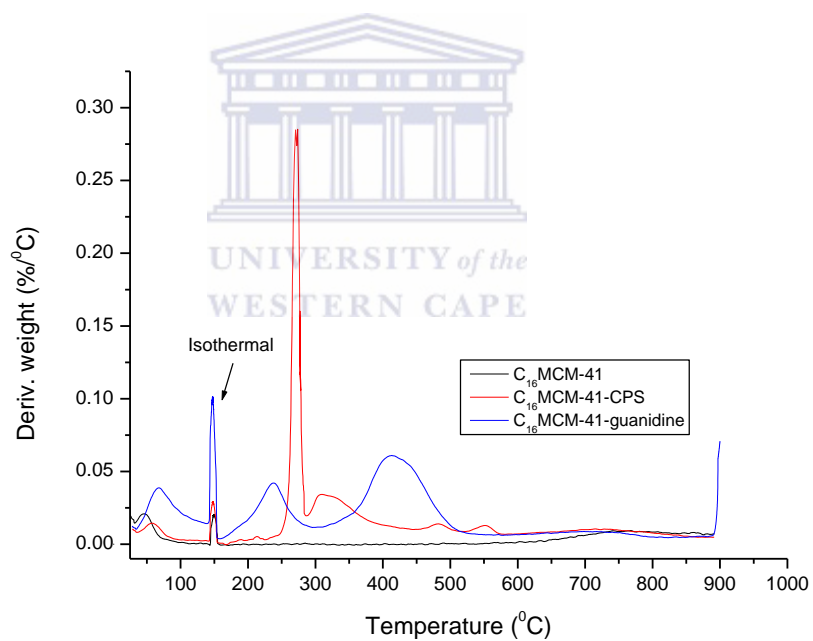
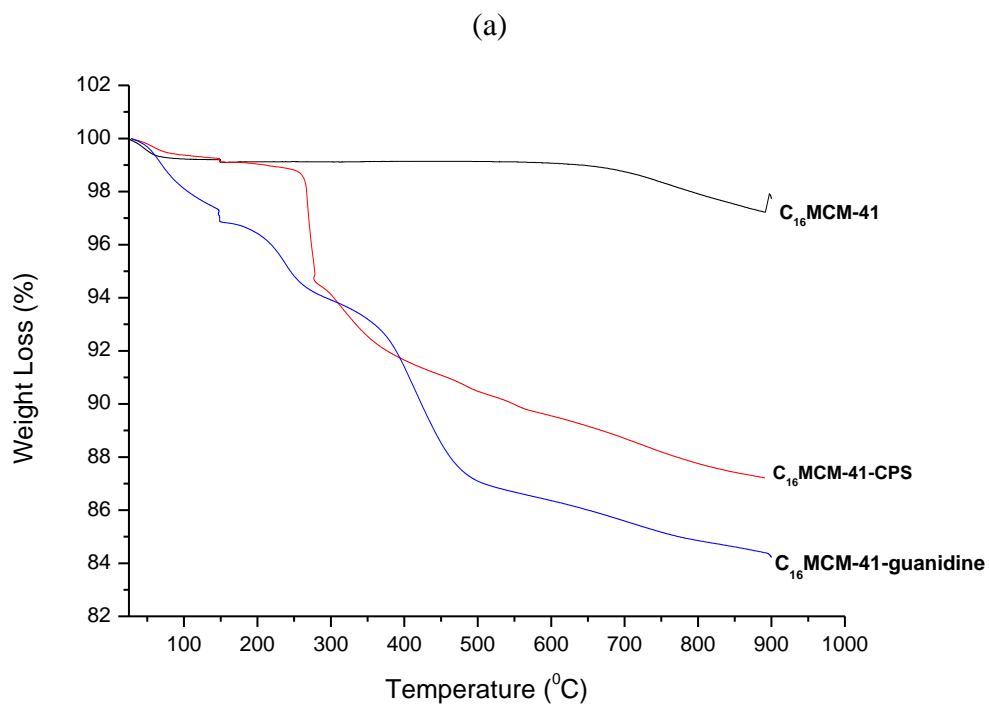
Figure 39 shows the sorbents that were analyzed by N<sub>2</sub> sorption studies at liquid nitrogen temperature (77 K) for evaluating the surface and pore properties. MCM 41 prepared adsorbents, C<sub>14</sub>MCM 41, C<sub>16</sub>MCM 41 and C<sub>18</sub>MCM 41 displayed type IV isotherms in the IUPAC classification. The initial part of the isotherms for C<sub>14</sub>MCM 41, C<sub>16</sub>MCM 41 and C<sub>18</sub>MCM 41 (Figure 39) is due to adsorption and multilayer film formation on the pore walls of the micropores [8]. C<sub>14</sub>MCM 41, C<sub>16</sub>MCM 41 and C<sub>18</sub>MCM 41 displayed a knee between 0.1-0.4 which was due to capillary condensation of N<sub>2</sub> into the mesopores [9-10]. A steep increase in the amount of nitrogen adsorbed at the relative pressure of 0.1, 0.2 and 0.3 was observed for C<sub>14</sub>MCM-41, C<sub>16</sub>MCM-41 and C<sub>18</sub>MCM-41 respectively. C<sub>14</sub>MCM-41, C<sub>16</sub>MCM-41 and C<sub>18</sub>MCM-41 displayed multilayer adsorption on the outer surface in the pressure range  $P/P_0$  (0.5-1). The BET surface area, pore volume and pore size of C<sub>14</sub>MCM 41, C<sub>16</sub>MCM 41 and C<sub>18</sub>MCM 41 are shown in Table 16. The PSD curves were calculated from the adsorption branch of the isotherm according to the DFT kernel method for cylindrical silica pores. MCM-41 materials synthesized with different carbon alkyl chain lengths showed narrow pore size distributions, owing to the uniform pores of hexagonal lattice.

Upon silylation with CPS the volume of nitrogen absorbed decreased (Figure 39). Consequently the knee was not as steep as in the case of the parent materials. The relative pressures of condensation for CPS grafted C<sub>14</sub>MCM-41, C<sub>16</sub>MCM-41 and C<sub>18</sub>MCM-41 was reduced to 0.05, 0.8 and 0.28 respectively in comparison to the unmodified MCM-41 materials, due to the grafting of CPS and is also reflected by the slightly broader pore size distribution observed after the grafting of CPS. BET surface area, pore volume and pore size decreased after grafting MCM-41 with CPS (Table 16) [7].

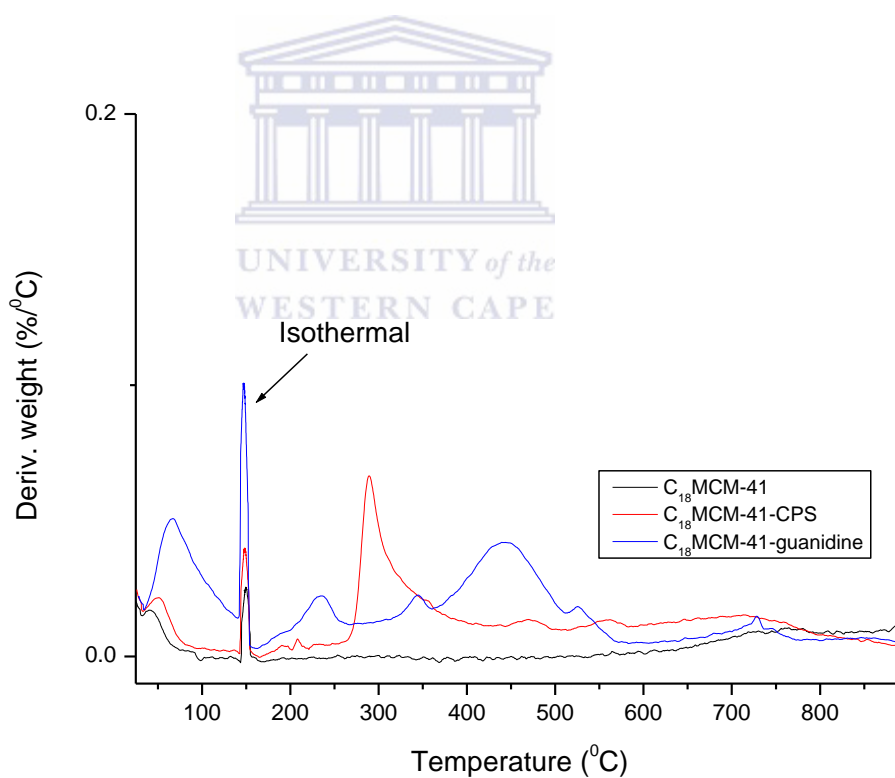
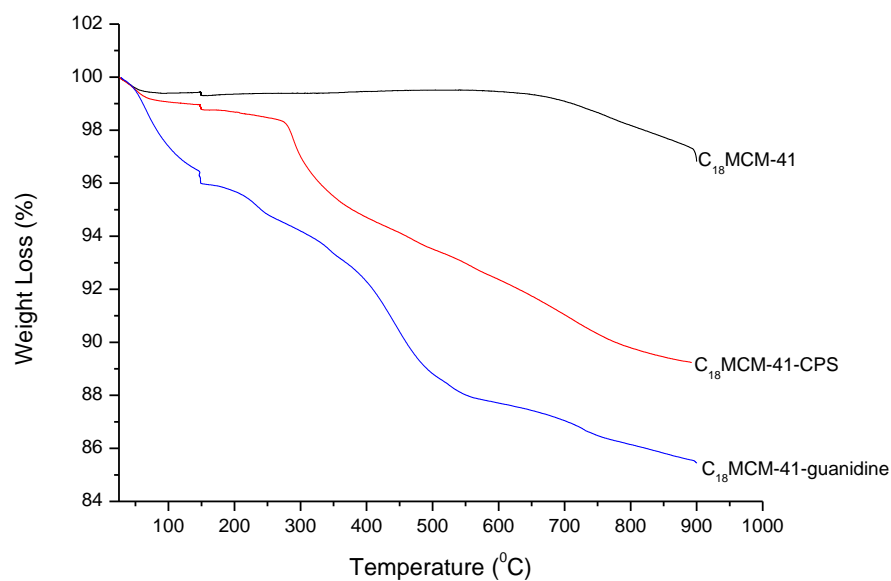
Guanidine attachment on the CPS grafted MCM-41 materials resulted in a further decrease in the amount of  $N_2$  absorbed.  $N_2$  isotherms obtained for guanidine grafted MCM-41 materials displayed diminished adsorption branches where capillary condensation of  $N_2$  into the mesopores occurs (Figure 39), caused by pores becoming partially filled with guanidine (Table 16). The partial filling of the pores is also evident by the broad PSD (Figure 39). Pore filling was further justified by the irregular hysteresis obtained for  $C_{18}$ MCM-41-guanidine [11-12].

### 7.5 TG studies of guanidine grafted MCM-41 supports





(b)



(c)

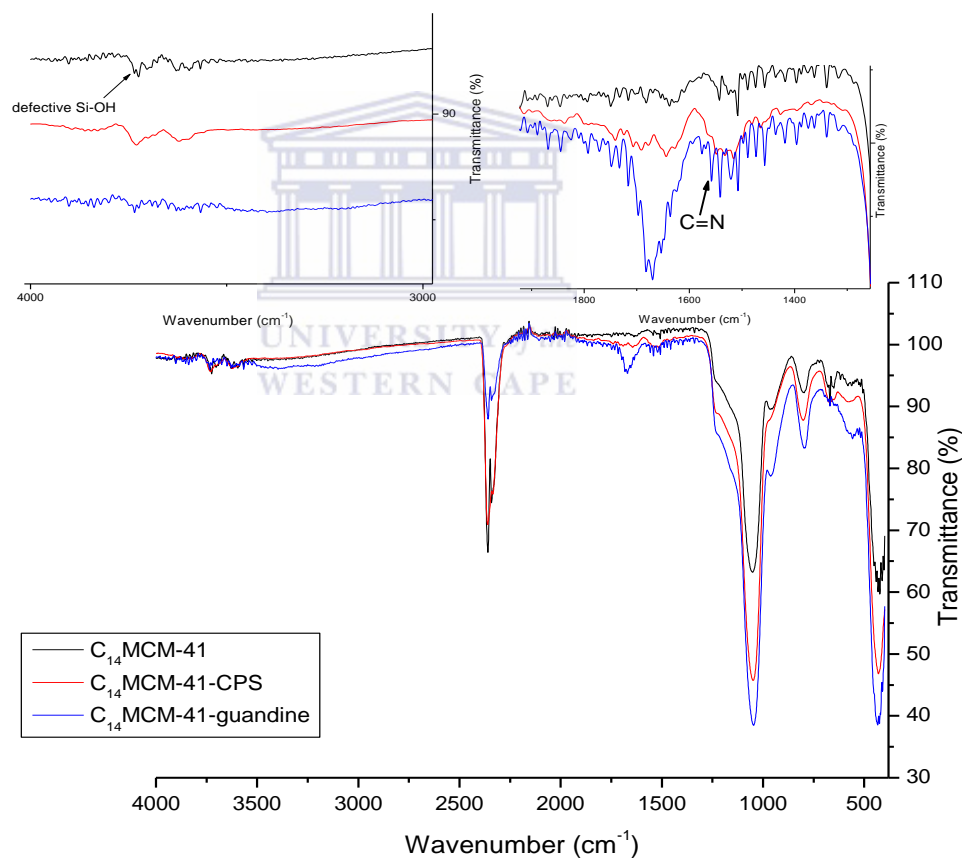
**Figure 40:** TG profiles of guanidine grafted MCM-41(C<sub>14</sub>TABr, C<sub>16</sub>TABr and C<sub>18</sub>TABr).

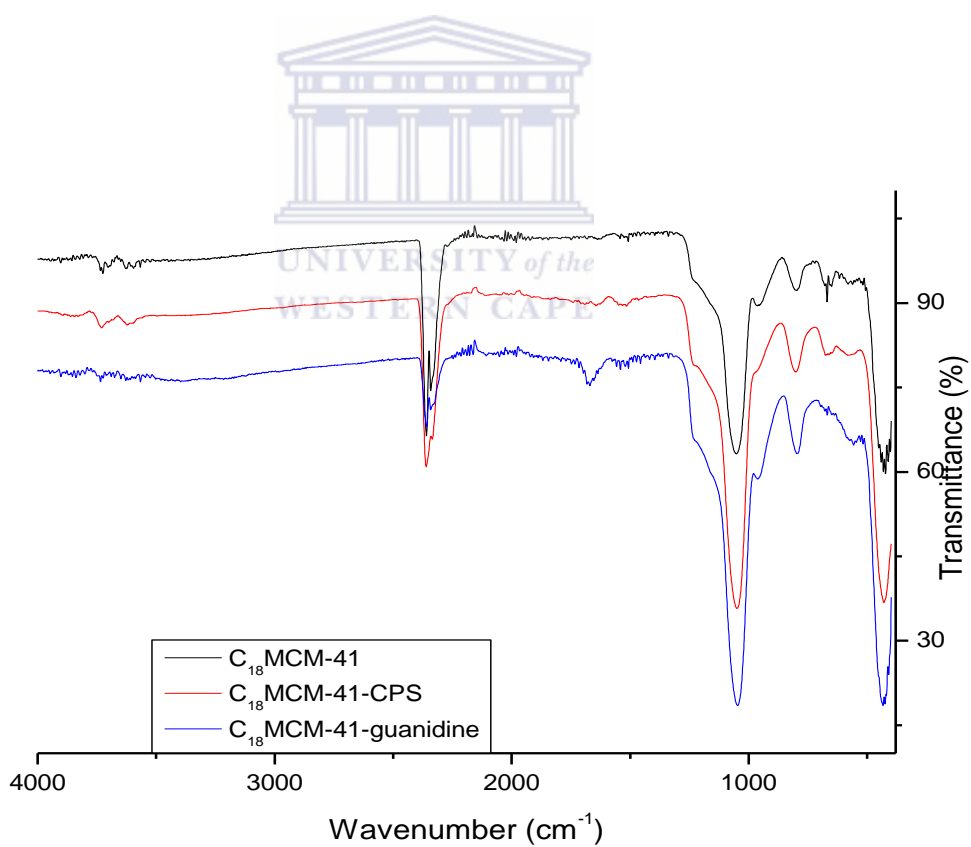
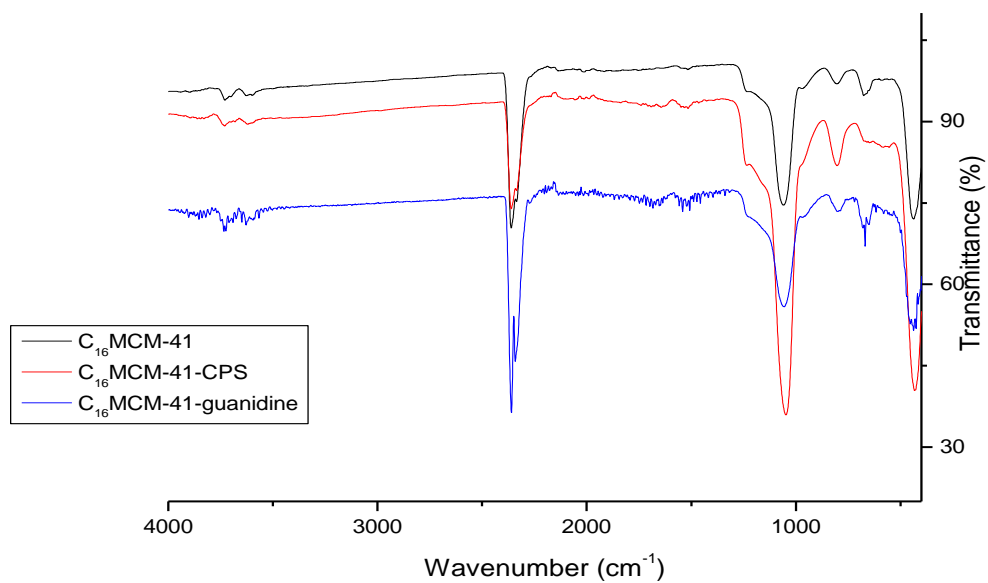
$$\text{Surface coverage} = \frac{\Delta Wt \% \times N_A}{EMW \times S_{BET}} \times 10^{-20} (\text{number}/\text{nm}^2) \quad (7.1)$$

Figure 40 shows the TG/DTA profiles of MCM 41, MCM 41-CPS and MCM-guanidine synthesized with different surfactant carbon chain lengths (C<sub>14</sub>TABr, C<sub>16</sub>TABr and C<sub>18</sub>TABr). As seen from the TGA profiles (Figure 40) both unmodified and modified MCM 41 materials displayed different decomposition profiles. MCM-41(C<sub>14</sub>TABr, C<sub>16</sub>TABr and C<sub>18</sub>TABr) displayed 2 weight loss regions around 25-150 and above 500 °C which may be attributed to the loss of physisorbed water as well as the dehydroxylation by condensation of the silanols of MCM-41 materials. Upon functionalization with CPS the TGA profile showed a weight loss in the region 250-600 °C of 6.9 %, 4.6 % and 4.4 % for C<sub>14</sub> MCM 41, C<sub>16</sub> MCM 41 and C<sub>18</sub> MCM 41 respectively, which was due to the decomposition of CPS groups [13]. Dehydroxylation that may occur at these temperatures may be neglected, since all samples were pre-dried before the grafting step, and anhydrous solvents were used [6]. Huang *et al.* showed that free surface hydroxyl groups react with the silane during the grafting step [14]. Sayari and co-workers also showed that the non-hydrolyzed alkoxy groups that could potentially add to the weight loss observed are removed below 200 °C [15]. Surface coverage of CPS on MCM 41 supports was calculated assuming that each CPS group occupies a cylindrical volume of 0.43 nm [16-17]. The surface coverage was 4.6, 5.2 and 5.0 for C<sub>14</sub> MCM 41, C<sub>16</sub> MCM 41 and C<sub>18</sub> MCM 41 respectively. The attachment of guanidine to the chlorosilane grafted MCM supports displayed an additional decomposition step. The weight loss in the region 150-250 °C may be attributed to the decomposition of guanidine groups that were attached on MCM-41 supports. Mass loss of 3.3, 2.9 and 2.8 % were observed for C<sub>14</sub>MCM-41, C<sub>16</sub>MCM-41 and C<sub>18</sub>MCM-41-guanidine, respectively

[18]. The loading of guanidine was lower than the theoretically calculated loading. This may be due to steric hindrances between the guanidine molecules and the chlorosilanes grafted onto the surfaces of the MCM 41 supports during the attachment of guanidine.  $C_{14}$ MCM-41 guanidine displayed the greatest loss during the decomposition step, which is in good accordance with the weight loss of  $C_{14}$ MCM-41-CPS, indicating that more guanidine was attached to the support having the greater number of  $-Cl$  available on the surface.

## 7.6 FT-IR





**Figure 41:** FT-IR of guanidine grafted MCM-41( $C_{14}$ TABr,  $C_{16}$ TABr and  $C_{18}$ TABr).



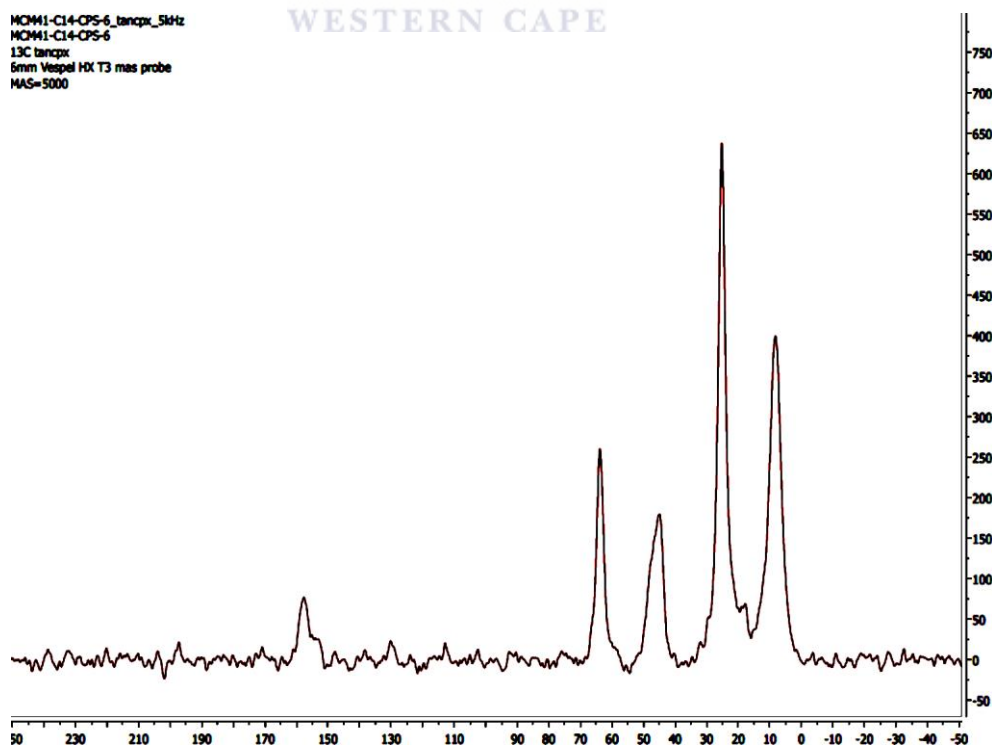
Figure 41 shows the FT-IR spectra of parent MCM-41 materials ( $C_{14}$ TABr,  $C_{16}$ TABr and  $C_{18}$ TABr), CPS and guanidine functionalized MCM 41 supports. Parent MCM-41 prepared with different alkyl surfactant chain lengths all showed similar characteristics peaks. FT-IR spectra of  $C_{14}$ MCM-41-guanidine including inserts is shown in this regard as a representative spectra for the functionalized supports. Asymmetric Si-O-Si stretching was observed at  $1234.3\text{ cm}^{-1}$  and  $1051.4\text{ cm}^{-1}$ . Symmetric Si-O-Si stretching was observed at  $787.7\text{ cm}^{-1}$ . Characteristic bending of Si-O-Si was observed at  $451.3\text{ cm}^{-1}$ . Broad bands were observed in parent MCM-41 materials, which may be due to surface silanol groups as well as pre-adsorbed water, although samples were dried prior to measurements [13, 19].

For MCM-41 functionalized with CPTES, the intensity of the Si-OH band around  $950.4\text{ cm}^{-1}$  decreased, and this was due to some of the surface silanol groups being used up during the functionalization step. The defective Si-OH groups and CPS was clearly observed by the decrease in the intensity of the band in the region of  $3734\text{ cm}^{-1}$ . Weak absorption bands at  $2962\text{ cm}^{-1}$  and  $2920\text{ cm}^{-1}$  were also observed - these are characteristics of -CH of the methyl group. The decrease in intensity of Si-OH and the appearance of new -CH confirms that CPTES was grafted onto the MCM-41 supports prepared with different alkyl surfactant chain lengths [7, 20-21].

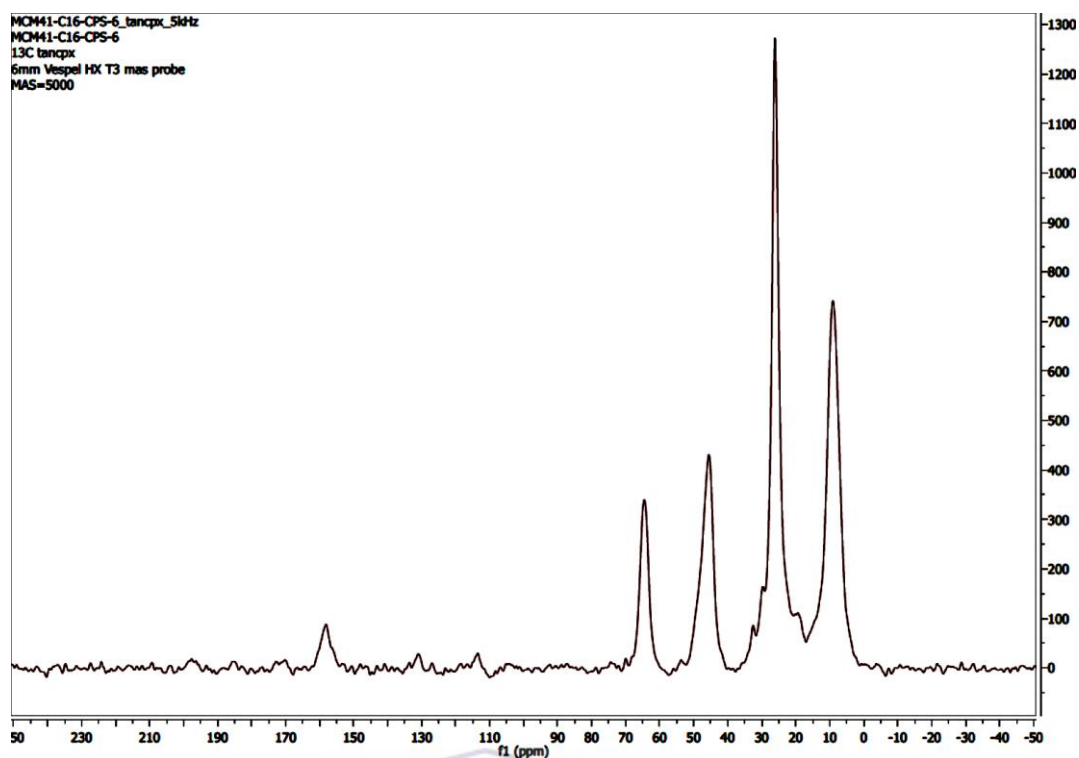
To determine whether guanidine was attached to the CPTES functionalized MCM-41 supports, C-N, -NH<sub>2</sub> as well as C=N bands would be confirmation of attachment. C-N bands are normally observed in the region of  $1000\text{--}1200\text{ cm}^{-1}$ , but in this case the bands could not be seen as the Si-O-Si bands overlay this region. The broadness of the bands in this region after the attachment of guanidine seems to suggest that these bands are present [22]. N-H stretching peaks should also appear near the region of  $3350\text{ cm}^{-1}$ , but was not clearly visible as pre-adsorbed water shows a broad band in

this region, thus overlapping N-H stretching bands. Pre-drying did not remove all the moisture due to the hydrophilic nature of the adsorbents [23-26]. A band around  $1557\text{ cm}^{-1}$  was observed in guanidine grafted MCM-41. The band at  $1557\text{ cm}^{-1}$  may be attributed to C=N stretching bands. Wang and Ma [27] previously reported C=N stretching bands of guanidine in the region  $1598\text{-}1638\text{ cm}^{-1}$ . The absorbance bands of guanidine in this region were also confirmed by Colthup *et al.* [28]. Bellomy was also quoted as finding these bands in higher regions between  $1718\text{-}1590\text{ cm}^{-1}$  for C=N stretching bands of guanidine [29]. Nevertheless the appearance of the above mentioned peaks found the FT-IR spectra of the guanidine functionalized MCM-41 materials, confirming that grafting of guanidine onto the supports was done successfully [30-31].

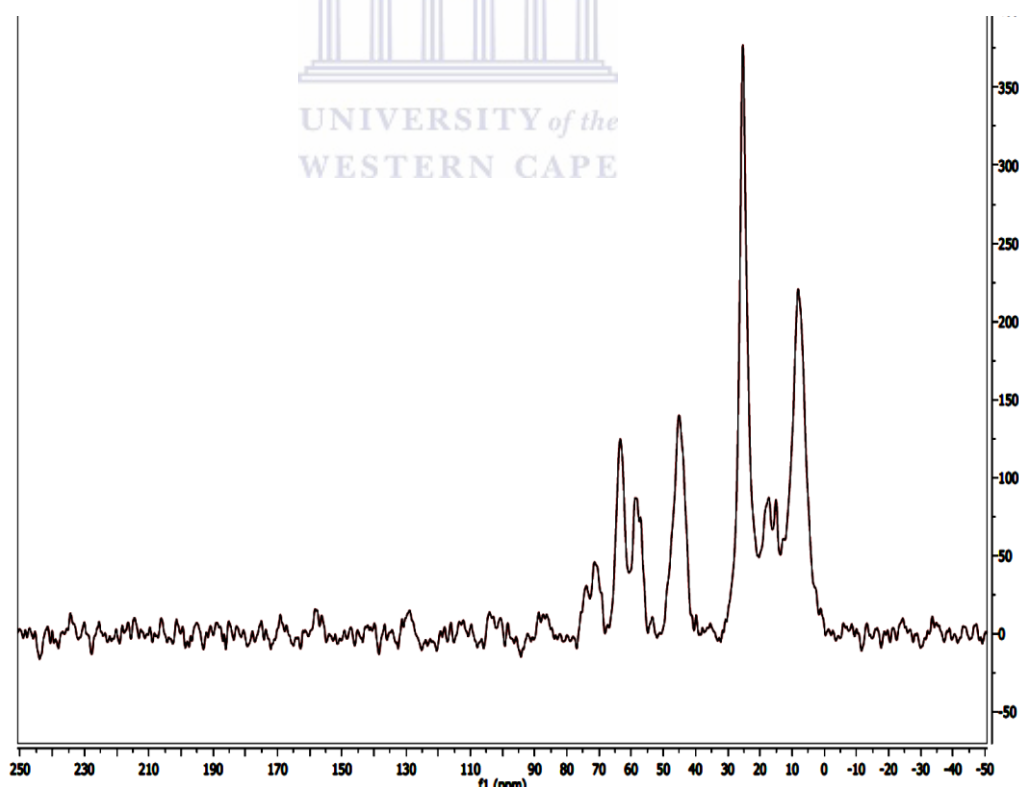
### 7.7 $^{13}\text{C}$ CPMAS NMR



(a)



(b)



(c)

**Figure 42:**  $^{13}\text{C}$  CPMAS NMR spectrum of (a)  $\text{C}_{14}\text{MCM-41-guanidine}$ , (b)  $\text{C}_{16}\text{MCM-41-guanidine}$  and (c)  $\text{C}_{18}\text{MCM-41-guanidine}$ .

**Table 17:**  $^{13}\text{C}$  CPMAS NMR shifts of C14-MCM-41-guanidine shown as representative.

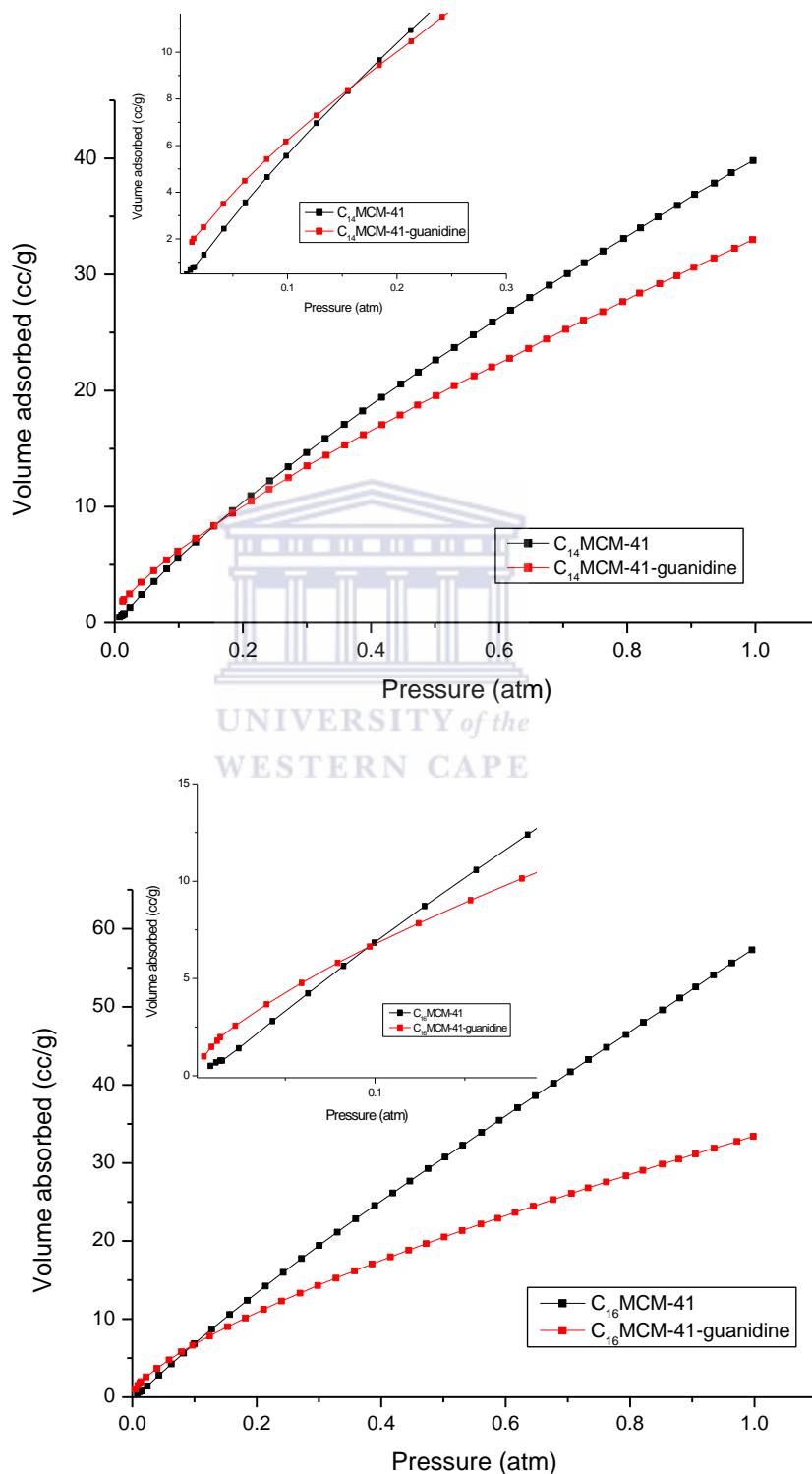
C <sub>14</sub> -MCM-41-guanidine	
Assignment	Resonance (ppm)
-Si-CH <sub>2</sub>	9
-Si-CH <sub>2</sub> -CH <sub>2</sub> -	25
-Si-OCH <sub>3</sub>	45
-CH <sub>2</sub> -CH <sub>2</sub> -N=	64

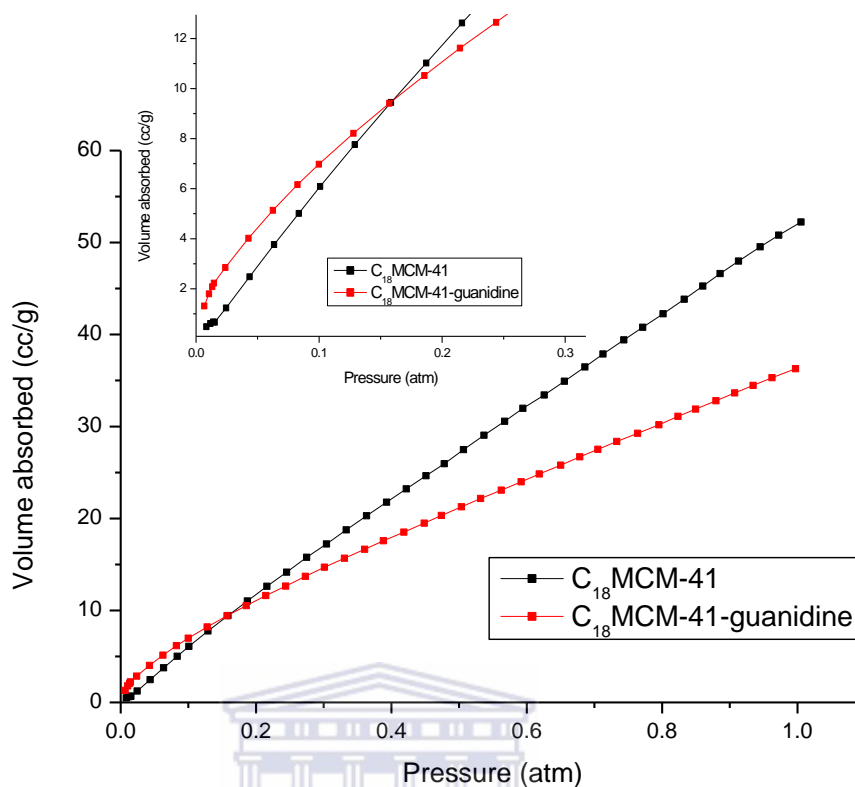
Figure 42 shows the  $^{13}\text{C}$  CPMAS NMR spectrum of C<sub>14</sub>MCM-41, C<sub>16</sub>MCM-41 and C<sub>18</sub>MCM-41 grafted with guanidine. C<sub>14</sub>MCM-41-guanidine (Figure 42a) is discussed as representative. The spectrum shows four clear peaks with an additional peak at a higher ppm. The peaks show the presence of carbon atoms, from the most shielded that is bonded directly to the silicon atom to the least shielded carbon atoms bonded to the nitrogen atom [8].

Three resonance peaks were observed in the spectrum of C<sub>14</sub> MCM-41-guanidine, i.e. 8, 23 and 45 ppm (Figure 42a) that may be attributed to CPS propyl chain carbons [32-33]. The resonance peak at 70 ppm is due to the carbon from the guanidine molecule. The weak resonance peak observed at 160 ppm may be attributed to carbamate formation due to the reaction of CO<sub>2</sub> with the amine groups on the surface of MCM-41 [33]. The  $^{13}\text{C}$  CPMAS NMR spectrum of C<sub>14</sub> MCM-41-guanidine therefore confirms that guanidine was successfully grafted on C<sub>14</sub> MCM-41. The  $^{13}\text{C}$  CPMAS NMR spectrum of C<sub>18</sub>MCM-41- guanidine is shown in Figure 42c. Figure 42c displayed more than four peaks in the spectrum. The splitting of the peaks was possibly due to the presence of the surfactant in C<sub>18</sub>MCM-41, which was not completely removed during the calcination step, as C<sub>18</sub>MCM-41 was up scaled. Nevertheless  $^{13}\text{C}$  CPMAS NMR spectrum showed that the grafting of guanidine was

successful.  $^{13}\text{C}$  CPMAS NMR spectrum, together with structural and textural properties, shows that guanidine was grafted on MCM-41 supports.

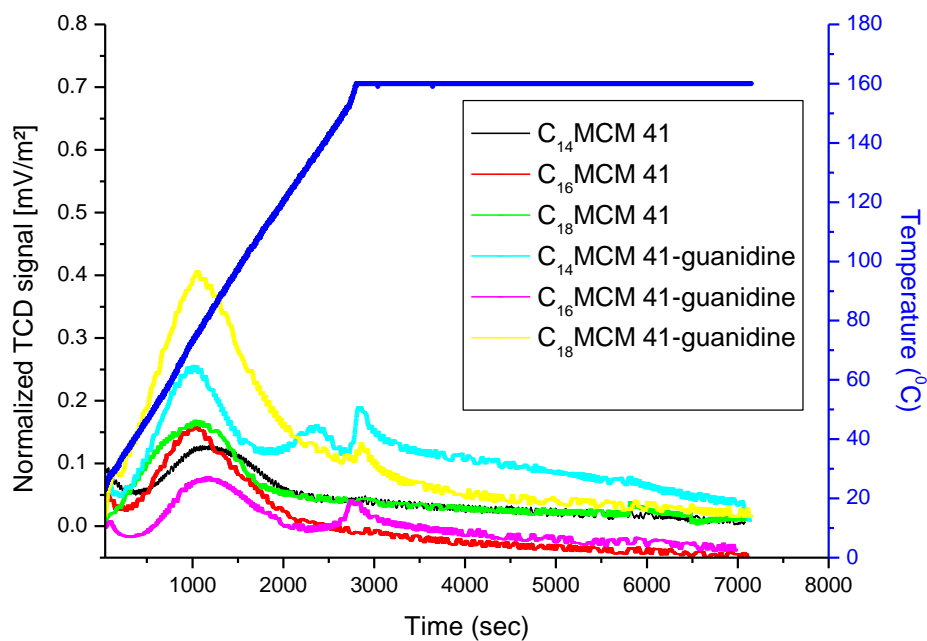
### 7.8 $\text{CO}_2$ isotherms





**Figure 43:** CO<sub>2</sub> isotherms of guanidine grafted MCM-41 (C<sub>14</sub>TABr, C<sub>16</sub>TABr and C<sub>18</sub>TABr).

Figure 43 shows the CO<sub>2</sub> isotherms of guanidine modified C<sub>14</sub>MCM-41, C<sub>16</sub>MCM-41 and C<sub>18</sub>MCM-41 performed at 0 °C. It is clear from the isotherms that interaction between the materials and CO<sub>2</sub> exists. The modified MCM 41 materials adsorbed slightly, with CO<sub>2</sub> at a low pressure as a result of guanidine being grafted on C<sub>14</sub>MCM-41, C<sub>16</sub>MCM-41 and C<sub>18</sub>MCM-41 materials. CO<sub>2</sub> isotherms mainly display the physical interaction between the sorbent material and CO<sub>2</sub>; however it is clear from the isotherms at low pressure that it is not only physical but chemical interaction as well, which would explain the slight increase in adsorption capacity at low pressures. The same trend was observed in all adsorbents prepared. The increase in adsorption capacity at low pressure further justifies that guanidine was indeed chemically grafted on the surface of MCM-41 silica.

7.9 CO<sub>2</sub> TPD

**Figure 44:** CO<sub>2</sub>-TPD profiles of C<sub>14</sub>MCM-41, C<sub>16</sub>MCM-41 and C<sub>18</sub>MCM-41 grafted with guanidine.

**Table 18:** CO<sub>2</sub> adsorption capacities of guanidine grafted MCM-14 (C<sub>14</sub>TABr, C<sub>16</sub>TABr and C<sub>18</sub>TABr).

Sample	CO <sub>2</sub> capacity (mmol/g)	N content (mmol/g)	N <sub>2</sub> efficiency (CO <sub>2</sub> /N <sub>2</sub> )
C <sub>14</sub> MCM-41	0.19	-	-
C <sub>16</sub> MCM-41	0.16	-	-
C <sub>18</sub> MCM-41	0.11	-	-
C <sub>14</sub> MCM-41-guanidine	0.09	1.12	0.08
C <sub>16</sub> MCM-41-guanidine	0.28	0.71	0.40
C <sub>18</sub> MCM-41-guanidine	0.30	0.70	0.43

Figure 44 shows the CO<sub>2</sub> TPD profiles of C<sub>14</sub>MCM-41, C<sub>16</sub>MCM-41 and C<sub>18</sub>MCM-41 grafted with guanidine with the TCD signal normalized with respect to the surface area of the adsorbents and baseline correction. CO<sub>2</sub> TPD experiments were performed at a maximum desorption temperature of 160 °C, which was a suitable temperature as TGA profiles showed that the guanidine modified supports were stable up to 200 °C. C<sub>14</sub>MCM-41, C<sub>16</sub>MCM-41 and C<sub>18</sub>MCM-41 supports CO<sub>2</sub> desorption peaks began in the range of 30-100 °C, which was attributed to physisorbed CO<sub>2</sub>. As observed from the profiles MCM-41 supports adsorption capacity which increased according to textural properties, i.e. surface area and pore size (Table 18). The results obtained confirm that surface area as well as pore-size has a direct effect on the CO<sub>2</sub> adsorption capacities. Functionalization with guanidine proved to increase the adsorption capacity of the MCM-41 supports (Figure 44). TPD profiles of guanidine modified MCM-41 supports (Figure 44) showed additional desorption peaks at higher temperatures, i.e. in the range of 120-140 °C. C<sub>14</sub>MCM-41)-guanidine displayed three desorption peaks around 30-100, 130 and 140 °C respectively. The phenomenon can be explained by a mechanism whereby the adsorption pathway between the amine groups and CO<sub>2</sub> during anhydrous conditions, forms carbamates [9, 34]. The difference observed in the desorption profiles is due to the fact that primary and secondary amine have slightly different adsorption energies for CO<sub>2</sub> [35-36]. Therefore the enhanced adsorption may be attributed to both physisorption as well as chemisorbed CO<sub>2</sub>; further proving that guanidine was successfully attached to C<sub>14</sub>MCM-41, C<sub>16</sub>MCM-41 and C<sub>18</sub>MCM-41 supports.

In conclusion several techniques showed that guanidine was successfully grafted onto MCM-41 materials with variations in pore size. A trend emerged from the



study. It was proved that the larger pore size C<sub>18</sub>MCM-41 adsorbed more CO<sub>2</sub> in comparison to C<sub>14</sub>MCM-41 and C<sub>16</sub>MCM-41, used in this study. The attachment of guanidine further enhanced the adsorption capacity proving that both support material and amine functionality contributes to the total adsorption capacity of the adsorbents.



**References**

1. Russo, P.A., Carrott, M.M.L.R. & Carrott, P.J.M. 2007, "Effect of hydrothermal treatment on the structure, stability and acidity of Al containing MCM-41 and MCM-48 synthesised at room temperature", *Colloids and Surfaces A: Physicochemical and Engineering Aspects*, vol. 310, no. 1-3, pp. 9-19.
2. Sayari, A., Yang, Y. 2000, "Highly ordered MCM-41 silica prepared in the presence of Decytrimethylammonium bromide", *Journal of Physical Chemistry.*, vol B, no. 104, pp. 4835-4839.
3. Loganathan, S., Tikmani, M. & Ghoshal, A.K. 2013, "Novel pore-expanded MCM-41 for CO<sub>2</sub> capture: Synthesis and characterization", *Langmuir*, vol. 29, no. 10, pp. 3491-3499.
4. Jiang, D., Gao, J., Yang, J., Su, W., Yang, Q. & Li, C. 2007, "Mesoporous ethane-silicas functionalized with trans-(1R,2R)-diaminocyclohexane: Relation between structure and catalytic properties in asymmetric transfer hydrogenation", *Microporous and Mesoporous Materials*, vol. 105, no. 1-2, pp. 204-210.
5. Huo, Q., Margolese, D.I. & Stucky, G.D. 1996, "Surfactant Control of Phases in the Synthesis of Mesoporous Silica-Based Materials", *Chemistry of Materials*, vol. 8, no. 5, pp. 1147-1160.
6. Zeleňák, V., Badaničová, M., Halamová, D., Čejka, J., Zukal, A., Murafa, N. & Goerigk, G. 2008, "Amine-modified ordered mesoporous silica: Effect of pore size on carbon dioxide capture", *Chemical Engineering Journal*, vol. 144, no. 2, pp. 336-342.
7. Zhao, X.S. & Lu, G.Q. 1998, "Modification of MCM-41 by surface silylation with trimethylchlorosilane and adsorption study", *Journal of Physical Chemistry B*, vol. 102, no. 9, pp. 1556-1561.
8. Mello, M.R., Phanon, D., Silveira, G.Q., Llewellyn, P.L. & Ronconi, C.M. 2011, "Amine-modified MCM-41 mesoporous silica for carbon dioxide capture", *Microporous and Mesoporous Materials*, vol. 143, no. 1, pp. 174-179.

9. Shang, F., Liu, H., Sun, J., Liu, B., Wang, C., Guan, J. & Kan, Q. 2011, "Synthesis, characterization and catalytic application of bifunctional catalyst: Al-MCM-41-NH<sub>2</sub>", *Catalysis Communications*, vol. 12, no. 8, pp. 739-743.
10. Das, D., Lee, J.-. & Cheng, S. 2004, "Selective synthesis of Bisphenol-A over mesoporous MCM silica catalysts functionalized with sulfonic acid groups", *Journal of Catalysis*, vol. 223, no. 1, pp. 152-160.
11. Zhao, H., Ma, Y., Tang, J., Hu, J. & Liu, H. 2011, "Influence of the solvent properties on MCM-41 surface modification of aminosilanes", *Journal of Solution Chemistry*, vol. 40, no. 4, pp. 740-749.
12. Mody, H.M., Kannan, S., Bajaj, H.C., Manu, V. & Jasra, R.V. 2008, "A simple room temperature synthesis of MCM-41 with enhanced thermal and hydrothermal stability", *Journal of Porous Materials*, vol. 15, no. 5, pp. 571-579.
13. Taib N. I., Endud. S., Ehsan. S. D. 2011, "Functionalization of Mesoporous Si-MCM-41 by Grafting with Trimethylchlorosilane", *International Journal of Chemistry*, vol. 3, no. 3, pp. 1-10.
14. Huang, H.Y., Yang, R.T., Chinn, D. & Munson, C.L. 2003, "Amine-grafted MCM-48 and silica xerogel as superior sorbents for acidic gas removal from natural gas", *Industrial and Engineering Chemistry Research*, vol. 42, no. 12, pp. 2427-2433.
15. Harlick, P.J.E. & Sayari, A. 2007, "Applications of pore-expanded mesoporous silica. 5. triamine grafted material with exceptional CO<sub>2</sub> dynamic and equilibrium adsorption performance", *Industrial and Engineering Chemistry Research*, vol. 46, no. 2, pp. 446-458.
16. Kresge, C.T., Leonowicz, M.E., Roth, W.J., Vartuli, J.C. & Beck, J.S. 1992, "Ordered mesoporous molecular sieves synthesized by a liquid-crystal template mechanism", *Nature*, vol. 359, no. 6397, pp. 710-712.
17. Huo, Q., Leon, R., Petroff, P.M. & Stucky, G.D. 1995, "Mesostructure design with gemini surfactants: Supercage formation in a three-dimensional hexagonal array", *Science*, vol. 268, no. 5215, pp. 1324-1327.

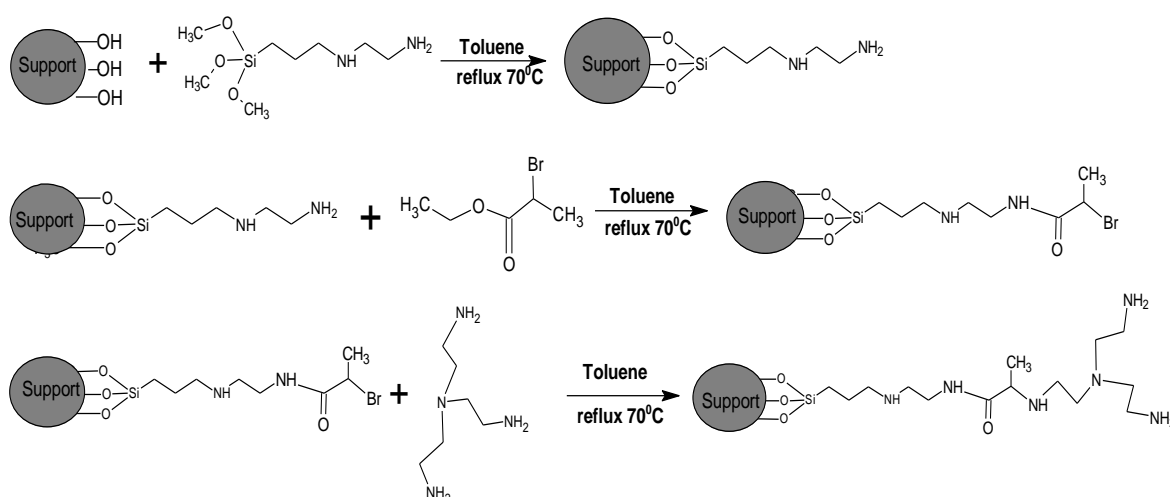
18. Alizadeh, A., Khodaei, M., Beygzadeh, M., Kordestani, D., Feyzi, M. 2012, "Biguanide-Functionalized Fe<sub>3</sub>O<sub>4</sub>/SiO<sub>2</sub> Magnetic Nanoparticles: An Efficient Heterogeneous Organosuperbase Catalyst for Various Organic Transformations in Aqueous Media", *Bull. Korean Chem. Soc.*, vol. 33, no. 8, pp. 2546-2552.
19. Liu, S., Hsiao, W. & Sie, W.-. 2012, "Tetraethylenepentamine-modified mesoporous adsorbents for CO<sub>2</sub> capture: Effects of preparation methods", *Adsorption*, vol. 18, no. 5-6, pp. 431-437.
20. Hamzah, Z., Narawi, N., Rasid, H. M., Yusoff, A.N. 2012, "Synthesis and Characterization of mesoporous material functionalized with different silylating agent and their capability to remove Cu<sup>2+</sup>", *The Malaysian Journal of Analytical Sciences*, vol. 16, no 3, pp. 290 – 296.
21. Vinoba, M., Jeong, S.K., Bhagiyalakshmi, M. & Alagar, M. 2010, "Electrocatalytic reduction of hydrogen peroxide on silver nanoparticles stabilized by amine grafted mesoporous SBA-15", *Bulletin of the Korean Chemical Society*, vol. 31, no. 12, pp. 3668-3674.
22. Meléndez-Ortiz, H.I., Perera-Mercado, Y., Mercado-Silva, J.A., Olivares-Maldonado, Y., Castruita, G. & García-Cerda, L.A. 2014, "Functionalization with amine-containing organosilane of mesoporous silica MCM-41 and MCM-48 obtained at room temperature", *Ceramics International*, vol. 40, no. 7 PART A, pp. 9701-9707.
23. Dutcher, B., Fan, M., Cui, S., Shen, X.-., Kong, Y., Russell, A.G., McCurdy, P. & Giotto, M. 2013, "Characterization and stability of a new, high-capacity amine-functionalized CO<sub>2</sub> sorbent", *International Journal of Greenhouse Gas Control*, vol. 18, pp. 51-56.
24. Battjes, K.P., Barolo, A.M. & Dreyfuss, P. 1991, "New evidence related to reactions of aminated silane coupling agents with carbon dioxide", *Journal of Adhesion Science and Technology*, vol. 5, no. 10, pp. 785-799.
25. Giovannetti, R., Alibabaei, L. & Samanipour, S. 2009, "Structure investigations of binary azeotrope of diethyl amine-acetone by FT-IR and <sup>1</sup>H NMR spectroscopy", *Spectrochimica Acta - Part A: Molecular and Biomolecular Spectroscopy*, vol. 72, no. 2, pp. 390-393.

26. Truica-Marasescu, F. & Wertheimer, M.R. 2008, "Nitrogen-rich plasma-polymer films for biomedical applications", *Plasma Processes and Polymers*, vol. 5, no. 1, pp. 44-57.
27. Wang, B., and Ma, H.Z. 2007, "Chiroptical Lanthanide (III) Schiff base complexes derived from *p*-Nitrophenyl-hydrazine and D-Camphor- $\beta$ -sulphonic acid", *Inorganic Chemical Communications*, vol. 4, pp. 248-251.
28. Roeges, N.G.P. 1994, "A Guide to the Complete Interpretation of the Infrared spectra of organic structures", Wiley, NewYork.
29. Kumler, W.D. 1954, "The infrared spectra of nitroguanidine and related compounds", *Journal of the American Chemical Society*, vol. 76, no. 3, pp. 814-816.
30. Pinto, M.L., Pires, J. & Rocha, J. 2008, "Porous materials prepared from clays for the upgrade of landfill gas", *Journal of Physical Chemistry C*, vol. 112, no. 37, pp. 14394-14402.
31. Bollini, P., Choi, S., Drese, J.H. & Jones, C.W. 2011, "Oxidative degradation of aminosilica adsorbents relevant to postcombustion CO<sub>2</sub> capture", *Energy and Fuels*, vol. 25, no. 5, pp. 2416-2425.
32. Sayari, A. & Belmabkhout, Y. 2010, "Stabilization of amine-containing CO<sub>2</sub> adsorbents: Dramatic effect of water vapor", *Journal of the American Chemical Society*, vol. 132, no. 18, pp. 6312-6314.
33. Knöfel, C., Martin, C., Hornebecq, V. & Llewellyn, P.L. 2009, "Study of carbon dioxide adsorption on mesoporous aminopropylsilane- functionalized silica and titania combining microcalorimetry and in situ infrared spectroscopy", *Journal of Physical Chemistry C*, vol. 113, no. 52, pp. 21726-21734.
34. Yu, J., Le, Y. & Cheng, B. 2012, "Fabrication and CO<sub>2</sub> adsorption performance of bimodal porous silica hallow spheres with amine-modified surfaces", *RSC Advances*, vol. 2, no. 17, pp. 6784-6791.

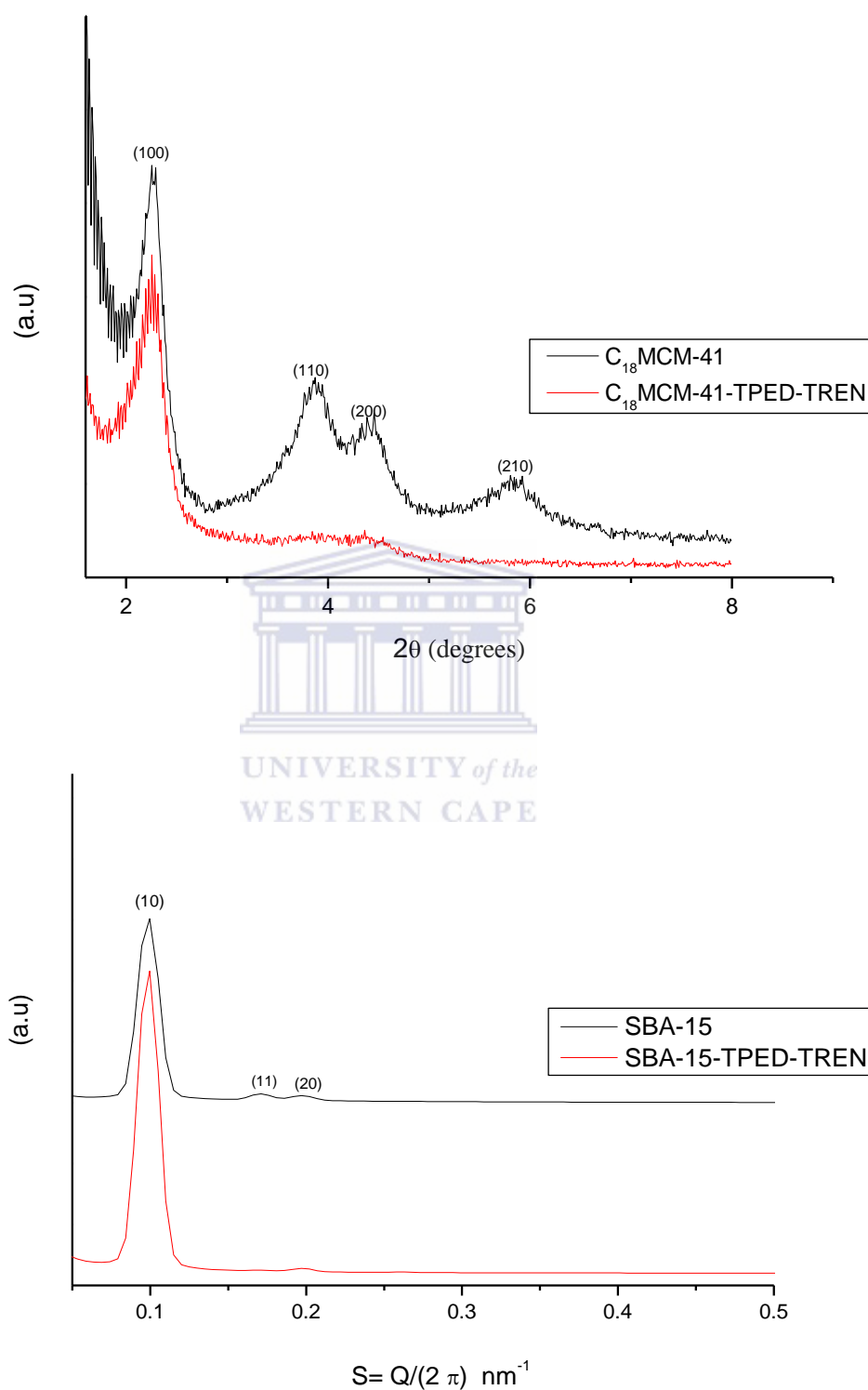
## Chapter 8: Expansion of amine groups

Chapter 8 focuses on the expansion of amine groups through using a bromopropanoate linker to achieve the expansion. The synthetic protocol was employed so that amine groups may be expanded in a “branched out” manner while still allowing sufficient space for gas diffusion from the surface into the cavities of the mesoporous silica used in the study. The sorbents discussed in this chapter would be denoted as 3<sup>rd</sup> generation (G3) as it requires multiple grafting steps in order to achieve the expanded amine groups on the surface.

The G3 adsorbents were prepared to investigate whether increasing the chain length and the number of NH groups would increase the CO<sub>2</sub> capturing capabilities. The chain length would assist in gas diffusion through the proposed materials and the number of amines would provide more sites for CO<sub>2</sub> to react with. The synthetic protocol employed to prepare the amine expanded adsorbents are displayed in the scheme below.



**Scheme 8:** Synthetic route to TPED-TREN grafted C<sub>18</sub>MCM-41 and SBA-15.

8.1 XRD and SAXS of TPED-TREN grafted  $C_{18}$ MCM-41 and SBA-15

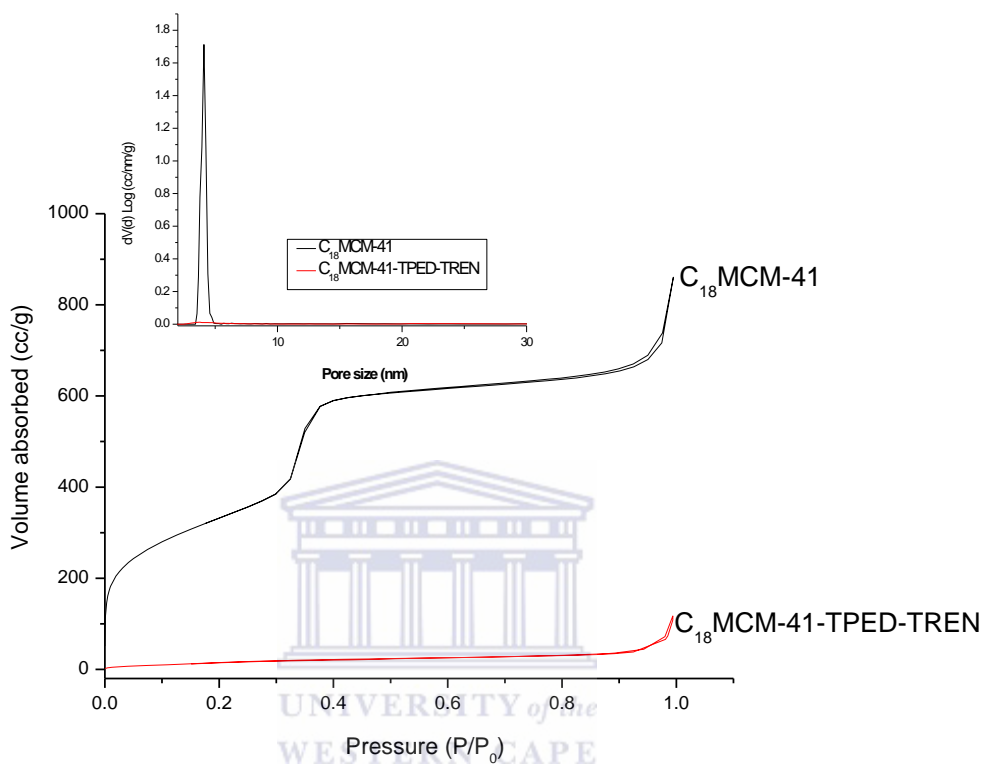
**Figure 45:** Powder XRD and SAXS patterns of TPED-TREN grafted  $C_{18}$ MCM-41 and SBA-15.

Figure 45 a shows the powder XRD patterns of TPED-TREN grafted C<sub>18</sub>MCM-41. C<sub>18</sub>MCM-41 showed a strong diffraction peak (100) at 2.3° and higher order peaks (110), (200) and (210) at 3.9°, 4.5° and 6.0°, respectively. These can be indexed to the hexagonal symmetry of mesoporous silica. The existence of the higher order indices (200 and 210) indicates the long range ordering of C<sub>18</sub>MCM-41. The d spacing value for C<sub>18</sub>MCM-41 calculated from the (100) peak was 4.20 nm. Grafting C<sub>18</sub>MCM-41 with TPED-TREN yielded a different diffraction pattern. The long range ordering was diminished, along with the main (100) peak. The decrease in intensity of the diffraction patterns indicated that TPED-TREN was incorporated into the silica matrix. The d-spacing remained relatively unchanged after grafting C<sub>18</sub>MCM-41 with TPED-TREN which suggests the structure was not compromised or altered during the grafting step. SBA-15 grafted with TPED-TREN SAXS patterns are displayed in Figure 45 b. SBA-15 displayed three peaks which may be indexed to (10), (11) and (20) and which are associated with p6mm 2D hexagonal shape. The existence of the peaks confirms the highly ordered structure of SBA-15. The s value of the indexes at (10), (11) and (20) were 0.1, 0.17 and 0.20 nm<sup>-1</sup> respectively. The d-spacing value was calculated from the main peak indexed at (100), and was calculated to be 10 nm, with an a<sub>0</sub> of 11.56 and wall thickness of 4 nm. Grafting SBA-15 with TPED-TREN resulted in a reduction in the intensity of the SAXS patterns. The (10) peak shifted to a slightly higher s value, but was still comparable to SBA-15, as the shift in s was not significant enough to change the d-spacing. The d-spacing value of SBA-15-TPED-TREN was estimated to be 10.4 nm with unit cell parameter a<sub>0</sub> = 12.03 and the resultant wall thickness was 4.35 nm. The unit cell parameter and wall thickness increased after the grafting steps, which could be an indication that the organic materials were situated on and inside the pores of SBA-



15. Grafting TPED-TREN onto the pore walls of SBA-15 did not affect the structural ordering.

## 8.2 Textural properties of TPED-TREN grafted $C_{18}$ MCM-41 and SBA-15



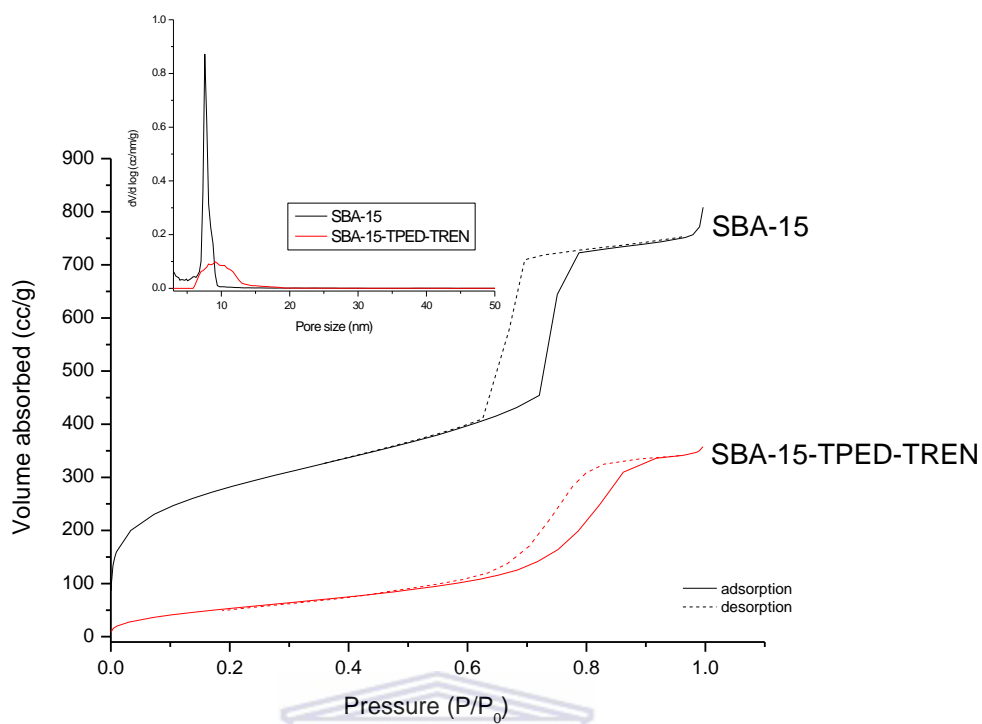


**Figure 46:** N<sub>2</sub> Physisorption isotherms of TPED-TREN grafted C<sub>18</sub>MCM-41 and SBA-15.

**Table 19:** Textural properties of TPED-TREN grafted C<sub>18</sub>MCM-41 and SBA-15.

Sample	Surface area (m <sup>2</sup> /g)	Pore volume (cm <sup>3</sup> /g)	Pore size (nm)	D spacing (nm)	a <sub>0</sub> (nm)	Wall thickness (nm)
C <sub>18</sub> MCM-41	1211	1.3	4.4	2.8	3.31	1.1
C <sub>18</sub> MCM-41-TPED-TREN	82	0.1	3.8	2.6	3.2	1.0
SBA-15	1024	1.3	7.6	10.0	11.56	4.0
SBA-15-TPED-TREN	200	0.33	6.6	10.4	12.03	5.4

Figure 46 shows the N<sub>2</sub> physisorption isotherms of C<sub>18</sub>MCM-41- TPED-TREN and SBA-15- TPED-TREN. The specific surface area of C<sub>18</sub>MCM-41, SBA-15, C<sub>18</sub>MCM-41-TPED-TREN and SBA-15- TPED-TREN was evaluated using the BET method. The pore sizes were obtained using the BJH method. Table 19 summarizes the textural properties of TPED-TREN grafted C<sub>18</sub>MCM-41 and SBA-15. Figure 46 shows that all the isotherms are type IV according to the IUPAC classification that is associated with the presence of mesopores [2].

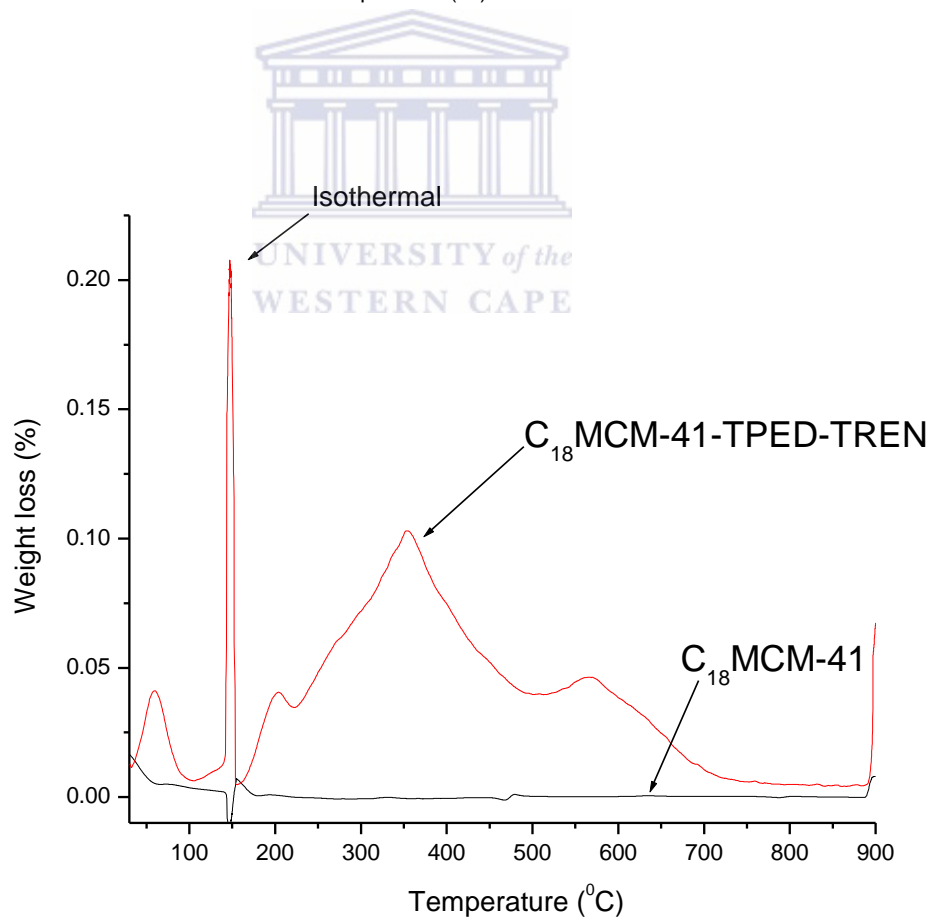
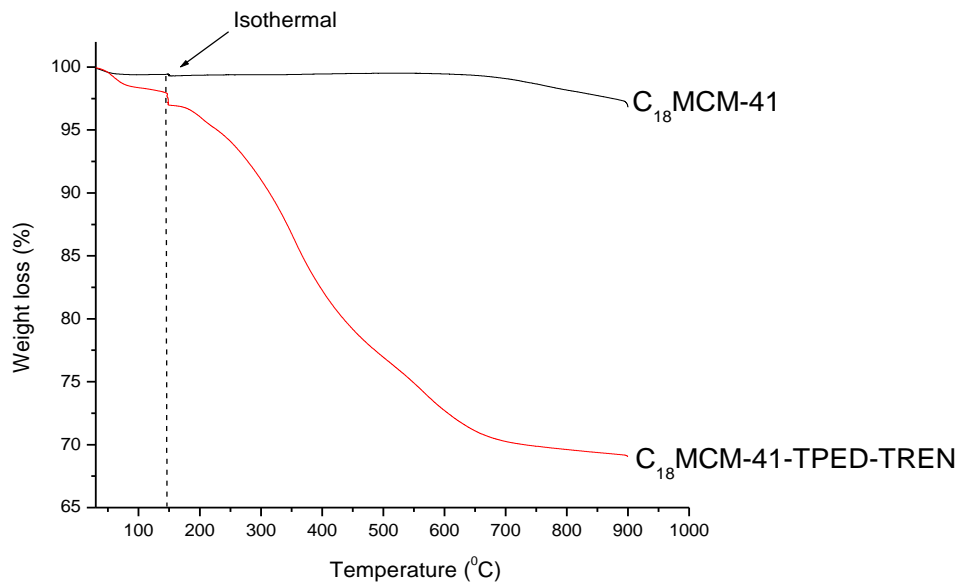
C<sub>18</sub>MCM-41-TPED-TREN isotherm displayed that considerably less N<sub>2</sub> uptake was achieved in comparison to the parent material. The specific surface area was reduced from 1211-82 m<sup>2</sup>/g, accompanied by a reduction in pore volume from 1.3 to 0.1 cc/g and pore size from 4.4 to 3.8 nm. Grafting of TPED-TREN constituted the change in structural properties. The steep uptake due to the condensation of N<sub>2</sub> in the mesopores of C<sub>18</sub>MCM-41 in the relative pressure range  $P/P_o$  (0.2-0.4) was non-existent in C<sub>18</sub>MCM-41- TPED-TREN. This implies that the mesopores of C<sub>18</sub>MCM-41 were almost completely filled with organic material, and the resultant shape of the isotherm was due to multilayer absorption in the relative pressure range. The N<sub>2</sub> isotherm of C<sub>18</sub>MCM-41-TPED-TREN therefore revealed that multiple grafting step immobilizing amine functionalities on C<sub>18</sub>MCM-41 drastically decreased the structural properties of the support material. The PSD of C<sub>18</sub>MCM-41-TPED-TREN is displayed in Figure 46. C<sub>18</sub>MCM-41-TPED-TREN showed a broad size distribution owing to the uneven successive grafting of organic materials in the pore walls of C<sub>18</sub>MCM-41.

SBA-15 showed a sharp increase in a narrow range of relative pressure  $P/P_o$  (0.6-0.8) which was due to the capillary condensation of nitrogen in the mesopores. The adsorption and desorption branches are parallel with one another showing the highly

ordered structure of SBA-15. SBA-15- TPED-TREN isotherms displayed differences in comparison to the parent SBA-15.  $N_2$  uptake was reduced. The shape of the adsorption/desorption branches did not coincide, compared to the unmodified SBA-15. The adsorption/desorption branches obtained was possibly attributed to uneven pore filling. Moderate uptake of  $N_2$  in the range of relative pressure  $P/P_o$  (0.6-0.9) was displayed by SBA-15. SBA-15- TPED-TREN, indicated a smaller volume of mesopores (Table 19) caused by pore filling of organic materials. The PSD of SBA-15- TPED-TREN is shown in Figure 46. It can be seen that a much broader PSD was obtained for SBA-15- TPED-TREN in comparison to the parent support. This was indicative of the pore filling of organic materials due to the multiple grafting steps.



8.3 TG analysis



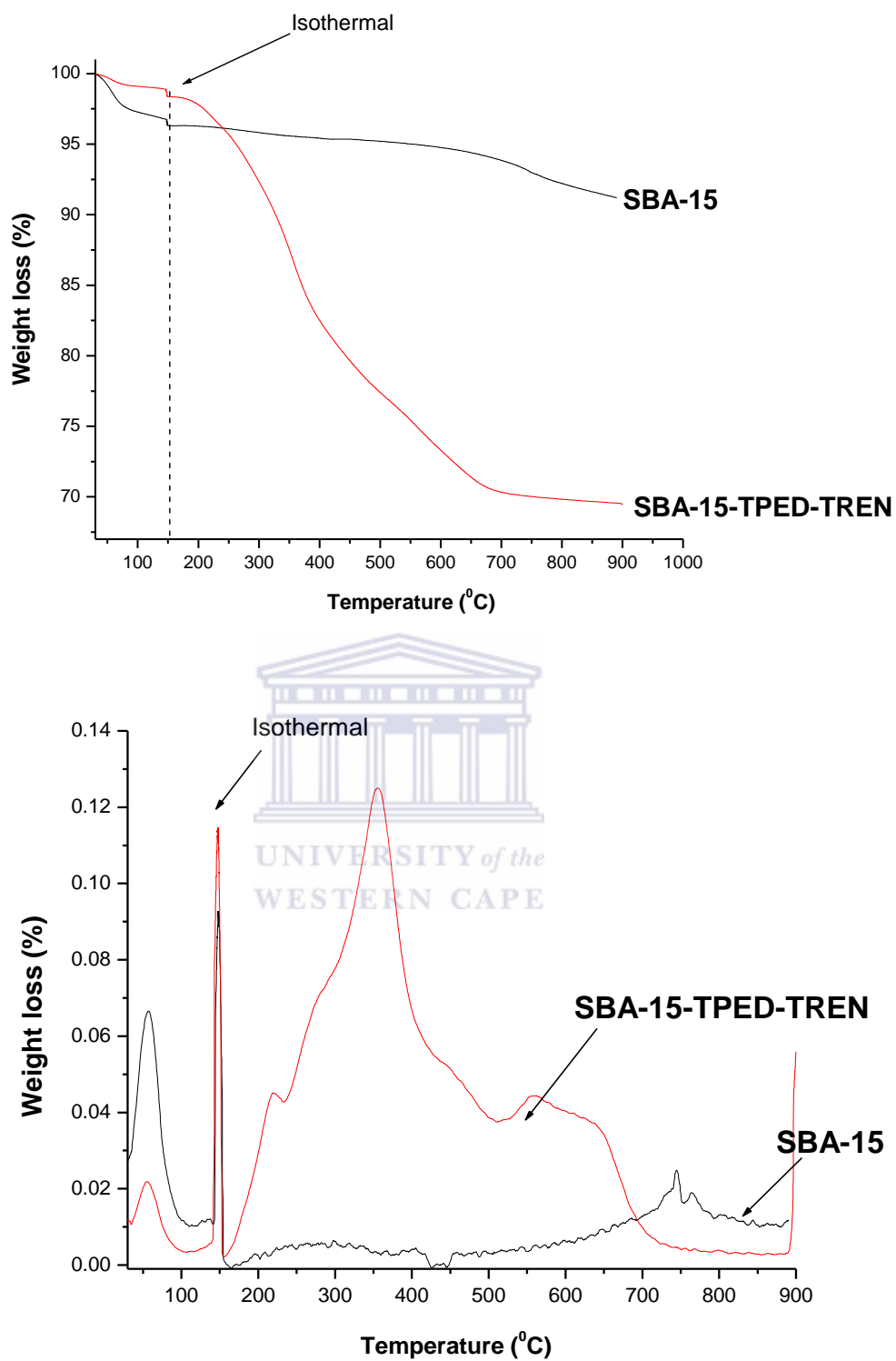
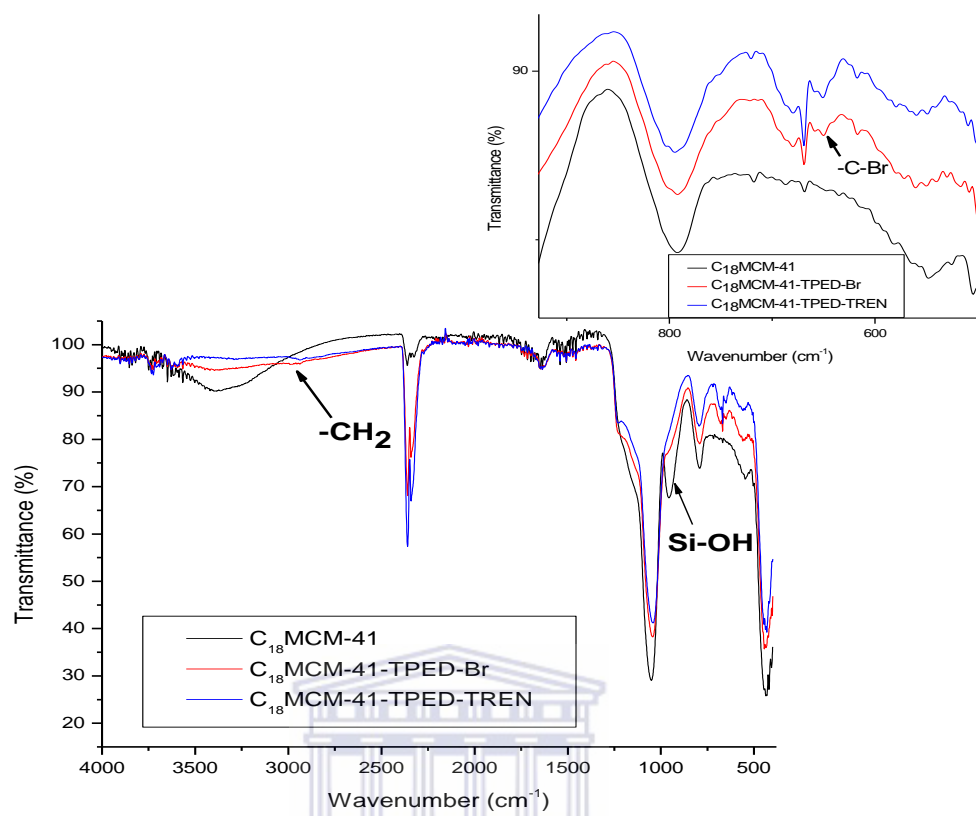


**Figure 47:** TGA/DTA profiles of TPED-TREN grafted C<sub>18</sub>MCM-41 and SBA-15.

Thermal decomposition profiles of TPED-TREN grafted C<sub>18</sub>MCM-41 and SBA-15 were evaluated by TGA/DTA. Figure 47 shows that the decomposition profile of C<sub>18</sub>MCM-41-TPED-TREN appears to be different to TPED-TREN. Initially pre-adsorbed water is evolved below 150 °C, and this was observed for all samples. Isothermal treatment was necessary to remove moisture from the sample, which was indicated in Figure 47. Upon further heat treatment weight loss occurred in a step-wise manner for TPED-TREN grafted supports. C<sub>18</sub>MCM-41-TPED-TREN showed three distinct peaks in the DTA profile which occurred roughly at 200 °C, 350 °C and 580 °C. The weight loss at these temperatures corresponded to 1.8, 18.3 and 7 % respectively. The weight loss can be attributed to the decomposition of organic materials that were grafted in a stepwise manner on C<sub>18</sub>MCM-41. The initial loss possibly attributed to the decomposition of TREN groups, and the subsequent decomposition due to TPED-Br in order of bond strength with respect to the support. SBA-15-TPED-TREN displayed a similar decomposition profile to C<sub>18</sub>MCM-41-TPED-TREN. SBA-15-TPED-TREN weight loss was observed in the temperature range between 210-650 °C. The DTA profiles in this temperature range are shown in Figure 47. Three not so well resolved peaks are observed in this region corresponding to a weight loss of 2, 19.5 and 7 %. It is clear that the weight loss in these regions was due to the decomposition of organic materials that were grafted on SBA-15. Interestingly both C<sub>18</sub>MCM-41 and SBA-15 displayed similar loading of organic material, with SBA-15 having slightly higher loading, even though both supports had different structural properties. C<sub>18</sub>MCM-41, however, would expect to lose its sorption properties as SBA-15 offers a large surface area and greater pore size in comparison to C<sub>18</sub>MCM-41. This was confirmed by N<sub>2</sub> physisorption properties of C<sub>18</sub>MCM-41-TPED-TREN (Table 19).

## 8.4 FT-IR analysis



UNIVERSITY of the  
WESTERN CAPE



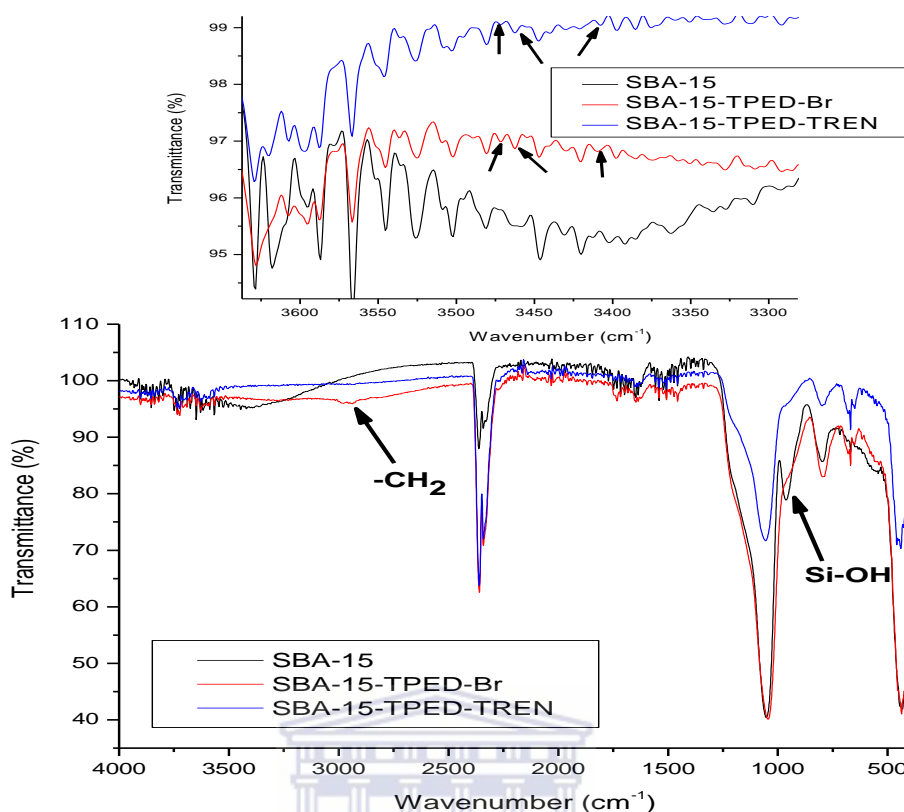


**Figure 48:** FT-IR spectra of  $C_{18}$ MCM-41, SBA-15,  $C_{18}$ MCM-41-TPED-TREN and SBA-15-TPED-TREN.

FT-IR was used to determine the chemical composition of support materials ( $C_{18}$ MCM-41 and SBA-15) as well as to determine whether TPED-TREN was grafted onto the surface of the supports. Figure 48 shows the FT-IR spectra of  $C_{18}$ MCM-41, SBA-15 as well as TPED-TREN grafted  $C_{18}$ MCM-41 and SBA-15. Both  $C_{18}$ MCM-41 and SBA-15 displayed characteristic peaks associated with silica materials. A strong band at  $1052\text{ cm}^{-1}$  for  $C_{18}$ MCM-41 and  $1053\text{ cm}^{-1}$  for SBA-15 was due to Si-O-Si stretching vibrations. The bands at  $957\text{ cm}^{-1}$  and  $963\text{ cm}^{-1}$  were attributed to Si-OH vibrations for  $C_{18}$ MCM-41 and SBA-15 respectively. Broad absorption bands in the range of  $3359\text{--}3404\text{ cm}^{-1}$  for the unmodified  $C_{18}$ MCM-41 and SBA-15 materials was attributed to the  $-\text{OH}$  stretching vibrations of silanol groups and pre-adsorbed water molecules [3]. Upon functionalization an immediate

difference in FT-IR spectra was observed. A consumption of silanol groups was observed by the reduced intensity of the absorption band at  $957\text{ cm}^{-1}$  and  $963\text{ cm}^{-1}$  for C<sub>18</sub>MCM-41 and SBA-15 (Figure 48) during the grafting step as a result of the alkoxy silanes with the surface of the supports. Absorption bands at 2938 and  $2928\text{ cm}^{-1}$  (Figure 48) can be attributed to the alkyl ( $\nu\text{CH}$ ) stretching vibrations. FT-IR spectra obtained suggest the formation of Si-O-CH<sub>3</sub> due to the grafting process. A C-Br stretch was observed at  $650.3\text{ cm}^{-1}$  that confirms the presence of the halogen after the attachment of bromopropanoate molecule [4]. SBA-15-TPED-TREN displayed new absorbance bands in the region  $3400\text{-}3500\text{ cm}^{-1}$  which are due to asymmetric and symmetric NH<sub>2</sub> stretching. The appearance of the new bands after successive grafting steps with TPED and TREN confirms that the grafting process was successfully carried out, although the intensity of the bands are weak, which is expected as small quantities of the amine functionalities were added, not forgetting the steric hindrances that may occur as the number of amine groups are expanded on the surfaces of the supports used.

8.5 CO<sub>2</sub> isotherms

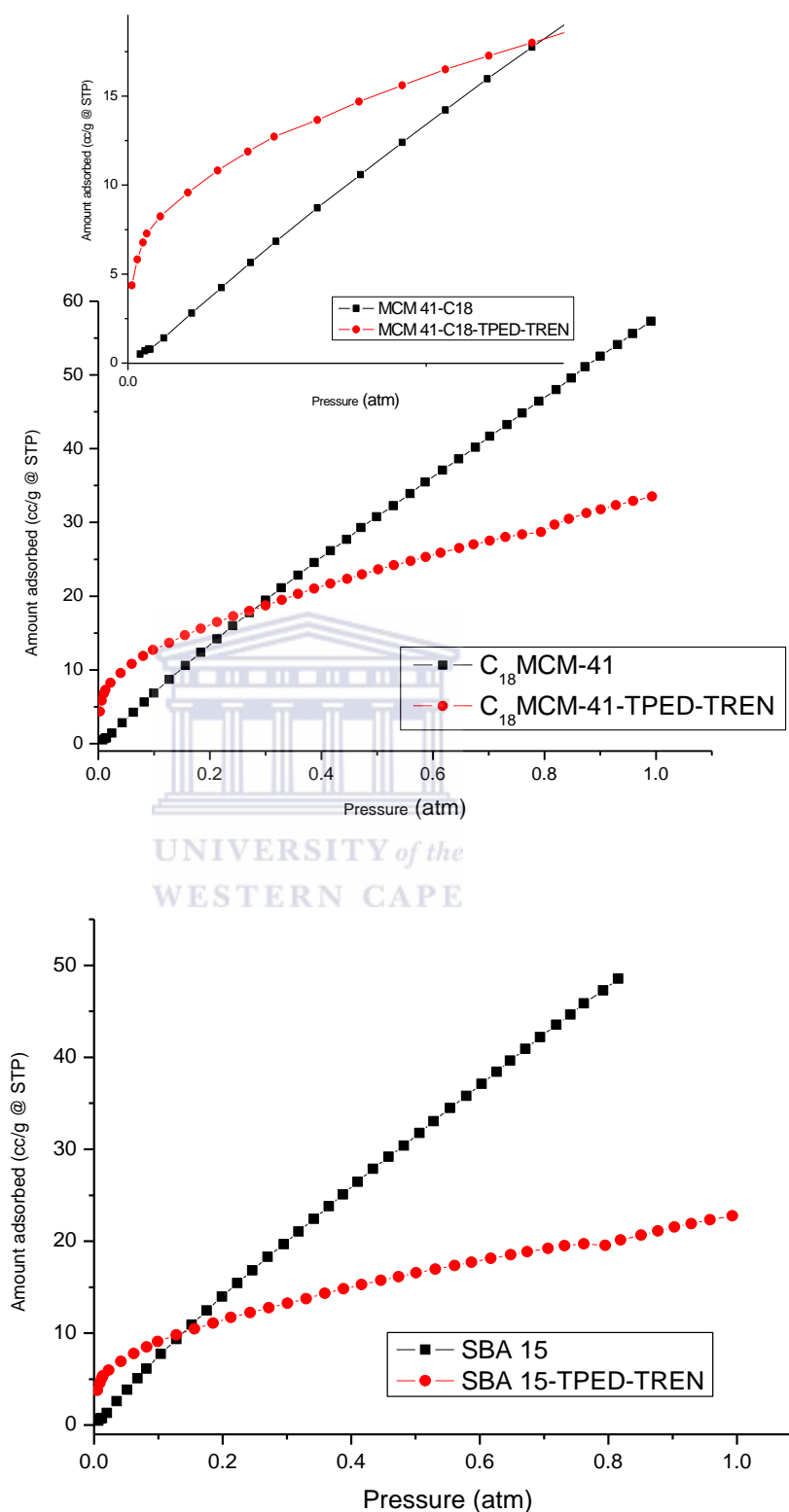


**Figure 49:** CO<sub>2</sub> isotherms of C<sub>18</sub>MCM-41- TPED-TREN and SBA-15- TPED-TREN performed at 0 °C.

Figure 49 showed that at low pressure both C<sub>18</sub>MCM-41- TPED-TREN and SBA-15-TPED-TREN showed superior CO<sub>2</sub> uptake in comparison to the unmodified supports. The adsorption capacity of TPED-TREN grafted supports was taken at a partial pressure of 0.15 bar that equates to approximately 0.148 atm, because it is at this partial pressure that the CO<sub>2</sub> concentration corresponds to the effluent gases from a typical power plant. CO<sub>2</sub> uptake of unmodified supports was minimal at low pressure and gradually increased as the pressures increased, which revealed the pressure dependence on the adsorption capacity of the sorbents. These characteristics are attributed to physical adsorption processes, which have been reported before [5-7]. The CO<sub>2</sub> adsorption capacity of C<sub>18</sub>MCM-41- TPED-TREN and SBA-15- TPED-TREN was higher at low pressures, and the pressure dependence was not as apparent as observed from the unmodified sorbents, as the CO<sub>2</sub> uptake did not increase as in the case of the unmodified sorbents. This phenomenon is characteristic of chemisorption and is observed by the “knee” at low pressure, which was reported before [5]. CO<sub>2</sub> adsorption capacity of C<sub>18</sub>MCM-41- TPED-TREN and SBA-15-TPED-TREN at partial pressure 0.148 atm was 0.06 and 0.05 mmol/g. The adsorption capacity of TPED-TREN grafted supports was almost similar, which is in good accordance with the thermal decomposition profiles of the sorbents having similar organic loading (Figure 49), as mentioned before. CO<sub>2</sub> adsorption capacity of TPED-TREN grafted supports are relatively low and this could be due to adsorption being performed at 0 °C. At higher temperature (e.g. 25 and 75 °C) the adsorption capacity might be higher than the obtained values. Nevertheless the adsorption capacity of the modified adsorbents was relatively higher in comparison to the unmodified sorbents, which proves that the successive grafting of amine groups on sorbents increased the sorbent’s adsorption capacity.

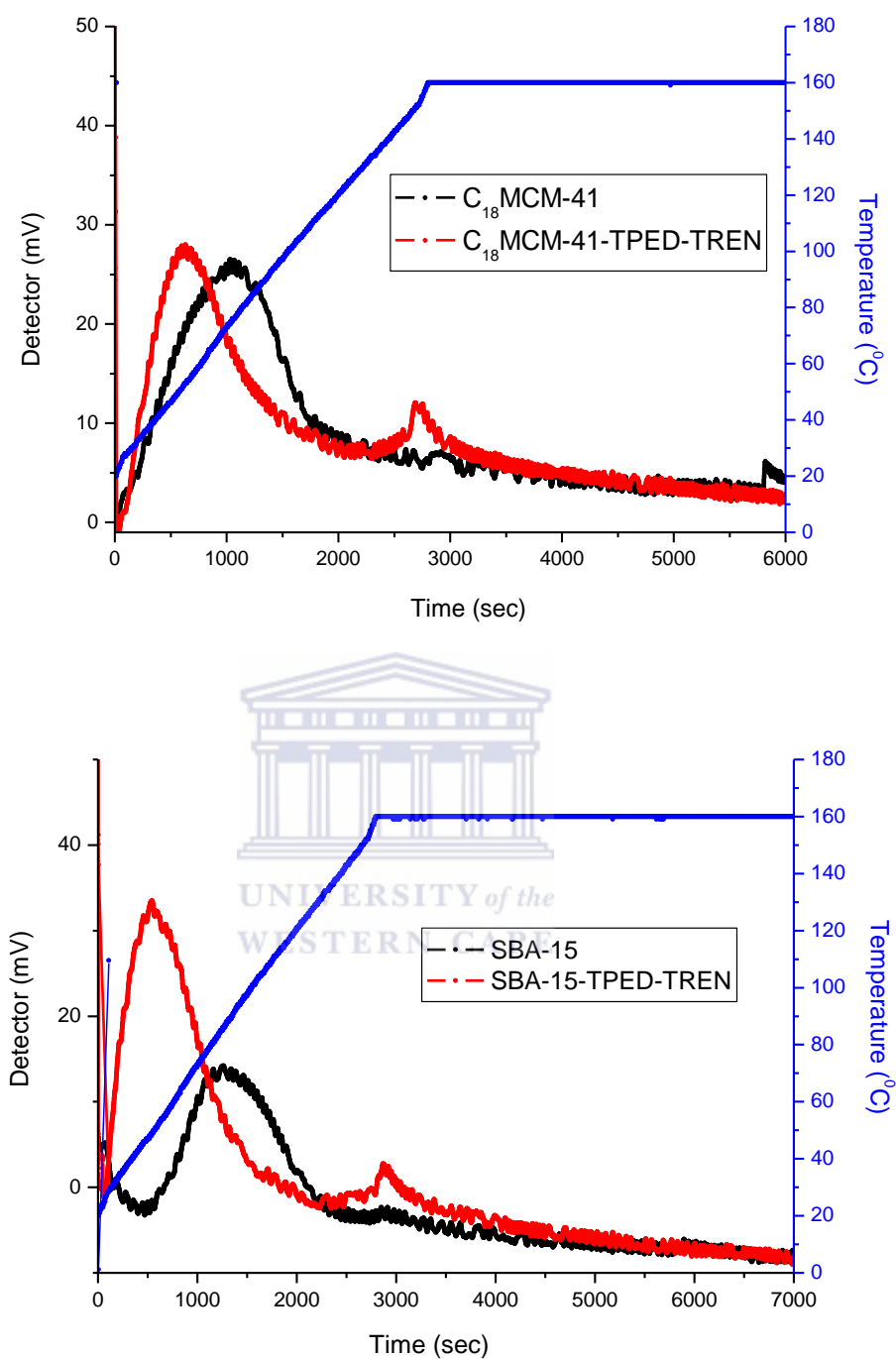
8.6 CO<sub>2</sub> TPD studies

Figure 50: CO<sub>2</sub> TPD profiles of TPED-TREN modified C<sub>18</sub>MCM-41 and SBA-15.

**Table 20:** CO<sub>2</sub> adsorption capacities of TPED-TREN modified C<sub>18</sub>MCM-41 and SBA-15.

Sample	CO <sub>2</sub> capacity (mmol/g)	N content (mmol/g)	N <sub>2</sub> efficiency (CO <sub>2</sub> /N <sub>2</sub> )
C <sub>18</sub> MCM-41	0.02	-	-
C <sub>18</sub> MCM-41-TPED-TREN	0.14	4.82	0.03
SBA-15	0.08	-	-
SBA-15-TPED-TREN	0.14	4.61	0.03

The CO<sub>2</sub>-TPD profiles of C<sub>18</sub>MCM-41 and SBA-15 grafted with TPED initially, followed by the subsequent attachment of TREN, is shown in Figure 50. The adsorption capacity of C<sub>18</sub>MCM-41-TPED-TREN and SBA-15-TPED-TREN was obtained from the area under the curve of the CO<sub>2</sub>-TPD profiles (Figure 50). Parent C<sub>18</sub>MCM-41 and SBA-15 materials showed a single desorption peak (Figure 50) which was attributed to the desorption of physisorbed CO<sub>2</sub>. C<sub>18</sub>MCM-41-TPED-TREN and SBA-15-TPED-TREN (Figure 50) displayed two desorption peaks, the first peak due to physisorbed CO<sub>2</sub>, and the second at a higher temperature which was attributed to the desorption of chemisorbed CO<sub>2</sub>. Amine grafted TPD profiles showed that more CO<sub>2</sub> (Table 20) was desorbed when observing the peak maxima of C<sub>18</sub>MCM-41-TPED-TREN and SBA-15-TPED-TREN (Figure 50). The enhanced CO<sub>2</sub> adsorption capacity was attributed to the increased number of amine groups, as well as the terminal primary amine groups provided by TREN. The terminal primary amine groups provide sufficient active sites for CO<sub>2</sub> absorption, which was previously reported in the literature [3].

Table 20 shows the adsorption capacity, nitrogen content and amine efficiency of TPED-TREN grafted C<sub>18</sub>MCM-41 and SBA-15. The low amine efficiencies obtained (Table 20) were possibly due to minimized accessibility of CO<sub>2</sub> molecules to the grafted amine groups, which are caused by entangled aliphatic carbon chains inside

the mesoporous framework. The reduced amine efficiency may also be brought about through the amine groups not in relative proximity to one another, which is required as 1 mole of CO<sub>2</sub> requires two adjacent amine groups for carbamate formation [8].

In conclusion the increased adsorption capacity of C<sub>18</sub>MCM-41 and SBA-15 grafted TPED-TREN showed that the presence of amine groups on the surface enhances sorbents adsorption capacity. TPED-TREN was grafted onto the supports for the first time to the best of our knowledge. Characterization of C<sub>18</sub>MCM-41-TPED-TREN and SBA-15-TPED-TREN, including desorption studies, proved that the grafting process was carried out successfully and increased the adsorption capacity, when comparing adsorption capacities of parent materials.



**References**

1. Puanggam, M., Unob, F, 2009, "Preparation and use of chemically modified MCM-41 and silica gel as selective adsorbents for Hg(II) ions", *Journal of Hazardous Materials*, vol. 154, pp. 578-587.
2. Sing, K. S. W., Everett, D. H., Haul, R. A. W., 1985, "Reporting physisorption data for gas/solid systems with special reference to the determination of surface area and porosity", *Pure and Applied Chemistry*, vol. 57, no. 4, pp. 603-619.
3. Bhagiyalakshmi, M., Park, S.D., Cha, W.S. & Jang, H.T. 2010, "Development of TREN dendrimers over mesoporous SBA-15 for CO<sub>2</sub> adsorption", *Applied Surface Science*, vol. 256, no. 22, pp. 6660-6666.
4. Andrade, G.F., Soares, D.C.F., Almeida, R.K.D.S. & Sousa, E.M.B. 2012, "Mesoporous silica SBA-16 functionalized with alkoxy silane groups: Preparation, characterization, and release profile study", *Journal of Nanomaterials*, vol. 2012.
5. Sanz, R., Calleja, G., Arencibia, A. & Sanz-Pérez, E.S. 2012, "Amino functionalized mesostructured SBA-15 silica for CO<sub>2</sub> capture: Exploring the relation between the adsorption capacity and the distribution of amino groups by TEM", *Microporous and Mesoporous Materials*, vol. 158, pp. 309-317.
6. Drage, T. C., James, M., Blackman, Pevida, C., and Snape, C. E., 2009, "Evaluation of Activated Carbon Adsorbents for CO<sub>2</sub> Capture in Gasification", *Energy & Fuels*, vol. 23, pp. 2790-2796.
7. Cavenati, S.; Grande, C. A.; Rodrigues, A. E. 2004, "Adsorption equilibrium of methane, carbon dioxide, and nitrogen on zeolite 13X at high pressures", *Chemical Engineering Data*, vol. 19, pp. 1095-1101.
8. Knowles, G. P., Delaney, S W., and Chaffee, A. L., 2006, "Diethylenetriamine[propyl(silyl)]-Functionalized (DT) Mesoporous Silicas as CO<sub>2</sub> Adsorbents", *Industrial Engineering Chemistry, Research*, vol. 45, pp. 2626-263.



## Conclusion

In conclusion, parent support OMS materials were successfully prepared. MCM-41 materials were prepared with different pore sizes with the use of surfactants with different alkyl chain lengths, i.e. with C<sub>14</sub>TABr, C<sub>16</sub>TABr and C<sub>18</sub>TABr. The results obtained showed that the pore size of MCM-41 materials increased with an increasing number of carbons in the surfactant. The pore size increased from 2.6 nm for C<sub>14</sub>MCM-41 to 4.4 nm for C<sub>18</sub>MCM-41. This was ideal as a large surface area and large pore size materials are required for CO<sub>2</sub> adsorption processes. SBA-15 was also prepared using the tri block co polymer. SBA-15 material with a high surface area and large pores of up to 8 nm in diameter was achieved. For comparative purposes, commercial amorphous silica gel (Davalis) was used, as it also had structural characteristics of an adsorbent for capturing CO<sub>2</sub>, such as large pores, although the surface area was not as high. Characterization of structural and textural properties of sorbents used in the study revealed that MCM-41(C<sub>14</sub>TABr, C<sub>16</sub>TABr and C<sub>18</sub>TABr) and SBA-15 was highly ordered, with large surface areas of up to 1302, 1186, 1211 and 1024 m<sup>2</sup>/g for C<sub>14</sub>MCM-41, C<sub>16</sub>MCM-41, C<sub>18</sub>MCM-41 and SBA-15 respectively. The sorbents were thermally stable up to 500 °C. TG studies revealed that supports displayed different concentration of OH groups. OH group content for C<sub>14</sub>MCM-41, C<sub>16</sub>MCM-41, C<sub>18</sub>MCM-41 and SBA-15 was 1.4, 1.1, 1.3 and 4.0 OH groups per nm<sup>2</sup> respectively. The OH group content provided key information as the hydroxyl groups on the surface act as reactive sites for further chemical modification. CO<sub>2</sub> adsorption capacity of C<sub>14</sub>MCM-41, C<sub>16</sub>MCM-41, C<sub>18</sub>MCM-41 and SBA-15 was 0.19, 0.16, 0.11 and 0.26 mmol/g. The trend in

adsorption capacity was found to increase with structural properties such as surface area and pore size.

Both synthetic protocols for MCM-41 materials and SBA-15 were optimized and the ease of synthesis allowed for up scaling, with a fair amount of reproducibility. Mesoporous silica supports were then chemical grafted, initially with APS and TPED, APS having terminal primary amines, and TPED having both primary and secondary amine groups. Powder XRD patterns showed that post modification the structural integrity of the supports remained unchanged, with a slight decrease in intensity of diffraction patterns. Textural properties revealed that the grafting process led to a decrease in specific area, pore volume and pore size, which was brought about by partial pore filling by organic molecules (amine groups). After the grafting step of C<sub>18</sub>MCM-41 with APS, the specific surface area, pore volume and pore size was reduced to 631 m<sup>2</sup>/g, 0.5 cc/g and 2.9 nm respectively. SBA-15 grafted with APS specific surface area, pore volume and pore size was also reduced to 405 m<sup>2</sup>/g, 0.6 cc/g and 6.2 nm respectively. For comparative purposes amorphous silica gel was also grafted with APS and its specific surface area, pore volume and pore size was 405 m<sup>2</sup>/g, 0.6 cc/g and 6.2 respectively. Supports grafted with TPED showed similar trends, with reduction in surface area, pore volume and pore sizes. TG studies of APS and TPED grafted sorbents showed that APS and TPED grafted sorbents were stable up to 250 °C, and displayed additional weight loss in the region of 250-500 °C, which was due to the decomposition of organic molecules (APS and TPED) that were grafted on the supports. FT-IR confirmed the presence of C-H stretching vibrations of propyl chains of APS and TPED. The presence of asymmetric NH<sub>2</sub> stretching, symmetric NH<sub>2</sub> stretching and NH<sub>2</sub> deformation of hydrogen bonded amino groups, also confirmed the grafting of APS and TPED on supports and was

carried out successfully. CO<sub>2</sub>-TPD studies showed that APS and TPED grafted supports desorbed more CO<sub>2</sub> in comparison to the unmodified supports. This confirmed mesoporous supports grafted with amine groups increased the adsorption capacity of the sorbents. C<sub>18</sub>MCM-41-APS and SBA-15-APS adsorption capacity was 0.50 and 0.55 mmol/g, respectively (adsorbed at 25 °C, flow rate 30 ml/min, 99 % CO<sub>2</sub>). Amorphous SG-APS proved to have slightly superior CO<sub>2</sub> adsorption capacity of 0.68 mmol/g. C<sub>18</sub>MCM-41-TPED, SBA-15-TPED and amorphous SG-TPED desorbed 0.50, 0.46 and 0.47 mmol/g of CO<sub>2</sub>, respectively. Amorphous SG-APS desorbed more CO<sub>2</sub> in comparison to C<sub>18</sub>MCM-41 and SBA-15 grafted APS and TPED due to the presence of terminal primary amine of APS, as well as the large pores which facilitate gas diffusion.

G2 TREN grafted sorbents were also prepared with the use of CPS linker. C<sub>18</sub>MCM-41 and SBA-15 was grafted with TREN and fully characterized. Powder XRD patterns showed the structures of both C<sub>18</sub>MCM-41 and SBA-15 were preserved. Textural studies revealed that after the grafting step the surface area, pore volume and pore size was reduced. The total N<sub>2</sub> uptake was reduced but the isotherms still displayed type IV isotherms according to the IUPAC classification, owing to the mesoporous character of the supports post grafting. TG analysis of C<sub>18</sub>MCM-41-TREN and SBA-15-TREN showed three decomposition steps. The first step was due to the loss of physisorbed water followed by the step-wise decomposition of TREN and CPS molecules. C<sub>18</sub>MCM-41-TREN and SBA-15-TREN showed weight loss of 4.3 and 9.6 wt% respectively in the region of 250-500 °C, which was an indication of the extent of the grafting of organic molecules on the two supports. The adsorption capacity of C<sub>18</sub>MCM-41-TREN, SBA-15-TREN and amorphous SG-TREN reached 0.42, 0.51 and 0.27 mmol/g of CO<sub>2</sub> adsorbed at 25 °C (flow rate 30 ml/min, 99 %

CO<sub>2</sub>), respectively. SBA-15-TREN superior adsorption capacity was attributed to high surface area and larger pores, which could accommodate more CO<sub>2</sub> molecules as well as the amine groups grafted on the surface.

Guanidine was grafted on MCM-41 materials with different pore sizes during this study. C<sub>14</sub>MCM-41, C<sub>16</sub>MCM-41 and C<sub>18</sub>MCM-41 grafted guanidine was synthesized via CPS linker. A systematic study was undertaken to track the structural and textural properties during the sequential grafting steps. Grafting MCM-41(C<sub>14</sub>TABr, C<sub>16</sub>TABr and C<sub>18</sub>TABr) with CPS did not lead to any structural changes, as XRD patterns showed the long range ordering was still present after the grafting step, although textural studies showed that the surface area, pore volume and pore size decreased. The narrow PSD indicated the even pore grafting of CPS groups. TG studies showed that CPS decomposed at temperatures above 250 °C, showing the stability of the chemical bonds formed between the silanol and ethoxy groups of CPS. FT-IR confirmed the presence of alkyl carbon stretching frequencies, indicating that CPS was successfully grafted on C<sub>14</sub>MCM-41, C<sub>16</sub>MCM-41 and C<sub>18</sub>MCM-41. The attachment of guanidine on as C<sub>14</sub>MCM-41, C<sub>16</sub>MCM-41 and C<sub>18</sub>MCM-41 reduced the long ranged ordering, which was evident in the XRD patterns. The main (100) peak was still prevalent but shifted to slightly higher 2θ values. HRTEM and HRSEM images confirmed this. <sup>13</sup>C CPNMR was used to confirm the attachment of guanidine in conjunction with FT-IR and elemental analysis. FT-IR confirmed the presence of NH<sub>2</sub> and C=N stretching vibration, together with four resonance peaks observed at 8, 23, 45 and 70 ppm from the <sup>13</sup>C CPNMR, which confirmed the attachment of guanidine. Elemental analysis showed that C<sub>14</sub>MCM-41-guanidine, C<sub>16</sub>MCM-41-guanidine and C<sub>18</sub>MCM-41-guanidine contained 1.12, 0.17 and 0.5 N content (wt%) respectively. The successful grafting of

guanidine on C<sub>14</sub>MCM-41, C<sub>16</sub>MCM-41 and C<sub>18</sub>MCM-41 was further justified by CO<sub>2</sub> isotherms and CO<sub>2</sub>-TPD measurements. Guanidine grafted MCM-41 materials desorbed more CO<sub>2</sub> than the parent MCM-41 materials. All of the above mentioned results confirmed that guanidine was successfully grafted on MCM-41 materials and that the attachment of the amine group increased the supports' adsorption capacity. The systematic change in pore size also attributed to the adsorption capacity as C<sub>18</sub>MCM-41-guanidine displayed the highest adsorption capacity, owing to its larger pore size.

In this work C<sub>18</sub>MCM-41 and SBA-15 grafted with TPED and TREN (G3) using bromopropanoate as a linker was also conducted for the first time to the best of our knowledge as an adsorbent for capturing CO<sub>2</sub>. XRD and SAXS patterns, showed that the structural integrity was maintained after the stepwise grafting process. Textural properties showed a dramatic decrease in surface area up to 82 and 200 m<sup>2</sup>/g for C<sub>18</sub>MCM-41-TPED-TREN and SBA-15-TPED-TREN, respectively. The pore size of the parent materials was also reduced owing to pore filling with organic material. TG showed stepwise decomposition of organic molecules that were grafted on C<sub>18</sub>MCM-41 and SBA-15. FT-IR measurements confirmed the presence of –CH, Br, NH and NH<sub>2</sub> stretching vibrations that confirm their structures. CO<sub>2</sub> isotherms showed that at low pressures C<sub>18</sub>MCM-41-TPED-TREN and SBA-15-TPED-TREN adsorbed more CO<sub>2</sub> due to chemisorption, which confirms the presence of amine groups grafted on the surface. CO<sub>2</sub> adsorption capacity of C<sub>18</sub>MCM-41-TPED-TREN and SBA-15-TPED-TREN reached 0.06 and 0.05 mmol/g, respectively, at 0.15 atm. Interestingly C<sub>18</sub>MCM-41-TPED-TREN and SBA-15-TPED-TREN both desorbed 0.14 mmol/g of CO<sub>2</sub> during TPD measurements, even though both sorbents had different structural

properties such as surface area and pore size. The adsorption capacity obtained was possibly be due to inaccessible amine groups due to steric hindrances.

## **9.2 Future work**

Future work would involve optimization of G2 and G3 sorbents. Fixed-bed studies of the synthesized solid sorbents in order to model a CO<sub>2</sub> effluent gas concentration (15 % CO<sub>2</sub>), and to study the behaviour of sorbents under these conditions, are recommended. Further studies would also be required to investigate the effect temperature and moisture has on the adsorption capacity of as prepared solid sorbents synthesized using a fixed bed setup. Cyclic tests using a fixed bed system in order to determine the durability of the sorbents prepared during this study.

